University of Southampton
School of Civil Engineering and the Environment

Methane Gas Hydrate Morphology and its Effect on the Stiffness and Damping of some Sediments

by
Emily V. L. Rees (née Kingston)

A Thesis Submitted in Fulfillment of the Degree of Doctor of Philosophy in the School of Civil Engineering and the Environment at the University of Southampton

March, 2009

UNIVERSITY OF SOUTHAMPTON

ABSTRACT

SCHOOL OF CIVIL ENGINEERING AND THE ENVIRONMENT

Doctor of Philosophy

METHANE GAS HYDRATE MORPHOLOGY AND IT'S EFFECT ON THE STIFFNESS AND DAMPING OF SOME SEDIMENTS

By Emily V. L. Kingston

Gas hydrates are ice–like compounds found in deep sea sediments and permafrosts. Concise detection and quantification of natural methane gas hydrate deposits, will allow for a more robust assessment of gas hydrate as a potential energy resource or natural geohazard. Current seismic methods, used to identify and quantify gas hydrates, have proved to be unreliable in providing accurate information on the extent of natural gas hydrate deposits, due to the lack of understanding on how gas hydrate affects the host sediment. Direct measurement of some hydrate bearing sediment properties has been made possible in recent years through advances in pressure coring techniques, but methods for dynamically testing these samples at *in–situ* pressures are still unavailable. Laboratory tests on synthetic hydrate bearing sediments have shown that factors such as formation technique, sediment type and use of hydrate former affects the form and structure of hydrate in the pore space and how it interacts with the sediment. The aim of this research was therefore to create methane hydrate in sediments under a variety of conditions, so that the influence of hydrate morphology could be investigated.

A number of experiments were conducted using two distinct formation techniques. The first technique formed methane hydrate from the free gas phase in almost fully water saturated conditions. Five sand specimens, with a range of hydrate contents from 10% to 40% were formed and tested in the gas hydrate resonant column (GHRC). Results from these tests were compared with previous results from tests where methane hydrate had been formed from free gas in partially saturated conditions. It was found that formation method had a significant influence on the properties of the hydrate bearing sand, and therefore the morphology of the hydrate in the pore space. The second set of experiments formed methane hydrate from free gas within partially saturated sediments, but where the sediments were made up of coarse granular materials with a variety of particle size and shape. As it had been established that hydrate acts as a cement when formed under partially saturated conditions, the experiments aimed to observe the effect of particle size and shape on hydrate bonding mechanisms. The results showed that the influence of disseminated hydrate on the physical properties of the specimens was affected by both mean particle size and by particle shape, with the surface area of the sediment grains influencing the volume and distribution of hydrate throughout a material and therefore it's bonding capabilities.

In addition to the experiments on synthetic hydrate specimens, five core sections containing naturally occurring gas hydrate in fine grained sediments were made available to the University of Southampton from the Indian National Gas Hydrate Program (NGHP) 01 expedition. High resolution CT imaging of the core sections observed large volumes of methane hydrate as a network of veins throughout the specimens. Due to sample disturbance caused during the depressurisation and subsequent freezing of the samples prior to delivery, dynamic testing in the gas hydrate resonant column apparatus was not feasible. Therefore, the hydrate was dissociated and a number of geotechnical tests were undertaken on the remaining host sediment. Results from these tests suggested that hydrate dissociation could affect host sediment properties, due to a change in water content, salinity and structure.

Contents

List of Figures

List of Tables

List of Symbols and Abbreviations

Symbols

a	Peng–Robinson constant
b	Peng–Robinson constant
b	Velocity stress exponent
d	Diameter of specimen
e	Void ratio
f	Frequency of excitation
$f_{1,2}$	Frequency either side of ω_r obtained from half-power method
g	Acceleration due to gravity
h	Height above specimen
h_{0i}, h_{1i}	Heights of bottom and top, respectively, of added masses m_i
k	Spring stiffness
l	Length of specimen
m	Lumped mass
m_T	Mass of specimen (m_i added masses at top of specimen)
m_w	Mass of water in specimen
n	Number of moles
x_1, x_2	Consecutive peaks of amplitude during free vibration decay
$\ddot{x}$	Angular acceleration
y_{ci}	Center of gravity of mass m_i measured from top of specimen
y_T	Total deflection of a beam in flexure from the neutral axis

A	Stiffness coefficient
C_p	Particle characteristic coefficient
D	Distance to a point on a beam perpendicular to the neutral axis
D	Damping ratio

E	Youngs modulus (E_{flex} Youngs modulus from flexural excitation)
G	Shear modulus
G_{max}	Small strain shear modulus
G_{sat}	Shear modulus of saturated specimen
G_s	Specific gravity
H_c	Hydrate content
I	Mass polar moment of inertia of specimen
I_b	2nd moment of area of specimen
I_o	Mass polar moment of inertia of drive plate
I_{am}	Mass polar moment of added mass
I_{yi}	Area moment of inertia of mass m_i
K	Bulk modulus
K_d	Bulk modulus of dry frame
K_f	Bulk modulus of fluid
K_m	Average bulk modulus of sediment grains
K_{sat}	Bulk modulus of saturated specimen
L	Length of specimen
M_g	Molar mass of methane hydrate
M_w	Molar mass of water
N	Number of additional masses
P	Pressure
Q	Quality factor
Q_{lf}^{-1}	Longitudinal wave attenuation
Q_s^{-1}	Shear wave attenuation
R	Radius of specimen
R	Universal gas constant
T	Temperature
V	Voltage
V_{lf}	Longitudinal wave velocity
V_p	Compressional wave velocity
V_s	Shear wave velocity
V_v	Volume of voids
X_{max}	maximum amplitude of resonance
Z	Accelerometer constant
α	Peng–Robinson constant
δ	Logarithmic decrement

ε	Flexural strain
ε_{avg}	Average flexural strain
γ_c	Cyclic strain in torsion
ρ	Density of specimen
ρ_{hy}	Density of methane hydrate
θ	Angle of rotation
ω_f	Natural frequency of vibration in flexure
ω_n	Natural frequency of vibration in torsion
σ'	Effective confining pressure
ν	Poisson's ratio
ϕ	Porosity
ϕ_c	Critical porosity

Abbreviations

ASTM	American Society for Testing and Materials
BS	British Standard
BSR	Bottom simulating reflector
CCT	Contact cement theory
CH_4	Methane
CO_2	Carbon dioxide
CT	Computed tomography
DDL	Diffuse double layer
DEM	Differential effective medium
DLF	Distributed, low flux
DPC	Digital pressure controller
EMF	Electromotive force
FHF	Focused, high flux
FPC	Fugro pressure corer
FVD	Free vibration decay
GDS	Global Digital Systems
GHASTLI	Gas Hydrate and Sediment Testing Laboratory Instrument
GHRC	Gas Hydrate Resonant Column
HRC	HYACE rotary corer
HSZ	Hydrate stability zone
LBB	Leighton Buzzard sand grade B

LBE	Leighton Buzzard sand grade E
LVDT	Linear variable differential transformer
mbsf	metres below sea floor
MSCL–P	Multi–sensor core logger – pressure
NGHP	National Gas Hydrate Program
ODP	Ocean Drilling Program
PAV	Proportional air valve
PCS	Pressure core sampler
SEM	Scanning electron microscope
THF	Tetrahydrofuran

Acknowledgements

Firstly, I would like to thank all those who gave me technical support over the course of my PhD. Special thanks go to Harvey Skinner and Mike Rose from the Civil Engineering labs for helping me solve endless plumbing and electronic problems, as well as Karl Snelling and Jerry Sutton from GDS instruments, who were always on the other end of the phone for all my GHRC maintenance needs. Coming from outside the Civil Engineering field, their help and support was invaluable in familiarising me with the laboratory equipment, and I could not have completed my experiments without them.

I would like to thank Ian Sinclair and Andrew Moffat for their assistance in using the CT scanner in the Mechanical Engineering department, and for their expertise in interpreting the results. With regard to analysis of the NGHP-1 natural hydrate samples in Chapter 5, I would also like to thank Belinda Alker and Darryl Green from the National Oceanography Centre, Southampton for assisting in a number of salinity and organic content tests. Thanks also go to the staff from Surrey Geotechnical Consultants for the geotechnical testing they undertook on my behalf.

I must also give great thanks to my supervisors Chris Clayton, Jeff Priest and Angus Best, who gave me the opportunity to study gas hydrates with them, and have always been there to support and encourage me. I particularly want to thank Jeff, as he has patiently helped me understand and use the gas hydrate resonant column to complete this research, and without his guidance I could not have finished this thesis. I also thank EPSRC for the financial support of this research.

I want to thank my fellow PhD students Gabi, Man and Jon, who have helped me in numerous ways, but mostly by just being great listeners. I also need to thank Ollie and John for their vast knowledge of Latex, and in helping me with various mathematical problems.

I wish also to thank my Mum and Dad, who have always believed in me, even if sometimes I didn't believe in myself. And finally, I thank my husband Lew, who has always been there to help and inspire me. His knowledge, experience and constant pep talks kept me going through the tough stages of this research, and without him I would not have started this project, let alone finished it.

Chapter 1

INTRODUCTION

Naturally occurring gas hydrates are ice–like, crystalline solids that form when water and gas molecules are brought together in a low temperature and high pressure environment. Under these conditions, water molecules can form a lattice or cage that surrounds small gas molecules, such as methane or a number of other hydrocarbon gases. The water molecules encase the gas, or guest molecule, in a structure similar to that of ice. However, unlike ice, the presence of a guest molecule means that under high pressure, hydrate can form at temperatures above 0°C.

The most common naturally occurring gas hydrate is methane. Methane hydrate is stable at temperatures above the freezing point of water when pressures exceed 2.5MPa (Figure 1.1). There are a number of natural environments where the right pressures and temperatures for methane hydrate formation exist. Submarine sediments in a water depth of over 400m have the potential to harbour methane hydrate (Sloan, 1998), as well as sediments over 200m deep in the Arctic permafrost.

1.1 Background

Gas hydrates in natural sediments have been studied since they were first discovered in the Russian permafrost in 1965 (Makogon 1965 cited in Makogon et al. (2007)). By means of drilling, coring and seismic surveying operations, methane gas hydrate has now been identified in most continental shelf and permafrost environments worldwide (Figure 1.2). The estimated volume of methane gas trapped within natural hydrate deposits is thought to exceed $10^{16}\mathrm{m}^3$ (Dawe &

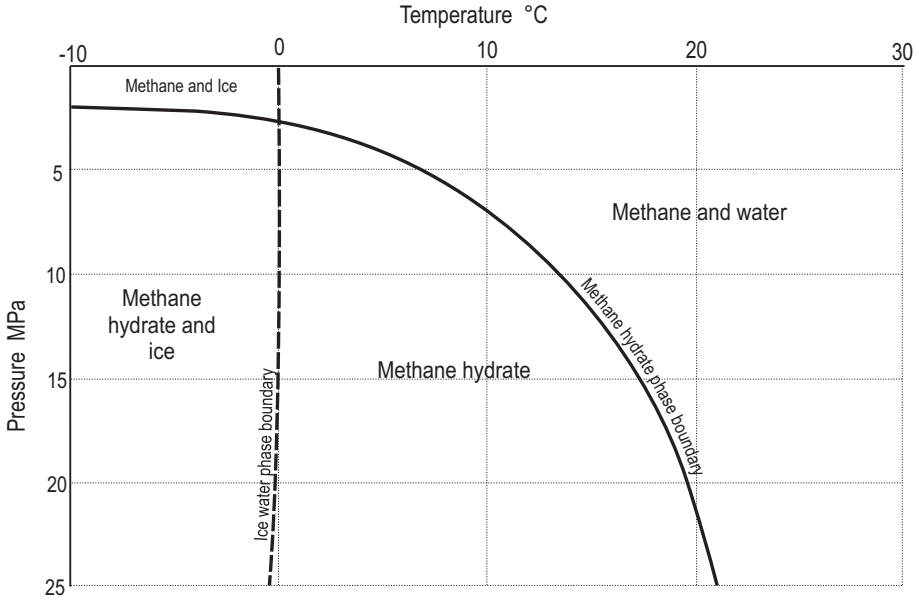

Figure 1.1: Graph showing methane hydrate phase boundary with regards to temperature and pressure

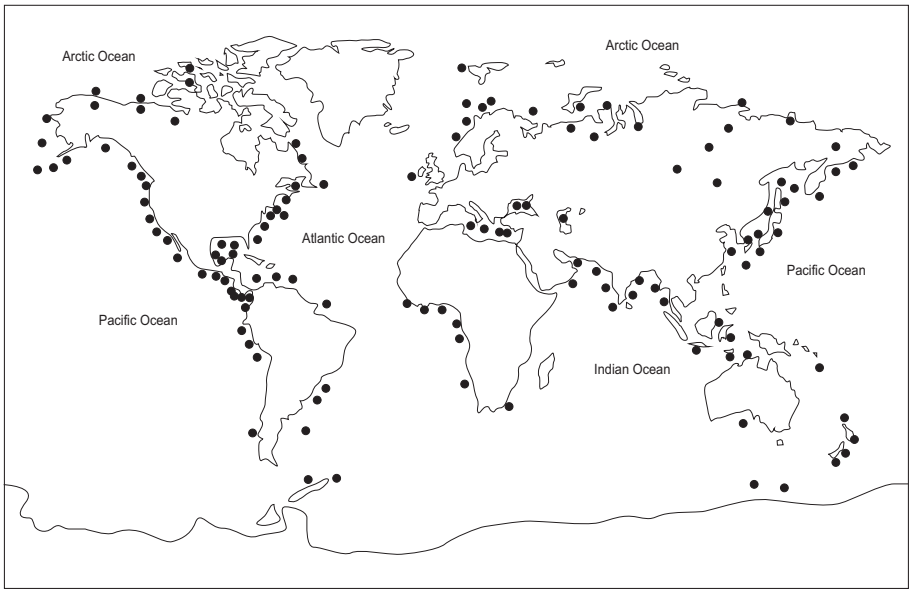

Figure 1.2: Locations of worldwide hydrate deposits, discovered via sediment coring or seismic surveying. Redrawn from Kvenvolden et al. (1993) and Makogon et al. (2007)

Thomas, 2007; Milkov, 2004; Katz & Lee, 1990). The identification of such large accumulations of methane gas has important implications with regard to the global environment, in terms of climate change and submarine slope stability. Additionally, there is the considerable effect that this quantity of gas could have on the economy in terms of global energy resources.

Environmental Impacts

Methane, as a greenhouse gas, is 20 times more effective at retaining atmospheric heat than carbon dioxide. At present, methane causes 4 - 9% of the greenhouse effect in the Earth's atmosphere. If the quantity of methane in the atmosphere were to rise sharply, this contribution would escalate. Some evidence has been documented that connects gas hydrate dissociation to global climate change events in the past. Dickens et al. (1995) describe the connection between the Late Paleocene thermal maximum (55.6Ma) and a voluminous release of methane from gas hydrate contained in marine continental sediments. There is also evidence of hydrate dissociation in relation to the Early Toarcian ocean anoxic event (183Ma) and a severe period of global warming in the Mesozoic (Hesselbo et al., 2000; Jahren et al., 2001). As methane hydrate is only stable at low temperature and high pressure, changes in sea temperature and level could cause mass dissociation of near surface deposits.

In addition to the impact that methane hydrate could have on global climate change, submarine hydrates have also been connected to slope instability on continental margins (Ashi, 1999; Paull et al., 2000). It is thought that the dissociation of gas hydrate in submarine sediments could have been the cause of a number of major underwater landslides, including the Storegga Slide off the coast of Norway (Mienert & Buenz, 2001). Slide and slump scars along the US Atlantic margin have also been well documented which show a possible relationship between gas hydrate decomposition and sediment failures (Booth et al., 1994).

Natural gas hydrates have been acknowledged as a hazard in the oil and gas industry for many years (Katz & Lee, 1990). Hydrate growth causes blockages in high pressure pipelines, and there is a lucrative business in the prevention of its growth by developing efficient hydrate inhibitors. There is also the danger of hydrate formation within the well tubing and drill string of a producing well. Blockage in these situations can create gas kicks and other dangerous situations (Katz & Lee, 1990). As deep sea exploration and production from deep oil and gas reservoirs becomes more common, another gas hydrate hazard has been recognised by the oil industry. When drilling through a hydrate bearing sediment, the heat from circulating drilling fluids can change the stability conditions of the surrounding sediment. Gas hydrate

decomposition could cause free gas to be released, or the subsequent 'slush' from melting hydrate could trigger tubing collapse, sea floor instability and slope failures (Dawe & Thomas, 2007).

Economical Impacts

Economically, gas hydrates may provide a new energy resource for many countries in the future. There are a number of nations keen to produce from gas hydrates, including Japan, Korea and India, as they have little other hydrocarbon resources. The Messoyakha gas field in northern Russia, has been producing from methane gas hydrate for almost 40 years (Makogon et al., 2007). The dissociation of methane hydrate in the area has provided the free gas that is extracted using conventional techniques. This field could prove that production is possible from hydrate bearing sediments, however, there is some geological evidence suggesting that hydrate dissociation is not the cause of the gas accumulation at Messoyakha (Collett & Ginsburg, 1998). Even so, methods of extracting the gas from *in–situ* methane hydrates are still being investigated, with the prospect of future large scale production (Majarowicz & Osadetz, 2001; Collett, 2004; Pooladi-Darvish, 2004; Dawe & Thomas, 2007; Makogon et al., 2008). There is no doubt over the scale of energy resource that the worldwide accumulations of gas hydrate represent, even though a large volume of the methane trapped within hydrates is potentially non–recoverable. Recent estimates suggest that at current rates, successful exploitation of gas hydrates could provide a further 200 years of world wide energy consumption (Makogon et al., 2007).

1.2 Defining the Gas Hydrate Problem

To properly assess the hazards and economic possibilities of gas hydrates, accurate detection and quantification of methane hydrates is necessary (Makogon et al., 2007). Current geophysical methods still rely on the identification of a sub–surface horizon named the "bottom simulating reflector" or BSR to detect hydrate presence, even though this has been proven to be unreliable (Chand & Minshull, 2003; Singh et al., 1993; Pecher et al., 1996). It is therefore necessary for the seismic signatures of hydrate bearing sediments to be better understood. In order to do this, hydrates can be tested in the laboratory. Ideally, natural hydrate samples are tested and although advances in pressure coring have allowed for intact methane hydrate samples to be recovered, the methods for dynamically testing hydrate bearing sediments at *in–situ* conditions are still unavailable. Therefore, there is a high demand for synthetic hydrates to be

made and tested in the laboratory.

Results from laboratory tests to find the seismic velocities of synthetic hydrate bearing sediments have yielded a wide range of values. Some researchers have reported high compressional wave velocities, over 3000ms^{-1}, for certain concentrations of hydrate in the pore space (Waite et al., 2004), whereas others predict values over 1000ms^{-1} lower at the same concentrations (Spangenberg & Kulenkampff, 2005). Results suggest that hydrate does not have the same affect on seismic velocity for different host sediments. It appears that the form and structure of hydrate is dependant on a variety of factors such as saturation state, sediment type, and whether hydrate forms from a free gas state or from gas dissolved in the pore water. Investigation into hydrate morphology in sediments is therefore key to eventually understanding natural hydrate seismic signatures.

The goal of this research is to investigate how hydrate morphology affects the physical properties of host sediments by utilising previously developed equipment that measures the stiffness and damping of sediment specimens containing methane hydrate (Priest, 2004). Results would provide information on the morphology of hydrate in the pore space, and allow hypotheses to be drawn on the form and structure of methane hydrate in natural sediments. In order to study the affect of hydrate dissociation on host sediment properties, natural hydrate samples have also been investigated and have provided information on the complex morphology of natural hydrate in fine grained sediments.

The aims of this research can therefore be summarised as follows:

- To synthesise methane gas hydrate in fully water saturated porous media, from the free gas state, using the same equipment and materials that were utilised by Priest (2004), so that results from the two sets of experiments can be directly compared. Once methane hydrate has been formed, the aim is to determine the stiffness and damping values of the hydrate bearing sediments so that conclusions on the morphology of hydrate in different formation conditions can be made.
- To form methane hydrate in sediments with a variety of particle size and shape in order to investigate the effect of sediment type on the way hydrate interacts with a host sediment.
- To investigate the morphology of natural methane hydrate through imaging of samples from the field, and subsequent geotechnical testing of these frozen natural samples in the laboratory.

1.3 Outline of Thesis

The thesis consists of the following chapters:

Chapter 2 presents a review of the current literature on methane hydrates including recent developments in sampling, detecting and synthesis in the laboratory. Different techniques used to form hydrates in the laboratory are discussed, highlighting the discrepancies in results obtained with these different techniques.

Chapter 3 introduces the set of laboratory tests undertaken to investigate hydrate morphology. The chapter begins with a description of the equipment used for testing hydrate bearing sediments, followed by a brief discussion on the reduction of data from the resonant column tests. The chapter then describes two testing programmes, detailing the methodology for specimen preparation, hydrate formation and resonant column testing for each set of tests. Typical results from the tests are then given.

Chapter 4 gives the results from the series of tests on hydrates bearing sediments in the resonant column. A discussion of the results from both sets of tests is made, with particular attention given to the comparison of the results in this research to those from previous gas hydrate resonant column work.

Chapter 5 describes the investigation of a number of natural hydrate samples taken from the Indian Ocean during NGHP-1. Results and analysis of three dimensional imaging of the frozen samples gives information on the morphology of hydrates in natural sediments. There is also a description of the sequence of geotechnical tests made on the host sediment, undertaken by the author and various collaborators including research staff at the National Oceanography Centre, Southampton, and Surrey Geotechnical Consultants (SGC). Results from these tests provide information on the *in–situ* properties of hydrate bearing sediments.

Chapter 6 presents the conclusions from each chapter, bringing together a summary of all the findings from each body of work. There are also recommendations for future work using the resonant column apparatus to investigate gas hydrate bearing sediments.

Chapter 2

A Review of Gas Hydrates in Sediments

Gas hydrates have become important to the research community not only because of the potential energy resource they represent, but also due to the impact gas hydrate dissociation could have on the global climate. It is estimated that the quantities of hydrate in sediments globally could exceed the volume of known gas resources by 3000% (Dawe & Thomas, 2007; Milkov, 2004; Makogon et al., 2007). These values however, are based on seismic surveys, and recent drilling suggests that these assessments may be incorrect. There is subsequently a need for greater knowledge of the effects of gas hydrate on host sediment properties, to assist in the correct interpretation of the amounts of hydrate in sub–sea sediments.

This chapter will begin by introducing the chemistry of gas hydrates, before describing the morphology of hydrate in sediments and the problem this poses to the interpretation of sub–surface seismic signatures. It will then continue by detailing the impact hydrate has on the mechanical properties of a host sediment, with a final discussion on why continuing research in this area is necessary.

2.1 An Introduction to Methane Gas Hydrate

Clathrates have interested scientists for almost two centuries. The original discovery of chlorine hydrate by Sir Humphrey Davy in 1811 (Davy, 1811) was the first instance where the inclusion

Structure	I		II		H		
Crystal System	cubic		cubic		hexagonal		
Cavity	small	large	small	large	small	medium	large
Description	5^{12}	$5^{12}\,6^2$	5^{12}	$5^{12}\,6^4$	5^{12}	$4^3\,5^6\,6^3$	$5^{12}\,6^8$
No cavities/unit cell	2	6	16	8	3	2	1
Average cavity radius $\mathring{A}$	3.95	4.33	3.91	4.73	3.91	4.06	5.71
Ideal Unit Cell Formula	$6x\,2y\,46H_2O$		$8x\,16y\,136H_2O$		$1x\,3y\,2z\,34H_2O$		

Table 2.1: Geometry of hydrate crystal cages. Adapted from Sloan (1998).

of molecules of one kind was seen within cavities in the crystal lattice of another (Max, 2000). The term "hydrate" is given to clathrate compounds in which the crystal lattice is made up of water molecules with inclusions of gas molecules. A number of hydrate structures have been catalogued since the original discoveries.

Although gas hydrates had been identified in the laboratory in the 1800's, it was not until the 1965 that Makogon first discovered and studied natural hydrate in the geological environment (Makogon 1965 cited Makogon et al. (2007)). It has been found that hydrates form in a range of sedimentary environments worldwide (Kvenvolden et al., 1993), and that their occurrence is constrained by certain features such as temperature and pressure conditions, gas supply and tectonic setting. The first part of this chapter gives a summary of the chemistry of all clathrate hydrates, before focusing on natural methane hydrate.

2.1.1 Chemistry and Crystalline Structures

Clathrate hydrate has similarities to that of ice, as hydrate contains 85% water on a molecular basis (Sloan, 1998). The difference lies in the crystalline structure, with ice showing a non–planar array of hexagonal rings, compared to that of hydrate which forms 3D water cages in which guest molecules reside. For natural gases, hydrate will form one of three crystallographic lattice types: Structure I (cubic), Structure II (cubic) and Structure H (hexagonal). Until recently it was thought that all hydrate formers fit into these structures, however new research has reported that other lattice types exist (Udachin & Ripmeester, 1999).

Figure 2.1 shows the pentagonal dodecahedron (5^{12}) which is the building block of all hydrate structures. From Table 2.1 it can be seen that this cage is present as the small cavity for all hydrate structures, accompanied by a number of different size cages for each lattice type.

Which of these lattices form depends solely on the the size of the guest molecule (Kirchner

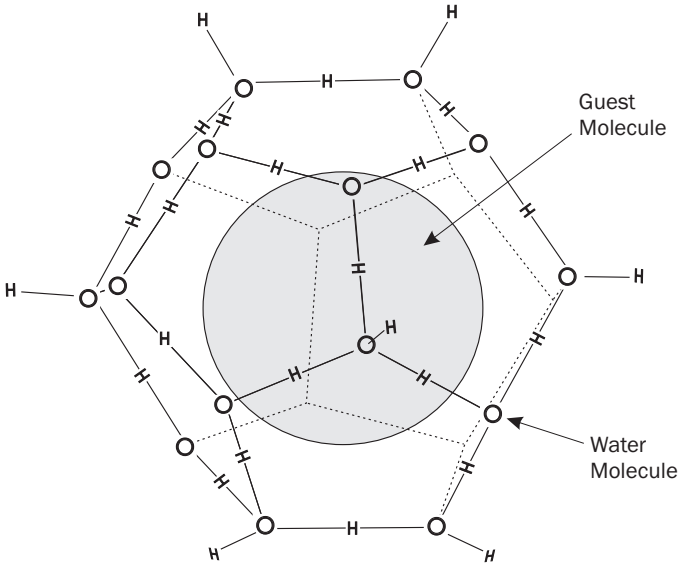

Figure 2.1: Pentagonal Dodecahedron cage shape in clathrates, showing water and guest molecules.

et al., 2004; Koh, 2002; Sloan, 1998). Structure H hydrate has the ability to encase the larger gas molecules (between 7.1Åand 9Åin diameter), whereas structures I and II can only contain those with a radius of less than 6.5Å(Sloan, 1998).

Structure I (sI) hydrates will form with gases that have the smallest molecule diameters. They therefore contain biogenic gases such as methane (4.36Å), carbon dioxide (5.12Å), ethane (5.5Å) and hydrogen sulphide (4.58Å) which makes them the most common naturally occurring hydrates. Structure II (sII) hydrates form from gases with molecules larger than ethane, but smaller than n–butane (7.1Å). This means that Structure II hydrates are more common in the hydrocarbon production and processing industry. Structure H (sH) hydrate incorporates the larger hydrocarbon molecules present in crude oil, and has consequently become more important in the hydrocarbon industry.

2.1.2 Properties of Solid Hydrate

Table 2.2 details the fundamental properties for solid methane and solid propane hydrate. The measurements have been derived from a number of sources, using a number of measurement techniques. Kiefte et al. (1985) used Brillouin spectroscopy on a small volume of relatively pure propane hydrate samples, whereas Waite et al. (2000) used pulse wave transmission through dense polycrystalline methane hydrate to obtain results. Also given are the properties of pure methane hydrate derived from first principles by Miranda & Matsuoka (2008).

Property	Water Ice[a]	Methane Hydrate[a]	Propane hydrate[a]	Methane hydrate[b]
Density (gcm^{-3})	0.916	0.91	0.88	0.89
Shear Modulus G (GPa)	3.5	3.3	2.4	4.3
Bulk Modulus K (GPa)	8.8	7.7	5.6	–
Young's Modulus E (GPa)	9.3	8.5	8.3	11.07
V_p/V_s	1.96	1.93	1.95	1.80
Poisson's Ratio	0.325	0.317	0.32	0.2776

Table 2.2: The elastic properties of solid methane (sI) and propane (sII) hydrate with comparison to that of water ice. [a]Experimental results on hydrate after Waite et al. (2000); Davidson (1983); Kiefte et al. (1985). [b]Calculated properties from Miranda & Matsuoka (2008)

Their results predict the density of hydrate to be slightly lower than experimentally measured values, as well as suggesting that the shear and Young's moduli of methane hydrate are higher than that of water ice.

Durham et al. (2003) conducted triaxial tests on dense polycrystalline methane hydrate, which showed that over their range of test temperatures and strain rates, methane hydrate was on average 20–30 times stronger than ice. This high strength of hydrate compared to water ice has significant implications for the mechanical behaviour of hydrate bearing sediments. Durham et al's (2003) results also suggest that the theoretical derivation of hydrate strength from Miranda & Matsuoka (2008) could be closer to the truth than the experimental values found by Kiefte et al. (1985) and Waite et al. (2000).

2.1.3 Methane Sources and Conditions for Hydrate Deposition

Natural hydrate presence is limited on the earth's surface due to the specific stability conditions shown in Figure 1.1. As well as having the correct temperature and pressure conditions, the sediment must also have sufficient influx of gas and water in order for hydrate to form. Environment, gas origin and gas supply are therefore the factors that dictate the presence of the world's hydrate resource.

The appropriate thermobaric conditions coupled with the availability of water, initially control the occurrence of natural hydrate in a sediment. This makes the deep sea an ideal location for hydrate growth as pressure increases and temperature decreases with depth. In deep sea sediments however, hydrate is only stable in the top 0.7km on average due to the geothermal gradient (Figure 2.2), with the area of stability being termed the hydrate stability zone (HSZ). This zone can vary in depth across the oceans due to a number of factors:

- The change in ocean depth worldwide means that thickness of the HSZ can differ, with increasing thickness correlating with increasing water depth.
- The chemistry of the guest molecule has a large effect on the stability region. In areas such as the Gulf of Mexico where the gas is not pure methane, the base of the HSZ has been observed to occur at temperatures 2°C higher than a pure methane deposit (Dillon & Max, 2000).
- Change in fluid flux rate can cause the top of the stability zone to lie closer to the sea floor (Hyndman & Davis, 1992).

The stability region for permafrost hydrate differs slightly from oceanic hydrate in that it extends deeper into the sediment (Figure 2.3). In the MacKenzie Delta-Beaufort Sea Region of the Arctic the HSZ has been suggested to be 1.2km deep (Collett & Dallimore, 2000), over 300m deeper than the depth limit of the HSZ in the open ocean.

In conjunction with the appropriate thermobaric conditions, gas source and supply are key to hydrate development. In oceanic and permafrost environments, methane is generated by the breakdown of organic matter that is contained within the sediment, either *in-situ* or deeper in the sediment column. Two types of methane can be identified due to a six stage reduction process: Biogenic and thermogenic. Biogenic methane is derived through the first four stages of bacterial decay, ultimately ending with the breakdown of CO_2 by bacteria after the sulphate in the organic matter has been reduced. Thermogenic methane is produced in two further stages of organic matter decay, due to the thermal breakdown of heavier hydrocarbons at high temperatures. Methane produced in this fashion is often found in conjunction with ethane, propane or butane (Wellsbury & Parkes, 2000).

Oceanic hydrates predominantly contain methane of biogenic origin (Kvenvolden, 1995), as do hydrates found in arctic permafrost. However, deposits containing ethane and propane accompanying methane have been found in the Gulf of Mexico (Brooks et al., 1984) that suggests thermogenesis may also produce the gases found in some hydrates. Methane produced biogenically could form hydrate in–place but generally migrates to the HSZ from deeper sediments. However, thermogenic gases must be transported to the HSZ as it is produced at temperatures too high for gas hydrate to form. There are currently two models for methane migration into the HSZ. Firstly, free gas could migrate through fissures and permeable sediments to the HSZ where the correct conditions and water availability allow for hydrate formation (Minshull et al., 1994; Soloviev & Ginsburg, 1997). Alternatively, water containing dissolved methane becomes super–saturated when the temperature decreases as it rises into the hydrate stability

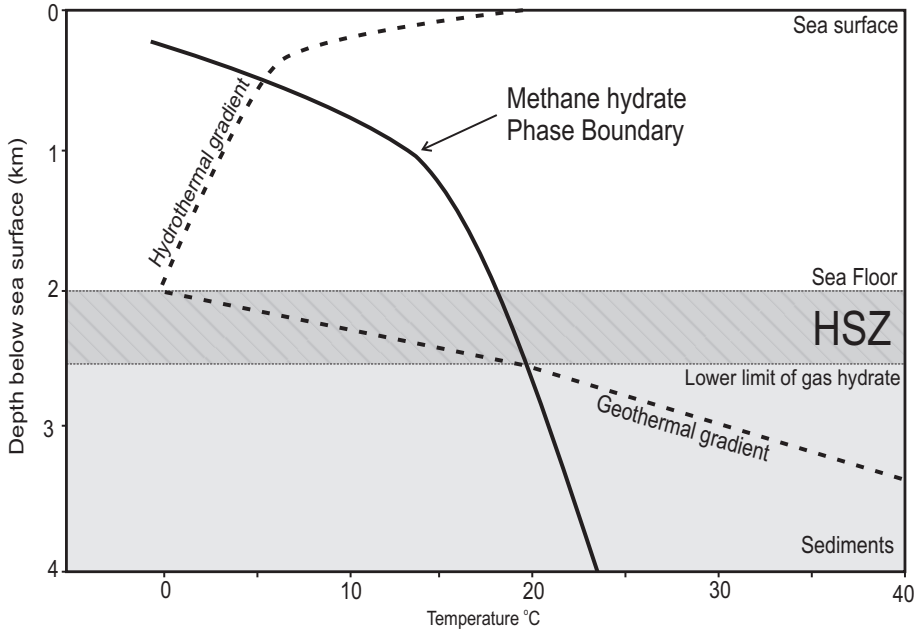

Figure 2.2: Stability region of methane hydrate in the oceans as defined by temperature and pressure (as indicated by water depth below sea surface). Redrawn from Dillon & Max (2000).

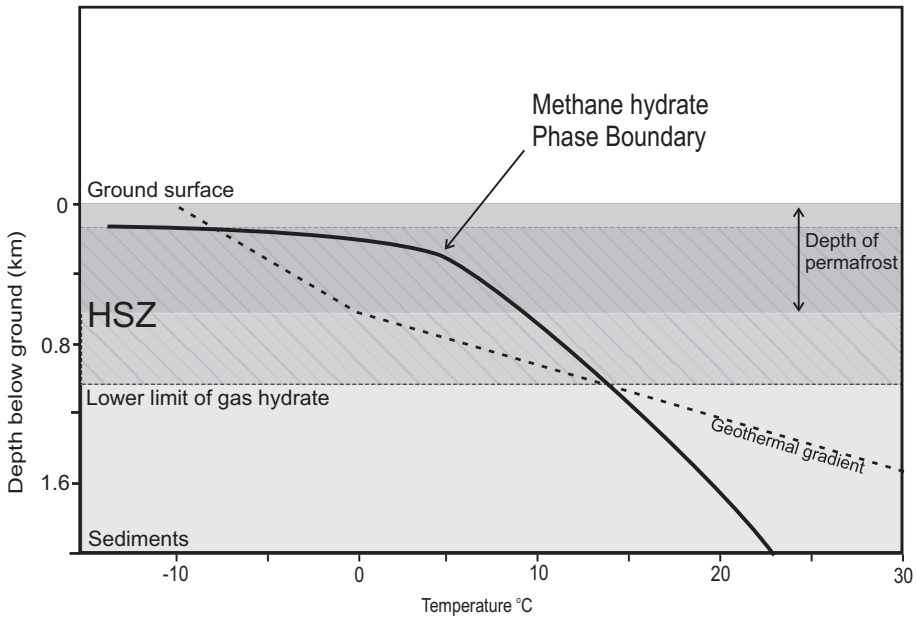

Figure 2.3: Stability region of methane hydrate in the permafrost as defined by temperature and pressure (as indicated by depth below ground). Adapted from Kvenvolden (1988).

zone (Hyndman & Davis, 1992). This would mean hydrate crystallising out without a gas phase.

Due to the conditions described above, the location of hydrate in the earth is restricted to deep ocean and permafrost environments with particular tectonic and sedimentary features. Passive continental shelves and active accretionary prism margins harbour the deep–sea hydrate resources, as they combine a gas supply from appropriate source rocks with a compatible thermobaric environment. The extent of permafrost hydrate is seemingly controlled by an availability of gas, as all permafrost environments have the appropriate thermobaric conditions for hydrate stability.

2.2 Gas Hydrate Morphology

Gas hydrate is a solid material, which as it grows in a sediment, takes on a form and structure. Hydrate can be considered on two scales: Macro–morphology relates to the structure of large scale hydrate formation in a sediment, with micro–morphology referring to the grain scale interaction of hydrate and host sediment particles. Evidence from visual observation of natural and laboratory grown hydrate is that hydrate takes a variety of morphologies that are dependent on host sediment type, gas supply to the HSZ, and tectonic setting. As hydrate is a material with significant mechanical properties (section 2.1.2), an understanding of the morphology is crucial when considering it's effect on host sediment properties, and the application of this knowledge to detection and quantification of hydrate in the sub–surface. This section discusses the variety of hydrate morphologies that occur in nature, and the environments in which they have been observed.

2.2.1 Macro–Morphology

Four distinct morphologies are widely recognised for methane hydrate growth in sediments (Figure 2.4). **Disseminated** hydrate describes a deposit that is homogeneously distributed throughout the soil macro–structure (Clennell et al., 1999; Ginsburg, 1998; Booth et al., 1998). Larger accumulations of hydrate can be described as either **nodular** or **layered** deposits. If the supply of gas and water is sufficient, each of these hydrate morphologies then has the potential of developing into **massive** hydrate deposits (Malone, 1985).

Malone's morphologies are well established within the research community. However, recent

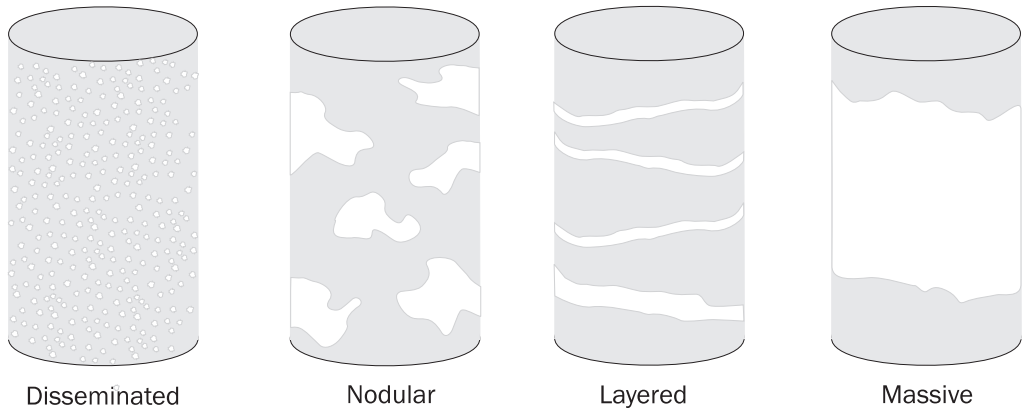

Figure 2.4: The four types of natural hydrate deposit in sediment. From Malone (1985)

advances in natural hydrate sampling and imaging (Section 2.2.3) has led to another classification system which describes hydrate in terms of two morphological types: Pore–filling and grain–displacing (Collett et al., 2008; Holland et al., 2008; Riedel et al., 2006). **Pore–filling** morphology describes hydrate that forms in the pore space of a sediment, replacing the pore fluid without significantly displacing the sediment grain matrix (Collett et al., 2008). **Grain–displacing** hydrate does not occupy the pore space, but forms between grains as discrete nodules, layers and lenses of pure hydrate (Holland et al., 2008). In terms of Malone's (1985) classification, "pore–filling" and "grain–displacing" morphologies can occur for each of the macro–morphologies in Figure 2.4, but these two terms allow for the interaction of the hydrate and the sediment grains to also be considered when discussing hydrate morphology.

2.2.2 Micro–Morphology

The interaction of hydrate with sediment grains, or "micro–morphology" has been developed over time through the efforts of Dvorkin et al. (1993; 1994; 1999b; 2000) and Clennell et al. (1999) through modeling, and more recently by modern sampling and imaging techniques (Riedel et al., 2006; Collett et al., 2008; Holland et al., 2008). Dvorkin et al. (2000) deduced by using rock physics modelling (Section 2.4.3), that hydrate could form in a sediment in four ways based on cementing or pore–filling morphologies. Figures 2.5 (a) and (b) show the two configurations of hydrate if it were to form in the pore space. Figure 2.5(a) shows the hydrate as a particle in suspension. Figure 2.5(b) shows a hydrate morphology where hydrate forms in the pore space, but close to grain contacts, so as to become part of the sediment load bearing frame. The other possibility for hydrate growth is that it acts as a cementing agent. Figures 2.5 (c) and (d) show the two configurations that hydrate cement may take. Figure 2.5(c) locates

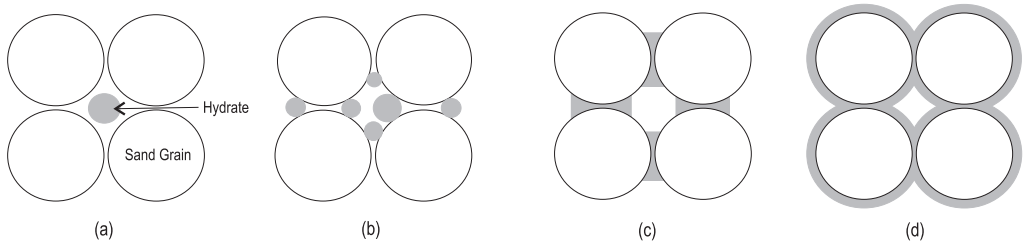

Figure 2.5: Diagrams showing the possible location of hydrate in a sand. (a) Hydrate grows in the pore space between the grains. (b) Hydrate grows between grains becoming part of the sediment supporting frame. (c) Hydrate nucleates and grows at grain boundaries forming a cement at the grain contacts. (d) Hydrate grows to envelop the grains.

hydrate solely at grain contacts, whereas Figure 2.5(d) represents hydrate that envelops the sediment grains and bonds where the surface coating cement comes into contact.

The pore–filling morphology described by Collett et al. (2008) and Holland et al. (2008) appears to fit into the modelled morphologies of Figure 2.5. Pore–filling hydrate can either form inside the pore space (Figures 2.5(a) and (b)), or by cementing the grains together (Figures 2.5 (c) and (d)). Grain–displacing hydrate however, interacts with the sediment by pushing grains aside, and so cannot be modelled by the configurations in Figure 2.5.

2.2.3 Visual Observation of Hydrate Morphology

There have been a number of attempts to observe hydrate growth in porous media directly, both on the macro and micro scale. Brewer et al. (1997) created hydrate *in situ* at a depth of 910m in the ocean, by bubbling gas through a variety of sediments. It was observed that in fine grained sediments the hydrate formed in veins, whereas in coarse sediments it showed a more dispersed nature. These observations have been validated by hydrate sampling, but the direct observation of actual hydrate growth gave the first view of formation mechanisms.

Since the work of Brewer, visual observation of hydrate growth has moved to non–destructive 3D imaging techniques. High resolution X–ray computer tomography (CT) scanning is becoming a major contributer to the understanding of hydrates in sediments. Work by Mikami et al. (2000) shows the use of CT scanning in investigating hydrate dissociation in sediments. More recently, computer tomography has been used to monitor hydrate growth inside artificial sediment samples at the Lawrence Berkeley National Laboratory (Kneafsey et al., 2007). The goal was to observe the formation and dissociation of hydrates in sands, so as to evaluate

the importance of hydrate dissociation kinetics in porous media. The most recent advances in visual observations come from the developments of CT scanning within the pressurized core barrels of the HYACINTH system described in Section 2.3.1. Successful implementation of the system during the NGHP–1 expedition has provided new images of hydrate morphology in fine grained sediments (Collett et al., 2008).

The use of CT scanning in observing the micro–morphology of hydrates is likely to develop as the technology improves and allows for higher resolution imaging. At this stage, however, other methods have been used to observe gas hydrate micro–morphology. In order to investigate hydrate at the grain level, Tohidi et al. (2001) developed glass micro models, which allowed direct observation of the formation of gas hydrate at a microscopic scale. The initial experiments were based on the observation of hydrate formation from the different phases: THF as a soluble hydrate former, carbon dioxide as a dissolved gas, and methane in the free gas phase. From these experiments hydrate was directly observed forming from each phase, which was used to validate models based on chemical analysis. Other grain–scale observation of hydrates have been made using scanning electron microscope (SEM) (Kuhs et al., 2000). Although the hydrate observed was pure, and unconnected with a porous medium, the imaging technique may be used in the future for observing hydrate in the pore spaces of sediments.

2.2.4 Controlling Factors on Hydrate Morphology

The major controls on hydrate morphology in a sediment are lithology along with the availability of components and subsequently geological setting. The numerous Ocean Drilling expeditions that have observed natural gas hydrate (Lee et al., 1982; Aubouin et al., 1982; Kvenvolden & McDonald, 1985; Paull et al., 1996; Larsen et al., 1999; Tréhu et al., 2006; Riedel et al., 2006; Collett et al., 2008) document the importance of lithology, specifically grain size, on how hydrate grows in a sediment. Coarse sediments, as seen at the Mackenzie Delta (Winters et al., 1999) usually contain disseminated hydrate. Veined and nodular hydrates, like those drilled on the Cascadia Margin (Suess et al., 2001) and off the east coast of India (Collett et al., 2008) are generally found in fine grained sediment, with small pore sizes. The experimental work of Brewer et al. (1997) highlights the lithological control, as the sediments of a small pore size preferentially formed hydrate into veined and layered structures, whereas the sand experiment with large grain sizes, produced a disseminated morphology.

The availability of gas and water also controls the morphology of a hydrate deposit. Partial saturation of sediment in the HSZ can cause hydrate to form in discrete regions where wa-

ter is available. The layered morphology of the hydrates observed by Soloviev & Ginsburg (1997) was caused in this manner by a chimney of gas penetrating the HSZ and the reduced availability of water at the hydrate front. The control posed by the availability of gas is directly related to gas source and supply. Methane produced biogenically *in–situ* could generate a disseminated hydrate deposit regardless of sediment type (Sloan, 1998), however only small hydrate concentrations could be grown in this manner. Hydrate deposits where methane has been transported into the HSZ (either from biogenic or thermogenic sources) may show a number of morphologies depending on the mechanisms that control the gas transport (Trehu et al., 2006).

Two end–member regimes have been identified with regard to gas transport. Focused, high–flux (FHF) hydrate systems involved large volumes of methane concentrated through focused conduits, either as gas or dissolved in pore fluids. Distributed, low–flux (DLF) systems, involve methane produced near to where the hydrate is formed and where fluid flow is gradual and consistent throughout the HSZ (Trehu et al., 2006). Where methane is delivered through a FHF system, large, focused accumulations of hydrate are usually found showing layered and nodular morphology (Riedel et al., 2006; Holland et al., 2008). These morphologies most likely form due to the increased pore pressure induced in an FHF system. Cracks and fractures will form in a sediment when fluid or gas is forced into pores until pore pressure exceeds the tensile strength of the sediment (Hatcher, 1995). If the pore fluid (or free gas) remains under pressure, fractures can propagate through the sediment column. These fractures can then be filled with hydrate if this occurs in the HSZ. DLF systems are more likely to yield widely distributed hydrate deposits of a disseminated nature (Trehu et al., 2006), due to the lower and more dispersed pore pressures associated with the regime.

Which of the FHF and DLF transportation systems occur, depends on the geological setting. Continental margins, where tectonic activity is low and fluid flow is pervasive throughout the sediment column, tend to harbour hydrates formed from DLF systems (Trehu et al., 2006). Alternatively, accretionary prism hydrate formations are more likely to have FHF transport systems (and associated morphologies) as the tectonically active regions often contain rapidly upward migrating pore fluids through focused conduits such as faults (Chand & Minshull, 2003). Evidence from the field lends weight to the transportation systems of Trehu et al. (2006). The passive continental margins of the Blake Ridge and the east coast of India have both been found to contain some disseminated hydrate in fine grained, clay–rich sediments (Guerin et al., 1999; Collett et al., 2008), where previous, lithology based models may not have predicted this morphology. In addition to this, areas of the NGHP–1 cruise in the Indian Ocean (Collett et al., 2008), where tectonic folding had produced faulted basement sediments (FHF system), were

found to have high concentrations of hydrate in a veined morphology (Holland et al., 2008).

2.3 Detecting and Quantifying the Hydrate Resource

The first discovery of natural gas hydrate in sediments was made in the Soviet Union in the 1960's (Makogon et al., 2007). The identification of hydrate as a resource and potential geohazard prompted widespread investigation into the worldwide hydrate presence. The bulk of the knowledge on oceanic and permafrost hydrate deposits has come from the drilling and sampling of deep sea sediments, or by seismic surveying techniques.

2.3.1 Drilling and Sampling

The pressure and temperature conditions of hydrate stability make the drilling and sampling of methane gas hydrate a difficult task. Gas hydrate will decompose rapidly when removed from it's high pressure/low temperature environment and therefore much of the gas that is present in the sediment, either as free gas or as hydrate, is lost during transportation to the surface. Thus, any attempt to quantify hydrate content from samples recovered using standard drilling rigs may not be accurate.

Testing of Hydrate Samples from the Field

Due to the difficulty in transferring hydrate from the natural environment into laboratory test equipment, there has been little work on directly testing natural samples for their mechanical properties. The only group of note to report success in testing natural hydrate is the USGS community at Woods Hole, Massachusetts. Their GHASTLI (Gas Hydrate and Sediment Test Laboratory Instrument) system allows for natural samples, as well as synthetic, to be tested in controlled laboratory conditions (Winters et al., 2000, 2004). The natural samples tested in GHASTLI are frozen in liquid nitrogen for storage prior to testing. The samples are then prepared for the equipment in a cold room of -30°C so that dissociation is minimised during preparation. Once inside GHASLTI, the sample is then subjected to a confining pressure and the temperature increased to melt the pore water, but retain the hydrate. The only published data from these natural sample tests (Winters et al., 2000, 2004) shows results from cores retrieved from the Mallik 2L–38 test well drilled in the Canadian Arctic during 1998.

Even though results were obtained from these tests, there are certain aspects to the coring, transportation and storage of the tested cores that makes the results unreliable. Firstly, al-

though pressure corers were used in both the Mallik well location and on ODP 164, neither cores tested in GHASTLI were taken using a pressure corer. Therefore, dissociation of hydrate would have occurred during the journey to the surface, and in addition, the reduction in pressure could cause any dissolved methane gas in the pore water to come out of solution and distort the core structure. Furthermore, each core was stored in pressurised methane gas and at approximately -10°C during transportation and final storage before testing. Although likely to maintain hydrate already present in the sediment, storage conditions such as these could induce secondary hydrate formation – as noted by Winters et al. (2004). The solution, they suggest, can only be addressed by the use of *in–situ* measurements being taken inside a pressurised core barrel. It is this problem that the Ocean Drilling Program have tried to solve.

Pressure Coring

To address the pressure issues associated with recovering natural gas hydrate, the Ocean Drilling Program developed the Pressure Core Sampler (PCS). Initially designed to sample and understand the distribution and concentration of hydrocarbon gases, the apparatus allows for recovery of a 1m long section of core at *in–situ* pressures. The standard PCS is capable of retaining pressures up to 690bar (Pettigrew, 1992). Even though this progressed the sampling of hydrate at depth, there are still issues with the PCS system. The PCS does not have temperature control and so the core is exposed to a change in temperature as it is brought to the surface. There is concern that during transport through cooler bottom waters, excess hydrate that was not present *in–situ* may form (Dickens et al., 2000).

Even with the ability to collect hydrate bearing sediments at *in–situ* pressure, there are still problems of reliably testing them once at the surface. It has become standard to store hydrate samples in liquid nitrogen so as to slow dissociation, and for ease of storage. This however means rapid depressurisation of the samples before freezing which allows for the exsolution and movement of *in–situ* gases which may damage the core. With these issues in mind, the HYACINTH system was developed by a number of collaborators with funding from the European Union (Francis, 2001). The HYACINTH pressure corer recovers a 1m long core under *in–situ* pressure that can then be tested within a pressurised environment once at the surface (Trehu et al., 2004). The system comprises of two specialised corers, the Fugro pressure corer (FPC) and the HYACE rotary corer (HRC) which have the ability to deal with the potentially varied lithologies of hydrate deposits. Once recovered, the cores can then be transferred to a pressurised test chamber which contains a multi sensor core logger equipped to measure the geotechnical properties of the hydrate core by using P–wave velocity, gamma ray attenuation and X–ray imaging. Recent use of this pressurised core testing system has been successful in

obtaining valuable information on hydrate bearing sediments (Tréhu et al., 2006; Riedel et al., 2006; Collett et al., 2008), and the ability to sample and test hydrate bearing sediments under pressure is a significant step that has allowed further understanding of natural hydrate structure and properties.

2.3.2 Seismic Surveying

The detection of methane hydrate using seismic surveying traditionally relied on the detection of a bottom simulating reflector, or BSR. The BSR is an acoustic reflection that cuts across geological boundaries, mimicking the seafloor within the sediment column (Shipley et al., 1979; Kvenvolden & McDonald, 1985; Miller et al., 1991; Hyndman & Spence, 1992; Singh et al., 1993). The BSR was linked to hydrate presence due to its occurrence close to the sub–surface depth predicted for the base of the gas hydrate stability zone. The BSR's reversed polarity also suggested it was caused by high velocity sediment (containing hydrate) overlying low velocity sediments potentially containing free gas (Hyndman & Spence, 1992; Singh et al., 1993).

It has recently become evident however, that the BSR is not altogether reliable for predicting hydrate presence. ODP leg 164 (Paull et al., 1996) drilled through various BSRs on Blake Ridge, and failed to find hydrate at locations where a BSR was observed on the seismic survey. It has also been shown that hydrate can be present in areas without a BSR (Ashi et al., 2002; Pecher & Holbrook, 2000; Ecker et al., 2000). It is now thought that the BSR may only indicate the top of the occurrence of free gas, and not necessarily the base of the gas hydrate stability zone (Chand & Minshull, 2003; Singh et al., 1993; Pecher et al., 1996). Even so, most surveying of hydrate in the field still relies on the bottom simulating reflector to locate hydrate bearing zones within ocean sediments.

Once the presence of hydrate has been identified, other methods such as vertical seismic profiling and wireline logging can also be employed to help analyse and quantify hydrate in the subsurface. Vertical seismic profiling refers to measurements taken from inside the wellbore, and can be used to gain higher resolution data than surface seismics. The technique uses geophones placed inside a wellbore and a source on the sea surface near the well itself. As well as being used in conjunction with surface seismic data, it offers an opportunity to measure *in–situ* velocities of hydrate bearing sediment at seismic frequencies (Holbrook et al., 1996).

Measurements made from inside drill holes are another way of detecting and analysing hydrate bearing sediments. In the case of hydrate exploration, sonic and porosity logs are the most useful (Goldberg et al., 2000). Sonic velocities are affected by the presence of free gas and

Source	Location	V_p/ms^{-1}
Singh et al. (1993)	Offshore Vancouver Island	1600–1800
Holbrook et al. (1996)[a]	Blake Ridge	1800
Ecker et al. (2000)	Blake Ridge	1900
Tinivella & Accaino (2000)	South Shetland Margin	2000–2300
Goldberg et al. (2000)[b]	Hydrate Bearing Sediments	1700–3500
Guerin & Goldberg (2002)	Mallik 2L-38 Research Well	2000–3500
Collett (1993)[b]	North Slope of Alaska	2000–2800

Table 2.3: P–wave velocities from seismic surveys and well logging. [a]Velocity found though vertical seismic profiling. [b]Expected response from logging measurements

hydrate, becoming lower and higher respectively if present in the sediment (Helgerud et al., 2000). They can therefore be used to aid in seismic interpretation and even quantify hydrate and gas concentrations. Attenuation characteristics of hydrate bearing sediments can also be observed through sonic logging (Guerin & Goldberg, 2002). Porosity logs are useful in hydrate detection as the physical properties of a sediment play a significant role in the distribution and morphology of hydrate in the sediment column. Neutron porosity, density and resistivity logs are often used in combination to get the best estimate of a sediment's porosity. Recent gas hydrate drilling expeditions have found that gas hydrate bearing sediments exhibit relatively high electrical resistivities when compared with water saturated sediments (Collett et al., 2008). It is possible that resistivity logs could be used in the future to quantify hydrate in a sediment. A more detailed discussion of logging methods can be found in Goldberg et al. (2000) and Goldberg (1997).

P–Wave Velocity Data from Seismic Surveys

Table 2.3 gives a summary of P–wave velocities obtained from well logging and seismic surveys from several authors. The values seen in the table are taken from the region above the BSR in each case. The range of values shown by some of the authors is indicative of the varying hydrate content in the survey sites (Pecher & Holbrook, 2000).

The range of The P–wave velocities obtained in Table 2.3, as well as the unreliability of the BSR, mean that the research community still does not have a grasp of the seismic signatures expected from a hydrate deposit. Although hydrate can be readily identified from downhole logging (Riedel et al., 2006; Collett et al., 2008), detecting and quantifying hydrate from the sea surface is still an imprecise art. With the direction of hydrate research moving towards exploitation, there is a clear need to fully understand the velocity profiles of hydrate bearing sediments.

2.4 The Effect of Hydrate on Sediments

Section 2.3.2 has highlighted the need to understand and identify the seismic signatures of hydrate bearing sediments. This can only be done by gaining a thorough knowledge of how hydrate affects a host sediment's mechanical properties. Understanding can come from the investigation of natural and synthesised hydrate bearing sediments in the laboratory, or by the modelling of hydrate/sediment systems. This section will highlight the effects hydrate has on sediment properties, before discussing the current methods used to investigate them.

2.4.1 Possible Effects of Hydrate Formation

Gas hydrate is a crystalline solid, and its growth in the sediment column will have an effect on the host sediment that must be known if quantification of the hydrate resource is to be made. Section 2.2 detailed the different morphologies of natural hydrate in the pore space, and each morphology described, from macro– to micro–scale, will have a different effect on the host sediment properties.

Micro–Morphology Effects

Section 2.2.2 described the variety of forms that hydrate can take at the grain level. These morphologies will alter the properties of the host sediment by differing degrees. The different possible hydrate morphologies and their influence is discussed in the following section.

Hydrate Acting as a Cement

Cementation is the creation of chemical bonds between sediment particles. It can give soils a substantial increase in their unconfined compressive and shear strength that is mostly attributed to cohesive strength at low strains (Coop & Atkinson, 1993). If hydrate were to act as a cement in host sediments one would expect to see an increase in strength at low concentrations, however, the full degree of cementation is unpredictable as different cement types give rise to different bonding mechanisms, as detailed by Ismail et al. (2002). They investigated the differences between calcite, gypsum and Portland cement as cementing agents, and found that the different bonding mechanisms gave rise to differing engineering properties. Calcite precipitated out in granular form as well as showing a coating behaviour, whereas the gypsum cementing agent was observed to produce long crystals with a high aspect ratio that filled the intergranular space with overlapping crystals. The materials bonded with calcite showed a much higher shear strength than either the gypsum or Portland cement at comparable cement concentrations, with the gypsum cement giving the lowest shear strength overall. As the

method of hydrate formation may influence the morphology of hydrate in the pore space (section 2.2), it is possible that a number of bonding mechanisms could arise from crystallisation of hydrate in sediments.

Hydrate as a Pore Filling Component

If hydrate was to form solely in the pore space, the change in unconfined compressive and shear strength of the host sediment may not be as great as that of a cemented sediment. The inclusion of hydrate would primarily affect change by altering the bulk modulus of the sediment (Lee et al., 1996). In this situation there are two possible models for how the hydrate will contribute to the sediment: either as a component of the sediment frame, or by forming solely in the pore space (Helgerud et al., 1999; Dvorkin et al., 2000). If hydrate were to form purely in suspension, the shear properties of the sediment would be unaffected, but the bulk values would change due to hydrate replacing pore fluid (Lee et al., 1996; Helgerud et al., 1999; Dvorkin et al., 2000). If the hydrate became a component of the sediment frame, the strength of the sediment would be altered in that the solid phase would now consist of the original mineral grains plus gas hydrate grains. If the strength of pure hydrate was less than that of the original sediment grains, one might expect to see a decrease in strength of the overall sediment, due to a weaker sediment frame of combined mineral and hydrate grains. This is unlikely to be the case however, due to hydrate formation changing sediment porosity and having an overriding affect on bulk modulus (Dvorkin et al., 2000).

The inclusion of hydrate into a sediment as either a cement or a pore filling component as described above, will reduce the sediment's porosity by filling the void space with a solid material. The "grain–displacing" morphology described by Holland et al. (2008) may not have the same affect, as the hydrate does not replace void space with a solid material, but pushes grains aside.

Macro–Morphology Effects

The veined, nodular and massive morphologies described in Section 2.2.1, as well as the "grain– displacing" morphologies of Collett et al. (2008) and Holland et al. (2008) may not be expected to have the same effect on the seismic signatures of host sediments as the hydrate/grain interactions described above. There is little literature available on the effect of veins and nodules of crystalline material on the seismic signatures of soft sediments, however, analogies can potentially be made between fracturing and fissuring studies conducted in sedimentary rocks. Experimental and modelling studies have shown that the inclusion of fractures to sedimentary rocks decreases the seismic velocity of that rock (Leucci & Giorgi, 2006; Boadu,

1997; Boadu & Long, 1996). Factors such as fracture density, length, aperture, frequency and type of infilling material all contribute to the affect of fracturing on a rock (Boadu & Long, 1996), with the general trend that as the frequency and density of fractures increases, the shear and compressional wave velocities of the rock decrease. Boadu (1997) notes however, that at high fracture density, measured seismic velocities are dominated by fracture properties, and not those of the host rock. With regard to hydrate bearing sediments, it may therefore be possible that the presence of hydrate veins could reduce the seismic velocity of a host sediment, unless the density of hydrate veins is very high. It must be noted however, that fracture modelling in rocks assumes the infill of the fractures has a weaker mechanical properties than the host rock (Leucci & Giorgi, 2006). This is likely to be the opposite for hydrate veins and nodules in sediments, and so the effect of hydrate on host material seismic signatures may be converse to those suggested by the fracturing literature.

Effects on Attenuation

In addition to the changes hydrate formation will cause to the stiffness of sediments, there are also the changes it will cause to the attenuation of the seismic waves that pass through a hydrate bearing zone. Predicting how gas hydrate will affect attenuation, can also be achieved by considering the morphology of hydrate in the pore space.

It is generally thought that attenuation in marine sediments should decrease with decreasing porosity (Hamilton, 1972). If hydrate is considered as a pore filling component, it could be suggested that as hydrate content in the pore space increased, the porosity should decrease, and so would the attenuation. This hypothesis has been tested by Gei & Carcione (2003), who modelled gas hydrate bearing sediments containing a mixture of free gas, water and hydrate. The work hypothesised that the inclusion of a material stiffer than water (hydrate) and then grain cementation with increasing hydrate content, would make a porous material more cohesive, and therefore reduce attenuation. The results from their models apparently validated this theory. Further support for this hypothesis came from Pecher & Holbrook (2000), who stated that the inclusion of hydrate within a sediment should decrease the attenuation, if the hydrate acted as a cement.

However, there have been studies into the effects of silica diagenesis on attenuation that disagree with the theories of Hamilton (1972) and Pecher & Holbrook (2000). Goldberg et al. (1985) describe data from marine sediments that were drilled and cored from the Baltimore Canyon trough. The sediments were observed to have an increasing degree of porcellanite cementation with depth, that decreased the porosity as well as affecting the size and aspect

ratio of the sediment pores. The compressional velocity of the sediments increased with depth (and decreasing porosity), however the attenuation was also seen to increase. This increase in attenuation as the porosity decreased lead to Goldberg et al. (1985) investigating the surface area of the pores, and how diagenetic effects decrease the porosity yet increase the pore surface area. It was concluded that the mechanism responsible for attenuation in the sediments was stress relaxation, a mechanism analogous to the squirt flow mechanism of Mavko & Nur (1979). 'Squirt flow' is a process where the passing of a seismic wave through porous media induces pore pressure gradients across individual pores and grains. This causes the movement of water and resultant viscous dissipation of energy (Mavko & Nur, 1979; Mavko et al., 1998). As hydrates most often form in water saturated sediments, this mechanism could contribute to attenuation in hydrate bearing zones.

2.4.2 The Study of Hydrates from Laboratory Tests

The previous section indicated the variety of effects different hydrate morphologies can have on a host sediment. In order to determine and quantify these effects, laboratory experiments can make and test gas hydrates in controlled environments. There are several methods of synthesising and testing hydrate in the laboratory, which will first be described in detail before being critically examined.

Apparatus

A range of methods can be used to measure the properties of hydrate and with and without associated sediments. Non–contact, nondestructive methods are favoured, with Brillouin Spectroscopy and pulse transmission techniques dominating the field. Whiffen et al. (1982) and Kiefte et al. (1985) utilised Brillouin spectroscopy to determine acoustic velocities in a number of pure clathrate hydrates. Brillouin spectroscopy involves the scattering of light from hypersonic (acoustic) waves which are thermally induced inside a material (Comins, 2001). Stoll & Bryan (1979), Bathe et al. (1984), Berge et al. (1999), Waite et al. (2000) and Winters et al. (2004) measured the properties of hydrate bearing sediments by pulse (wave) propagation, a technique that can be used over a range of frequencies. The generated waves can be detected either by two separate receivers or by detecting the reflection of the wave with a single receiver. Yun et al. (2005) used S-wave bender elements to measure the shear wave velocities in THF hydrate bearing sands. Bender elements measure shear wave velocity by the detection of induced voltage in piezo–ceramic elements (Atkinson, 2000).

Recent advances in gas hydrate research have come from the work of Priest (2004), who inves-

tigated the properties of hydrate bearing sediments by making hydrate in a specially developed resonant column device. The resonant column is a non-destructive geotechnical testing apparatus that allows for sediments to be tested at frequencies relevant to those in seismic surveying. Shear wave and longitudinal wave velocities were obtained by exciting a column of sediment in torsion and flexure to determine its resonant frequency (Novak & Kim, 1981; Cascante et al., 1998).

Formation Techniques

The first attempts to synthesise gas hydrate in sediments were conducted by Evrenos in 1971 (Kaplan, 1974). Gas and water were alternately flowed through a sediment core at pressure until it was plugged with hydrate. Although this method was basic and the experiments were conducted with little intention other than to see if hydrate could form an impermeable plug, the simulation of a free gas phase flowing through a saturated sediment in order to form hydrate was novel. After the success of Evrenos' experiments, Baker (1974), and Stoll et al. (1971; 1974; 1979) used the percolating free gas technique to measure the seismic velocities and thermal conductivity of a sediment/hydrate mix. More recent applications of this method have been by Brewer et al. (1997), who formed methane hydrate in sediment samples 910m deep in the Monterey Bay submarine canyon, by bubbling free gas through a range of sediment samples (previously mentioned in Section 2.2.3). The most recent use of the gas percolation method was by Winters et al. (2004), who made methane hydrate in sand in their GHASTLI (Gas Hydrate and Sediment Test Laboratory Instrument) system. 130mm by 70mm cylindrical sand specimens were saturated with water before having a confining pressure applied. The sediments were then slowly injected with methane gas until a predetermined amount of water was pushed out. The temperature was then dropped to allow for hydrate growth. Berge et al. (1999) also adopted a percolation procedure, but used the liquid R11 as the guest molecule, or hydrate former. Berge et al. (1999) made hydrates in 1 litre volume sand specimens by taking evacuated dry sand and flooding it with fresh water. R11 was then injected into the specimen to replace some of the water, with the content of R11 in the specimen determined by the volume of water displaced. The continued used of the gas percolation method is due to the belief that it mimics the migration of free gas into water saturated deep sea sediments, as well as it being a relatively easy method of hydrate synthesis.

Once it had been established that the growth of hydrate in sediments was achievable in the laboratory, other formation methods were developed. The first of these methods involves the formation of hydrate in partially saturated sediments and has been utilised by Stern et al. (2000), Waite et al. (2004) and Priest (2004). A known amount of water, in the form of ice is mixed with

a sediment (sand in each case) and a back pressure applied by methane gas. Hydrate content is controlled by making water the limiting factor during hydrate formation. Stern et al. (2000) achieved homogeneously saturated specimens by pre–mixing sand with seed ice, and forming the specimens below 0°C. Priest (2004) also mixed sand with seed ice to ensure homogeneously distributed moisture, but allowed the ice to melt before specimen formation. Once formed, Priest refroze each specimen so the moisture could not migrate during testing. Hydrate growth was then induced by increasing the pressure followed by an increase in the temperature of the specimen to just above freezing. Waite et al. (2004) simply mixed free water with sand at room temperature, before increasing the pressure and dropping the temperature to induce hydrate growth. In each case, a 140mm by 70mm cylindrical specimen was formed. This method of hydrate synthesis is characterised by the continuous gas phase present during hydrate formation, and so can be referred to as an "excess gas" method.

An alternative method of hydrate formation mimics the natural conditions where gas could come out of solution to form hydrate in water saturated sediments. Buffett & Zatsepina (2000) showed that they could make hydrate without a free gas phase by using carbon dioxide as the guest molecule, as it can be formed out of solution. A fully water saturated sand was exposed to carbon dioxide at room temperature and at a pressure of 2MPa to allow for saturation of the water with the gas. The specimen was then allowed to mix through a diffusive process over a period of 4 weeks, before the base of the container was cooled to just above the freezing point of water (-1.5°C in this case). Hydrate formation was observed by a change in resistivity and temperature. Tohidi et al. (2001) also made hydrate from dissolved carbon dioxide, although they used a micromodel of etched glass to observe the process, rather than sediment specimens. Distilled water containing dissolved carbon dioxide was flowed into the micromodel at 6.2MPa. The temperature of the system was then reduced to 9°C to induce hydrate growth. Spangenberg & Kulenkampff (2005) succeeded in forming methane gas hydrate out of solution by flowing water containing dissolved methane into a "sediment" made from glass beads. The low solubility of methane in water meant that the experiments took 55 days to complete, but Spangenberg and Kulenkampff managed to achieve hydrate saturations of 95% of the pore space over this time.

Tohidi et al. (2001) utilised another technique that allows for a continuous water phase to be present during hydrate formation. A known quantity of gas is flowed into a glass micromodel, and then water is slowly injected. The gas is allowed to remain in the pore spaces creating small gas bubbles. They observed that hydrate initially grew at the gas–water interface, but that redistribution occurred the longer the hydrate remained in the models. This method of hydrate synthesis allows for homogeneous hydrate distribution in water saturated conditions,

but from a free gas phase, and can therefore be described as an “excess water” method.

The final technique that has been developed involves forming hydrate from a soluble hydrate former, tetrahydrofuran (THF). THF is a liquid at room temperature, and forms hydrate at low temperatures at atmospheric pressure. Cameron et al. (1990) and Yun et al. (2005) have formed THF hydrates in sediments by mixing finite quantities of THF with saturated sands. Yun et al. (2005) made their specimens by creating a THF–water liquid, that was mixed with a fine grained sand before specimen formation. Due to the nature of THF, they were able to synthesise specimens that contained 100% hydrate in the pore space. Cameron et al. (1990) made hydrates by first forming a cylindrical specimen of dry Ottawa sand, that was then flooded with a THF/water solution. They then froze the specimen before removing it from the former and testing it in equipment located in a cold room. This technique was only possible due to the use of a hydrate former that is miscible with water (THF).

Critical Examination of Laboratory Testing

The stability conditions for gas hydrate make testing in the laboratory challenging. A consideration to all wishing to form hydrate in the laboratory is to make sure results are applicable to real world conditions. Therefore, one needs to be sure the morphologies of hydrate grown in the laboratory are the same as those seen in nature. Researchers make choices with regard to apparatus, hydrate former and formation technique in order to ease synthesis of hydrate in the laboratory, which may have an affect on the way hydrate forms, or how the results are interpreted.

Morphology Induced by Formation Methodology

Two main factors could have a significant affect on the way hydrate forms in a sediment when considering formation methodology: saturation state and the hydrate former phase (either free gas or dissolved gas).

Whether the host sediment is fully or partially water saturated prior to hydrate formation has been found to have a major control on hydrate micro–morphology in the pore space. Results from Waite et al. (2004) and Priest (2004), the two bodies of research that use partially saturated conditions, are given in Table 2.4. Both sets of results show high seismic velocities for hydrate bearing sands at both 20% and 40% hydrate contents, that have been attributed to a cementing morphology. Hydrate in “excess gas” or partially saturated conditions forms where the water resides. As this tends to be at grain contacts, hydrate acts as a bonding agent. There is some concern as to whether this formation method is analgous to natural hydrate formation in the real

world. Most natural hydrates are found in deep sea settings where sediments are water saturated (Sloan, 1998; Kvenvolden et al., 1993). The methods where partially saturated specimens are used (Priest, 2004; Waite et al., 2004) are therefore unlikely to provide results applicable to marine hydrate deposits. Permafrost environments however, are a potential analogy to this formation method, where hydrate is formed in sediments containing ice.

The laboratory tests that formed hydrate in water saturated conditions (Berge et al., 1999; Spangenberg & Kulenkampff, 2005; Yun et al., 2005) are more likely to produce the morphologies of hydrate seen in deep sea sediments. Analysis of the results from each test (Table 2.4), has lead to the conclusion that hydrate initially takes on a pore filling morphology in these conditions. Yun et al. (2005) concluded from their tests using THF as a soluble hydrate former, that hydrate nucleated on the surface of sand grains and grew out into the pore space. They acknowledged a critical volume ($\approx$40% pore space) whereby the shear wave velocity of the sediment began to increase from a base level of around 300ms^{-1}, due to the hydrate beginning to interact with the sediment grains. This change in properties at a critical hydrate content has also been documented by Berge et al. (1999) and Spangenberg & Kulenkampff (2005), at around the same hydrate content as Yun et al. (2005). The consistency of these results would suggest the same morphologies are being produced in each test, at least prior to the 'critical hydrate content'. After this point however, the results appear to diverge. Berge et al. (1999) state that hydrate cements the grains together once the critical volume is exceeded, as at hydrate volumes of 52% of the pore space they found a P–wave velocity of 3810ms^{-1}. Spangenberg & Kulenkampff (2005) show a sharp increase in P–wave velocity at around 40% hydrate, but followed by a gradual increase in velocity with increasing hydrate content. Although they observed an end–state of their tests, where glass beads were suspended in a matrix of hydrate, Spangenberg & Kulenkampff (2005) were unable to make any conclusions as to how the hydrate was forming in the pore space at lower hydrate contents.

Although the tests of Berge et al. (1999); Spangenberg & Kulenkampff (2005) and Yun et al. (2005) appear comparable, it is still hard to draw reliable conclusions due to the differences in hydrate former phase, guest species and host materials used. The influence of hydrate former phase on the morphology of hydrate has been investgated by Tohidi et al. (2001). They compare hydrate formed from a soluble hydrate former (THF), dissolved gas (carbon dioxide) and free gas (methane). It was shown that hydrate would form at the gas water interface in the case of the free methane gas and water system, with hydrate taking a granular form as it crystallised out. Hydrate formed from the dissolved carbon dioxide was 'skeletal', with the hydrate taking on an almost dendritic morphology across the whole specimen (Tohidi et al., 2001). The carbon dioxide hydrate made from the soluble phase showed a similar granular

form to the methane hydrate. It is apparent from these observations that there is a difference in crystal morphology with regard to the hydrate former, but as the tests conducted by Tohidi et al. (2001) could not investigate the physical properties of the specimens, it is not clear what affect these morphologies may have on the mechanical properties of hydrate. The tests of Yun et al. (2005) and Spangenberg & Kulenkampff (2005) can be compared with regard to hydrate former phase however, with Spangenberg & Kulenkampff (2005) using dissolved methane gas, and Yun et al. (2005) forming hydrate from THF. The results given in Table 2.4 suggest that the hydrate formed from the dissolved gas Spangenberg & Kulenkampff (2005) gives slightly higher seismic velocity values than the soluble hydrate former (Yun et al., 2005). The results of Berge et al. (1999) also come from a soluble hydrate former (R11), and when compared with Spangenberg and Kulenkampff's results also appear to be lower by approximately $300 ms^{-1}$. This hypothesis must be made with care however, as each experiment used different host materials.

Even though slight differences are observed between the results of Berge et al. (1999); Spangenberg & Kulenkampff (2005) and Yun et al. (2005), they may not be important when considering the subject of morphology. As stated in the above discussion on water saturated tests, the results do seem to agree on the change of state of the host materials, and therefore the likely morphology of hydrate in the pore space regardless of the small scale differences in seismic velocity values. The subject of hydrate former phase may be more important if it were to cause larger changes in host sediment properties that lead researchers to draw the wrong conclusions on morphology in the pore space.

Hydrate Former

It is still not clear what influence guest molecule, referred to here as hydrate former, has on the morphology of hydrate and therefore how it affects a host sediment. Of the little work that has been done comparing different hydrate formers, Durham et al. (2005) have found that guest species significantly influences the physical properties and behaviour of hydrates. It was concluded that methane gas hydrate behaviour in sediments could not be compared to that of ice, or other hydrate formers such as THF (Durham et al., 2005). Information in Table 2.2 agrees with the determinations of Durham et al. in that it shows slight differences between solid methane and propane hydrate properties. With this in mind the results presented by Yun et al. (2005) (Table 2.4) should be observed with certain considerations. It is possible that the use of THF as a hydrate former promotes lower seismic velocities than should be expected for a methane gas hydrate bearing sand. Although Spangenberg & Kulenkampff (2005) do not present shear wave velocity values, their P–wave velocity results do suggest that the seismic velocities for methane hydrate grown out of solution are slightly higher than the equivalent

Source	Material	V_p/ms^{-1}	V_s/ms^{-1}
Shaw (1986)	Water Ice	3890	1900
Waite et al. (2000)	Water Ice	3900 ± 40	1970 ± 20
Whiffen et al. (1982)	Pure Methane Hydrate	3369	–
Waite et al. (2000)	Pure Methane Hydrate	3650 ± 50	1890 ± 30
Bathe et al. (1984)	Pure THF Structure II Hydrate	3513	1663
Stoll & Bryan (1979)	Propane–Methane hydrate and Sand	1800–2260	–
Winters et al. (2004)	≈100%(?) Methane hydrate and sand	3950	–
Berge et al. (1999)	20% R11 Hydrate and sand	1700[c]	–
	40% R11 hydrate and sand	2500[c]	1500[c]
Waite et al. (2004)	20% Methane Hydrate and sand	3080	2120[b]
	40% Methane hydrate and sand	3360	2300[b]
Priest (2004)	20% Methane Hydrate and sand	2476[a]	1423
	40% Methane Hydrate and sand	2908[a]	1636
Spangenberg & Kulenkampff (2005)	20% Methane hydrate and glass beads	2000[c]	–
	40% Methane hydrate and glass beads	2800[c]	–
Yun et al. (2005)	40% THF hydrate and sand	–	300[c]
	90% THF hydrate and sand	–	1500[c]

Table 2.4: P–wave (V_p) and shear wave (V_s) velocities gained by various workers of hydrate synthesized in the laboratory. [a]Calculated saturated V_p values.[b]Values calculated by Waite et al. (2004) using standard rock physics relations.[c]Approximate values.

values found by Yun et al. (2005). This may be a slight red herring however, as Spangenberg & Kulenkampff (2005) formed hydrate in glass beads and not natural sand. Bui (2009) has shown that specimens formed from glass ballotini have a much higher seismic velocity than specimens formed of sand of a similar grain size. By using glass beads, Spangenberg & Kulenkampff (2005) may have produced results that are not comparable to those of Yun et al. (2005).

In addition to the work of Yun et al. (2005), Buffett & Zatsepina (2000), Tohidi et al. (2001) and Berge et al. (1999) have each deviated from using methane as the guest molecule in hydrate formation, with Buffett & Zatsepina (2000) and Tohidi et al. (2001) using CO_2, and Berge et al. (1999) using R11 to form hydrate. Although Buffett & Zatsepina (2000) and Tohidi et al. (2001) do not present physical property measurements, the mechanisms of hydrate formation they observe may not be comparable to those of methane hydrate. Details from Ismail et al. (2002) show that different cement types have different morphologies in the pore space and so it seems unwise to assume that all hydrate formers will take the same form in a host sediments without testing this hypothesis.

Choice of Apparatus

The implications of apparatus choice are not as direct as those specifically affecting hydrate

growth, but can still lead to a mis–understanding of hydrate morphology. It has been shown that the velocity of water–saturated sediments is dependent on the frequency of measurement (Best et al., 2001; Stoll, 2002; Lee & Collett, 2008). Lee & Collett (2008) have modelled the effect of frequency change on partially saturated sediments and found that P–wave velocity can increase by 500ms^{-1} between seismic frequencies ($<$500Hz) and those above 1kHz. Experimental work by Best et al. (2001) and Stoll (2002) also show an increase in P–wave velocities for unbonded sediments when testing over a range of frequencies from seismic to ultrasonic. Some of the non–destructive methods for testing gas hydrate bearing sediments may therefore distort the results from many synthetic hydrate bearing sediments and make them seem stiffer, or weaker than they actually are. This effect could be evident when one compares the results from Waite et al. (2004) and Priest (2004). The same formation technique was used in both tests, along with comparable materials, however, Waite et al. (2004) obtained much higher values than Priest (2004) for the same hydrate contents (Table 2.4). Priest used a resonant column device to measure shear wave velocity, in which the frequency of excitation did not exceed 600Hz. The P–wave transducers of Waite et al. (2004) used 1MHz sources, which could increase the measured P–wave velocity of a sediment by 500ms^{-1} according to Lee & Collett (2008). The use of high frequency sources could therefore lead to mis–interpretation of hydrate morphology and how it is affecting the sediment, which will in turn lead to detecting and quantification errors during seismic surveying.

It seems clear that in order to draw solid conclusions on the morphology of hydrate in the pore space, a direct comparison must be made between laboratory synthesised hydrates formed in consistent conditions. All the tests described above have differences in formation method, guest molecule, and hydrate former phase that cast doubt on the ability to compare between them reliably.

2.4.3 Modelling Gas Hydrate in Sediments

In addition to laboratory methods, modelling of the hydrate–sediment system has proved a valuable tool in determining the effect hydrate has on the properties of sediments. Rock physics modelling is based on the knowledge of the relationship between wave speeds and the elastic moduli of a rock's components. The variety of modelling techniques available each manage the arrangement and interaction of these components differently, and so each have their benefits and drawbacks in the application to hydrate research. Lee et al. (1996) was the first to model gas hydrate in a sediment and utilised the weighted equation method which averages a sediment as a solid phase plus a suspension phase. The differential effective medium (DEM) model also

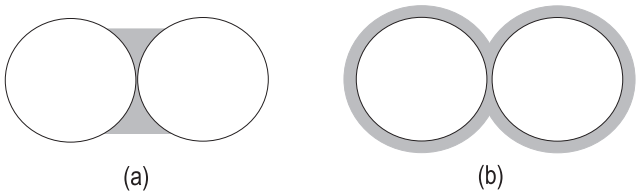

Figure 2.6: The two forms of hydrate as cement (a) Hydrate forms a cement at the grain contacts. (b) Hydrate grows to envelop the grains. From Dvorkin et al. (2000)

uses a two phase system, and creates composites by incrementally adding inclusions of one phase to another "matrix" phase (Zimmerman, 1991; Mavko et al., 1998). The DEM method has been notably used by Jakobsen et al. (2000) to predict the seismic properties of clay rich hydrate bearing sediments.

Further modelling methods utilise a three phase system, and are based on modelling the sediment as a random packing of spherical grains (Mavko et al., 1998). The three phase system considers hydrate as a component of the sediment either as a cementing agent, a pore filling material, or a frame building material (Ecker et al., 2000). In a continuation of the hypotheses described in Section 2.4.1, the three phase modelling methods are now briefly described.

Cementing Models

The work of Dvorkin et al. (1999a) describes the application of a model that explores the way hydrate would affect a sediment if forming as a cement at grain contacts. The models are based around the CCT (contact cement theory) of Dvorkin et al. (1994) which calculates the shear and bulk moduli of a dense, random packing of spherical grains with a small amount of elastic cement at contacts. The model depends on the original porosity of the sediment (without gas hydrate), the hydrate content of the pore space, the elastic moduli of both the hydrate and original mineral phase, and the average number of grain contacts per grain (called the coordination number) of the grain pack. The model can also take into account the cement distribution, allowing for the difference in cementing morphology for a cement that coats the grains, or one that solely forms at grain contacts (Figure 2.6). The equations that are used in this model are shown in Appendix A.

Pore Filling Models

The modelling of gas hydrate as a pore filling material is more straight forward than modelling it as a cement. As mentioned previously in Section 2.4.1, hydrate forming in the pore space would only alter the bulk modulus of the sediment, without affecting the interaction of the

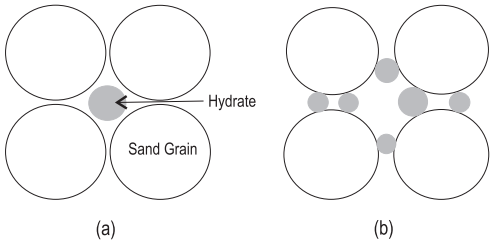

Figure 2.7: Two configurations of hydrate forming in the pore space (a) Hydrate forms in suspension (b) Hydrate grows to become part of the sediment load bearing frame.

sediment grains. Standard models for the bulk moduli of saturated materials can therefore be modified to include the hydrate as an additional component. Equations by Gassmann (1951) derive the bulk modulus of a saturated sediment by using the bulk moduli of the sediment frame and the sediment's constituent parts, i.e. the mineral grains and the pore fluid. If hydrate were to form in suspension in a saturated pore space (Figure 2.7a) it can then be assumed to alter only the bulk moduli of the fluid. This altered value can then be used instead of the bulk modulus of water for the pore fluid in Gassmann's (1951) equation. The equations for this modelling method can be found in Appendix A.

Frame Building Models

Hydrate can affect a sediment by growing in a way that the grains of hydrate become part of the load bearing structure of the sediment (Figure 2.7b). If this was the case, the stiffness of the sediment would be altered by the fact that instead of only grain–grain contacts, there would also be grain–hydrate contacts. The adjustments to the stiffness of a material can be calculated by determining the difference in properties of a hydrate grain compared with a grain of the host sediment. The sediment can be considered as having a mixed mineralogy and the Equation from Gassmann (1951) can once again be used to determine bulk modulus.

Figures 2.8 and 2.9 compare the results generated from the three phase models described above for a range of hydrate contents from 0 to 45% of the pore space. As predicted, hydrate acting as a cement produces high compressional and shear wave velocities at low hydrate concentrations. The two cement configurations show that there is a smaller increase in seismic velocity when the hydrate is evenly distributed over the grains, but that as the hydrate concentrations become larger, this difference diminishes. The P– and shear wave results of the other two models also illustrate the behaviour discussed in Section 2.4.1.

The modelling of gas hydrate in sediments has mostly been in order to quantify hydrate con-

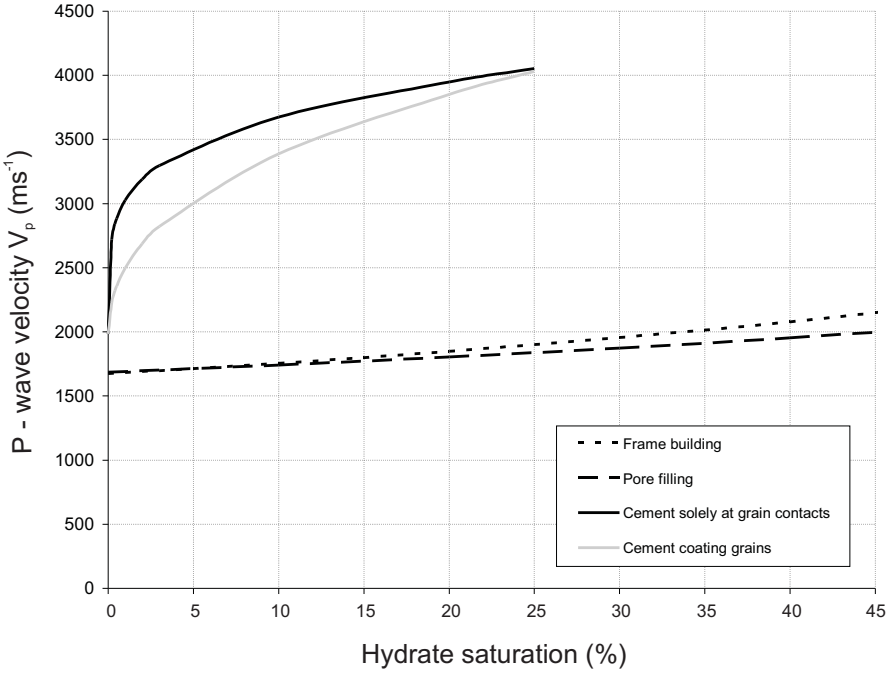

Figure 2.8: A comparison of P–wave velocities generated by different morphological models over a range of hydrate saturations

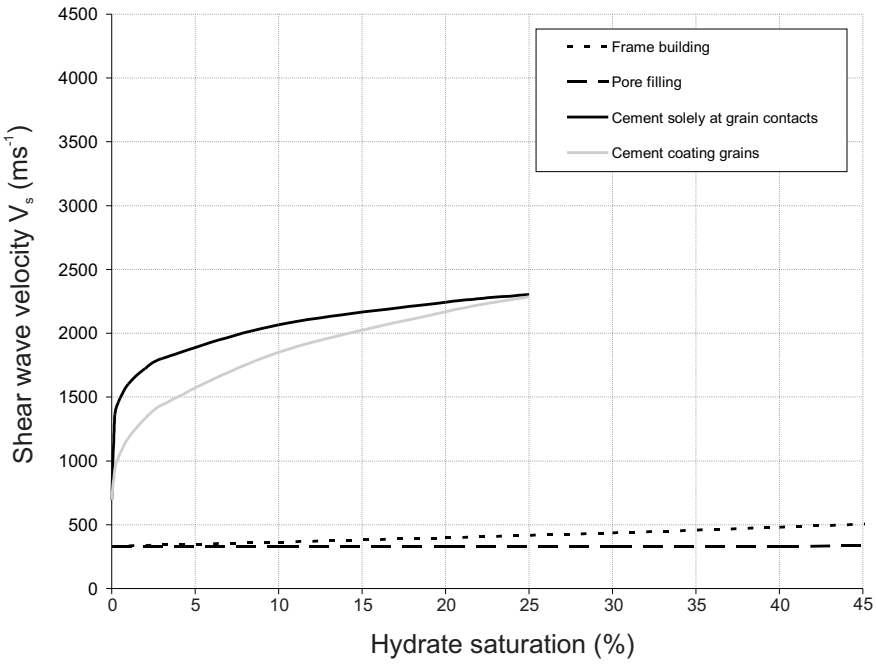

Figure 2.9: A comparison of shear wave velocities generated by different morphological models over a range of hydrate saturations

centrations (Lee et al., 1996; Yuan et al., 1999; Ecker et al., 2000; Jakobsen et al., 2000). The first attempt to infer the morphology of hydrate in a sediment was by Ecker et al. (1998). They compared the seismic data from a BSR on the Blake Ridge with the results from a three phase model where hydrate was modelled using the above conditions as either a cementing or pore filling component. They deduced that the morphology of the hydrate at their location was of a pore filling type. Further analysis has then been made on the morphology of hydrates by comparing laboratory and natural data with model results. Lee & Collett (2001) conclude that hydrate must also be pore filling in the permafrost region of the MacKenzie Delta, as their weighted equation models better predict this morphology for the well log and seismic data observed. Seismic data from the Mackenzie Delta has also been analysed by Winters et al. (2004), who came to the conclusion that hydrates were acting as part of the sediment frame. This verdict has been mirrored by Chand et al. (2004) who modelled a number of different seismic traces from clay rich sediments on the Blake Ridge and in the MacKenzie Delta, and concluded that "hydrate forms a connected phase affecting the rock framework". Although the general consensus from the modelling literature is that hydrates do not form as a cement in nature, there are some reports that suggest some cementation could occur. Yuan et al. (1999) measured a seismic response in the Cascadia Margin that could only be reproduced in a model that located hydrate as a cement at grain contacts. Guerin et al. (1999) have also reported a cementing nature in hydrate bearing sediments of the Blake Ridge, however, their results are in direct conflict with those of Helgerud (2001) who, when using the same modelling techniques, on the same site came to the conclusion that the hydrate was frame building, not cementing.

2.4.4 Attenuation Measurements for Hydrate Bearing Sediments

The only experimental work to have measured attenuation of hydrate bearing sediments is that of Priest et al. (2006). Results from tests on hydrate grown in partially saturated ("excess gas") sands showed that shear wave attenuation was at a high around 3% to 5% hydrate content, where the quality factor Q, representing the ratio of stored energy to dissipated energy in a system was found to be approximately 50, before increasing to a reletively constant value from 10% to 40% hydrate content (Q=125) indicating a lower attenuation. The low attenuation with high hydrate content was attributed to the cementing morphology of the hydrate in the specimens, coupled with the lack of free water. The attenuation peak observed between 3% and 5% hydrate content was due to patchy and weak cementation across the specimen (Saxena et al., 1988; Priest et al., 2006). The results were in agreement with the hypotheses of Pecher & Holbrook (2000) that stated hydrate inclusion in a sediment should see a decrease in attenuation if cementing occurred.

Field measurement of attenuation in sediments containing gas hydrate is a relatively new endeavour. Guerin & Goldberg (2002) were the first to document a relationship between attenuation and hydrate content in the field, by measuring the attenuation of sonic waves in the Mallik 2L-38 well in the Mackenzie Delta, Canada. They observed a P-wave velocity increase in the sediment with increasing hydrate content, however the attenuation of the sediment also increased as the proportion of hydrate in the pore space became larger. This pattern is not in agreement with that expected if hydrate were to act as a pore filling component and reduce porosity (Hamilton, 1972). However, the data conforms with that of Goldberg et al. (1985), who observed the same behaviour in sediments with varying degrees of silica diagenesis. Survey data from the Nankai Trough also shows the same relationship between sonic attenuation and hydrate content (Matsushima, 2005). It was observed that both compressional and shear wave attenuation increased with increasing hydrate content. Matsushima suggested that attenuation change may become a more helpful tool than seismic velocity in detecting and characterising hydrate bearing sediments.

2.5 Summary

From a review of the literature into gas hydrate research, it can be seen that the information needed to accurately detect and quantify methane hydrate accumulations in the sub–surface is not complete. The following lists the conclusions that can be drawn from the literature and the direction future research must take.

- Gas hydrate is a solid material that takes on a variety of morphologies in the pore space of a host sediment, controlled by tectonic setting, gas supply and host sediment type.
- Gas hydrate effects the mechanical properties of a sediment in different ways depending on it's morphology.
- Current methods of quantifying hydrate in natural sediments are seismic surveying, drilling and sampling, of which seismic surveying is used initially to detect hydrate presence in the sub–surface.
- Seismic surveying still relies heavily on the location of a BSR to identify hydrate presence in marine and permafrost environments, even though this has been shown to be unreliable as a detection method (Ashi et al., 2002; Paull et al., 1996).
- A wide range of shear and compressional wave velocities have been obtained for hydrate bearing sediments by seismic surveying and logging techniques (Table 2.3). This dis-

crepancy means that researchers still do not know what velocity profiles to expect from a hydrate deposit.

- Laboratory testing can be undertaken in order to get a better understanding of hydrate bearing sediments and their seismic signatures.
- Laboratory testing of natural methane hydrate samples has been limited due to the difficulty of maintaining stability conditions during recovery and transference to apparatus. Recent advances in pressure coring have allowed for intact hydrate samples to be recovered, but a method for transferring them to equipment for in–depth geotechnical testing does not currently exist.
- Synthetic hydrate growth in the laboratory utilises a number of methods, although analysis suggests application of any results to natural hydrate deposits must be used with care:
  - Many laboratory methods for testing sediment hosted gas hydrates, use high frequency measurement techniques that do not lend themselves to satisfactory comparison with results from seismic surveying. The only current low frequency method of testing hydrate bearing sediments is the resonant column technique of Priest (2004).
  - Some previous laboratory tests on gas hydrate have used a variety of hydrate formers other than methane, to more easily form gas hydrate. As the influence of hydrate former on hydrate mechanical properties is not fully understood, results from these tests are ambiguous.
  - Measurement techniques for laboratory synthesised hydrate require homogeneous specimens for correct interpretation, however a number of previous experiments have shown no control of hydrate distribution (Berge et al., 1999; Winters et al., 2004).
  - The saturation state of hydrate formation must be analogous to natural environments if results are to be applicable to seismic surveying.
- Analysis of synthetic hydrate formation and laboratory testing has suggested that formation methodology in the laboratory has an affect on hydrate morphology in the pore space.
- Due to the complexity of forming hydrate in the laboratory, little work had been conducted on forming hydrate in sediments other than homogeneous sands.

- Attenuation results from the field suggest that attenuation changes in hydrate bearing sediments could provide a more reliable method for the detection and quantification of sub–surface hydrate deposits (Guerin & Goldberg, 2002; Matsushima, 2005), but more detailed investigation is necessary to support this hypothesis.

Chapter 3

TESTS ON SYNTHETIC HYDRATE BEARING SEDIMENTS: EXPERIMENTAL METHODS

3.1 Introduction

The literature reviewed in Chapter 2 highlights the difficulties in attempting to synthesise and measure the properties of gas hydrate in the laboratory. Compromises, either in choice of hydrate former or in formation technique, are necessary in most cases in order to form hydrate under controlled conditions. It is also evident that little work has been done to investigate the growth of hydrates in sediments with a variety of particle size and shape. This chapter describes a series of tests that investigated the influence of formation method and sediment type on the way hydrate impacts a sediment. The methods and equipment used in the testing also aimed to resolve some of the issues described in the literature review with regard to homogeneity and application to natural environments.

The chapter begins with an introduction to the Gas Hydrate Resonant Column, a device specifically designed at the University of Southampton to synthesise and test gas hydrate. The resonant column test methodology is discussed, including the data reduction techniques used to obtain the physical properties of the sediment.

The first series of tests will then be described, where a methodology was developed to make

homogeneous methane gas hydrate in sands that were almost fully saturated. The second sequence of tests formed methane hydrate in sediments with a variety of particle shapes and sizes. A description of these tests will then be followed by some typical observations seen in specimen preparation, hydrate formation and resonant column testing.

3.2 The Gas Hydrate Resonant Column Apparatus

The apparatus used in this research was the Gas Hydrate Resonant Column (GHRC). It was developed by Priest (2004) and GDS Instruments Ltd, as part of a collaborative grant funded by the 'HYDRATECH' project. The original aim was to design an apparatus that allowed formation and subsequent testing of methane gas hydrate bearing sediments at frequencies and strain rates comparable to those frequently used in seismic surveys. A number of features were added to a standard Stokoe resonant column to make it suitable for gas hydrate testing (Priest, 2004).These included a pressure cell rated to 25MPa, and an environment chamber capable of temperatures between -20°C and 50°C, that allow for specimens inside the resonant column to be taken into the methane hydrate stability field. Inlets were also included that allowed for back pressure to be applied by using either gas or water pressure.

This section summarises the theory behind the resonant column device and the associated equations used in data reduction, as well as giving a brief description of the control mechanisms of the gas hydrate resonant column.

3.2.1 Resonant Column Test Procedure

The resonant column device is a laboratory apparatus that measures the dynamic properties of sediments at small strains (10^{-3} to 10^{-6}). As the resonant test is nondestructive, the same specimen can be tested over a range of confining pressures in one test sequence. The principle of the resonant column test is to excite a cylindrical column of sediment at its first torsional or first flexural mode and so determine shear modulus and vertical Young's modulus respectively. By monitoring the motion of one end of the column, the natural resonant frequency of the specimen is measured. This can then be used to evaluate the shear wave velocity V_s through the column of sediment (Bennell & Smith, 1991) from torsional excitation, or longitudinal wave velocity V_{lf} from flexural excitation (Cascante et al., 1998). Attenuation measurements (Q_s^{-1} and Q_{lf}^{-1} for torsion and flexure respectively) can also be made using the resonant column device.

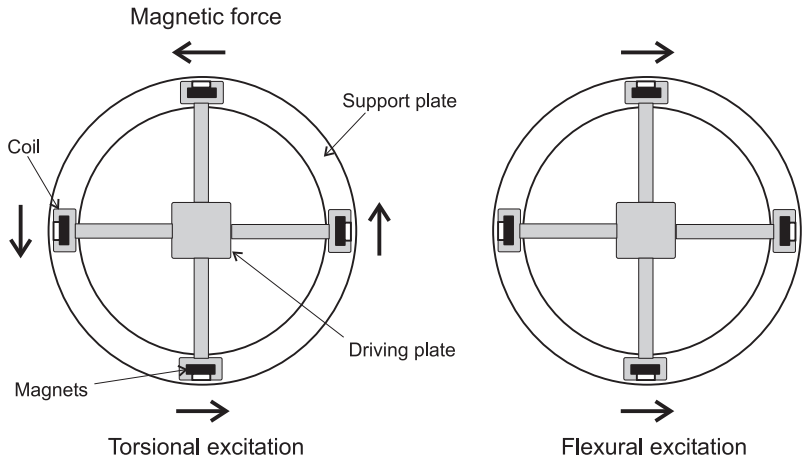

Figure 3.1: Motion of the magnets in torsional and flexural excitation. From Cascante et al. (1998).

There are a number of different designs of the resonant column device. The GHRC is based on a Stokoe resonant column that utilises fixed–free boundary conditions. In the fixed-free test a cylindrical specimen is fixed at its base and excited via a drive mechanism attached to the free end. The GHRC also makes use of modifications to the Stokoe resonant column adopted by Cascante et al. (1998) for flexural excitation. In a standard resonant column, four pairs of coils are connected in series to induce torsional excitation. For flexural movement, two coils are used to produce a horizontal force on the specimen (Figure 3.1). This allows for the same coil and magnet arrangement to be used for both excitation modes.

Stiffness Measurements

The reduction of data from the resonant column test to calculate wave velocity depends upon the boundary conditions. The system is modelled as having a single degree of freedom, which allows for ease in data reduction.

Stiffness Measurements from Torsional Vibration

By measuring the natural frequency in the resonant column, the velocity of the propagating wave and the degree of damping of the system can be found. Shear wave velocity can then be used along with the density of the specimen to determine the shear modulus.

The natural frequency of torsional vibration allows for shear wave velocity (V_s) to be calculated from the relationship (Richart et al., 1970):

$$\frac{I}{I_o} = \beta \tan \beta \qquad \text{where} \qquad \beta = \frac{\omega_n l}{V_s} \tag{3.1}$$

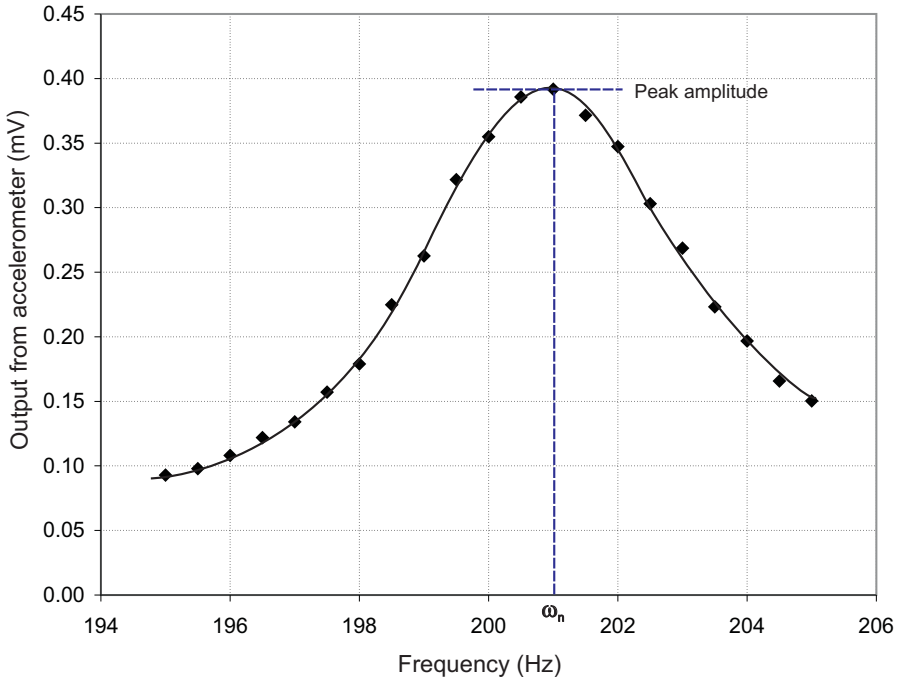

Figure 3.2: The frequency response curve for a specimen of Leighton Buzzard sand, showing the resonant frequency when a peak amplitude is observed

Where ω_n is the natural circular frequency vibration of the specimen; l is the length of specimen; I_o is the mass polar moment of inertia of drive unit; and I is the mass polar moment of inertia of specimen. Once V_s has been found, shear modulus G can be determined from:

$$G = V_s^2 \rho \tag{3.2}$$

Where ρ is the density of the specimen. Equation 3.1 is the basic equation for the fixed-free resonant column.

The natural frequency, ω_n, is the only parameter in Equation 3.1 that is measured during a resonant column test. From standard equations of forced harmonic vibration (Thomson, 1993), it has been shown that the peak amplitude from an applied frequency of excitation approaches the natural frequency of the system when damping approaches zero. It can be assumed, with regard to resonant column testing of soils, that at low strains damping will be less than 10% (Vucetic & Dobry, 1991). With this assumption, the natural frequency ω_n can be determined by conducting a frequency sweep, with the measured amplitude of vibration of the specimen reaching a peak at the natural frequency (Figure 3.2).

Stiffness Measurements from Flexural Vibration

In flexural excitation, the resonant column system is considered to be a flexing cantilever beam with a lumped mass attached at the free end. In a single degree of freedom system, the natural frequency of a cantilever beam ω_f is represented by (Hulse & Cain, 2000):

$$\omega_f^2 = \frac{3EI_b}{mL^3} \tag{3.3}$$

where I_b is the second area moment of inertia of the beam; m is the lumped mass; and L is the length of the beam. Equation 3.3 represents a system where the beam has no mass, and a lumped mass is attached to the beam at a single point. Figure 3.3 illustrates the idealised state of the resonant column as a cantilever beam. From this figure, it can be seen that allowances must be made for the mass of the specimen (representing the beam) and the distribution of the mass of the top cap, drive mechanism and other additional masses. Rayleigh has shown this can be done by using the "energy method", which accounts for mass distribution by calculating the equivalent acting mass, or *effective mass* of each mass component at a point on the end of the cantilever beam (Thomson, 1993). Utilising this method, Cascante (1996) has shown that the natural frequency of a specimen in flexure in a resonant column can be found from:

$${\omega_f}^2 = \frac{3EI_b}{\left[\frac{33}{140}m_T + \sum_{i=1}^{N} m_i h(h_{0i}, h_{1i})\right] L^3} \tag{3.4}$$

where

$$h(h_{0i}, h_{1i}) = 1 + \frac{3(h_{1i} + h_{0i})}{2L} + \frac{3}{4}\frac{(h_{1i}^2 + h_{1i}h_{0i} + h_{0i}^2)}{L^2} \tag{3.5}$$

where N additional masses have their masses m_i evenly distributed between $h0_i$ and $h1_i$ (Figure 3.3); and m_T is the mass of specimen.

Equations 3.4 and 3.5 allow the derivation of Young's modulus from flexural excitation E_{flex} by measuring the flexural resonant frequency and using the geometric properties of the specimen and drive mechanism. In order to find the longitudinal wave velocity V_{lf} from E_{flex}, a similar relationship between V_s and G as seen in Equation 3.2 can be used:

$$V_{lf}^2 = \frac{E_{flex}}{\rho} \tag{3.6}$$

By assuming that the specimen being tested is made up of a single–phase isotropic medium, the P-wave velocity V_p of the specimen can be found through the relationship (Cascante et al., 1998):

$$V_p = V_{lf}\sqrt{\frac{1-\nu}{(1+\nu)(1-1\nu)}} \tag{3.7}$$

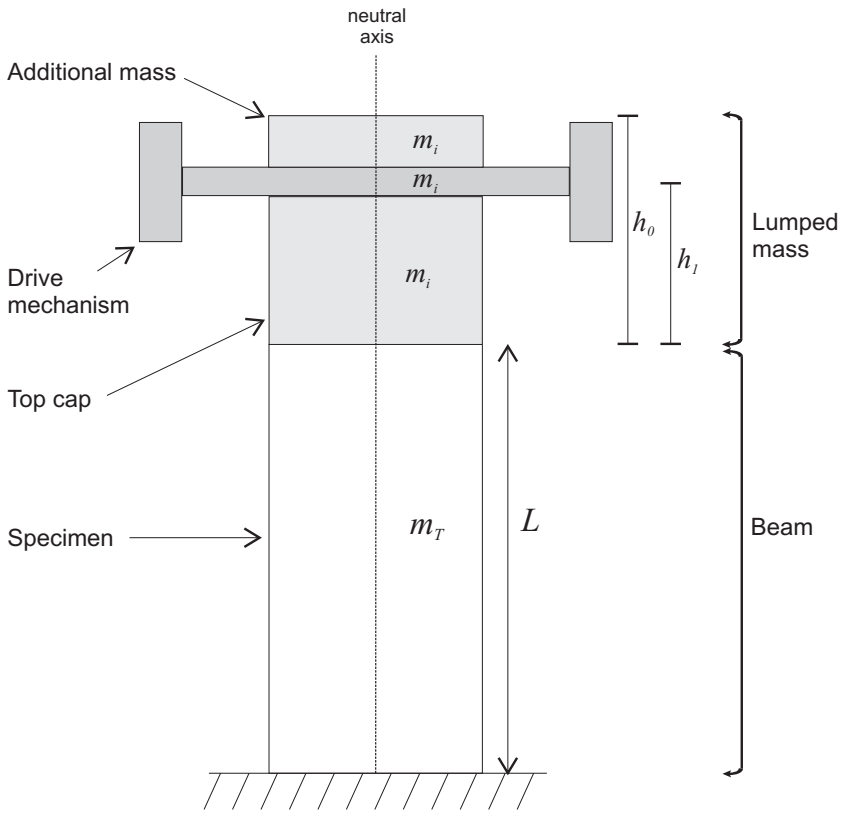

Figure 3.3: A representation of the resonant column as a cantilever beam, where the specimen is idealised as a beam with a lumped mass which consists of the top cap, drive mechanism and additional mass.

Where ν is the Poisson's ratio of the specimen, and is found by:

$$\nu = \frac{1}{2}\frac{V_s^2}{V_{lf}^2} - 1 \tag{3.8}$$

Strain Measurements

Torsional Strain

The calculation of strain in the resonant column is based on the strain of a solid cylindrical bar subject to pure torsion, which is (Hulse & Cain, 2000):

$$\gamma_c = \frac{R\theta}{L} \tag{3.9}$$

Where R is the radius of the specimen; θ is the angle of rotation; and L is the length of the

specimen. In order to consider the average strain across the cross section of a solid specimen, the American Standards (ASTM) recommend taking $4/5R$ in place of R so that Equation 3.9 becomes:

$$\gamma_c = \frac{0.8R\theta}{L} \tag{3.10}$$

In the GHRC, R and L are the geometric properties of the specimen, with the angle of rotation calculated from the displacement derived from an accelerometer reading. The accelerometer used in the GHRC produces a voltage V that is multiplied by a constant Z to give the acceleration experienced by the specimen during resonance $\ddot{x}$:

$$\ddot{x} = ZV \tag{3.11}$$

For the GHRC accelerometer, Z is the value $\sqrt{2}g2/5$ (where g is the gravitational acceleration at the earth's surface). From simple harmonic motion, $\ddot{x} = \omega^2 x$ where $\omega = 2\pi f$. x can be considered as θl, which allows for the angle of rotation to be found from:

$$\theta = \frac{ZV}{(2\pi f)^2 l} \tag{3.12}$$

where f is the frequency of excitation, and l is the distance of the accelerometer from the central axis of the specimen ($= 0.03625$m in the GHRC). Substituting Equation 3.12 into Equation 3.10, the torsional strain in the GHRC is:

$$\gamma_c = \frac{\sqrt{2}grV}{15\pi f^2 Ll} \tag{3.13}$$

or

$$\gamma_c = \frac{1.56Vd}{f^2 L} \tag{3.14}$$

Where d is the diameter of the specimen.

Flexural Strain Measurements

The strain in a cantilever beam can be calculated from the deflection of the beam away from its neutral axis. The deflection of a beam is modelled as a circular arc, with the arc represented by the neutral axis with a length $R\theta$, where θ and R are the angle and radius of curvature respectively (Figure 3.4(a)). Basic strain in bending can therefore be described as:

$$\varepsilon = \frac{\mathrm{D}}{R} \tag{3.15}$$

Where D is the distance to a point on the beam perpendicular to the neutral axis. Considering this relationship in terms of deflection can be done by visualising the deflection of the beam

to have a slope dy/dx (Figure 3.4(b)). The rate of change of that slope is given as curvature $K = -d^2y/dx^2$. K is related to Figure 3.4(a), in that $K = 1/R$, therefore the strain in a cylindrical beam can be obtained from:

$$\varepsilon = \frac{d^2y}{dx^2}r \tag{3.16}$$

Where r is a distance from the neutral plane in the y direction. Cascante (1996) has shown that Equation 3.16 can be described in terms of the displacement of the cantilever beam y and the elevation x by:

$$\varepsilon = 6\alpha(L - x)r \tag{3.17}$$

where

$$\alpha = \frac{y_T}{L^2(2L + 3(x - L))} \tag{3.18}$$

In the GHRC, the total deflection y_T is comprised of the deflection of the specimen y added to the deflection of all the additional masses on the top of the specimen dy (Figure 3.5). The accelerometer mounted on the top of the specimen records the total displacement y_T, and from Equation 3.12 is equal to:

$$y_T = \frac{0.141V}{f^2} \tag{3.19}$$

The average strain in a cylindrical beam of radius R and length L, is obtained by summing all the strains in the beam along it's length and cross section (Priest, 2004). Therefore, Equation 3.17 becomes:

$$\varepsilon_{avg} = \frac{4}{\pi}RL\alpha \tag{3.20}$$

and so the average strain in flexure of a specimen in the GHRC can be found from:

$$\varepsilon_{avg} = \frac{0.18VR}{f^2L(2L + 3(x - L))} \tag{3.21}$$

where x is elevation from the base of the specimen.

Attenuation Measurements

In geophysical surveying, energy dissipation is represented by the quality factor Q, which is defined as the ratio of stored energy to dissipated energy in a system. In geotechnical testing, attenuation is normally termed damping, and given in terms of the damping ratio D. Q and D are related to each other through:

$$\frac{1}{Q} = 2D \tag{3.22}$$

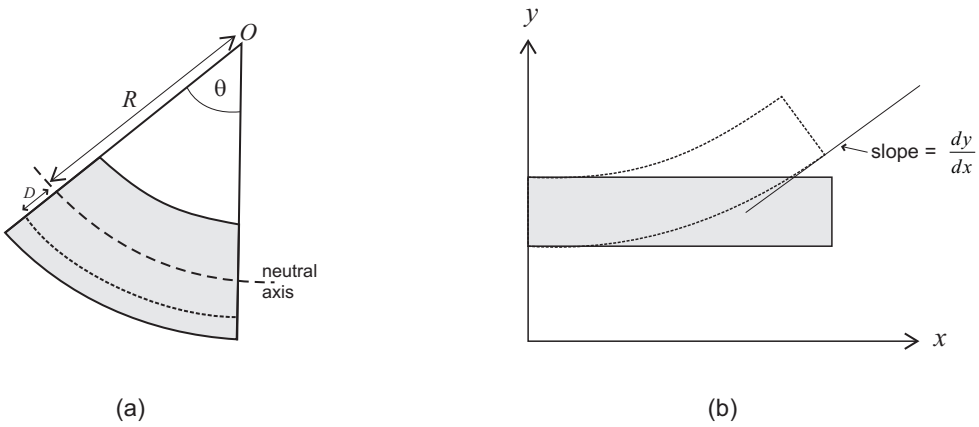

Figure 3.4: (a)A representation of the bending of a segment of a beam with regard to the radius of curvature R and the angle of curvature θ of the neutral plane. (b) The slope of a deflected beam in terms of dx and dy

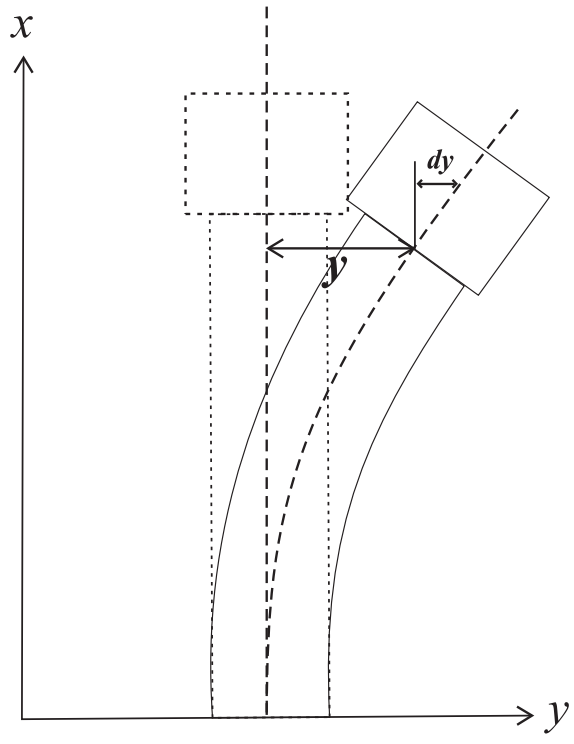

Figure 3.5: Deflection of a cantilever beam y with the additional deflection of an idealised lump mass dy situated at the end of the beam

Two different methods can be used for determining the damping of the specimen in the GHRC. The first uses the 'half power method', obtained from the curve generated from the frequency sweep at constant amplitude (Figure 3.6). If a hypothetical system were subject to zero damping, all the energy of the system would be directed into the single frequency when resonance occurred, creating an infinite peak of no width. In a damped system, some of this energy is transferred to other frequencies near resonance, widening the observed peak. The 'half power method' is a measure of the width of the peak, and therefore the degree of damping. Two points, f_1 and f_2 are identified on either side of the resonant frequency. These are referred to as half power points, as they represent the frequency where half the power of the of the system has been absorbed by damping. In a system undergoing harmonic motion, the power absorbed by damping is proportional to the square of the maximum amplitude X_{max} . Therefore the half power points will be found at the amplitude $X_{max}/\sqrt{2}$ (Meirovitch, 2001) (Figure 3.6). Once f_1 and f_2 have been found, damping D is given by:

$$D = \frac{f_2 - f_1}{2\omega_n} \tag{3.23}$$

D is a measure of the sharpness of resonance, and assumes the frequency response curve is symmetrical about the resonant frequency. In the resonant column system this is normally true at low strains. However, as strain increases, the curve becomes less symmetrical and introduces errors in the measurement of D.

The second method for determining damping in the GHRC is free vibration decay (FVD). FVD considers the relationship between successive peak amplitudes when the specimen is allowed to decay freely from resonance in an underdamped system (Thomson, 1993; Richart et al., 1970). To determine the damping of a system, the free vibration displacement amplitude history is measured and recorded after a specimen has been excited at resonance. Figure 3.7 shows the vibration decay history obtained from a specimen of Leighton Buzzard sand under 250kPa of effective stress. Damping is calculated by finding the logarithmic decrement δ, which is the natural logarithmic value of the ratio of two adjacent peak values of displacement (amplitudes x_1 and x_2):

$$\delta = \ln \frac{x_1}{x_2} \tag{3.24}$$

When considering the relationship between any two consecutive peaks x_0 and x_n, δ is written as:

$$\delta n = \ln \frac{x_0}{x_n} \tag{3.25}$$

A rearrangement of Equation 3.25 shows that δ can be found by plotting the natural logarithm

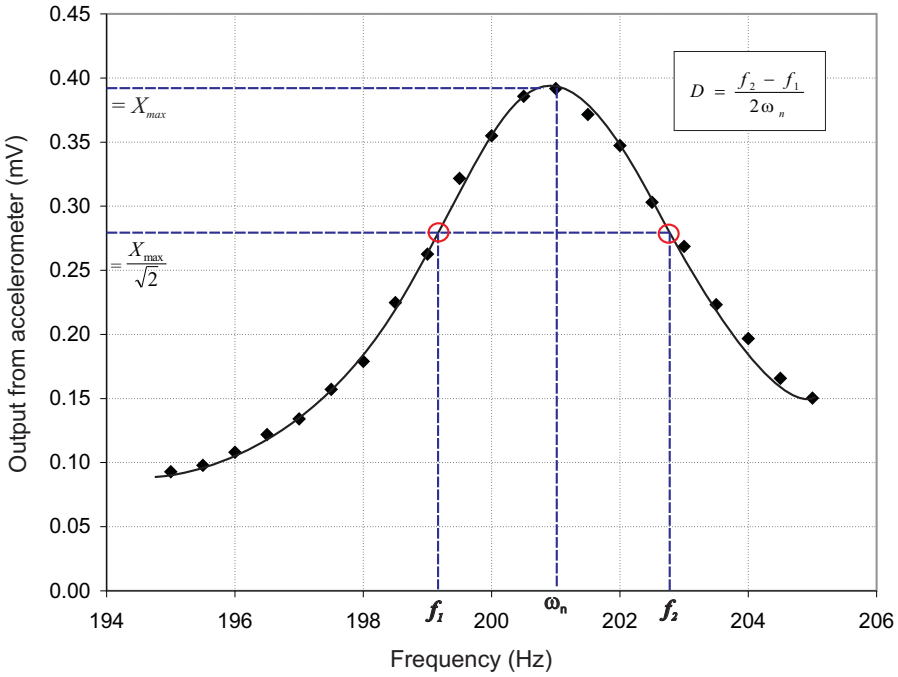

Figure 3.6: The frequency response curve for a specimen of Leighton Buzzard sand, showing the values for f_1 and f_2 found from the half power method

of each peak amplitude against cycle number (Figure 3.8). It has be shown that δ is related to damping ratio D by (Thomson, 1993):

$$\delta = \frac{2\pi D}{\sqrt{1 - D^2}} \tag{3.26}$$

and so D is established through a rearrangement of Equation 3.26:

$$D = \sqrt{\frac{\delta^2}{4\pi^2 + \delta^2}} \tag{3.27}$$

The value for D obtained by the half power and free vibration decay methods also includes an element of damping from the apparatus. Equipment damping in a resonant column comes from the natural damping of the drive mechanism as well as the damping induced by the movement of the magnets inside the coils, termed back–EMF. Equipment damping has the potential to mask the damping of the specimen, but the GHRC has the ability to have an 'open circuit' during FVD, which means the measured value for damping from FVD does not include equipment damping from back–EMF. The free vibration decay method is therefore more readily used in the GHRC to determine damping.

Although the relationships here have been with reference to torsional damping, the principles described are the same for any vibrating system that is modelled as having a single degree of freedom. The equations for FVD are therefore used when determining the damping in flexural excitation also.

Assumptions in GHRC Data Reduction

The derivations of shear and longitudinal wave velocity from GHRC tests make a number of assumptions. Primarily, the material is assumed to be isotropic and elastic. Natural sediments are rarely isotropic, and will have a certain degree of anisotropy that is either due to the application of anisotropic stress, or is an inherent characteristic of the sediment from the natural alignment of particles during deposition (Powrie, 1997). However, measures can be taken in the laboratory when testing specimens in the resonant column to reduce anisotropy. The GHRC has the ability to apply isotropic load, so that stress induced anisotropy is low. Additionally, if specimens consist of rotund materials (predominantly sands) this will reduce anisotropy caused by grain alignment (care must be taken when testing specimens of a mixture of materials). By taking these measures, it allows for the use of the resonant column to derive properties G and E_{flex}, as the device can not measure the additional elastic constants that would be needed to account for anisotropy in a specimen.

To interpret data from flexural excitation in the resonant column, more assumptions must be made. The cantilever beam approximation for the specimen and drive mechanism assumes that (a) the system has a consistent cross section along the entirety of it's length and (b) the specimens length is at least twice it's width. The data reduction also requires that the specimen is loaded in its plane of symmetry, and that the deformations it experiences are small. The dimensions of the specimen in the GHRC, as well as the way flexural excitation is applied, allow for these assumptions to be made in the GHRC tests.

3.2.2 Calibration of the GHRC

Torsion

Equation 3.1 used to reduce data from the GHRC requires the value I_o, the mass polar moment of inertia of the drive system, to be known. The complex shape of the drive mechanism means that the experimental determination of I_o is preferred over a geometrical calculation. In order to determine I_o experimentally, a bar of known stiffness can be used instead of the specimen in the resonant column. The system is then idealised as a torsional mass spring system, where the bar can be taken as a spring of stiffness k with a mass at the end represented by the drive

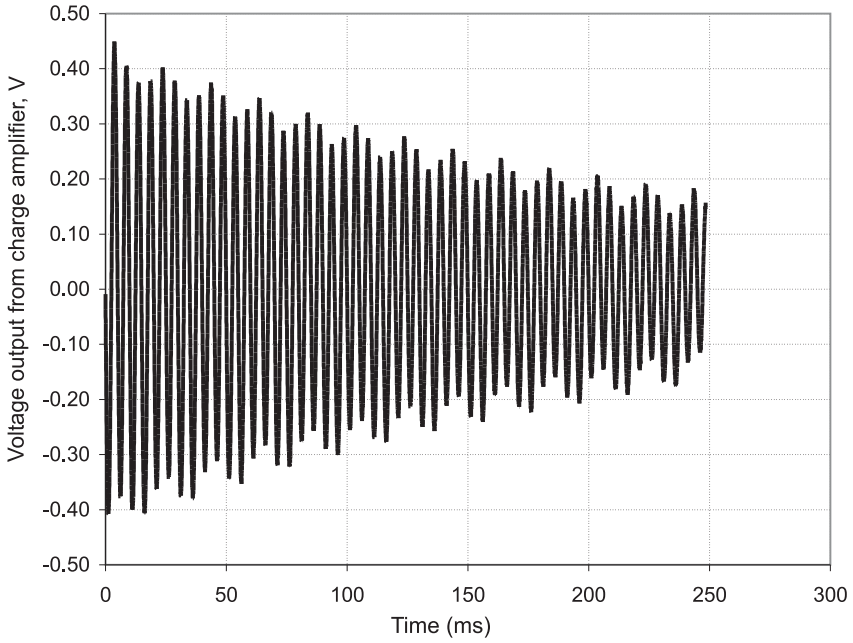

Figure 3.7: Free vibration decay curve for a specimen of Leighton Buzzard sand under 250kPa effective confining pressure

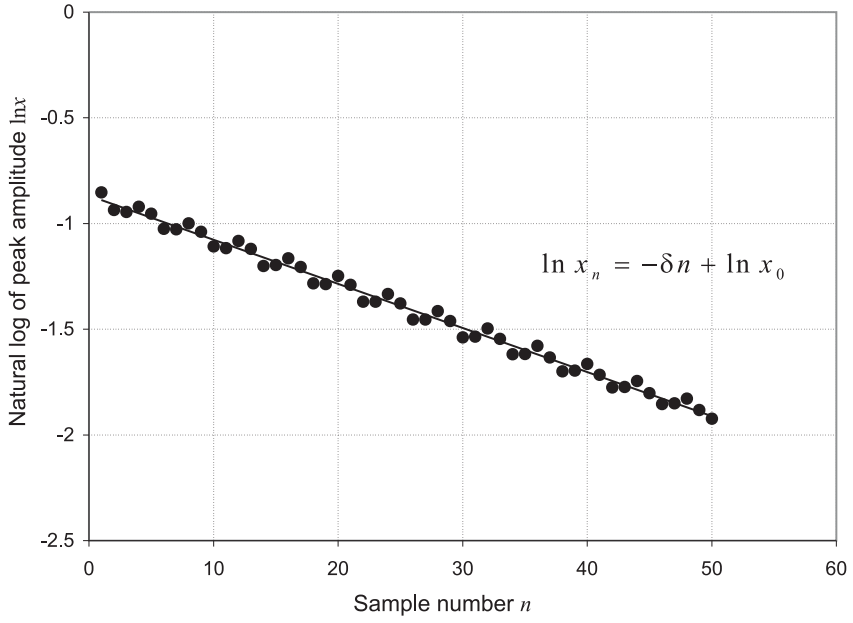

Figure 3.8: Plot of the natural log of the peaks from the free vibration decay trace seen in Figure 3.7. The equation of the best fit straight line fitted to the plot is also displayed

	Bar number	Frequency	$V_s(ms^{-1})$	% Error
Experimental I_o	Bar 1	199.8	3072.7	-0.79
	Bar 2	306.5	3056.5	-1.33
	Bar 3	384.2	3064.1	-1.07
	Bar 4	457.5	3116.5	0.63
Corrected I_o	Bar 1	199.8	3096.1	-0.03
	Bar 2	306.5	3086.2	-0.35
	Bar 3	384.2	3104.7	0.25
	Bar 4	457.5	3088.4	-0.28

Table 3.1: Experimental and corrected values for shear wave velocity V_s for each aluminium calibration bar given with error for the true value of shear wave velocity for aluminium (3097ms^{-1})

mechanism. The natural frequency ω_n can then be obtained from:

$$\omega_n = \sqrt{\frac{k}{I_o}} \tag{3.28}$$

To derive I_o in the GHRC, an aluminium calibration bar is placed in the resonant column and it's natural frequency determined via a resonant column test. This test is repeated in turn by adding additional masses to the top of the calibration bar, and obtaining the new resonant frequencies for each mass. The value for I_o in Equation 3.28 can then be written to include the mass polar moment of inertia of the added masses I_{am}, so that the equation contains $I_o + I_{am}$. A rearrangement of the resultant equation gives:

$$I_{am} = \frac{k}{\omega_n^2} + I_o \tag{3.29}$$

Equation 3.29 takes the form of a standard linear equation. Plotted on a graph of $1/\omega_n^2$ against I_{am}, the value for I_o is given at the y axis intercept. A total of four bars were used in the GHRC, to represent the range of frequencies that may be expected when testing hydrate bearing sediments. Figure 3.9 shows the results obtained from the four calibration bars used in the GHRC. As mentioned previously, I_o is a geometrical property of the drive mechanism, and so should be a constant value. However, it can be seen in Figure 3.9 that as the natural frequency of the bar increases from bar 1 to bar 4, the value for I_o also increases. This characteristic of the resonant column has been addressed (Clayton et al., 2008b) by correcting the value of I_o due to frequency (Figure 3.10). Table 3.1 shows the determination of V_s from the results of the calibration tests compared with the actual value of V_s for aluminium ($3097ms^{-1}$). It can be seen that the error in the value of V_s from the experimental results is reduced when the corrected value for I_o is taken from Figure 3.10.

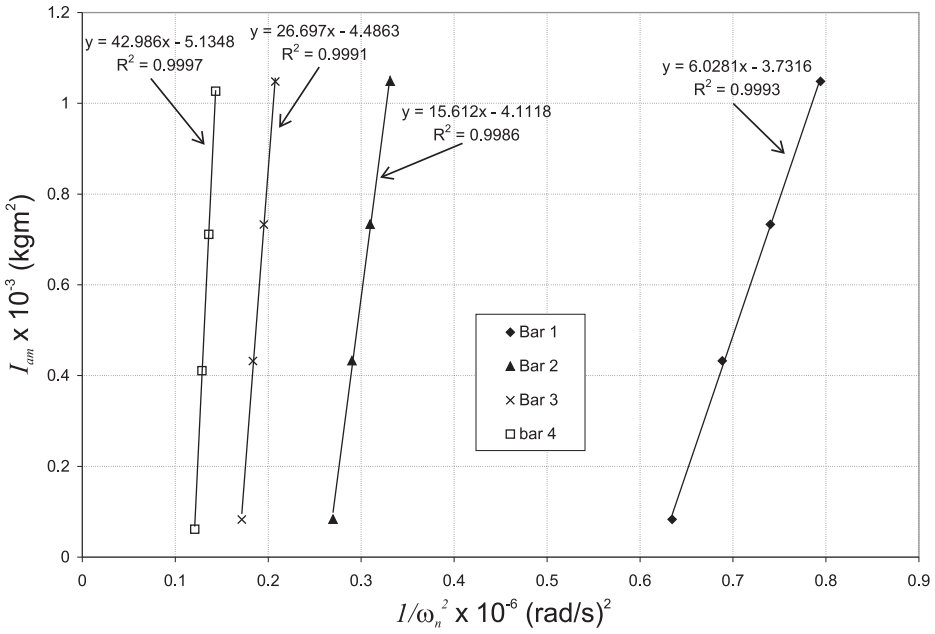

Figure 3.9: Results from a torsional calibration test in the GHRC using four aluminium bars, where the intercept of each straight line represents the value of I_o for each bar.

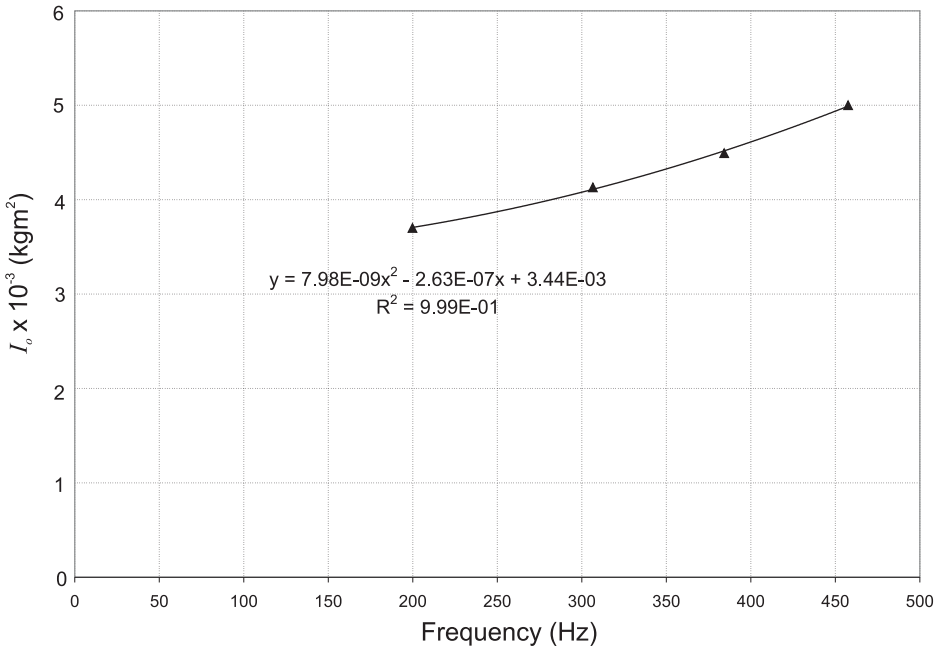

Figure 3.10: The values of I_o found from Figure 3.9 plotted for each calibration bar against resonant frequency.

Flexure

The determination of vertical Young's Modulus in the GHRC requires the rearrangement of Equation 3.4. The Equation allows for the effective mass of each component on the top of the specimen to be represented in terms of it's relative height and mass. Equation 3.5 can be rewritten to allow for masses of complex geometry by using the centre of gravity y_{ci} and the area moment of inertia I_{yi} of each component instead of $h0_i$ and $h1_i$. Thus, Equation 3.5 becomes:

$$h(y_{ci}, I_{yi}) = 1 + \frac{3y_{ci}}{L} + \frac{9}{4L^2}\left(\frac{I_{yi}}{m_i} + y_{ci}^2\right) \tag{3.30}$$

To establish the equivalent height of the drive mechanism, values of m_i, y_{ci} and I_{yi} are required. m_i can be measured for the drive mechanism, and y_{ci} can be taken as the geometric centre. I_{yi} is then found through a similar calibration procedure as for torsion.

The natural frequency of each bar is obtained with and without an additional mass. By using Equation 3.5, the values for the height of the top bar, top cap and added masses can be found. Equation 3.4 is then utilised to form two simultaneous equations for the bar with and without the added mass, containing the measured resonant frequency values from each resonant test, and those properties that are directly measurable. Solving these equations to find the height of the drive mechanism, and then substituting into Equation 3.30 gives the value for I_y.

As with the calibration for I_o, the experimental values for I_y from each bar are not consistent, but unlike I_o do not fall onto a single line. Thus, in order to obtain a value for I_y, Priest (2004) suggests using a regression analysis that uses the known material properties of the calibration bars and the measured frequencies to calculate I_y. As even this analysis shows some frequency dependency to the values of I_y, the empirical solution shown in Figure 3.11 is used here to determine I_y.

Determination of Equipment Damping

As mentioned previously, the damping values found from the 'free vibration decay' and 'half power' methods (Section 3.2.1) contain an element of equipment damping. The half power method incorporates damping from the drive mechanism and the retardant affect from back–EMF. Damping found from the free vibration decay method does not include the affect of back–EMF and so it is the method used in the GHRC. However, in order to obtain the true damping in a specimen from FVD, a value for equipment damping must be obtained and then deducted from measured damping values.

Equipment damping in the GHRC is calculated from the damping ratio obtained from the alu-

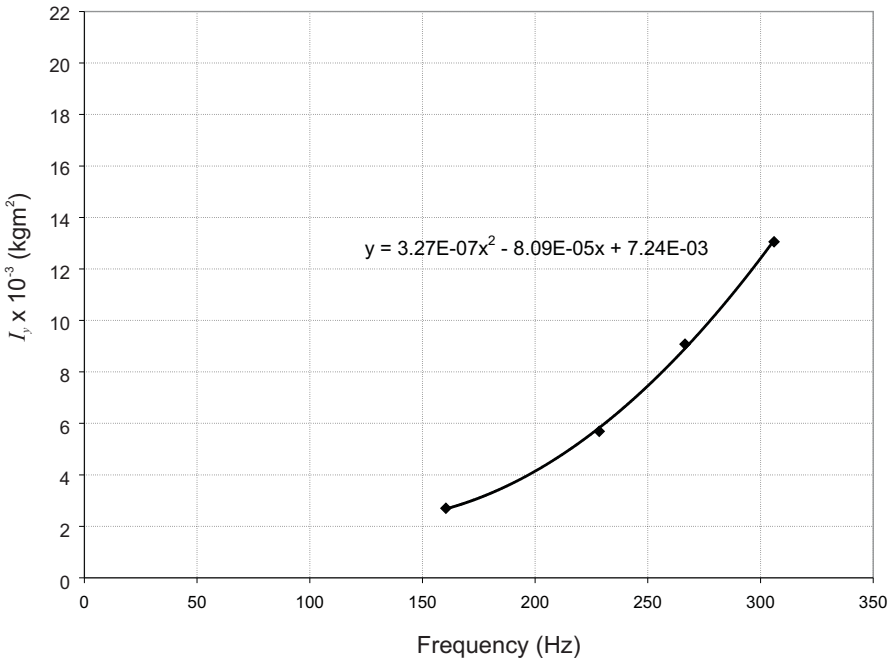

Figure 3.11: Values of I_y found from regression analysis, plotted against resonant frequency for each calibration bar.

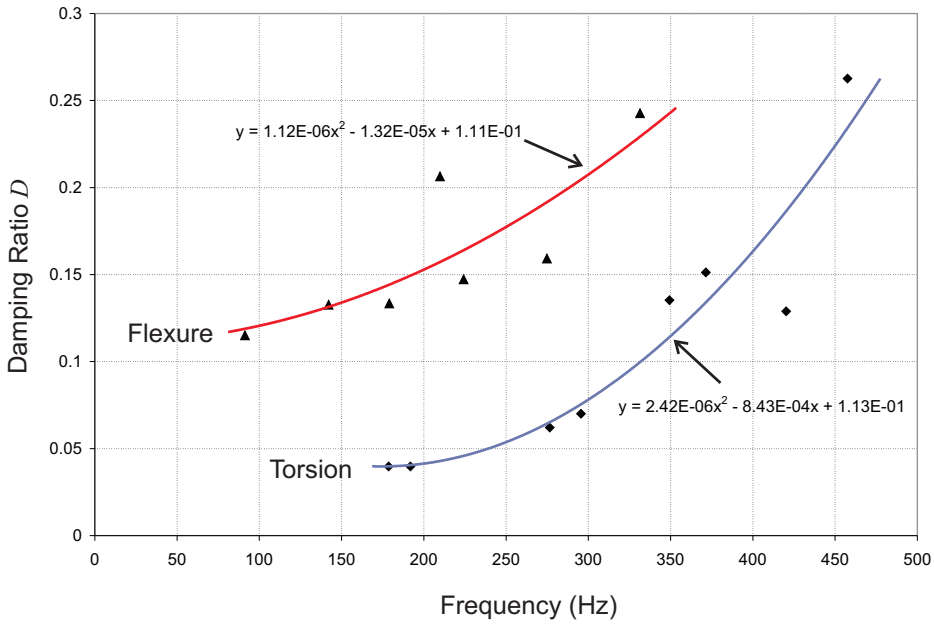

Figure 3.12: Damping values measured during tests of aluminium calibration bars, in both torsion and flexure. Correction curves are plotted for both sets of results.

minium calibration bars. The material damping for aluminium is considered negligible (standard tables give $Q = 350000$ for aluminium), and so the damping observed in the calibration tests is that of the equipment, in both torsional and flexural excitation. Figure 3.12 gives the results for the damping ratios measured for the different calibration bars in both torsion and flexure. It can be seen that equipment damping increases with frequency (Priest, 2004). To account for this frequency dependancy a regression curve is fitted to the data (shown in Figure 3.12). The equation of this line can then be used to correct the measured system damping, so that specimen damping can be calculated.

3.2.3 GHRC Operations and Controls

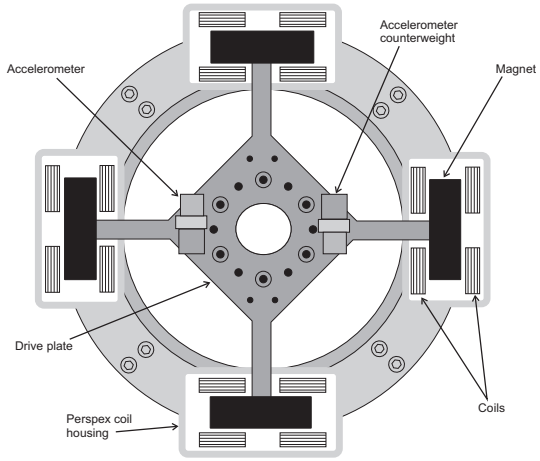

Figure 3.13: Plan view schematic of the GHRC drive mechanism

The resonant column device excites a specimen through an electromagnetic drive mechanism. A voltage is applied to a set of four coils surrounding four magnets (Figure 3.13), which causes the drive plate to vibrate at a defined frequency. The voltage supply to the coils is provided through a control pad outside the GHRC. The coils are set to run in series for torsional excitation. In the case of flexure, only two of the coils are used to provide a horizontal motion. The control pad facilitates the switching of the coil voltages so that flexure can be applied. The control pad is also designed to allow an open circuit to be created during FVD, which removes the back–EMF effect (see Section 3.2.2). The GHRC test is operated through specific software designed by Priest (2004) and written by GDS instruments. The program allows the user to define the voltage and range of frequencies of excitation. During a test, the software records data from the accelerometer mounted on the top of the drive plate, and provides a plot of peak output with corresponding frequency of excitation, from which resonant frequency can be determined (see Section 3.2.1).

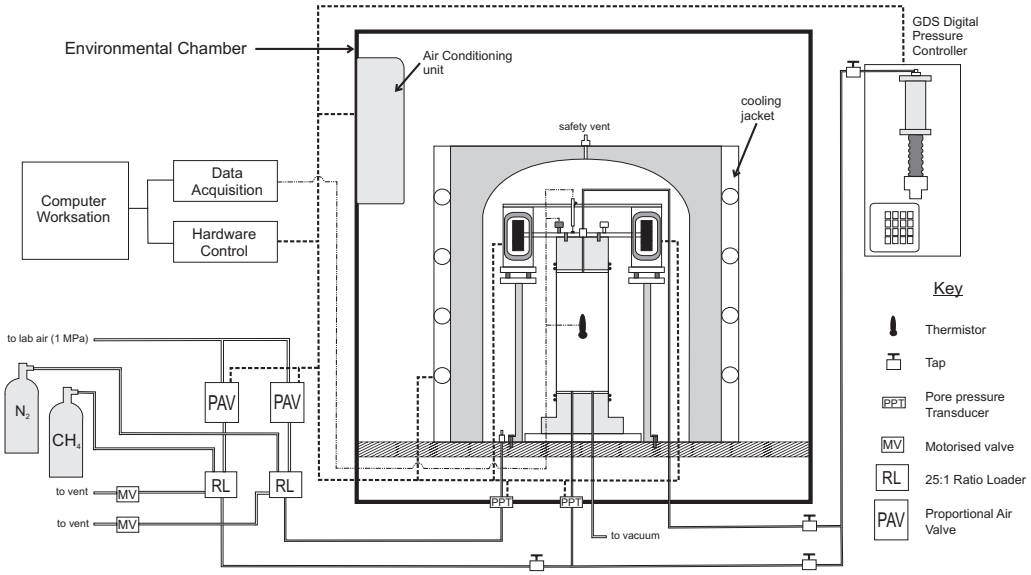

(a)

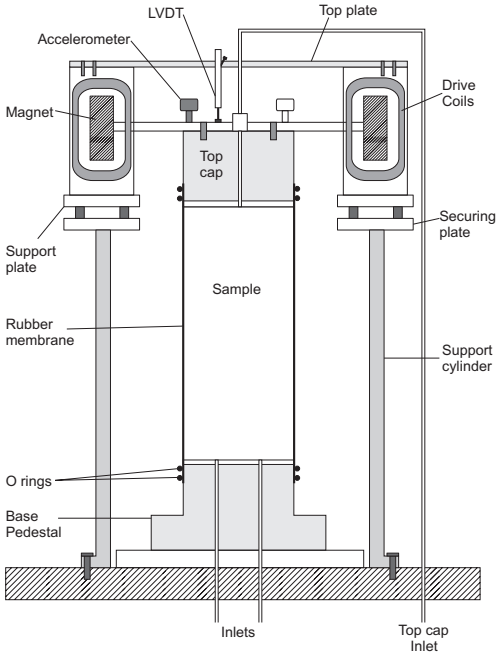

(b)

Figure 3.14: (a) Schematic showing the general layout of the resonant column control systems and apparatus, including pressure and temperature control systems. Re-drawn from Clayton et al. (2005). (b) Close up cross section of the gas hydrate resonant column.

Environmental conditions in the GHRC are provided via a fluid filled cooling jacket surrounding the cell, and an air conditioning unit on the wall of the environment chamber (Figure 3.14). The temperature of both systems can be controlled manually or via a computer software program provided by GDS instruments. The GDS computer software also provides control of the gas and water pressure systems in the GHRC. The gas pressure systems used in the GHRC consist of proportional air valves (PAVs) connected to 25:1 ratio loaders. The cell pressure is provided by nitrogen gas, with methane gas being used to provide back pressure. A motorised valve and a flow control regulator allows for the controlled venting of cell pressure and back pressure. Water back pressure is supplied by a digital pressure controller (DPC). Figure 3.14 shows the general layout of the GHRC, as well as a cross section of a specimen attached to the drive system.

3.3 Tests to Examine the Impact of Hydrate Formation Technique

The Gas Hydrate Resonant Column is capable of forming hydrates under a variety of environmental conditions. Priest (2004) has previously formed hydrates in the GHRC in un–saturated, or gas rich sands. The method Priest (2004) used can be referred to as “excess gas”, as the hydrate was formed from a limited amount of water in a sand that was flooded with methane gas. The set of experiments detailed in this section describe the development of a new technique that allows for hydrate to be grown in water rich sands, referred to here as “excess water” tests. The method would allow for hydrates to be grown from the gas phase in almost water saturated conditions. By using the same grade of sand and similar hydrate contents as used in Priest’s “excess gas” tests, comparisons between different formation techniques were made possible.

3.3.1 Material Properties

The material used in this series of tests was grade E Leighton Buzzard sand from the Lower Greensand formation. Table 3.2 gives a summary of the properties, including the minimum and maximum dry densities and void ratios for this particular material. In this thesis, grade E Leighton Buzzard sand will be referred to as “LBE”.

3.3.2 Hydrate Formation Technique

There are three methods of hydrate formation in excess water conditions in the laboratory:

	Leighton Buzzard sand
Supplier	David Ball Group plc
Description	natural, clean, uncrushed, silica sand, free from silt, clay or organic matter
Geological Formation	Lower Greensand group
Roundness	Rounded-subrounded
Particle size	Grade E ($90 - 150\mu$m)
Specific Gravity	2.65
Maximum dry density	1624kg/m^2
Minimum dry density	1331kg/m^2
Maximum void ratio	0.993
Minimum void ratio	0.633

Table 3.2: The properties of the sand used in the "excess water" tests (Priest, 2004)

1. A saturated specimen is injected with methane gas until a pre-determined amount of water is forced out as a measure of hydrate content (Winters et al., 2004).

2. A dry specimen is filled with gas to a defined pressure. Water is then injected into the specimen to drive the pore pressure up into the hydrate stability zone. As hydrate forms and consumes the gas, water is further injected to maintain pore pressure and the specimen will eventually contain only hydrate and water in the pore space (Tohidi et al., 2001).

3. Hydrate is formed out of the dissolved gas phase (Spangenberg & Kulenkampff, 2005; Tohidi et al., 2001).

Although methane hydrate has previously been synthesised using the first method (Winters et al., 2004), there are drawbacks to this method, as discussed in Section 2.4.2. As such, this method was not preferred for making hydrate in the GHRC. Making hydrate from the dissolved gas phase also has limitations. Methane gas has low solubility in water, although this solubility increases with increasing pressure and decreasing temperature (Chapoy et al., 2004). The GHRC is rated to a cell pressure of 25MPa. Therefore at that pressure, approximately 0.064 moles of methane would dissolve into the pore water of a saturated specimen. This would

Test Details	Position	Water Content (%)
A. Water injected through base only. Low pressure. Frozen	Top	Dry
		17.6
		18.6
		18.5
	Bottom	19.6
B. Water injected through base and top cap. High Pressure. Not Frozen	Top	8.9
		9.9
		12.8
		13.4
	Bottom	11.8

Table 3.3: Water content analysis of three different tests where water was injected into sands containing methane

equate to a maximum of 4% hydrate content in the pore space. Spangenberg & Kulenkampff (2005) obtain high hydrate contents (up to almost 100% of the pore space filled with hydrate), by continuously flowing methane saturated water through a specimen comprised of glass beads. Hydrate distribution using this method is not well controlled, and so was not considered ideal for use in the GHRC.

The second method was therefore instigated to form hydrate in excess water conditions. In order to investigate whether a sufficiently high hydrate content could be achievable, whilst obtaining a reasonably homogeneous distribution of water and gas, a number of tests were conducted where dry, gas saturated sands were flooded with water under pressure. The first test comprised of a dry sand that contained methane gas at 0.5MPa, with a 0.75MPa confining pressure. Water was injected into the specimen through the base, raising the back pressure to 2MPa, so as to compress the gas into 25% of the pore space. Cell pressure was raised during back pressure increase so as to maintain 250kPa confining pressure on the specimen. The specimen was then frozen, depressurised, and divided into 5 equal sections for water content analysis. This first test resulted in the top of the specimen being dry, but the remaining sand having a relatively homogenous water distribution (Test A in Table 3.3). It was apparent that some gas remained in the pore space at the base of the specimen, even though a proportion was pushed to the top. A second test was then conducted, where a sand specimen was injected with methane up to a back pressure of 3.4MPa, with a cell pressure of 3.66MPa. Water was then injected up to 15MPa, but with the water being injected through the top and the base of the specimen. Again cell pressure was increased to maintain a 250kPa effective stress on the specimen at all times. This specimen was not frozen prior to depressurisation, due to the high gas pressures, but drained through the base. When removed and sectioned for water content analysis, no dry portions of sand were evident (Test B in Table 3.3). A 3% difference in

	Position	EW–10	EW–20	EW–30	EW–40
Water Content %	Top	12.2	11.1	10.5	8.4
		15.6	13.7	12.7	11.1
		15.8	14.1	13.8	11.6
		15.9	14.6	14.1	12.3
	Bottom	15.6	14.4	13.1	11.6

Table 3.4: Water content analysis for excess water (EW) tests EW–10, –20, –30 and –40 after depressurisation and dissociation. Specimens were not frozen prior to depressurisation, and were drained through the base.

water content was measured from the top and bottom of the specimen. This difference may be due to the specimen being drained through the base, such that additional water was removed. As the error was small, it was considered that the water content distribution was sufficiently homogenous.

Water content analysis for a number of excess water tests which contained hydrate were undertaken after each test was completed and depressurized, with the results given in Table 3.4. Each specimen was removed from the GHRC after testing was complete and sectioned into five equal pieces. Consistent water distributions, that compare favourably with the results from preliminary tests in Table 3.3, were observed in each test specimen. The higher water contents near the base are considered to be an artifact of draining during depressurisation.

3.3.3 Calculating Hydrate Content

The water injection method of making methane hydrate requires the back pressure in the specimen to be applied and maintained by water from a GDS Digital Pressure Controller (DPC). Hydrate content in the specimen can be controlled by the quantity of gas in the pore space before water injection. Methane quantity can be established through pressure in the pore space. The volume the gas can occupy is constant (void volume of the specimen), and so the number of moles of CH_4 needed for hydrate growth is controlled by the pressure of the gas. By assuming 100% cage occupancy, and the molar ratio of 5.75:1 water to methane, the number of moles of gas needed for 1 mole of hydrate is 1. The number of moles of hydrate n needed for a given hydrate content H_c (%) is:

$$\frac{V_v H_c \rho_{hy}}{100 M_g} = n \tag{3.31}$$

where V_v is the total volume of voids in the specimen; ρ_{hy} is the density of methane hydrate (approximately 910g/l); and M_g is the molar mass of methane hydrate (119.63g/mol).

Hydrate Content	Moles of CH_4 before compensation	Moles of CH_4 after compensation	Starting pressure before compensation (kPa)	Starting pressure after compensation (kPa)
2	0.0340	0.0953	366	1012
5	0.0851	0.1464	905	1535
10	0.1702	0.2315	1775	2381
15	0.2552	0.3165	2611	3194
20	0.3403	0.4016	3415	3976
30	0.5105	0.5718	4935	5455
40	0.6807	0.7419	6350	6833

Table 3.5: Hydrate contents and associated starting pressures for methane in a specimen of fixed void volume, where hydrate would be formed at 15MPa and 2°C.

As methane is a non-ideal gas, the gas pore pressure that must be applied to the specimen to obtain the required moles in the pore space can be determined from the Peng–Robinson gas equation (Peng & Robinson, 1976):

$$P = \left(\frac{\mathrm{R}T}{V_m - \mathrm{b}}\right) - \left(\frac{\mathrm{a}\alpha}{V_m^2 + 2\mathrm{b}V_m - \mathrm{b}^2}\right) \tag{3.32}$$

Where T is temperature (°K); V_m is defined by V_v/n where n is the number of moles; R is the universal gas constant ($0.082058 latm/K/mol$); P is the applied pressure (atm); and a, b and α are Peng–Robinson coefficients relating to methane and are 2.4298, 0.0265, and 0.8201 respectively when $T = 293$K.

Although the solubility of methane in water is low, at 15MPa and 2°C (which are the average target temperature and pressure values for the GHRC hydrate tests respectively), there is a degree of dissolution of methane gas in water. The number of moles of methane gas which can go into solution can be calculated using the solubility mole fraction of 4.024 x 10^{-3} for methane at 15MPa and 0°C (Chapoy et al., 2004). Knowing the quantity of water within the specimen and the system, a maximum value for methane dissolution can be calculated and added to the original value calculated for each given hydrate concentration using Equation 3.31. Table 3.5 shows a range of hydrate contents with corresponding starting pore pressures, before and after allowing for dissolution of methane gas.

Five hydrate contents were chosen for this testing sequence: 10%, 15%, 20%, 30% and 40%.

3.3.4 Specimen Preparation

For each specimen tested, a sequence of steps were followed for specimen preparation, apparatus setup and hydrate formation, of which are detailed below:

1. A thin film of silcone lubricant was applied to the base pedestal and a butyl membrane placed on the pedestal and fitted with one O–ring.
2. A split sample mould to make a specimen of 140mm height and 70mm diameter was placed around the membrane with the top of the membrane stretched over the top edge to give a smooth tube in which the specimen to be formed.
3. All ports leading to the base pedestal were filled with de–aired water from the GDS DPC, except for the CH_4 inlet port and the vacuum port, so to reduce the quantity of free air in the system.
4. The top of the base pedestal and attached membrane were then surface dried with paper towel on the inside.
5. The sample mould was filled with pre-weighed dry sand in 15–18 equal layers, each layer tamped with a flat rubber bung (approximately 2cm diameter). The sample former was tapped 5 times after each sand layer to ensure a dense specimen. Care was taken to catch any spilled sand.
6. The top cap was placed on the top of the sand and levelled. A thin film of silicon grease was applied to the top cap and the membrane pulled up over the top cap. One O–ring was placed around the membrane and the top cap to ensure an air-tight seal.
7. A vacuum of 50kPa was applied to the specimen through the vacuum port in the base pedestal to allow for removal of the sample mould. Once a vacuum of 50kPa was applied, the vacuum tap was closed off. The specimen was then left for 30 minutes to check if there were any leaks between the membrane and the top cap or base pedestal or in the membrane.
8. Any leftover sand was weighed to determine the mass of sand within the specimen
9. An additional O–ring was applied to the top cap and base pedestal as an extra precaution due to the high pressures of the test.
10. The dimensions of the specimen were taken at equal intervals with vernier calipers. The height of the specimen was measured to include the top cap and base pedestal.

Once it had been insured that the specimen was secure and the dimensions recorded, the resonant column drive mechanism could then be attached along with the required instruments.

3.3.5 Apparatus Setup

1. The drive mechanism was slowly lifted over the specimen and lowered on to the specimen so that the drive plate rested flat on the top cap. The drive mechanism was loosened from the support plate to allow for alignment of the fixing holes in the top cap to match up to the corresponding holes in the drive plate. Six M5 countersunk screws were used to secure the top cap to the drive plate. The drive mechanism was then further aligned so that the magnets on the drive arms were located in the centre of the coils. The drive plate was secured with four M6 screws onto the support ring.

2. The base of the support frame was secured to the base of the cell with eight M5 screws.

3. To attach the top cap vent tubing, a continuous vacuum was applied to the specimen so that the stopper at the top of the top cap could be removed and the specimen would not collapse. The vent tubing was then swiftly fed through the top restraining plate and attached to the top cap. The vacuum was once again locked off with -50kPa back pressure applied.

4. The accelerometer cable was fed through the top restraining plate and attached to the accelerometer fixed to the drive plate. Two thermistors were also fed into the cavity between the support frame and the specimen, with care taken to locate one on either side of the specimen. The top restraining plate was then secured by eight M4 screws.

5. An LVDT was connected to the top plate and adjusted so that predicted movement would lie in range. The LVDT cable was then attached to the lead through the cell base, and zeroed so it would record displacement from that point on. It was then secured with two M3.5 screws.

6. Each of the four coils were attached to their corresponding lead through the base of the pressure cell. All connections were double checked.

7. The cell top was lowered slowly by use of a motorised lifting mechanism. Once in place, it was secured with two C–clamps and four M16 bolts.

Once the apparatus had been set up and the cell top lowered, a cell pressure of 250kPa was gradually applied to the specimen, whilst the vacuum was released. The specimen was left

for 30 minutes and then a resonant column test was conducted. The procedure that follows was used for each hydrate specimen made, with the target pressures changing for each hydrate content.

3.3.6 Hydrate Formation

Figure 3.15 shows the idealised thermobaric regime applied to the specimen. Also drawn is phase boundary for methane gas hydrate.

1. The methane port was opened and the back pressure raised by the injection of methane gas to a pre–determined pressure. During ramping of the back pressure, the cell pressure was also increased, so as to maintain an effective stress of 250kPa ± 50kPa on the specimen. The pressure ramp rate averaged 500kPa per minute.

2. Once the required back pressure of methane was reached, the methane tap was closed off. A resonant column test was conducted.

3. Distilled water was then injected into the specimen through the top cap and base pedestal in equal proportions by use of the GDS DPC. The base pedestal pipework had been arranged so that the water could be injected through the same port as the methane, to ensure all gas was pushed into the specimen. During the subsequent increase in back pressure, the cell pressure was also raised so as to maintain an effective stress of 250kPa ± 50kPa on the specimen.

4. Water was injected until a back pressure of 15MPa was reached, with a corresponding cell pressure of 15.25MPa. A resonant column test was carried out.

5. The specimen was then left at room temperature to allow for homogeneous water distribution and for methane gas to dissolve in the water.

6. The temperature of the system was then lowered from room temperature to 2°C to allow for hydrate formation. The back pressure was maintained by the GDS DPC, with the quantity of water going into the specimen monitored. The cell pressure was maintained by the PAV.

Once the temperature and pressures for hydrate formation stated above had been reached, these conditions were maintained for approximately 72 hours to allow for hydrate conversion. Regular resonant column tests were conducted to monitor the change in properties over the formation time (Section 3.6.1). Water input from the GDS DPC was also monitored closely (example

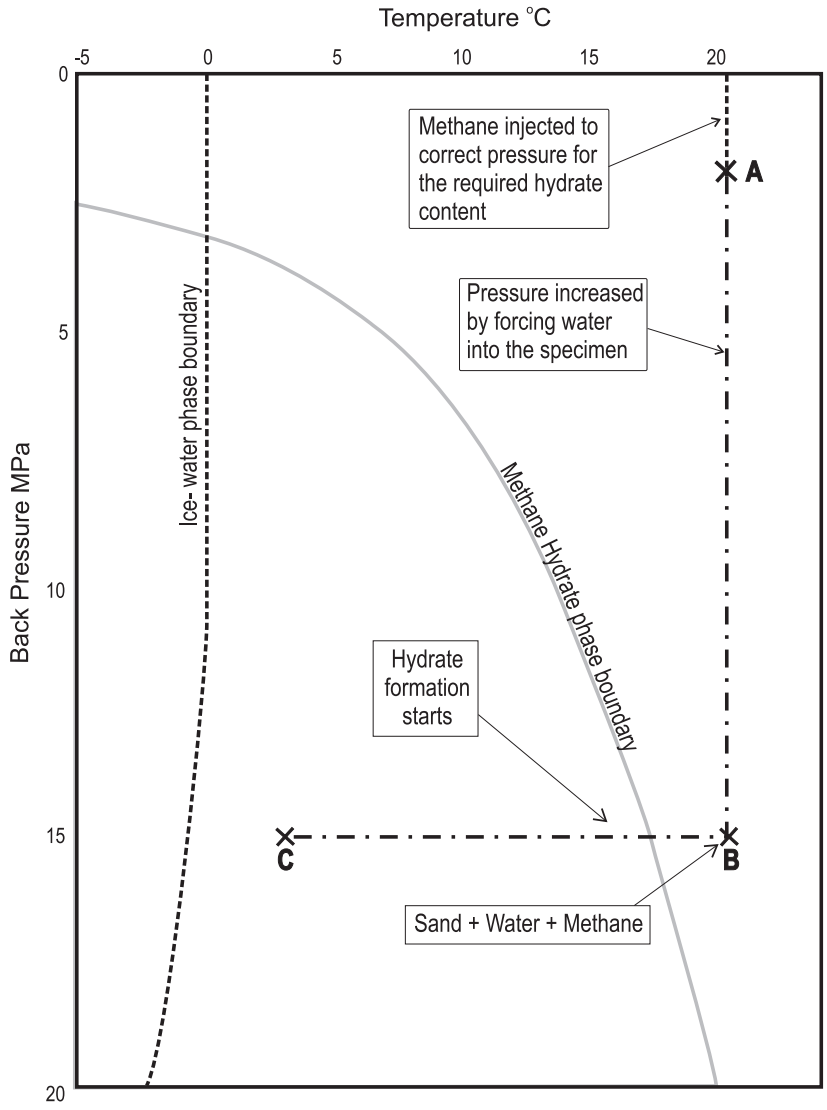

Figure 3.15: Thermobaric route and basic procedure when making methane hydrate in excess water conditions

plots given in Section 3.6.1). Once the resonant frequency and damping had reached a stable value, and there was no longer a water volume input into the specimens, the specimens were considered to have converted all methane into hydrate and full testing of the specimen could begin (Section 3.5).

3.4 Tests to Examine the Impact of Sediment Type

It is apparent from the literature that previous studies into the impact of hydrate on sediments within the laboratory have focused on materials with a uniform particle size and shape. The behaviour of granular soils is known to be influenced by characteristics of the soil such as particle size distribution and particle shape (Bolton, 1986; Mitchell, 1976), and so the impact of gas hydrate on sediment properties could also be altered by these basic characteristics. The following section describes a series of tests where hydrate is formed in "excess gas" conditions in a number of different sediments, so as to investigate the influence of sediment type on hydrate formation.

3.4.1 Material Properties

The granular materials used in the different sediment tests were chosen so as to give a variety of particle size and shape. The materials used were Leighton Buzzard sand grade B (LBB), Leighton Buzzard sand grade E (LBE) and 100 mesh muscovite mica (M). The properties of each material are given in Table 3.6. LBE is the same material used in the tests of Section 3.3. Leighton Buzzard sand is a natural, uncrushed silica sand that is free from silt, clay or organic matter (Figures 3.16(a) and 3.16(b)). LBB has a large grain size with the average particle measuring 1mm in diameter. The LBE sand grains have an average diameter of 0.1mm, but show a similar particle shape as LBB sand grains although they are more angular. The 0.1mm muscovite mica provides a variety in particle shape as it is flat and plate–like (Figure 3.16(c)).

To investigate the effect of particle size on hydrate formation, two specimens were prepared of only LBB sand and only LBE sand. LBB sand was then used as the main material in two further specimens, which would allow for hydrate to be formed in sediments with a variety of particle size and shape. The quantity of fines added to LBB needed to be high enough to maximise the variety in particle size, without allowing the fines to dominate the behaviour of the specimen. Investigations into the impact of fines on rotund materials (Clayton et al., 2004; Thevanayagam, 1998; Georgiannou, 2006) have shown that 20% mica added to a rotund sand

	Leighton Buzzard sand		Mica
Supplier	David Ball Group plc		Dean and Tranter Ltd.
Description	natural, clean, uncrushed, silica sand, free from silt, clay or organic matter		Dry ground muscovite mica powder
Geological Formation	Lower Greensand group		Muscovite Mica
Roundness[a]	Rounded–subrounded	Angular–subangular	Flat, platy
Particle size[a]	Grade B (1.18–0.6mm)	Grade E (90–50μm)	52-105μm
Specific Gravity[a]	2.65	2.65	2.90
Maximum dry density[a]	1752kg/m^3	1624kg/m^3	912kg/m^3
Minimum dry density[a]	1496kg/m^3	1331kg/m^3	728kg/m^3

Table 3.6: The properties of the materials used in the different sediment tests. [a]Tests conducted by Theron (2004) and Priest (2004) according to BS1377:2 (1990)

can change the sand's behaviour from dilative to contractive. Therefore, a proportion of 10% by weight fines (LBE or Mica) were added to the LBB sand to make specimens LBB/LBE and LBB/M. These mixtures were blended together prior to the addition of the water that would control hydrate content in the specimens (Section 3.4.2).

3.4.2 Formation Technique and the Calculation of Hydrate Content

The formation method utilised in the different sediment tests is the "excess gas" methodology that was followed by Priest et al. (2005) and Waite et al. (2004), where sediment of a known water content is used to form a specimen, which is then flooded with methane gas (Section 2.4.2). This approach to hydrate formation allows for hydrate content to be controlled by water volume.

So that sediment type effects on hydrate formation could be observed, each sediment type in Section 3.4.1 was intended to have the same target hydrate content (quantity of hydrate in the pore space). A hydrate content of 10% of the pore space was chosen for the different sediment specimens. Previous experiments by Priest et al. (2005) on LBE sand, using varying quantities of hydrate, had suggested that at hydrate contents greater than 5%, full bonding occurred. Therefore, to ensure bonding, the target hydrate content of 10% of the pore volume was chosen for the different sediment specimens. It was assumed that water volume in the pore space could

Specimen	Mass LBB (g)	Mass LBE (g)	Mass M (g)	% fine material in LBB	Total Vol. (cm^3)	Vol. voids (cm^3)	Dry density (kgm^{-3})	void ratio	Void ratio main sand fraction
LBB-0	940.9	–	–	0	551	196	1706.2	0553	0.553
LBE-0	–	800.7	–	n/a	517	203	1548.1	0.640	0.640
LBB/LBE-0	883.7	101.2	–	10.3	546	175	1804.3	0.469	0.637
LBB/M-0	870.7	–	98.3	10.1	541	174	1792.4	0.492	0.645

Table 3.7: Dry densities, void ratios and void volumes of dry specimens produced for the control different sediment tests (0% hydrate)

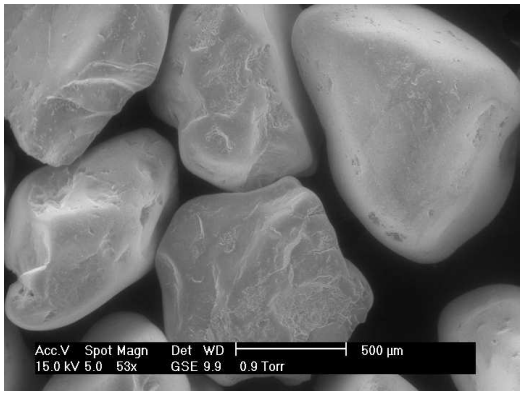

(a) Leighton Buzzard sand grade B (LBB)

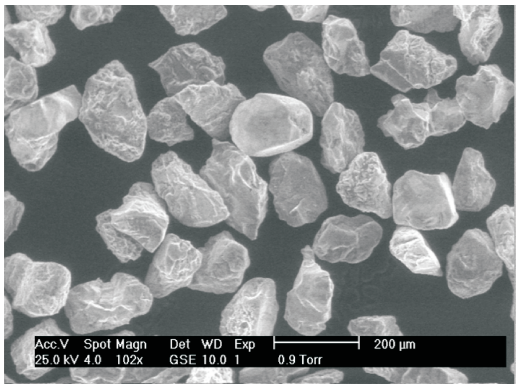

(b) Leighton Buzzard sand grade E (LBE)

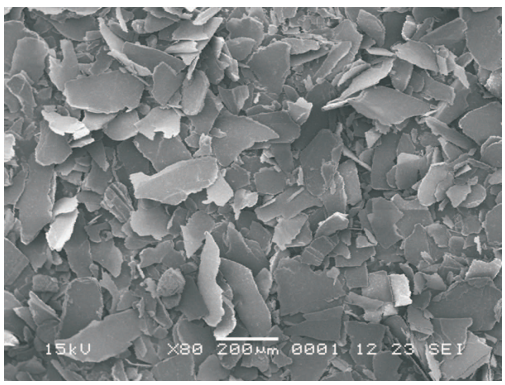

(c) 100 mesh muscovite mica

Figure 3.16: Scanning electron micrographs of the materials used in the different sediment tests. From Clayton et al. (2008a)(Mica), Clayton et al. (2006) (LBB) and Cabalar (2007) (LBE)

Specimen	Dry Density (kgm^{-3})	Void ratio	Void Ratio main sand fraction	Relative Density main sand fraction (%)	Water Content (%)	Hydrate Content (%)
LBB-10	1662.5	0.549	0.549	87	2.29	14.0
LBE-10	1505.5	0.768	0.768	62	2.49	12.4
LBB/LBE-10	1708.1	0.508	0.671	39	1.93	12.8
LBB/M-10	1676.0	0.560	0.718	20	2.33	17.1

Table 3.8: Basic properties of the specimens used in the different sediment hydrate tests

be taken as equivalent hydrate volume. Therefore, the required quantity of water needed for each sediment type was calculated from the volumes of voids measured in the control tests shown in Table 3.7. Resultant water contents of the specimens were between 2 and 2.5% dependant on soil mixture (Table 3.8). Hydrate content H_c was then calculated from the initial water content by:

$$H_c = \frac{100 m_w M_g}{5.75 V_v M_w \rho_{hy}} \tag{3.33}$$

or

$$H_c = \frac{0.1269 m_w}{V_v} \tag{3.34}$$

where V_v is the total volume of voids in the specimen; m_w is the mass of water in the specimen; M_g is the molar mass of methane hydrate (119.63g/mol); M_w is the molar mass of water (approximately 18.02g/mol); and ρ_{hy} is the density of methane hydrate (approximately $910 g/l$). It was found once hydrate content had been calculated in the different sediment specimens, that a larger hydrate content was produced than anticipated. The range of hydrate content values of 12.4% in specimen LBE-10 up to 17.1% in specimen LBB/LBE-10 are due to the original calculation of water contents. Initial calculations over estimated the amount of water required for 10% water volume in the pore space for each individual specimen, and did not take into account change void ratio with the addition of fines. The actual hydrate contents in each different sediment specimen are given in Table 3.8.

3.4.3 Specimen Preparation

The specimens were prepared by taking the required mass of material that would make up a 70mm by 140mm specimen, and mixing it with the calculated mass of water. The moist material was then left in a sealed container for 12 hours at room temperature to allow the moisture to distribute itself homogeneously within the material. The materials were taken from where they were stored in the laboratory, with no initial oven drying before being used in the tests. The residual water content of the air dry materials were found to be 0.2%, 0.1% and 0.02% for Mica, Leighton Buzzard grade E and Leighton Buzzard grade B respectively. These

water contents were disregarded when calculating hydrate content.

For each sediment type tested, the sequence of steps for specimen preparation were as follows:

1. A thin film of silcone lubricant was applied to the base pedestal and a butyl membrane placed on the pedestal and fitted with one O–ring.
2. A split sample mould to make a specimen of 140mm height and 70mm diameter was placed around the membrane with the top of the membrane stretched over the top edge to give a smooth tube in which the specimen to be formed.
3. The sample mould was then filled with the sediment/water mixture in 15–18 equal layers, each layer tamped with a flat rubber bung. Care was taken to catch any spilled sediment.
4. The top cap was placed on the top of the sand and levelled. A thin film of silicon grease was applied to the top cap and the membrane pulled up over the top cap. One O–ring was placed around the membrane and the top cap to ensure an air-tight seal.
5. A vacuum of 50kPa was applied to the specimen through the vacuum port in the base pedestal to allow for removal of the sample mould. Once a vacuum of 50kPa was applied, the vacuum tap was closed off. The specimen was then left for 30 minutes to check if there were any leaks between the membrane and the top cap or base pedestal or in the membrane.
6. Any leftover sand was weighed before and after drying, to determine the proportion of sediment and water not in the specimen.
7. An additional O–ring was applied to the top cap and base pedestal as an extra precaution due to the high pressures of the test.
8. The dimensions of the specimen were taken at equal intervals with vernier calipers. The height of the specimen was measured to include the top cap and base pedestal.

Once it had be ensured that the specimen did not have any leaks and the dimensions had been recorded, the resonant column drive mechanism could then be fitted.

3.4.4 Apparatus Setup

The set up of the resonant column apparatus for these tests follows the steps from Section 3.3.5, omitting step 3 as the top cap vent was not used here. After apparatus set up, a cell pressure

of 250kPa was applied to the specimen, whilst releasing the vacuum. The specimen was then left for 30 minutes at ambient temperature before a resonant column test was conducted. The following hydrate formation procedure was then adopted for each sediment type.

3.4.5 Hydrate Formation

Figure 3.17 shows the idealised temperature and pressure regime applied to the specimen. The hydrate stability field is also drawn on the figure.

1. The methane port was opened and the back pressure raised by the injection of gas to 10MPa. During ramping of the back pressure, the cell pressure was also increased, so as to maintain an effective stress of 250kPa $\pm$50kPa on the specimen. The pressure ramp rate averaged 500kPa per minute. Once a the chosen pressure, the methane tap was closed off and a resonant column test conducted. The cell pressure was set to maintain 10.25MPa of confining pressure.

2. The temperature of the system was then reduced to 2°C to induce hydrate formation. A flow of methane was continued into the specimen so that constant back pressure was maintained as gas was consumed in hydrate formation. The cell pressure PAV maintained the original target pressure throughout the temperature drop.

Once the temperature (2°C) and pressures (10MPa) for hydrate formation had been reached, these conditions were maintained for approximately 48 hours to allow for full hydrate conversion (plots of temperature and pressure are given in Section 3.6.2). Regular resonant column tests were conducted during this period to monitor the change in resonant frequency over the formation time (Section 3.6.2). Once the resonant frequency had stabilised, all the water was considered to have been converted into hydrate and full testing of the specimen could begin.

3.5 GHRC Testing Procedure

The testing programme used for both sets of specimens as described in Sections 3.3 and 3.4 allowed the dynamic response of the hydrate bearing specimens to be observed during loading and unloading. A load–unload cycle was applied to the specimens with resonant column measurements made at 250, 500, 750, 1000, 1500 and 2000kPa isotropic effective stress. Each load

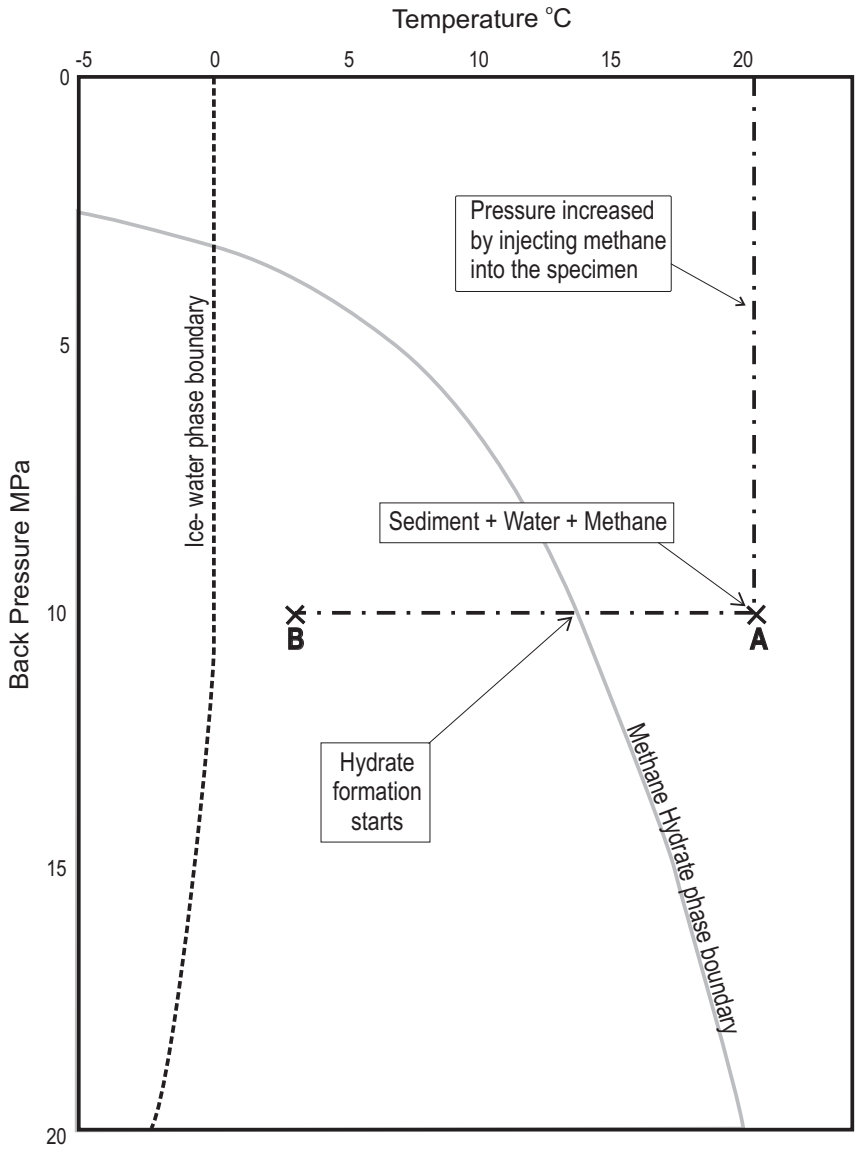

Figure 3.17: Thermobaric route and basic procedure when making methane hydrate in excess gas conditions

step was held for 30 minutes to allow for initial consolidation of the specimen before a resonant column test was undertaken. Torsional and flexural resonant frequencies were measured at each load–unload step, along with attenuation measurements. In order to allow for repetitive testing, and to ensure that the seismic velocities obtained from these tests would be comparable to geophysical survey data, the applied strain in both torsional and flexural excitation were kept below 9 x 10^{-6} strain.

3.6 Typical Observations during Preparation and Hydrate Formation

3.6.1 Tests Investigating Hydrate Formation Technique

Specimen preparation for the excess water tests was reasonably consistent for each specimen, with very few problems arising when the system was secure and free from leaks. The highest hydrate content test (EW-40), required a modification of the specimen preparation as the high pressures required for the initial gas injection led to significant migration of methane through the butyl membrane into the nitrogen cell pressure. To reduce the quantity of methane lost through the membrane, two butyl membranes were placed around the specimen. In addition, as soon as the specimen had been taken up to the target gas pressure, the temperature was dropped immediately so that hydrate formation could start as quickly as possible and all the methane gas would be converted into hydrate before it had a chance to escape. This technique did not allow time for the water and methane to evenly distribute, however, water content analysis after dissociation and depressurisation, suggest that there was still an acceptable distribution of moisture within the specimen (Table 3.4 in Section 3.3.2).

Each of the excess water specimens were monitored whilst the system temperature was reduced into the hydrate stability zone. Figure 3.18 shows the measurements taken during the temperature drop and subsequent hydrate formation for specimen EW-20. It can be seen that the axial displacement recorded an expansion as the temperature was dropped, and that this was independent of changes in effective stress. This behaviour was observed in each of the excess water tests. The volume of water injected during the temperature drop and subsequent hydrate formation was also monitored, and is shown in Figure 3.18(d). As gas was consumed during hydrate formation, the pressure inside the specimen decreased, and so more water was injected to maintain constant pore pressure. The water volume input seen in Figure 3.18(d) after the temperature had stabilised at 4°C, therefore marks hydrate formation within the specimen.

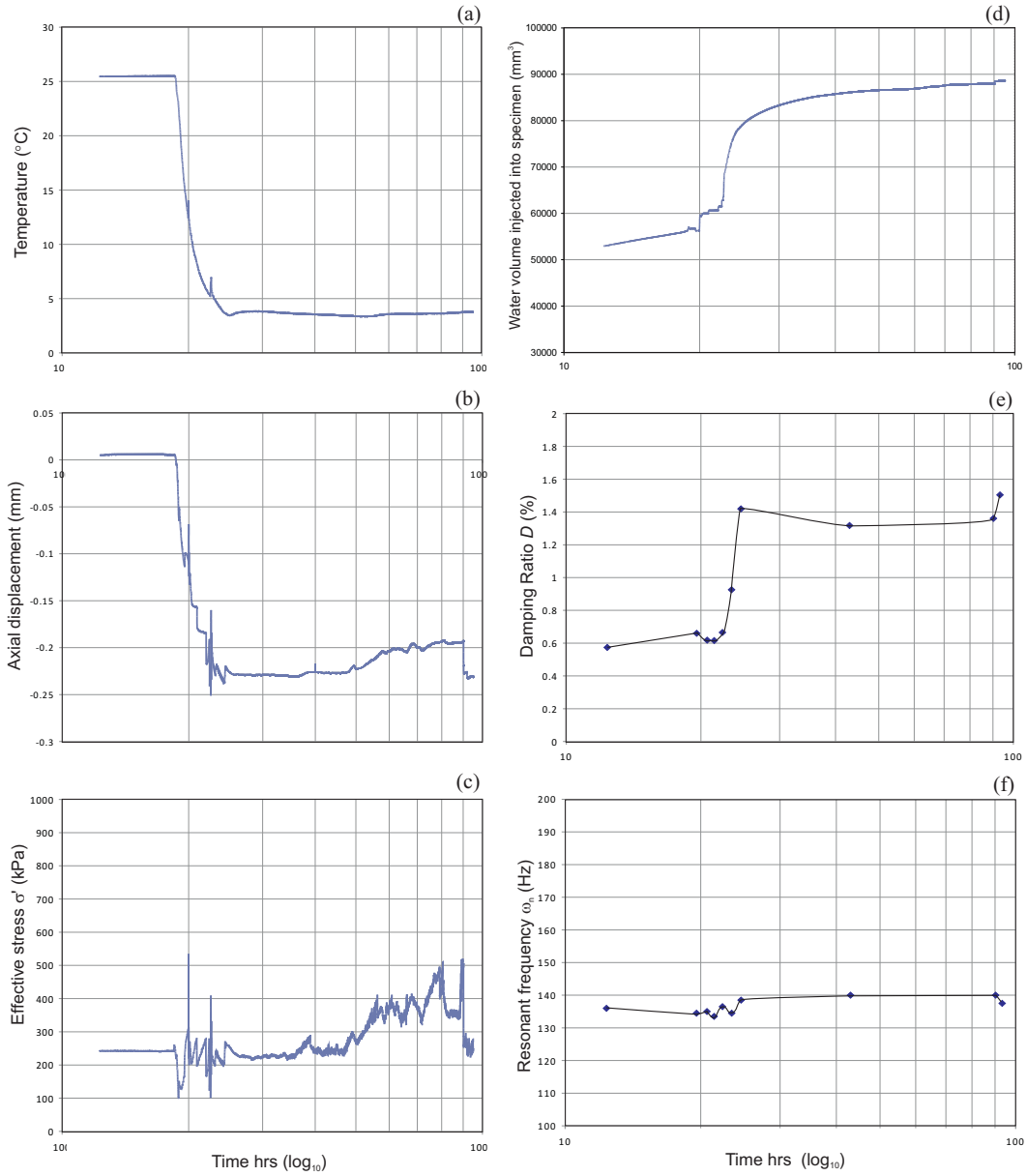

Figure 3.18: A range of measurements taken during the drop in temperature and subsequent hydrate formation for an excess water test after pressurisation to 15MPa. The results shown here are for specimen EW-20. (a) Temperature taken from outside the specimen. (b) Axial displacement of the specimen. (c) Confining pressure minus back pressure, shown here as effective stress on the specimen. (d) Volume of water injected into the specimen. (e) Damping ratio measured via FVD for the specimen inside the GHRC. (f) Resonant frequency of the specimen recorded during the formation stage.

This period could be identified in all the excess water tests.

Also plotted in Figure 3.18 are the measured changes in resonant frequency and damping ratio observed throughout the temperature drop and hydrate formation stages. By considering Figures 3.18(d) and (e) with regard to the temperature drop, it can be seen that there is no change in either damping or resonant frequency during the early temperature decrease. Once a temperature of 5°C was reached, the damping ratio began to increase. This increase in damping ratio (seen at the approximate time of 23hrs) coincides with the increase in water volume input, and so is considered to be caused by hydrate formation. As the threshold for hydrate stability at 15MPa is 17°C, there appears to be a lag for the start of hydrate formation and the entry of the specimen into the stability zone. This behaviour was characteristic of all the excess water specimens, and will be discussed further in Chapter 4.

3.6.2 Tests Investigating Different Sediment Types

The preparation of the different sediment tests was consistent across all specimens. Figure 3.19 gives the measurements taken during the temperature drop and hydrate formation of the specimen LBB/LBE-10. The temperature drop for this specimen was conducted in two stages. The specimen was first taken to 15°C, just outside the stability field at 10MPa pressure, and held for 12hrs. The temperature was then dropped into the hydrate stability field by setting a target of 2°C. The axial displacement and effective stress traces (Figures 3.19(b) and (c)) follow each other in the latter stages of the temperature drop and hydrate formation, however the axial displacement shows an expansion as the temperature is lowered to 15°C that appears independent of effective stress. An axial displacement change with temperature drop can also be observed in the other different sediment tests.

The onset of hydrate formation can be observed in the different sediment tests as an increase in resonant frequency and damping (Figures 3.19(d) and (e)). The resonant frequency of the LBB/LBE-10 specimen began to increase once the sample was at approximately 10°C, just inside the hydrate stability field at 10MPa. This increase was accompanied by an increase in damping ratio for the specimen. Once full hydrate conversion occurred, the damping ratio reduced to a value closer to the original seen at the start of testing.

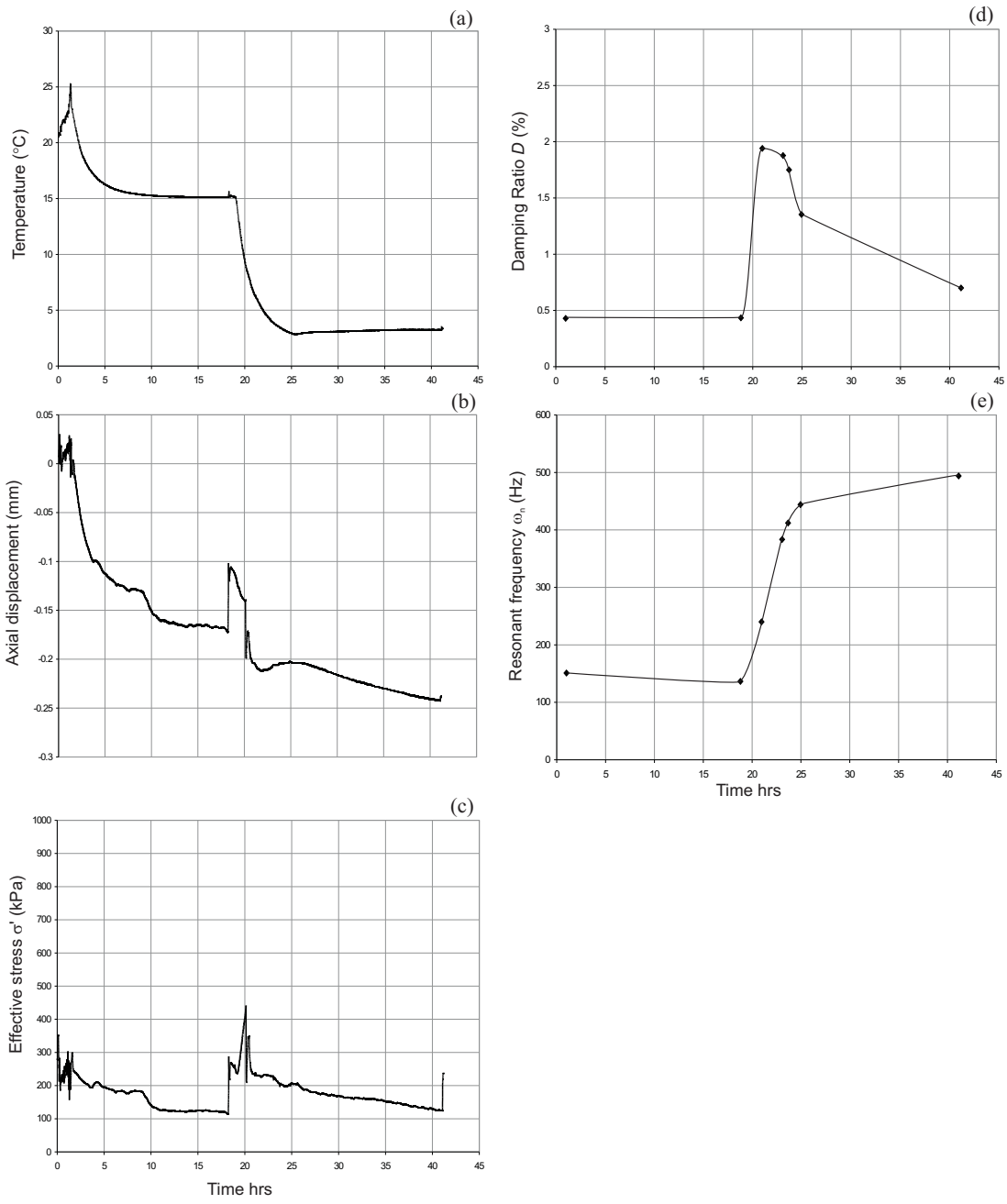

Figure 3.19: A range of measurements taken during the period of temperature drop and hydrate formation for a different sediment test. The readings shown here are for specimen LBB/LBE-10. (a) Temperature readings from the outside of the specimen. (b) Axial displacement of the specimen. (c) Confining pressure minus back pressure, shown here as effective stress on the specimen. (d) Damping ratio measured via FVD for the specimen inside the GHRC. (e) Resonant frequency of the specimen recorded from the GHRC.

3.7 Typical Observations During Resonant Column Testing

Figures 3.20 and 3.21 show the typical response curves seen when conducting resonant frequency sweeps in torsion and flexure respectively. The resonant frequency can be identified as the frequency where the highest voltage output from the accelerometer occurs. Once it was established, a free vibration decay curve was conducted so that the damping of the system could be determined (Figures 3.22 and 3.23). Strain was calculated from the peak voltage output at resonance, using Equation 3.14.

Shear wave velocity V_s was calculated from the resonant frequency using Equation 3.1. Once V_s is obtained, shear modulus G was determined using Equation 3.2. From the resonant frequency in flexure, Young's modulus in flexure E_{flex} was determined using Equations 3.5 and 3.6 using the geometrical properties of the system. From G and E_{flex}, other properties of the specimens could be obtained, namely Poisson's ratio ν, longitudinal wave velocity V_{lf}, P–wave velocity V_p and bulk modulus K.

Damping ratio D was determined by finding the logarithmic decrement δ as described in Section 3.2.1 from the free vibration decay responses measured. Once δ had been found, it could be used to determine D and associated attenuation Q^{-1} by using Equations 3.26 and 3.22.

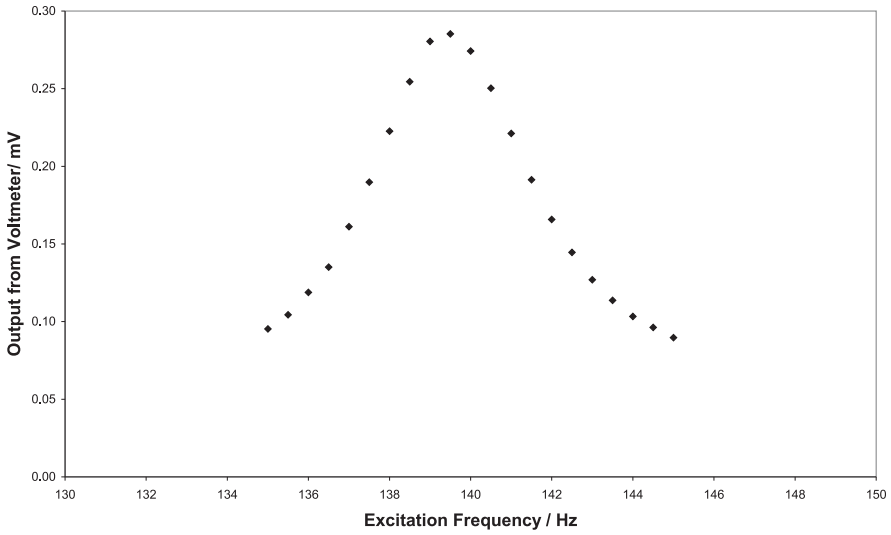

Figure 3.20: Typical resonant frequency sweep for torsion on a dry dense specimen of LBE sand containing no hydrate

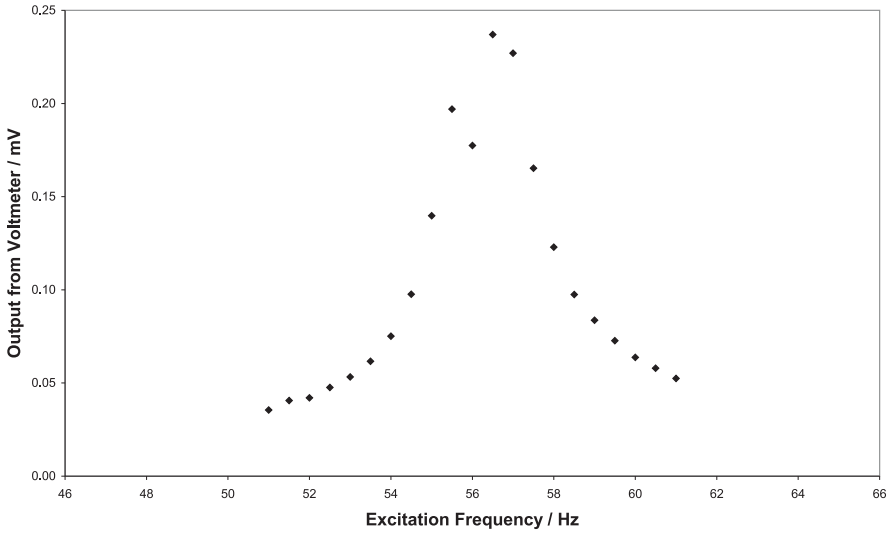

Figure 3.21: Typical resonant frequency sweep for flexure on a dry dense specimen of LBE sand containing no hydrate

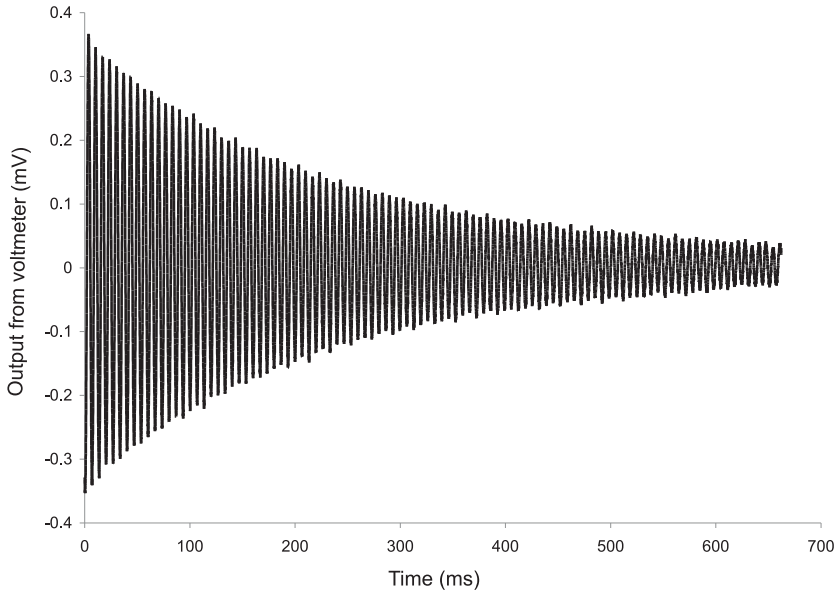

Figure 3.22: Typical free vibration decay trace for torsion of a dry dense specimen of LBE sand containing no hydrate

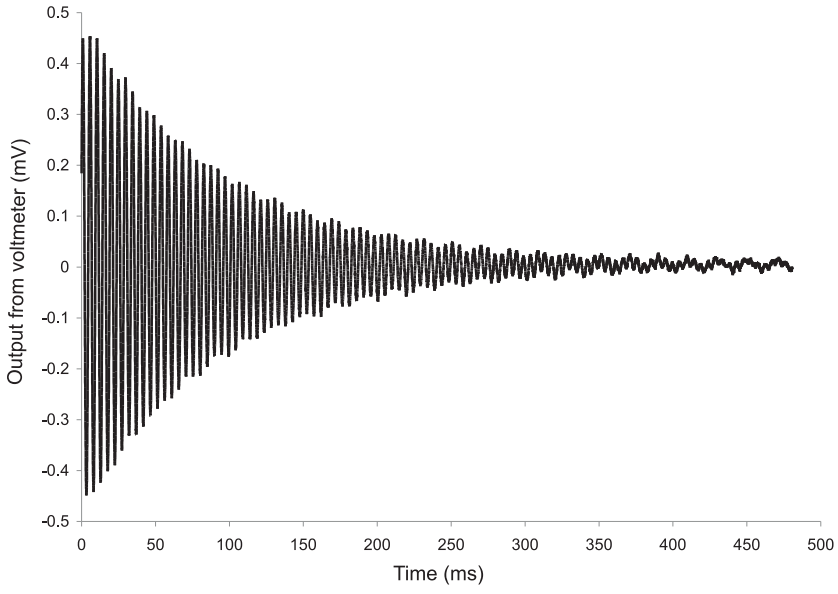

Figure 3.23: Typical free vibration decay trace for flexure of a dry dense specimen of LBE sand containing no hydrate

Chapter 4

TESTS ON SYNTHETIC HYDRATE BEARING SEDIMENTS: DISCUSSION

A literature review has been conducted to develop an understanding of how methane gas hydrate may affect sediment. After undertaking the review, it became apparent that the current knowledge of hydrate formation in different environments and sediment types, and what this might mean to hydrate morphology, was lacking. In order to investigate the different environment implications further, a set of experiments were conducted using the GHRC that allowed for hydrate to be formed in water saturated conditions. In addition, a set of experiments were conducted to understand the impact of different sediment type on hydrate growth. This chapter discusses the results from these tests, first addressing the impact of formation technique on how hydrate affects a sediment, and a subsequent discussion on hydrate morphology in the laboratory. The chapter then finishes with a discussion of the results from tests conducted in different sediment types.

4.1 Discussion of Hydrate Formation Technique Tests

Gas hydrates in sediments have been formed in the laboratory by other researchers such as Stoll & Bryan (1979), Pearson et al. (1986), Berge et al. (1999), Winters et al. (2004), Waite et al. (2004) and Yun (2005). A wide range of results have come from these tests (Table 2.4), which could be due to the choice of apparatus used, the hydrate former, or the method of hydrate formation (Section 2.4.2). The excess water tests described in this section were designed so

that direct comparison could be made between hydrates formed by different methods in the same apparatus.

This section presents and discusses the results from experiments that induce hydrate growth in water saturated or "excess water" conditions. The work is directly compared with that of Priest (2004), who formed hydrates in partially saturated or "excess gas" conditions (Section 2.4.2). Comparison will allow conclusions to be drawn about hydrate formation in the pore space under different formation conditions. As the technique developed to make the hydrate under excess water conditions was new, observations made in the preparation of specimens and during hydrate formation are discussed first. The test results are then discussed with regard to the changes observed in seismic velocity and attenuation caused by the methane hydrate.

4.1.1 Observations During Preparation and Hydrate Synthesis

The technique used to make water saturated hydrate bearing sands took the specimens into the stability zone by increasing the pressure of the system to around 15MPa before dropping the temperature to just above freezing (Section 3.3.6). By monitoring the gas and water intake into the specimen, axial displacement and mechanical property changes, hydrate growth inside the specimens could be identified.

Gas and Water Intake

Hydrate volume in the specimens was related to the gas injected into the specimen and the eventual final pressure. The intake of both the methane and water into the specimen was monitored, and hydrate growth could be observed by the changes seen.

Gas Volumes

Gas input into the specimen was measured by gas pressure. For each specimen a different hydrate content was required, therefore a different quantity of methane gas in the pore space and a different specific starting pressure was needed (Section 3.3.3, Table 3.5). To make hydrate in "excess water" conditions, water was injected systematically through the top and bottom caps up to a pressure of 15MPa for specimens EW-10, EW-15 and EW-20, and up to 20MPa for specimens EW-30 and EW-40 after gas injection. In order to check that the expected gas content remained in the specimen during water injection, the volume change of the gas with pressure change could be observed by the GDS digital pressure controller by measuring water input. If temperature remains constant, the change in methane gas volume as pressure increases can be calculated. The measured volume change of methane gas inside each specimen

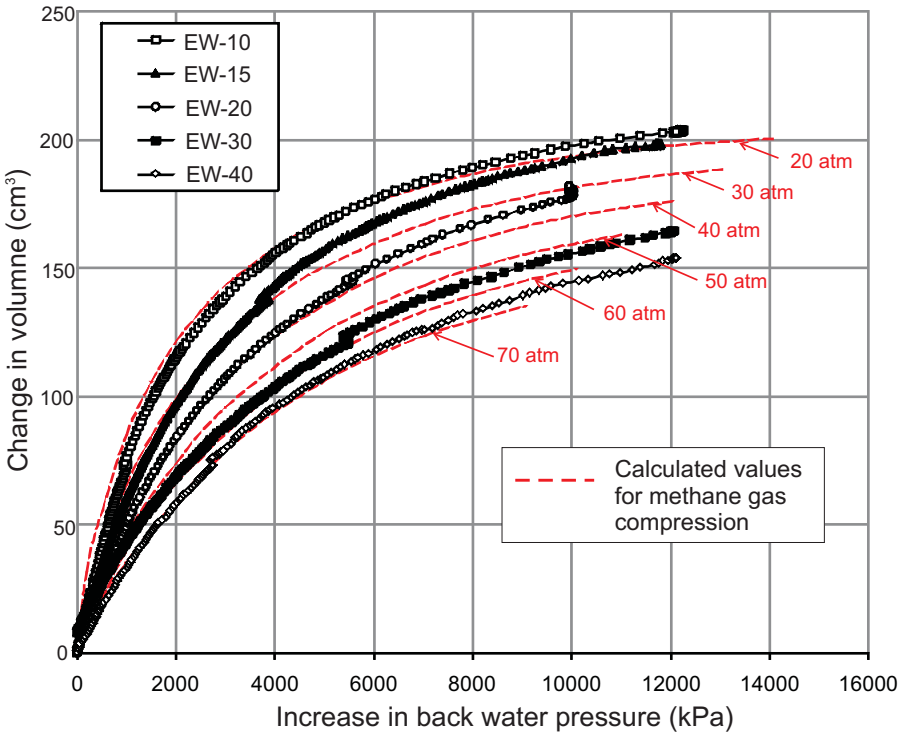

Figure 4.1: Volume of water injected into each specimen, plotted against the change in pressure of the system. The calculated values for methane gas volume change with pressure increase are also plotted.

during pressure increase is plotted in Figure 4.1. Also plotted in Figure 4.1 are the theoretical curves for the change in volume of methane gas as pressure is increased for a range of starting pressures (see Table 3.5 for reference to each specimen's starting pressure). The curves were calculated using the Peng–Robinson equation (Equation 3.32, Peng & Robinson (1976)). The volume changes observed in the specimens follow the predicted curves sufficiently closely to be sure that all the gas remained in the specimens as the water was injected.

Water Intake

Once a pressure of 15MPa was reached for specimens EW-10, EW-15 and EW-20, and 20MPa for specimens EW-30 and EW-40, the water pressure was maintained throughout the subsequent temperature drop by the digital pressure controller (DPC). Once inside the methane hydrate stability zone, hydrate formation was induced causing a reduction in methane gas pore pressure. Therefore, the DPC maintained the appropriate back pressure by injecting water into the pore space. The water volume injection histories for specimens EW-10, EW-20 EW-30 and EW-40 are shown in Figure 4.2 plotted against temperature. They show the initial water volume injected to bring the specimens up to the appropriate pressure, followed by the injection history during temperature drop and subsequent hydrate formation. Figure 4.3 gives a closer

Hydrate Content	Expected input (ml)	Measured input (ml)	discrepancy (ml)	% total water volume
10	217.27	219.07	+1.80	0.83
15	216.70	217.51	+0.81	0.37
20	210.48	216.50	+6.02	2.86
30	206.33	209.39	+3.06	1.48
40	203.14	203.47	+0.33	0.16

Table 4.1: Expected and actual water volumes injected into each specimen

view of the hydrate formation phase. This phase can be identified as the increase in volume injected after the highlighted temperature drop.

The injected water volume can also be used to quantify the hydrate content in the specimens. If full conversion of methane gas to hydrate is assumed, the total expected water volume injected into the specimen can be calculated by adding the percentage contained in the hydrate to the remaining pore space volume that would be filled with water. Table 4.1 gives the water volume values measured by the DPC, compared with water volume calculated from the expected hydrate content of each specimen. The discrepancies between the two values are between 0.1% and 3% of the total water volume injected into the specimens. It is likely that a combination of factors contribute to these errors in measured water input as discussed below.

The digital pressure controller (DPC) that was used to inject the specimens with water held a fixed volume of water (200ml). As this volume was not enough to fully saturate a specimen (each specimen had approximately 223ml void volume), the injection of water was undertaken in two stages, with a refilling of the DPC at some point during the injection process. This meant that the volume of water exposed to the methane gas under pressure was not consistent across each test, and it is therefore likely that more methane went into solution than predicted by the expected input values in Table 4.1. This increased dissolution of methane would suggest that hydrate volume in the specimen may be lower than predicted, however this discrepancy has been taken into account when stating hydrate contents in all the results shown in this thesis.

The predictions for hydrate content in all the excess water tests assumes full conversion of methane gas into solid hydrate. As discussed later in this section, the indicators for full hydrate conversion in each test were the cessation of changes in physical properties (see ‘Evolution of stiffness and damping’ section below). It is possible that specimen EW-20 did not have full hydrate conversion, even though indications suggested otherwise. This would mean less hydrate volume was present in the pore space than expected, with more water needed to fully saturate the specimen.

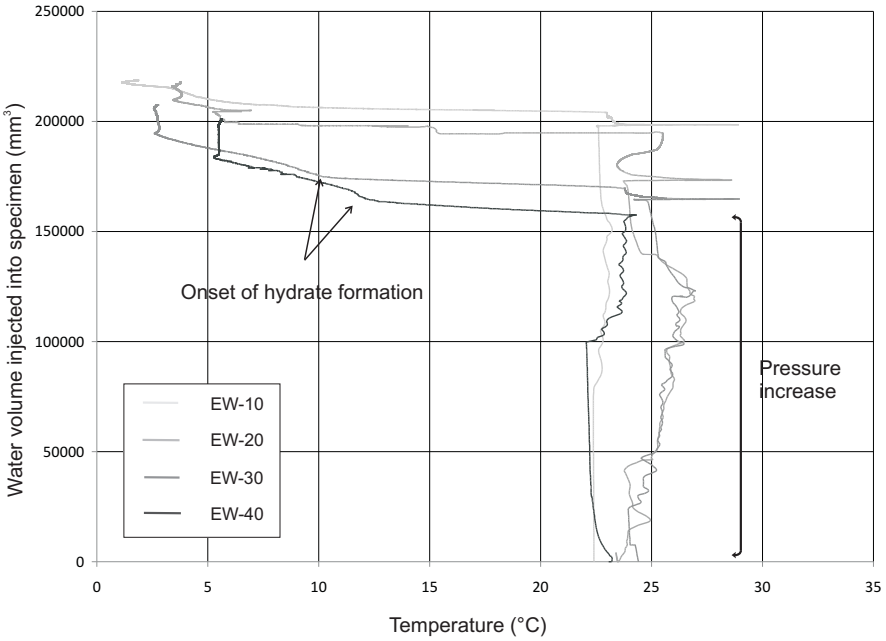

Figure 4.2: The volume of water injected into each specimen against temperature

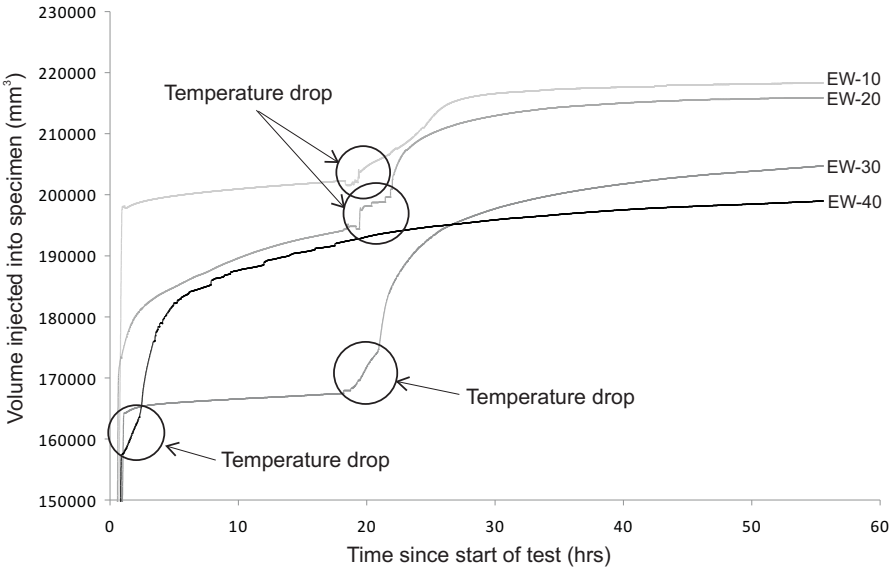

Figure 4.3: Focused view of volume of water injected into each specimen over time, during temperature drop and subsequent hydrate formation

It is also possible that pipework in the GHRC was not fully water saturated before testing. The pipes connecting the DPC and the GHRC have an approximate volume of 18ml. Although care was taken at the start of every test to fill all pipework with water, pockets of air could still remain. The extra volume injected into the excess water specimens may therefore be indicative of incomplete saturation of the pipework prior to testing.

Axial Displacement Changes

During specimen preparation and hydrate formation, the changes in height of the specimen were monitored by use of an LVDT mounted on the top support plate and resting on the top cap of the specimen. From observations by Priest (2004) during the "excess gas" tests, it was thought that the height change observed was due to hydrate growth in the pore space. It was hypothesised that as hydrate grew at the contacts between sand grains, it jacked the grains apart and so increased the height of the specimen. Due to the methods of hydrate formation in those tests (formation of ice followed by hydrate formation by an increase in temperature), the change in height of the specimen (axial displacement) caused by hydrate formation was not directly observed. The route into the stability field used in the excess water tests (Figure 3.15) meant that the axial displacement changes caused by hydrate formation could be closely monitored.

It was noted that in all the excess water tests, a degree of expansion could be seen during the temperature drop into the hydrate stability field. The change in axial displacement seen in each specimen is plotted against the change in temperature in Figure 4.4. The plot includes a water saturated sand specimen containing 0% hydrate (EW-0). It can be seen from this figure that there is a similar degree of axial expansion in all the specimens, including that with 0% hydrate content. Of the hydrate tests, the largest expansion is seen from the EW-30 specimen, with the next largest expansion in the EW-10 specimen. For each test, the effective confining pressure fluctuated around 250kPa, with some anomolous readings possibly the result of a higher or lower effective confining pressure than desired. For Priest's (2004) 'jacking apart of grains' hypothesis to be true in these tests, it would be expected that some distinction could be made between sands containing and lacking hydrate.

An investigation was made into the axial displacement changes that could be caused by the apparatus during a drop in temperature. All materials expand and contract to some degree during change in temperature. It was thought that the drop in temperature experienced during hydrate formation could cause the apparatus to contract in such a way as to register as an expansion of the specimen. To investigate this possible mechanism, the apparatus was divided into it's

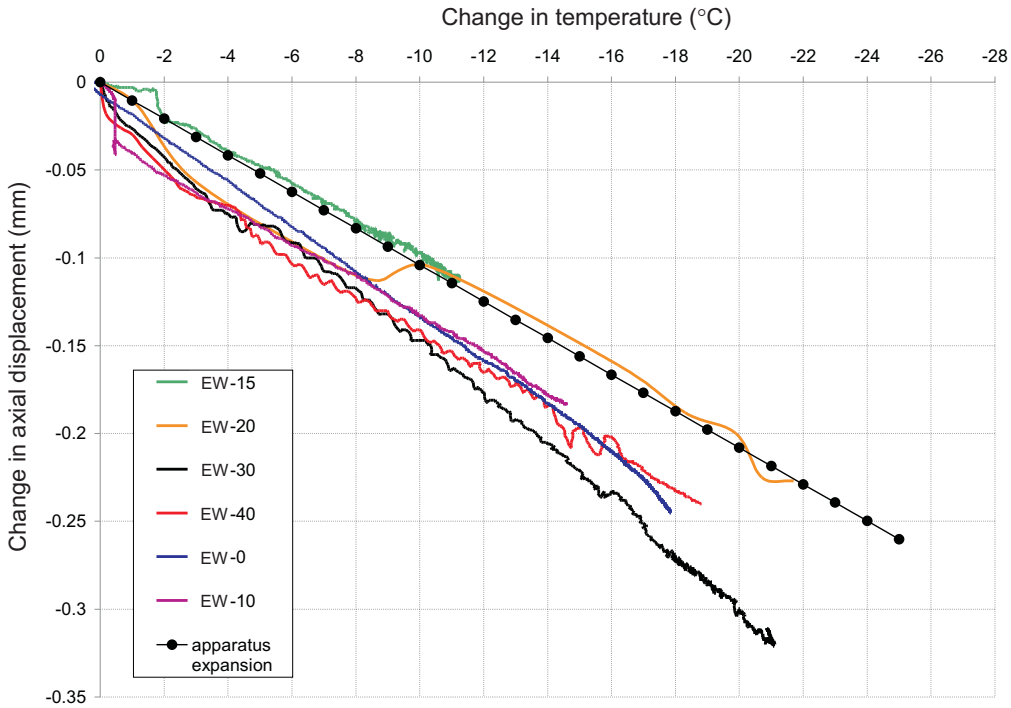

Figure 4.4: Comparison of axial displacement against system temperature during the temperature drop into the hydrate stability zone. A negative change in axial displacement corresponds to an increase in height of the specimen.

	Axial displacement (mm)			change during
Specimen	Start	End temp. drop	End hydrate form.	hydrate formation (mm)
DFM-10	0.051	-0.169	-0.209	-0.04
DFM-15	0.103	-0.104	-0.129	-0.025
DFM-20	0.005	-0.227	-0.236	-0.009
DFM-30	0.280	0.024	-0.060	-0.084
DFM-40	0.023	-0.209	-0.249	-0.04

Table 4.2: Axial displacement values recorded for all DFM hydrate tests at key stages in each test

separate parts, with each piece measured and the contraction due to temperature calculated from standard temperature coefficients. The changes in length for each component were then considered with regard to whether they would show as an increase or decrease in axial expansion. It was found that when combined, the contraction of different parts of the apparatus over a temperature drop of 25°C was over 0.25mm. The change in height that would be recorded by the LVDT due to apparatus contraction is displayed in Figure 4.4. The close correlation with the apparatus expansion and the results recorded from the excess water tests suggests that expansion of the specimens seen during the temperature drop is a result of the axial change in apparatus components due to thermal contraction.

After the temperature drop, each specimen was held at the end condition for a time, to allow for full hydrate formation. During this maturation period, the axial displacement of the specimens was monitored, with the observations recorded in Table 4.2. The temperature and effective confining pressure of each test was kept constant during the period of hydrate formation, with each recording in Table 4.2 taken at 250kPa effective confining pressure. The data suggests that the hydrate does not have a significant effect on the host sediment dimensions in the majority of the tests. Specimen EW-30 shows over double the expansion of the other excess water tests, however this is still below 0.1mm. If hydrate were to be seen to force sediment grains apart, this might be noticed as an increase in expansion with hydrate content. The lack of increasing expansion with hydrate content in the excess water tests suggests that hydrate does not form in such a way as to force grains apart, or that the pressure exerted by hydrate formation is not enough to overcome the effective confining pressure and cause the specimen to expand.

Evolution of Stiffness and Damping

Hydrate formation was originally assumed to cause a change in mechanical properties of the sands being tested in the GHRC (from the previous work by Priest (2004)). The stiffness of the sands was therefore expected to rise during hydrate formation, and could be used as a measure of the total conversion of methane gas into methane hydrate. By considering Equations 3.1 and 3.2, an increase in resonant frequency corresponds to an increase in shear wave velocity, and subsequently the stiffness of a specimen. Basic measurement of the resonant frequency could therefore be used as an indication of changes in stiffness. After the first test of EW-10 specimens, it became apparent that the hydrate did not have the same affect on the LBE sand as in previous experiments (Priest, 2004). Figure 4.5 shows the values for the resonant frequencies of each specimen as the temperature was dropped and hydrate formed in the pore space. For the specimens EW-10, EW-15 and EW-20, no increase in resonant frequency was observed during hydrate formation. It was not until the EW-30 and EW-40 specimens were

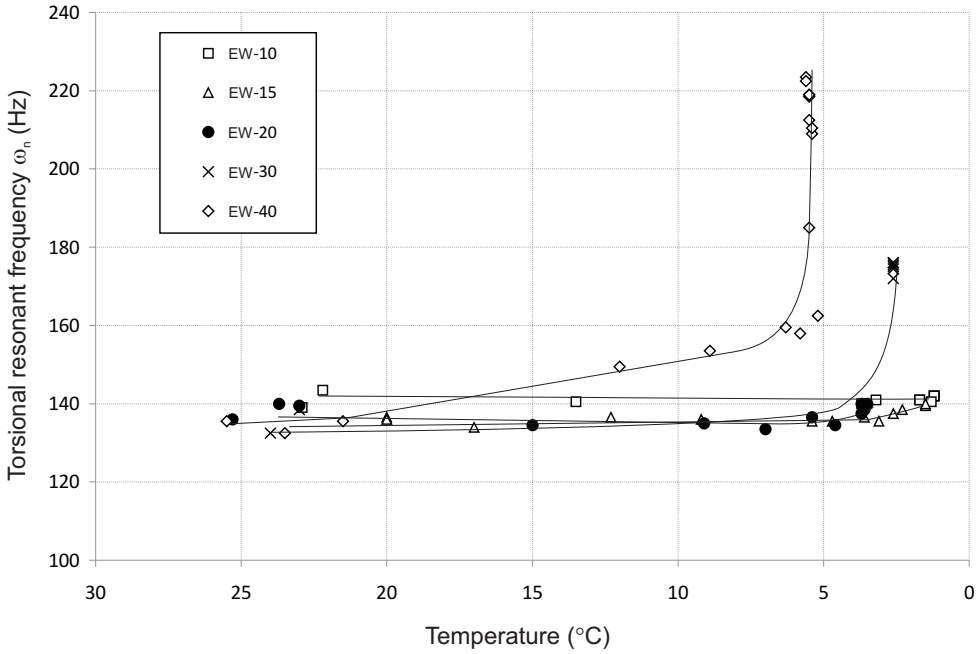

Figure 4.5: Change in torsional resonant frequency with temperature, during temperature drop and hydrate formation

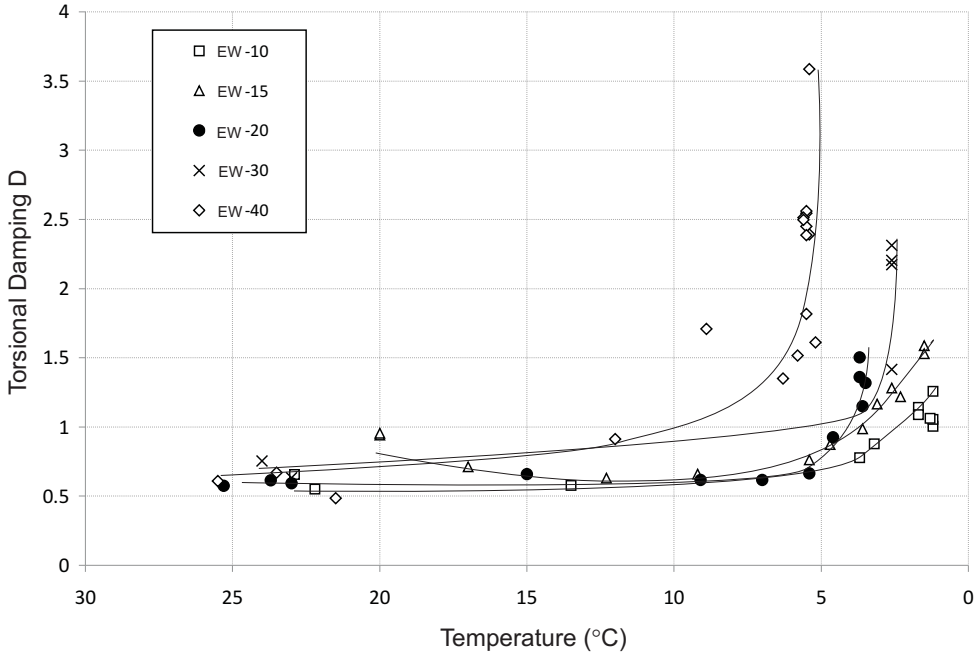

Figure 4.6: Change in torsional damping values with temperature, during temperature drop and hydrate formation

formed that the resonant frequency began to change as hydrate formed in the pore space.

Although the stiffness of the specimens was unaffected by hydrate formation at low hydrate contents, the damping measurements showed significant change during formation. Figure 4.6 shows the damping (D) values for each specimen as the temperature was dropped and hydrate formed in the pore space. Even at low hydrate contents, the damping showed an increase, that could be attributed to hydrate formation in the pore space. Once it became apparent that a change in damping in the specimen signified hydrate formation, the full conversion of methane gas to hydrate could be taken as the point where the damping increase ceased.

4.1.2 The Effect of Hydrate Formation Technique on Stiffness

As one of the aims of this research was to provide information to aid in the detection and quantification of hydrate in seismic surveys, the effect of hydrate on the stiffness of sand specimens will be represented by looking at the seismic velocity changes in the sediment specimens. Figure 4.7 shows the shear wave velocity for "excess water" test specimens containing 0% hydrate up to 40% hydrate in the pore space plotted against effective confining pressure. The pattern for longitudinal wave velocity from flexure against effective confining pressure is given in Figure 4.8. The first thing to note from these plots is that no change in seismic velocity is seen until 30% of the pore space is filled with methane hydrate. If this behaviour is compared with Priest's "excess gas" test data, it can be seen that the two formation methods give different results when compared with similar hydrate contents. Figure 4.9 plots shear wave velocity against hydrate content for both the excess water and excess gas test methods. In Priest's excess gas tests, the shear wave velocity increases sharply with hydrate content to 5% content, and then continues to increase at a lesser rate up to 40% hydrate content. However, in the excess water tests, no change is observed until 30% of the pore space is filled with hydrate, when there is a slight increase in seismic velocity of the specimen. Figure 4.9 would suggest that the morphology of hydrate in the pore space is therefore different depending on the method of formation used. In order to develop a hypothesis to explain these differences, the relationship between seismic velocity and effective confining pressure is analysed.

Influence of Effective Confining Pressure on Specimen Properties

It has been reported (Cascante, 1996; Saxena et al., 1988; Hardin & Drnevich, 1972) that the seismic velocity of a sediment is a function of isotropic effective stress. By looking at Figure 4.7, it can be seen that there is a significant increase in the shear wave velocity with increasing applied effective confining pressure, for all excess water tests. The same relationship can be

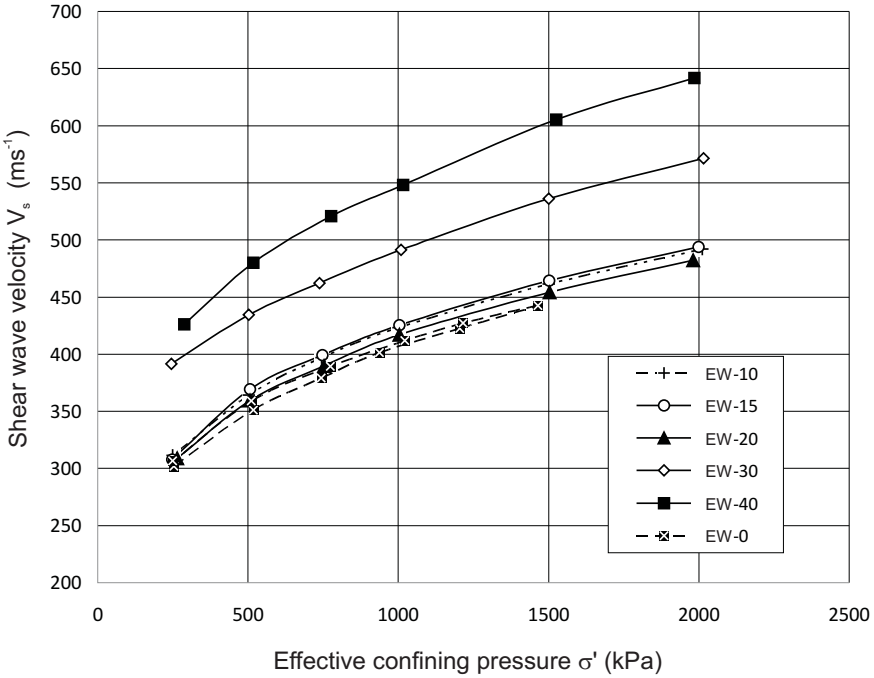

Figure 4.7: Shear wave velocity V_s against effective confining pressure σ' for all excess water tests

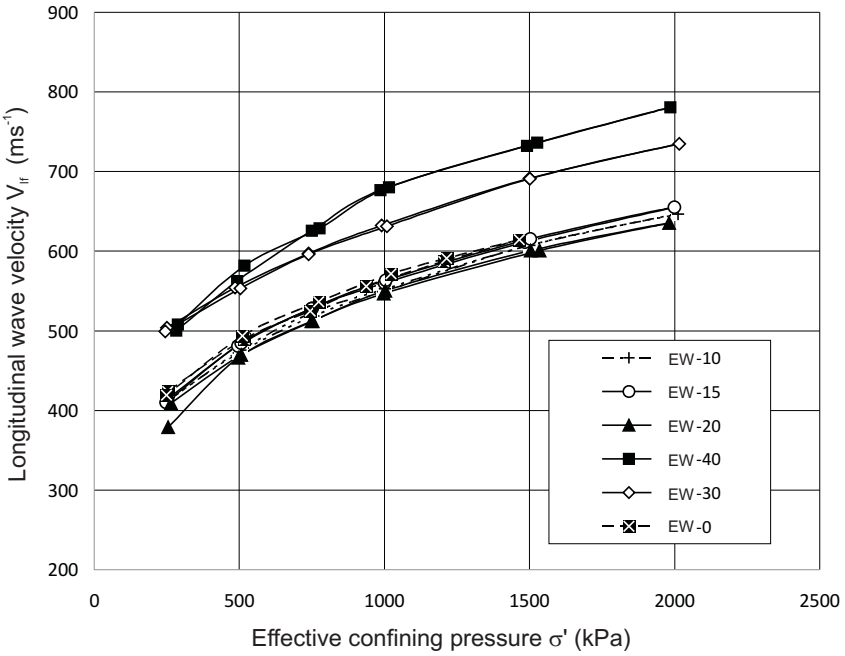

Figure 4.8: Longitudinal wave velocity from flexure V_{lf} against effective confining pressure σ' for all excess water tests

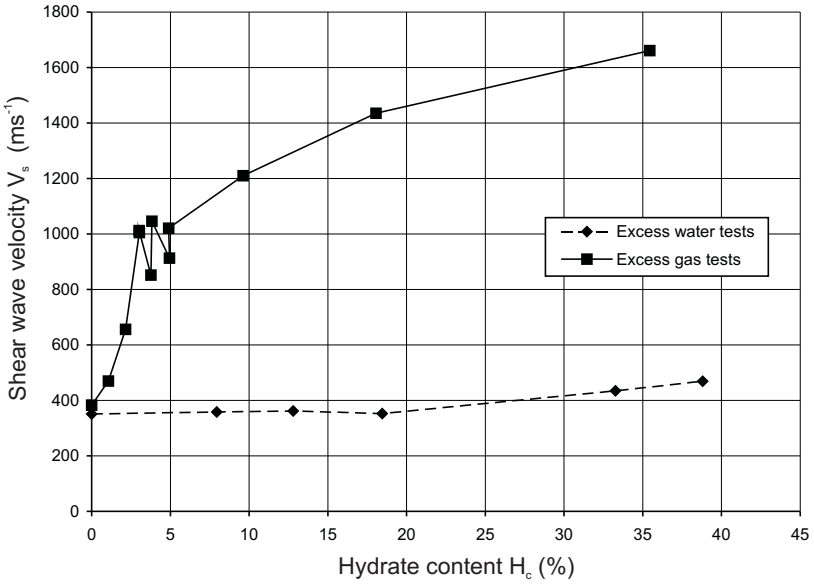

Figure 4.9: Comparison of Shear wave velocity V_s with hydrate content for excess water and excess gas tests

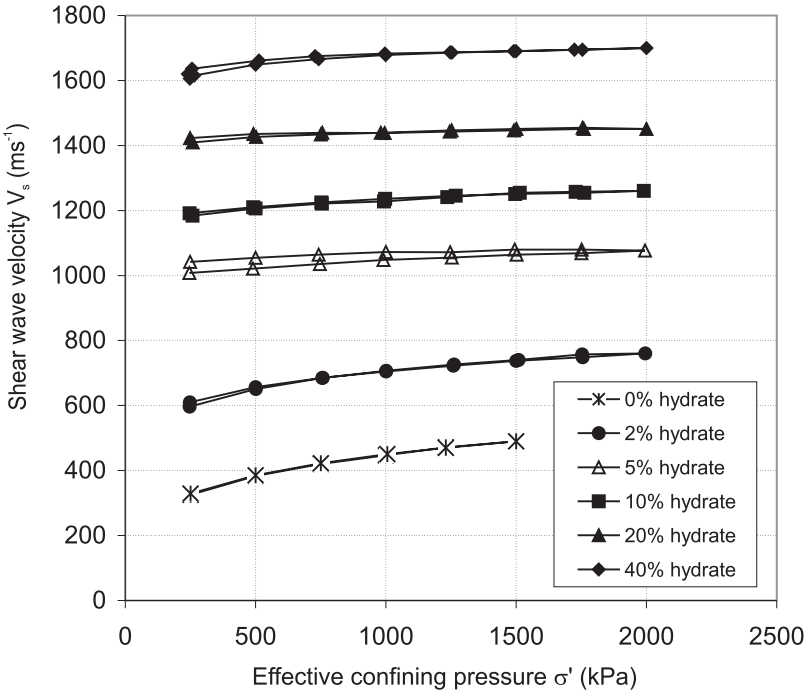

Figure 4.10: Shear wave velocity V_s against effective confining pressure σ' for a selection of excess gas tests. Data from Priest (2004)

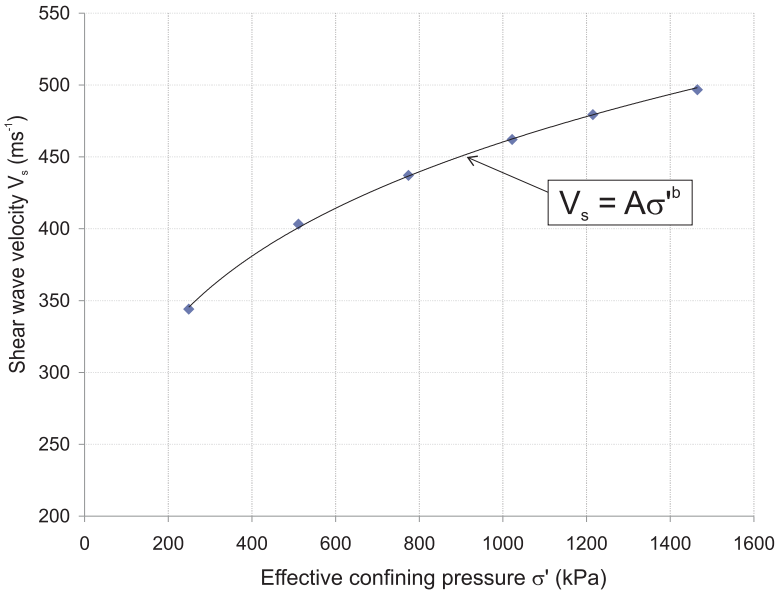

Figure 4.11: Shear wave velocity V_s plotted against effective confining pressure σ' for 0% hydrate specimen, showing power curve and equation with *b* exponent

observed in longitudinal wave velocity from flexure data in Figure 4.8. Conversely, in Priest's excess gas tests shown in Figure 4.10, the change in shear wave velocity with effective confining pressure reduces as the hydrate content increases. This relationship between effective confining pressure σ' and shear wave velocity V_s can be considered by fitting a power law relationship to the data (Figure 4.11) such as:

$$V_s = A\sigma'^{b} \tag{4.1}$$

Where A and b are constants. The same relationship can also be applied to longitudinal wave velocity from flexure V_{lf} in place of V_s. Cascante (1996) has shown that this relationship gives information on the degree of bonding in a sediment. Bonding reduces the compliance of sediments to effective stress, with the b value moving toward zero as bonding increases. Figure 4.12 shows the b values for both excess water and excess gas tests plotted against hydrate content. The plot shows that for both tests, the b value at 0% hydrate content is between 0.2 and 0.25, a value expected for a clean un-bonded sand (Cascante et al., 1998). In Priest's excess gas tests, the b value then drops to a value of around 0.025 for hydrate contents above 3%, whereas the excess water tests continue to show a high b value around 0.2.

The values for the power exponent, seen in Figure 4.12, show that when hydrate is formed in

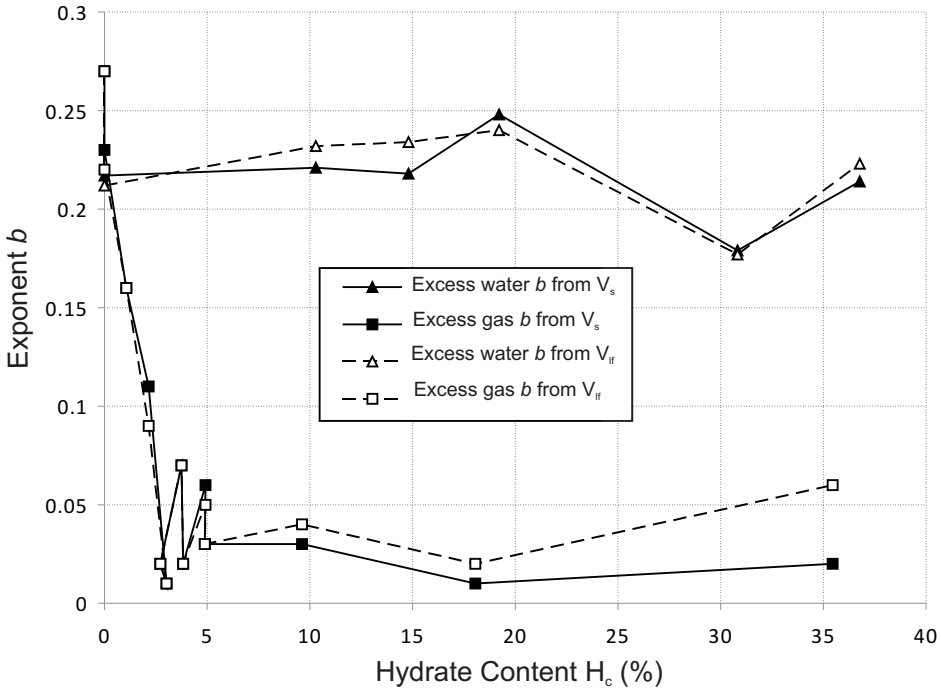

Figure 4.12: Comparison of b exponent for excess water and excess gas tests

excess gas conditions, small quantities of hydrate have a marked influence on the compliance of the sands to effective stress. This would suggest that hydrate acts as a bonding material after 3% of the pore space is filled under these formation conditions. The opposite appears to be the case for hydrate formed under excess water conditions. The b exponent for the excess water tests remains between 0.2 and 0.25 for all hydrate contents, only dipping to 0.18 for the 30% hydrate test. It is obvious that the same degree of bonding seen in Priest's tests is not prevalent in the tests conducted in this research.

Seismic Velocity and Void Ratio

The affect of void ratio e on the small strain shear modulus G_{max} of unbonded granular materials has been investigated and modelled by numerous geotechnical researchers (Hardin & Richart, 1963; Shibuya et al., 1997; Bui, 2009). Overall, sediments can be expected to gain in stiffness (show an increase in G_{max}) due to a reduction in void ratio (Hardin & Richart, 1963), although other aspects of the sediment such as grain size and shape must also be taken into account (Shibuya et al., 1997). Figure 4.13 plots the void ratio of each excess water test against G_{max} (derived from Equation 3.2) before and after hydrate formation. Table 4.3 gives the exact values for the void ratios that are plotted in Figure 4.13. Also plotted in Figure 4.13 is the universal void ratio function developed by Bui (2009), which plots the relationship be-

Specimen	Actual H_c (%)	e before hydrate formation	e after hydrate formation	Relative density (%)
EW–0	0	0.726	–	73.8
EW–10	8.0	0.662	0.579	91.7
EW–15	12.8	0.667	0.546	90.3
EW–20	18.5	0.668	0.506	90.0
EW–30	33.3	0.660	0.406	92.2
EW-40	38.8	0.657	0.365	92.9

Table 4.3: Exact hydrate content values for each excess water specimen, as well as the values for the void ratio in each specimen before and after hydrate formation.

tween void ratio and normalised G_{max}, allowing for particle characteristics by the inclusion of the parameter Cp, called the particle characteristic coefficient. Generally, the value of Cp can be seen to increase with increasing grain size, and decrease with increasing angularity. Bui (2009) has found experimentally that LBE sand has a Cp of approximately 50–60, and LBB sand has Cp of 80–85. Figure 4.13 shows that the increase in G_{max} of specimens EW-30 and EW-40 fits into the modelled values of G_{max} for the corresponding reduction in void ratio of the specimens, for a Cp of approximately 50. Specimens EW-10, EW-15 and EW-20 show no increase in normalised G_{max} (EW-20 even shows a slight decrease) even though the decrease in void ratio by hydrate formation should correspond to an increase in G_{max} by Bui's universal void ratio function (Bui, 2009).

In contrast to the excess water results, Figure 4.14 shows the results from Priest (2004) for sands including hydrate, from 1% hydrate content to 40%. The results from Priest's tests lie well outside the universal void ratio function limits. This deviation from Bui's (2009) universal void ratio function further enhances the view that the excess gas formation method of Priest causes bonding in the sediment.

Application of Resonant Column Results to Seismic Surveying

Seismic surveying is generally concerned with the interpretation of compressional wave velocities (V_p) in marine sediments. In order to make the results from a resonant column test useful to the geophysical community, it is important to be able to generate V_p from resonant column results. However, care must be taken during the interpretation of results from saturated sediments, due to the method of obtaining this sort of wave velocity. Longitudinal wave velocity is derived from the resonant column through bending (Section 3.2.1). Bending produces an unequal strain field across a cylindrical specimen, therefore on one side, the specimen is in compression, and on the other extension. In porous materials, such as those used in the excess water tests, water is free to move across the specimen to equilibrate the excess pore pressure

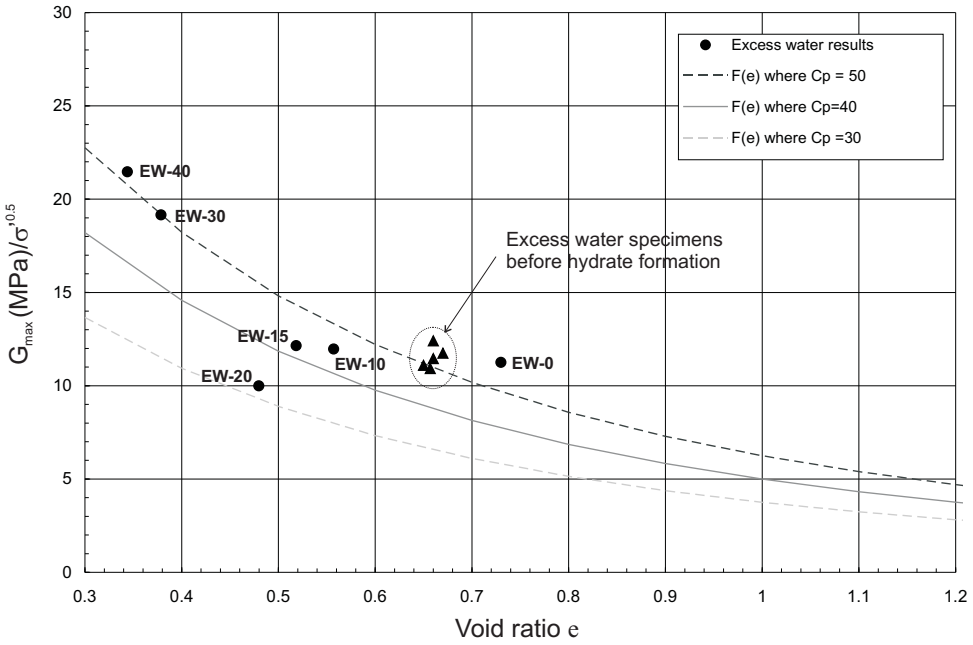

Figure 4.13: Void ratio e plotted against small strain shear modulus G_{max} for excess water tests. The universal void ratio function of Bui (2009) is also plotted for varying values of the particle characteristic coefficient Cp.

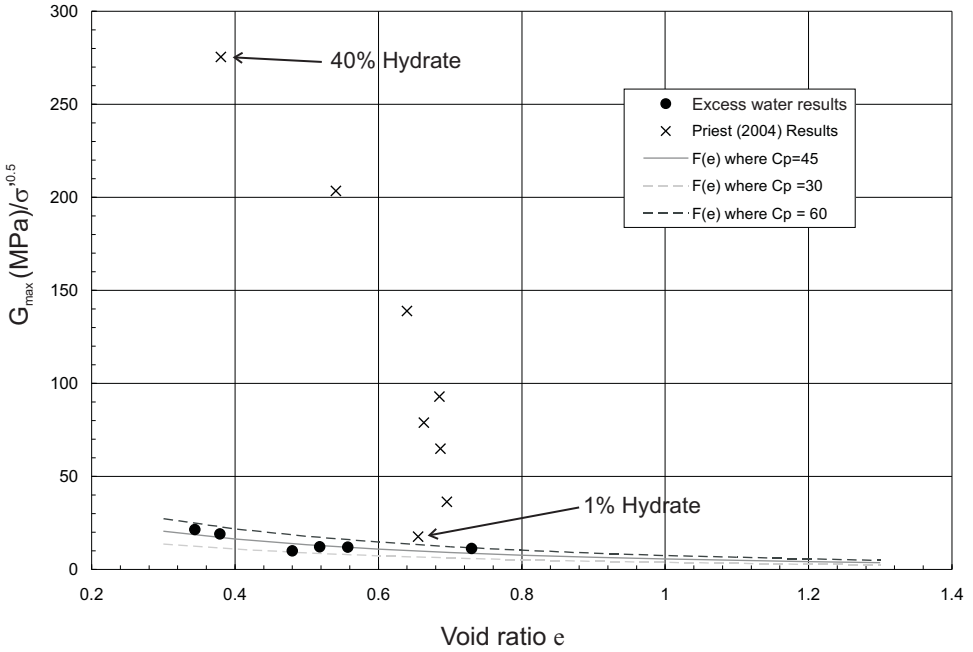

Figure 4.14: An extension of Figure 4.13 including the results from Priest (2004)

caused during bending, however this means that the vertical Young's modulus found through flexural excitation is representative of the dry sediment only. As the movement of a compressional wave through a specimen creates an even strain field in cross section, excess pore pressure can not dissipate, and the stiffness of the water and the frame are measured. In order to derive the saturated compressional wave velocity of the sediments in the resonant column test, the stiffness of the water must be factored into the flexural results.

Compressional wave velocity V_p can be found using the shear modulus G_{sat} and bulk modulus K_{sat} of the saturated sediment:

$$V_p = \sqrt{\frac{(K_{sat} + \frac{4}{3}G_{sat})}{\rho}} \tag{4.2}$$

where ρ is density of the specimen. G_{sat} can be derived from the measured V_s via Equation 3.2, as water is not a factor in shear deformation. K_{sat} in a saturated sediment however, depends on the bulk modulus of the sediment frame and that of the fluid in the pore space. Gassmann (1951) has shown that the bulk modulus of a saturated sediment can be found by using the bulk moduli of the constituent parts:

$$K_{sat} = K_d + \frac{(1 - \frac{K_d}{K_m})^2}{\frac{\phi}{K_f} + \frac{1-\phi}{K_m} - \frac{K_d}{K_m^2}} \tag{4.3}$$

Where K_f is the bulk modulus of the fluid; K_m is the average bulk modulus of the sediment grains; K_d is the bulk modulus of the dry frame; and ϕ is the porosity of the rock. This equation allows the saturated bulk modulus of the sediment to be found from the experimental results (that produce K_d), and the pore water component of K_{sat} that can be calculated from the known bulk moduli of water ($K_f = 2250$MPa) and a calculated value for K_m that accounts for hydrate content giving the sediment a mixed mineralogy. K_m is calculated using Hill's averaging formula (1952):

$$K_m = \frac{1}{2}\left[\sum_{i=1}^{N} \varphi_i K_i + \left(\sum_{i=1}^{N} \frac{\varphi_i}{K_i}\right)^{-1}\right] \tag{4.4}$$

Where φ_i is the volumetric fraction of the i-th constituent, K_i is bulk modulus for each constituent, and N is the number of mineral constituents. The bulk modulus of methane hydrate was taken as 7.9GPa (Waite et al., 2000) with the bulk modulus of the quartz sand grains as 36.6GPa (Mavko et al., 1998).

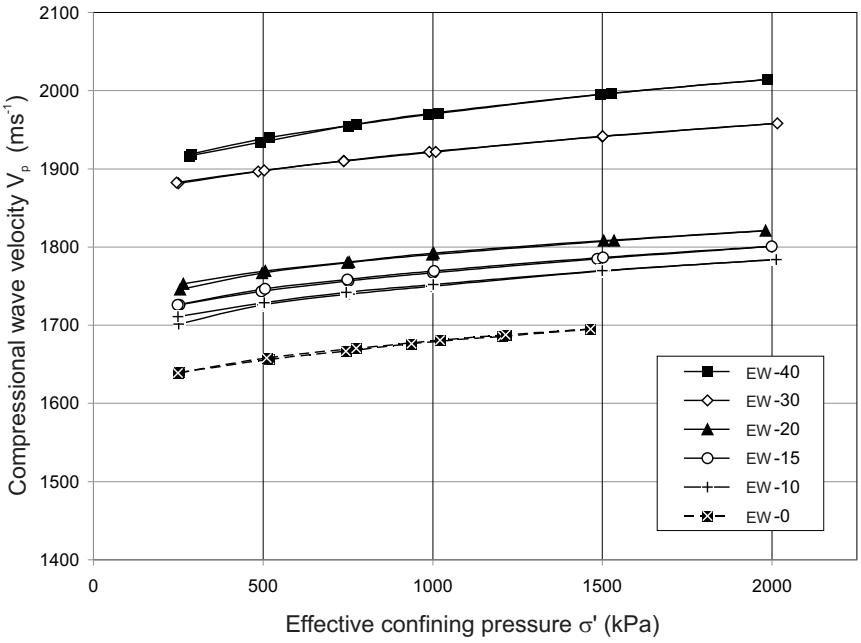

Figure 4.15: Calculated compressional wave velocity V_p against effective confining pressure σ' for excess water tests.

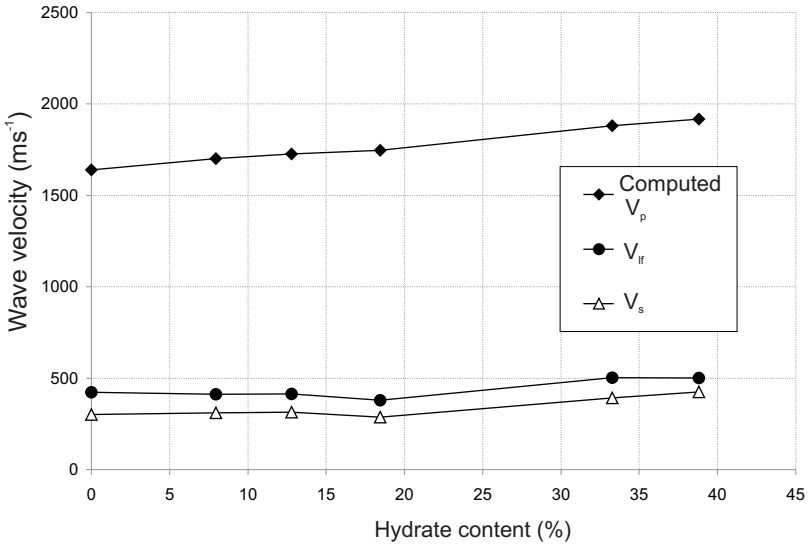

Figure 4.16: Calculated compressional wave velocity V_p plotted against hydrate content for all excess water tests. Shear wave velocity V_s and longitudinal wave velocity from flexure V_{lf} have also been plotted for comparison.

Figure 4.15 shows the computed V_p for all excess water tests. It shows the results for V_p to have a better spread than the results for V_s and V_{lf}, with the change in hydrate content giving an increase in P-wave velocity in all the excess water tests. This is in contrast to the measured results, which only show hydrate affecting specimens EW-30 and EW-40 (Figure 4.16).

The consistent increase in V_p with hydrate content is likely to be due to the way V_p is calculated using Gassmann's (1951) equation. Equation 4.3 finds the bulk modulus of the fluid component through porosity and the bulk moduli of the other sediment constituents. As the inclusion of hydrate to a sediment decreases the porosity, this will cause an increase in K_{sat} even though no increase is observed in the measured K_d from V_{lf}. Care must therefore be taken when finding V_p by using Gassman's equation in this case. The results in Figure 4.15 may very well represent the modelled change in V_p with hydrate content and σ', rather than the true values.

4.1.3 The Effect of Hydrate Formation Technique on Attenuation

The measurement of attenuation in gas hydrate bearing sediments has been limited, with only a couple of researchers providing information on attenuation in naturally occurring gas hydrate bearing sediments (Guerin & Goldberg, 2002; Matsushima, 2005)(Section 2.4.4). Attenuation measurements were therefore taken throughout the testing so as to obtain the first set of information on synthetic water saturated hydrate bearing sediments.

Figure 4.17 shows the pattern of attenuation in torsion Q_s^{-1} and flexure Q_{lf}^{-1} plotted against hydrate content for the excess water tests. Attenuation values were obtained through the free vibration decay method as described in Section 3.2.1, from which the equipment damping was then deducted to give the intrinsic attenuation of the specimens. Values from both torsional (Q_s^{-1}) and flexural (Q_{lf}^{-1}) excitation are plotted in Figure 4.17 and both show an increase in attenuation with increasing hydrate content, although Q_s^{-1} shows a more consistent increase than Q_{lf}^{-1}. The anomalously low flexural attenuation value for specimen EW-20 containing 18% hydrate content may be another indicator of incomplete hydrate formation in the specimen, as suggested previously in Section 4.1.1. Figure 4.18 gives the shear wave attenuation plots against hydrate content for different values of effective confining pressure. The general trend for increasing confining pressure is a decrease in attenuation seen in each specimen, however, this decrease is low enough to suggest that attenuation is constant throughout the effective stress load–unload cycle.

When comparing these results with those from Priest's (2004) excess gas tests, there is a no-

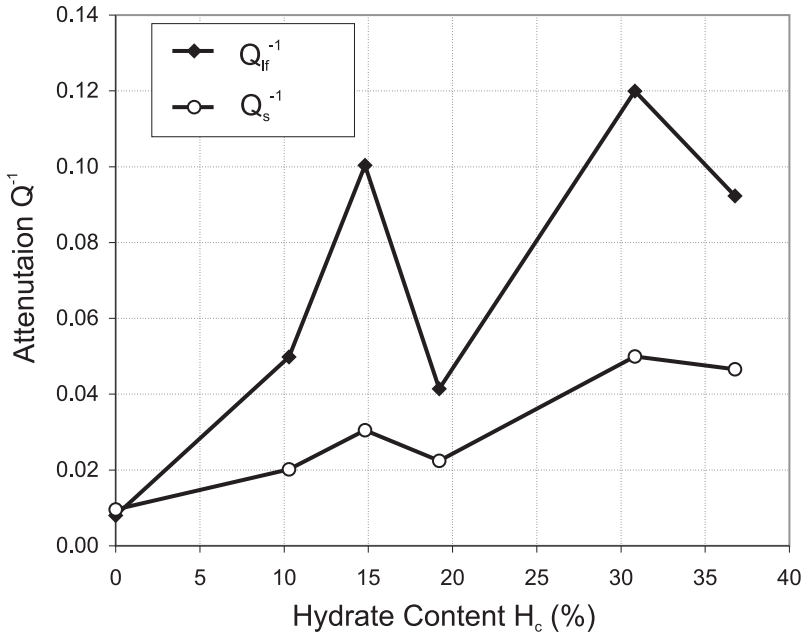

Figure 4.17: Attenuation in torsional (Q_s^{-1}) and flexural (Q_{lf}^{-1}) excitation plotted against hydrate content for excess water tests

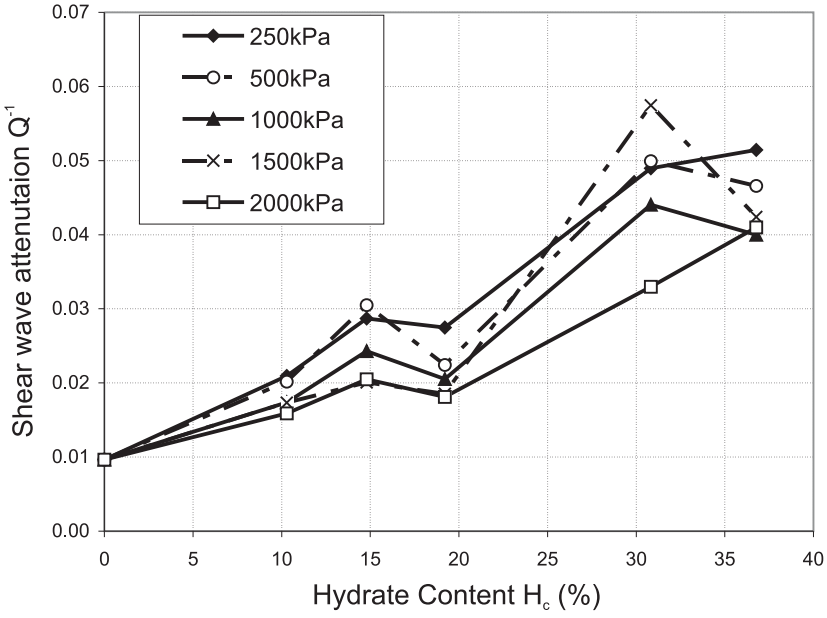

Figure 4.18: Shear wave attenuation (Q_s^{-1}) plotted against hydrate content for varying degrees of effective confining pressure

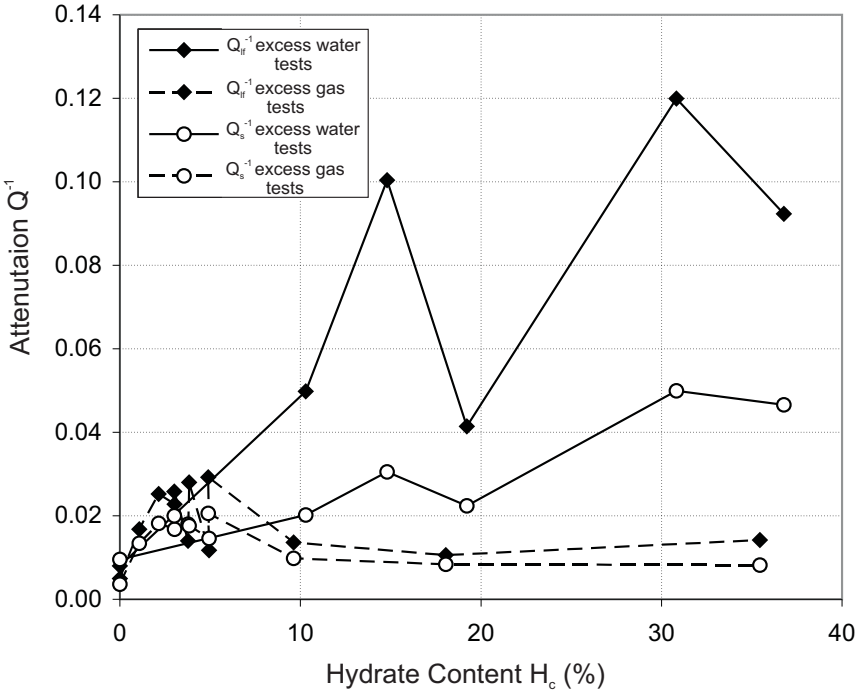

Figure 4.19: A comparison of attenuation in torsional (Q_s^{-1}) and flexural (Q_{lf}^{-1}) excitation plotted against hydrate content for wet and dry tests

ticeable difference. Figure 4.19 compares the shear wave attenuation (Q_s^{-1}) and longitudinal wave attenuation (Q_{lf}^{-1}) from both the excess water and excess gas tests for all hydrate contents tested. It can be seen that in Priest's tests, attenuation is at a high between 3 and 5% hydrate content. It then drops to a relatively constant value from 10 - 40% hydrate content. In the tests conducted in excess water conditions however, attenuation increases with increasing hydrate content.

As it has been established by Priest et al. (2005) that hydrate is acting as a cement in excess gas conditions, the behaviour between 1% and 5% hydrate content in Figure 4.19 could be unexpected. Increasing degrees of cementation should decrease attenuation by restricting grain movement and decreasing viscous energy dissipation (Pecher & Holbrook, 2000). However, Saxena et al. (1988) have recorded a similar attenuation pattern to Priest's excess gas tests when testing sands with various degrees of cementation by Portland cement. They record a point between 5% and 8% cement saturatation where the damping is at a peak, before it drops off as the sand becomes fully bonded. They hypothesise that the energy dispersion through a weakly cemented sand will be higher than through a sand where the clean grains are in contact. From 1% to 8% cement saturation, the sand is considered 'weakly bonded' and so the damping increases. After 8% cement saturation, the sand is fully bonded and the damping decreases. In the excess gas tests of Figure 4.19, the specimens may be 'weakly bonded' up to 5% hydrate content, after which attenuation decreases to a constant value as the specimens are fully bonded by hydrate. In addition to this hypothesis, Priest et al. (2006) concluded that attenuation in hydrate bearing sands formed in gas saturated environments is caused by the 'squirt flow' mechanism.

The energy dispersal in sediments at low strain is primarily due to viscous dissipation and not frictional losses (Winkler et al., 1979). In sediments that contain water, the dispersion of a wave is controlled by the degree of saturation and the frequency. In partially saturated porous materials the interaction of the water and gas phases plays an important role in energy dispersal, whereas in water saturated media, local fluid flow of water in pores and cracks is the primary contributor to damping (Jones, 1986; Murphy et al., 1986; Johnston et al., 1979; Cascante, 1996).

'Squirt' or 'local flow', is the mechanism by which the passing of a seismic wave through porous media, induces pore pressure gradients across individual pores and grains. This causes the movement of water and the resultant viscous dissipation of energy (Mavko & Nur, 1979; Mavko et al., 1998). Priest et al. (2006) suggest that adsorbed water on the surface of the LBE sand grains will move as seismic waves deform the grains at contacts. The decrease in

attenuation as hydrate content increases is due to the bonding effect of the methane hydrate, combined with reduced availability of water for squirt flow as it is all consumed during the hydrate formation.

The increased attenuation with hydrate content seen in the excess water tests could also be an unexpected behaviour. As hydrate is pore filling, and reduces the porosity of a sand, it has been shown that this should cause a decrease in attenuation (Hamilton, 1972). However, Goldberg et al. (1985) observed an increase in attenuation in sediments containing varying degrees of silica diagenesis. As the silica decreased the porosity of the host sands, they expected the attenuation to decrease also. The adverse results were explained by considering the changing aspect ratio and surface area of the pores with relation to local fluid flow mechanisms. The decreasing porosity led to an increase in pore surface area, that gave a greater availability of pore surface area that increased viscous fluid losses during local flow movement. This process could be the same in the excess water tests of this research. As hydrate grows in the pore space, a larger surface area for squirt flow also develops.

Another damping mechanism to consider in water saturated hydrate bearing sands is the flow of liquid inside the hydrate grains themselves. Methane hydrate is a porous material (Genov et al., 2004), and the method for generating hydrate in the excess water tests promotes a porous hydrate morphology. Tohidi et al. (2001) have shown that hydrate forms around gas bubbles in water rich environments, with further hydrate growth resulting from gas inside the bubble diffusing out through the porous hydrate structure. When a seismic wave passes through one of the excess water test specimens, the hydrate grains may promote extra squirt flow through their porous structure. The attenuation increases with increasing hydrate content, as more hydrate generates internal squirt flow and increases energy dissipation.

Comparison of attenuation results with previous studies

As mentioned earlier in this section, measurements of attenuation in hydrate bearing sediments are limited. However, the nature that has been recorded here has also been observed by Guerin & Goldberg (2002) and Matsushima (2005). Both reports described increasing attenuation with hydrate content during logging of natural hydrate bearing sediments. On the back of these observations, Matsushima (2005) went on to suggest that attenuation may become a more valuable tool for detecting and quantifying hydrate bearing sediments then seismic velocity, as attenuation appears to be more sensitive to hydrate content variations.

It has become apparent from this research that hydrate has a very different effect on homogeneous sands when grown in different conditions. If the results of the velocity studies seen

in Section 4.1.2 are considered alongside the attenuation results seen here, the suggestions of Matsushima (2005) could be relevant. In oceanic environments, hydrates are mostly grown in water saturated conditions. If the models of hydrate formation in these conditions as a non–bonding material are to be taken, the hydrate will not effect the seismic velocity of the host sediment until significant quantities are present in the pore space. Even once 40% of the pore space is filled, there may only be an increase in seismic velocity of 100 - 150ms^{-1}, as seen in the results of Figure 4.7, with lower hydrate contents not being detected at all. Attenuation results however, show an increase with increasing hydrate content even at lower hydrate volumes. The sensitivity of attenuation changes to increases in hydrate content when the hydrate does not appear to be affecting the stiffness of the sediment may allow the detection of hydrate in situations where it would not have been detected by standard seismic velocity surveys.

4.2 Hydrate Morphology in Synthetic Hydrate Bearing Sediments

The aim of the testing sequence described above was to enable a direct comparison of hydrate formation techniques by forming homogeneous methane hydrate in the same materials and apparatus as Priest (2004), but in water saturated conditions. The comparison between Priest's "excess gas", and this research's "excess water" methodology, allows for investigation into the morphology of methane hydrate in the pore space under different formation conditions. The results displayed above have shown that hydrate affects sediment differently depending on whether it was formed in gas rich (excess gas) conditions, or water rich (excess water) conditions.

The hydrate bearing specimens formed by Priest (2004) show a behaviour that is attributed to the bonding of the sediment. Analysis of effective stress dependency (b exponent), void ratio change and attenuation pattern have all pointed towards the cementation of the sediment with hydrate. Further comparison with cemented sand research (Saxena et al., 1988) led Priest et al. (2005) to establish this nature for hydrates formed under excess gas conditions. The results from the excess water tests in this research show a very different nature to excess gas results. Analysis of the b exponent suggests that there is no bonding in the excess water hydrated sands, even in specimens with high hydrate content (EW-30 and EW-40). Plots of void ratio against normalised shear modulus, follow a pattern predicted by Bui's universal void ratio function (2009) suggesting the reduction in void ratio of granular materials corresponds to an increase in shear modulus. Attenuation measurements from the excess water tests also suggest a different nature to the excess gas, with wave attenuation showing an almost linear increase with increasing hydrate content.

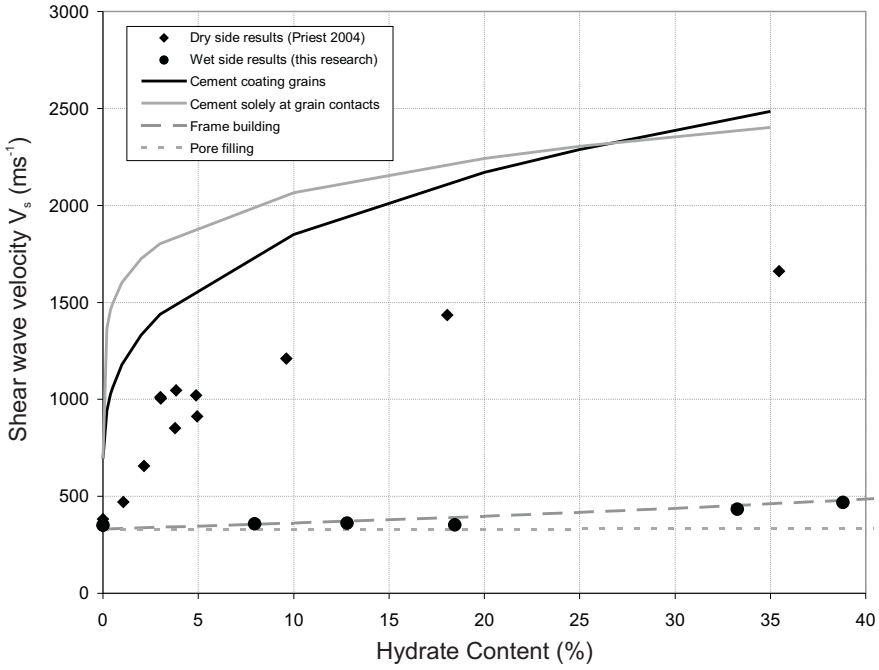

Figure 4.20: Shear wave velocity results from the dry side hydrate tests of Priest (2004) and the wet side results of this research, compared with hydrate morphology models (Chapter 2, section 2.4.3).

4.2.1 Hydrate Morphology Models

It seems clear that hydrate formed in the excess water tests does not cement the sediment. In order to help understand the grain scale interaction of hydrate and sediment, results can be plotted alongside the models from Section 2.4.3.

Figure 4.20 gives the shear wave velocity results from the excess gas tests of Priest (2004) and the excess water tests of this research along with the models described in Section 2.4.3. The cementing models in Figure 4.20 are those of Dvorkin et al. (2000), which describe the change in shear wave velocity when two different configurations of cement are considered for hydrate on grain surfaces (see Appendix A). The frame building and pore filling models in Figure 4.20 use equations that derive the shear modulus of the dry sediment frame from the modified Hashin–Shtrikman bounds (Dvorkin & Nur, 1996), and then take into account hydrate presence via the change in porosity (Appendix A).

Figure 4.20 shows that the increase in shear wave velocity seen in the excess water tests is similar to that predicted by the frame building model, where hydrate is modelled as changing the porosity of the sediment along with altering the shear modulus of the sediment frame.

The cementing models of Dvorkin et al. (2000), predict higher shear wave velocities than are observed in the excess gas tests. Qualitatively, the increase from the experimental results suggest cementing behaviour, however at no point do the specimens reach the predicted stiffnesses of the Dvorkin et al. (2000) models. It would appear that methane hydrate does not conform to the cementing mechanisms that the Dvorkin et al. (2000) models are based on. Further understanding of the cementing behaviour of hydrate is therefore needed to fit models to the excess gas test data.

The differences in excess water and excess gas morphologies can be explained if the hydrate methodology is considered.

In “excess gas” tests, or conditions where the environment is gas saturated, the hydrate will grow where the water resides, at the gas/water interface. In partially saturated sands, water tends to collect at grain contacts and coat individual sand grains. When hydrate is grown in these conditions, it is therefore forced to grow on grain surfaces and at contacts (Figure 4.21(a)). In “excess water”, or water rich conditions, the morphology of hydrate changes, due to the difference in gas/water interface. In this environment before hydrate formation, there are gas bubbles suspended in water filled pores. As the specimen is taken into the hydrate stability

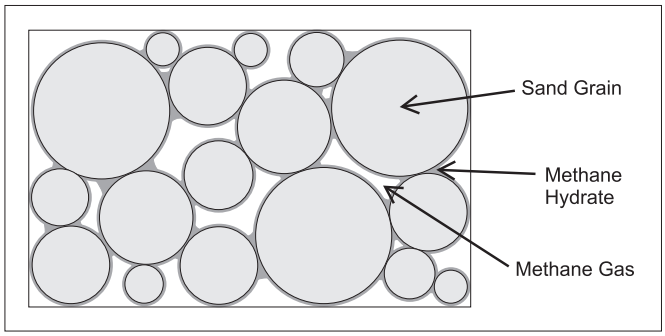

(a) Location of hydrate in the pore space in partially saturated (excess gas) conditions. The hydrate forms where water resides on grain surfaces and at contacts

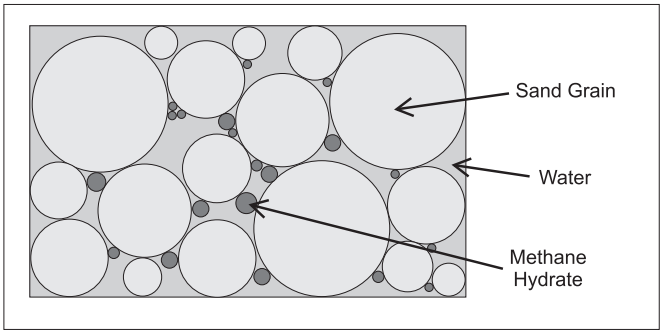

(b) Location of hydrate in the pore space in water saturated (excess water) conditions. The hydrate forms around gas bubbles

Figure 4.21: Locations of hydrate in the pore space under different formation conditions

field hydrate will form around gas bubbles at the gas/water interface (Tohidi et al., 2001; Sloan, 1998). Although there are two possible configurations for hydrate morphology in this situation (frame building and pore filling), it seems, from comparison with modelling results, that hydrate forms in such a way as to cause a reduction in void ratio and contribute to the sediment frame. This points towards hydrate formation near grain contacts (Figure 4.21(b)), rather than isolated gas hydrate forming in the pore space. The lack of shear wave velocity increase from 0% to 20% hydrate content however, does not fit with a purely frame building model. Yun et al. (2005) suggest a modified growth pattern for hydrate, which is a combination of the pore filling and frame building end members and can explain this deviation from the purely frame building model above. They consider that hydrate grows on the surface of grains, but grows outwards into the pore having little affect on sediment properties due to no bridging of the sediment grains by hydrate. Once sufficient hydrate content is reached so as to provide grain/hydrate interaction, the properties of the sediment sharply increase (Yun et al., 2005). It is possible that

aspects of this model are prevalent in the excess water tests of this research. Up to 20% hydrate, the excess water specimens do not show a change in seismic velocity as the hydrate is growing into the pore space. Once 30% hydrate content is reached however, the hydrate interacts with the sediment grains and affects the shear wave velocity. The results in Figure 4.13 giving the change in void ratio of the excess water specimens with normalised shear modulus, agree with this hypothesis. The reduction in void ratio by the presence of hydrate in each specimen, should have corresponded to an increase in normalised shear modulus with increasing hydrate content. Specimens EW–10, EW–15 and EW–20 deviated from this predicted increase curve, in that as the void ratio decreased, there was no corresponding increase in normalised G_{max}. This would suggest that the hydrate did not interact with the sediment frame in these specimens. Once 30% and 40% hydrate contents were reached in specimens EW–30 and EW–40, the values for normalised G_{max} plotted on the predicted curve for the observed change in void ratio in the specimen, indicating the hydrate was now a frame building componant of the sand.

The nature of formation in the excess water tests may account for the increase in shear wave velocity seen in these tests being at a lower hydrate content than that seen by Yun et al. (2005). Yun et al. formed hydrate out of solution, whereas a gas phase is present in the excess water tests. The ability of the gas bubbles to move around in the pore space, may mean that they are more likely to be situated near grain contacts before hydrate formation, than if hydrate were simply forming out of solution and could nucleate anywhere on the grain. Care must be taken when making such comparisions however, due to Yun et al. (2005) utilising THF to make hydrate rather than methane.

4.2.2 Comparison of Results with Previous work on Morphology

In addition to the work of Yun et al. (2005), other work on the morphology of hydrate and the effects it has on host sediment properties appears to corroborate with the results seen in the excess water and excess gas GHRC hydrate tests. Of the research on forming synthetic hydrates, only Waite et al. (2004) shows hydrate forming in gas rich conditions. They showed that hydrate acted as a cement in a similar fashion to the excess gas tests of Priest (2004), however their tests resulted in much higher values for compressional and shear wave velocities at comparable hydrate contents than the results of Priest (2004) (Table 4.4). This could be due to the high frequency (1MHz) P–wave transducers used by Waite et al. (2004) to measure compressional wave velocity, or that they allowed their hydrate specimens to mature for over 220 hours, compared to Priest's 48 hours (discussed further in Section 2.4.1). Regardless of this difference, the large seismic velocities of Waite et al's (2004) results add to the evidence

Source	Material	V_p/ms^{-1}	V_s/ms^{-1}
Excess water tests, this research	10% hydrate and sand	1701[a]	310
	15% hydrate and sand	1726[a]	313
	20% hydrate and sand	1745[a]	287
	30% hydrate and sand	1881[a]	392
	40% hydrate and sand	1916[a]	424
Stoll & Bryan (1979)	Propane–Methane hydrate and Sand	1800–2260	–
Winters et al. (2004)	≈100%(?) Methane hydrate and sand	3950	–
Berge et al. (1999)	20% R11 Hydrate and sand	1700[c]	–
	40% R11 hydrate and sand	2500[c]	1500[c]
Waite et al. (2004)	20% Methane Hydrate and sand	3080	2120[b]
	40% Methane hydrate and sand	3360	2300[b]
Priest (2004)	20% Methane Hydrate and sand	2476[a]	1423
	40% Methane Hydrate and sand	2908[a]	1636
Spangenberg & Kulenkampff (2005)	20% Methane hydrate and glass beads	2000[c]	–
	40% Methane hydrate and glass beads	2800[c]	–
Yun et al. (2005)	40% THF hydrate and sand	–	300[c]
	90% THF hydrate and sand	–	1500[c]

Table 4.4: Tabulated P–wave (V_p) and shear wave (V_s) velocities from excess water testing of this research, compared against results from various workers of hydrate synthesized in the laboratory.[a]Calculated saturated V_p values.[b]Values calculated by Waite et al. (2004) using standard rock physics relations.[c]Approximate values

of hydrate cementing in gas rich conditions.

The other tests on synthetic hydrate bearing sediments that have measured acoustic properties have been conducted in water saturated conditions (Berge et al., 1999; Winters et al., 2004; Spangenberg & Kulenkampff, 2005; Yun et al., 2005). The results from Yun et al. (2005) compare the most favourably with the excess water tests, as discussed above, as well as the 20% hydrate and sand velocities given by Spangenberg & Kulenkampff (2005). As both of these tests form hydrate out of solution, and in fully water saturated conditions, it appears that the method of hydrate formation used in the excess water tests does in fact simulate hydrate forming out of fully saturated sediment. Results such as those from Winters et al. (2004) are mis–leading with regard to comparison with the excess water test results. The high values seen from these tests may be due to the formation method of gas percolation giving an excess in hydrate former in the pore space which is essentially like forming hydrate in partially saturated, "excess gas" conditions.

With regard to measurements from the field, the hypothesis that hydrate is pore filling in water saturated sediments also corresponds to many real world observations. Sakai (2000), Jakobsen

et al. (2000), Lee & Collett (2001), Helgerud (2001) and Waite et al. (2004) have analysed seismic data from a variety of locations against morphology models for hydrate bearing sediments. In each case, it was concluded that hydrate did not act as a cement, but formed in the pore space.

4.3 Discussion of Different Sediment Tests

A series of tests were conducted on a variety of hydrate bearing sediments in order to determine the affect of grain size and shape on hydrate growth. Hydrate was formed in four different sediment types, using the "excess gas" methodology of Priest (2004). Hydrate content and pressure–temperature routes were consistent for all specimens so that the affect of particle characteristics could be analysed. This section describes the results from these tests, beginning with observations during hydrate formation, followed by seismic velocity and wave attenuation analysis.

4.3.1 Observations during Preparation and Hydrate Synthesis

Hydrate was formed in the different sediment specimens via the "excess gas" technique of Priest (2004), although the route taken into the stability zone during this research was different to that used by Priest. Hydrate was formed in the different sediment tests by increasing the pressure to 10MPa in normal laboratory conditions, before dropping the temperature into the hydrate stability field. Priest (2004) reduced the temperature to below freezing, before increasing the pressure therefore forming hydrate from the ice phase of water. Despite these differences, certain observations from Priest's experiments can also be expected in the different sediment tests. The hydrate content in each different sediment specimen should be large enough to cause bonding of the sediment, and so an increase in seismic velocity should be observed as hydrate forms. It is also possible that a change in axial displacement will occur in the specimens due to the hydrate "jacking" the sediment grains apart as it forms.

Evolution of Stiffness and Damping

As the temperature was dropped in each different sediment test to take the specimens into the hydrate stability zone, efforts were made to monitor the change in specimen properties in an attempt to directly observe hydrate formation. Figure 4.22 gives the change in resonant frequency as the temperature was dropped for each different sediment specimen. It can be seen that an increase in resonant frequency was observed in all the different sediment tests, which

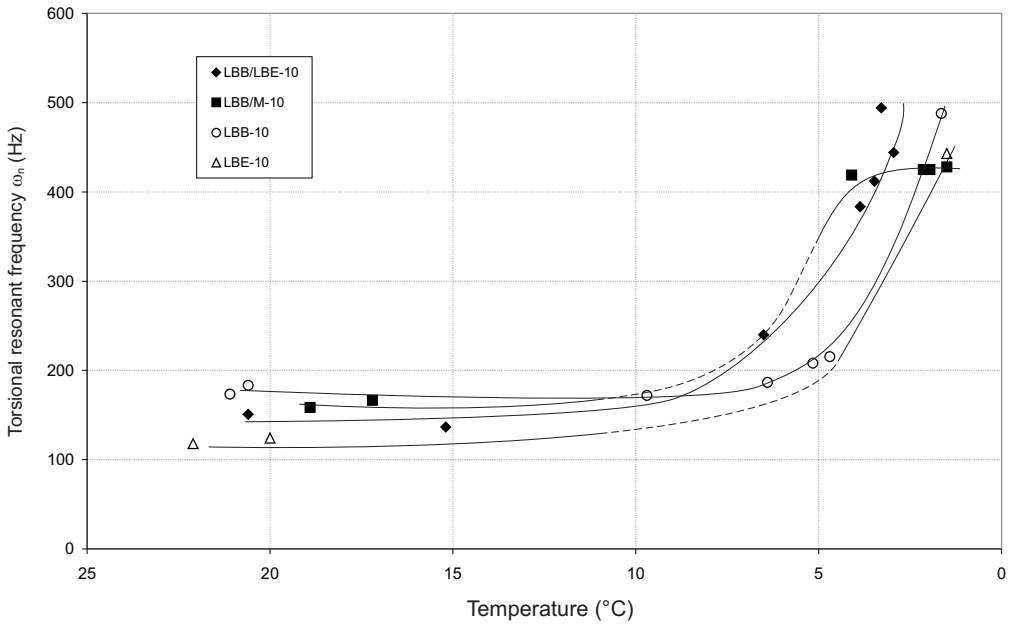

Figure 4.22: Change in torsional resonant frequency with temperature, during temperature drop and hydrate formation

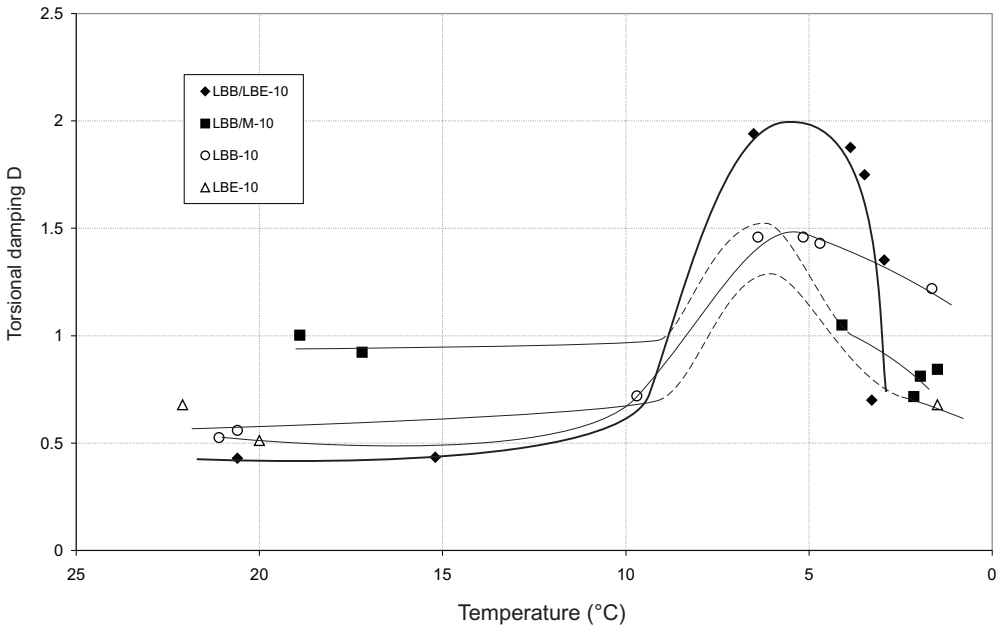

Figure 4.23: Change in torsional damping values with temperature, during temperature drop and hydrate formation

corresponded to hydrate formation. However, it was only with specimen LBB/LBE-10 that a gradual increase in resonant frequency could be observed due to consistent measurements being taken over the temperature drop. Measurements from the remaining different sediment tests could not be made due to the inability to identify resonant peaks during hydrate formation. This was because of the high level of damping from the specimens that flattened any observable peak in resonant frequency. Increased damping during hydrate formation can be attributed to incomplete cementation. Saxena et al. (1988) show that a weakly cemented sand has a higher rate of energy dissipation than a clean uncemented specimen of the same material. It has been established that hydrate forms as a cement in "excess gas" formation conditions (Priest et al. (2005) Section 4.2), and so the slow crystallisation of hydrate before full conversion represents patchy cementation of the specimen. This peak in damping during hydrate formation can be observed in LBB/LBE-10 specimen in Figure 4.23.

Axial Displacement Changes

The change in height of the specimen was monitored throughout the pressure increase, temperature drop and hydrate formation. From the excess water testing sequence (Section 4.1.1) it had been found that the apparatus contracted as the temperature of the system was decreased, showing as an expansion of the specimen by the LVDT. The change in axial displacement that was recorded from each different sediment specimen during temperature drop is given in Figure 4.24. Although all the specimens show an expansion during the temperature drop, only specimens LBB-10 and LBB/LBE-10 display a change close to what is calculated for the apparatus expansion. Specimens LBE-10 and LBB/M-10 both show an axial displacement change of around -0.06mm, which is much lower than expected.

The excess gas method of hydrate formation forces hydrate to grow on grain surfaces and at contacts. Priest (2004) hypothesised that hydrate formation could cause an expansion in sediments due to hydrate 'jacking' grains apart. Table 4.5 gives the values for axial displacement of each different sediment specimen at the beginning and end of the hydrate formation process.

	Measured axial displacement (mm)			change during
Specimen	Start	Beg. hydrate form.	End hydrate form.	hydrate formation (mm)
LBB-10	0.046	-0.112	-0.036	+0.076
LBE-10	0.115	0.05	0.081	+0.031
LBB/LBE-10	0.008	-0.202	-0.238	-0.036
LBB/M-10	0.400	0.363	0.337	-0.026

Table 4.5: Axial displacement values recorded for all different sediment hydrate tests at key stages in each test

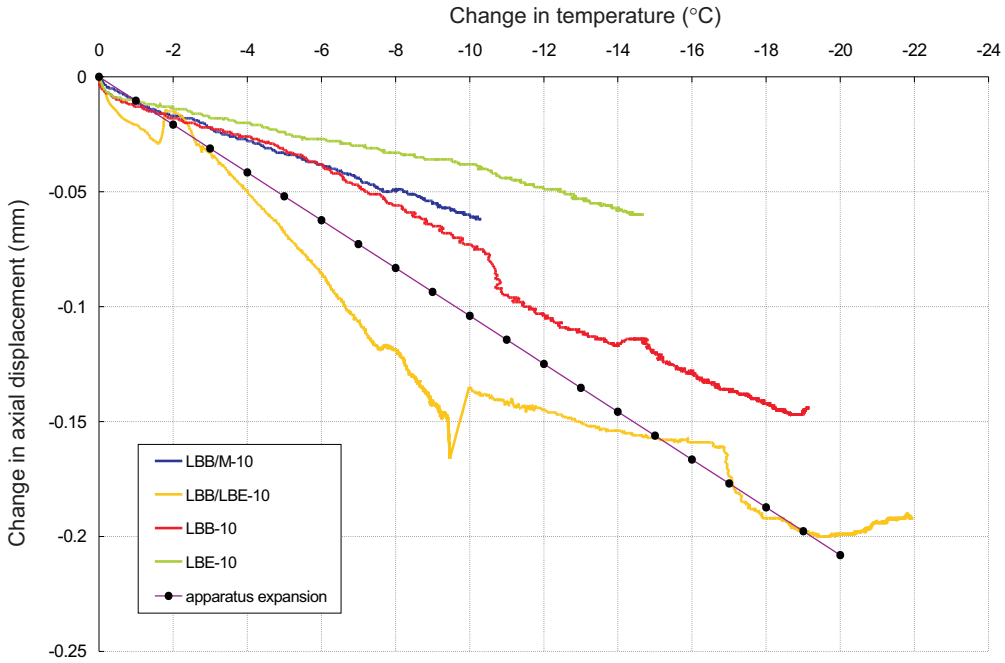

Figure 4.24: Change in axial displacement for the different sediment tests against change in temperature during the temperature drop into the hydrate stability zone. A negative change in axial displacement corresponds to an increase in height of the specimen.

From analysis of the stiffness and damping measurements above, the beginning of hydrate formation was taken to be at 10°C for each specimen. The observations that were made show that specimens LBB-10 and LBE-10 actually compress during hydrate formation, with only specimens LBB/M-10 and LBB/LBE-10 showing a very slight expansion.

4.3.2 The Effect of Different Sediment Type on Stiffness

Prior to conducting hydrate tests, four dry–dense specimens of each sediment type were formed so that baseline properties could be recorded. Figure 4.25 shows the results of these preliminary tests. It was found that the increase in grain size from LBE to LBB corresponded with an increase in V_s between the two specimens. This behaviour has been observed in the literature (Buckingham, 2005; Iwasaki & Tatsuoka, 1977). Once 10% by weight of LBE or Mica was added to the LBB specimen, V_s was seen to decrease from that of the pure LBB specimen. This decrease has also been documented in the literature (Hight et al., 1999; Lee et al., 2007; Clayton et al., 2004; Georgiannou, 2006) and can be considered due to a number of factors. Lee et al. (2007) and Hight et al. (1999) suggest that mica grains can sit in between sand grains as well as in the pores, changing the distribution of interparticle forces and thus reducing the

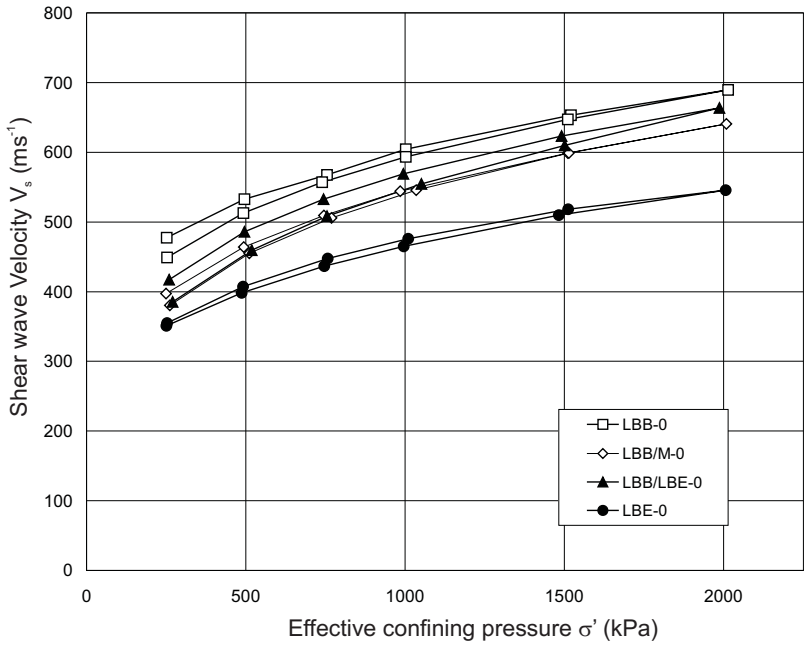

Figure 4.25: Shear wave velocity V_s against effective confining pressure σ' for different sediment tests containing no hydrate

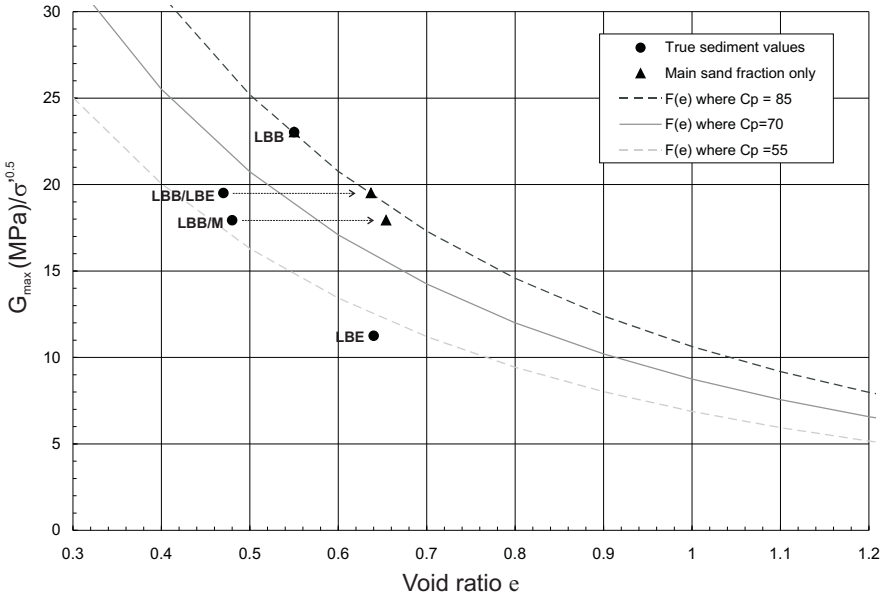

Figure 4.26: Void ratio e plotted against small strain shear modulus G_{max} for different sediment tests containing no hydrate. Normalised G_{max} for specimens LBB/LBE and LBB/M have also been plotted against void ratio of the main sand fraction. The universal void ratio function of Bui (2009) is also plotted for varying values of the particle characteristic coefficient Cp.

stiffness of a material. Georgiannou (2006) suggests that this is not the case for the inclusion of small diameter rotund particles to a larger diameter rotund sand , however results in Figure 4.25 indicate that there is some impact of the LBE on the LBB sediment. The stiffness of the different sediment baseline specimens can therefore also be considered with regard to the void ratio of the main sand fraction. Figure 4.26 plots normalised shear modulus G_{max} against void ratio for the different sediment baseline specimens (void ratio values are given in Table 3.7). Also plotted are the void ratios of the main sand fraction from specimens LBB/LBE and LBB/M. Figure 4.26 shows that the reduction in G_{max} seen in the LBB/LBE specimen is predicted by Bui's (2009) universal void ratio function when plotted against the void ratio for the main sand fraction. The reduction in V_s from specimen LBB to specimens LBB/LBE and LBB/M seen in Figure 4.25, may therefore be due to the increase in void ratio of the main load bearing sand fraction, even though the overall void ratio of the sediment is decreased by the inclusion of fines. The additional reduction in stiffness seen in specimen LBB/M may be due to the mica/sand grain interaction described by Lee et al. (2007).

It has been established in the previous section that hydrates formed by the excess gas method cement the host sediment. Taking this into consideration, certain hypotheses can be drawn as to what results to expect from the different sediment tests. If the formation of hydrate in each of the sediments was to have an equal cementing affect, one might expect the results to follow the same pattern as the baseline results in Figure 4.25. Specimen LBE-10 could be expected to show the lowest shear wave velocity, with specimen LBB-10 having the highest. However, as Priest (2004) has shown, hydrate bearing sands made using this technique are sensitive to hydrate content. The larger hydrate content of the LBB/M-10 specimen may therefore result in the highest shear wave velocity of all the specimens. Both baseline and hydrate test results have been plotted in Figure 4.27(a) for the torsional resonant column tests and Figure 4.27(b) for the flexural tests so that any connections between the results can be directly observed.

The first observation that can be made from Figure 4.27 is that the hydrate content in the pore space was sufficient to bond each type of specimen mixture, as shown by the large increase in shear and longitudinal wave velocity. To validate this observation, the relationship between wave velocity and effective stress given by Cascante (1996) in Equation 4.1 was calculated, and the values for the b exponent were found to fall to around the values obtained for the bonded sands of Priest (2004) (Table 4.6).

Although it is clear hydrate bonds the sediment mixtures, it is also apparent that it does not do so to an equal degree. The predicted distribution of velocities for the different sediment hydrate specimens suggested the LBE-10 specimen would have the smallest shear and lon-

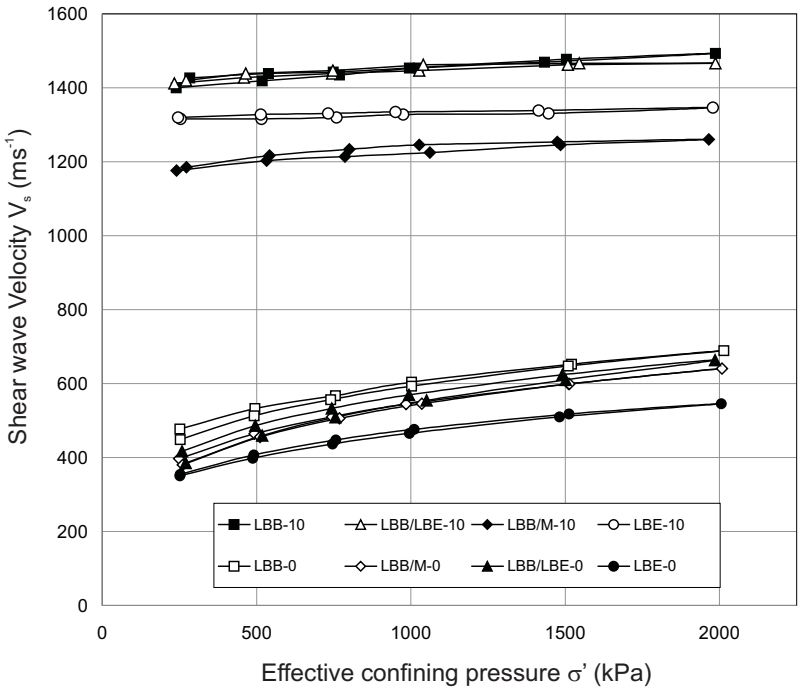

(a) Shear wave velocity V_s against effective confining pressure σ'

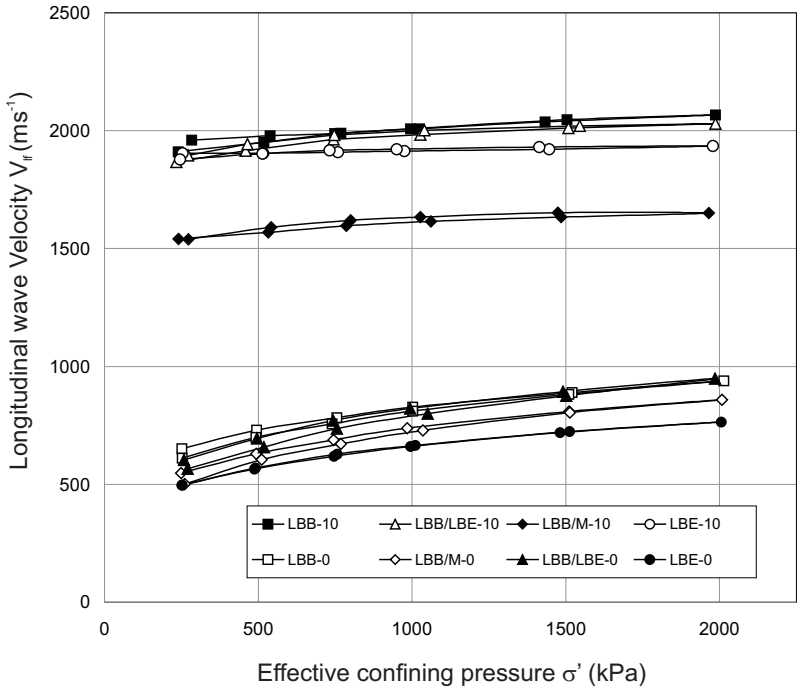

(b) Longitudinal wave velocity from flexure V_{lf} against effective confining pressure σ'

Figure 4.27: Results from torsional (a) and flexural (b) tests on all different sediment specimens

gitudinal wave velocity after hydrate formation, as the baseline tests in Figure 4.25 give this behaviour. It is clear from both Figure 4.27(a) and Figure 4.27(b), that specimen LBB/M-10 shows the smallest wave velocities when containing hydrate, even though it contains the largest hydrate content, and had a larger wave velocity than the LBE specimen in the baseline tests. Additionally, the LBB/LBE-10 specimen shows a shear wave velocity and longitudinal wave velocity from flexure that is comparable to the LBB-10 specimen, when the baseline results for the LBB/LBE sediment show it should be lower than the LBB. Two factors may be considered with regard to the interaction of the hydrate and the grains that can help explain these observations: Firstly, the impact from the change in surface area, and secondly, the interaction of coarse and fine grained particles at grain contacts.

Surface Area Effects

It has been established that in excess gas conditions, hydrates form on particle surfaces and contacts where the water resides (Section 4.2). The volume of water added to a specimen will be adsorbed on to the mineral surface and then additional water will form at the particle contacts due to capillary action between the grains. The volume of water adsorbed onto grain surfaces in the specimens is directly related to the surface area of the grains available, and to the grain surface roughness. The materials used in the different sediment tests each have a different surface area per grain. In order to estimate the total surface area in each specimen, the grains were approximated as smooth scalene ellipsoids (Clayton et al., 2008a). Although this method does not account for the additional adsorbed water due to the surface roughness of the LBE sand grains, it allows for a good approximation of the surfaces areas within the sediments to be made. The surface areas for LBB, LBE and Mica grains are therefore approximated as being 2.20 x 10^{-6}m^2, 1.52 x 10^{-8}m^2 and 1.29 x 10^{-8}m^2 respectively. By also knowing the volume of each scalene ellipsoid grain, the total surface area for the volume of material in each of the specimens could be calculated, and is given in Table 4.7.

The specimens with greater surface area, LBE-10 and LBB/M-10, appear to show slower wave velocities when hydrate is formed in the sediment. When comparing the values from Table 4.7

	A Constant		b exponent	
Specimen	V_s	V_{lf}	V_s	V_{lf}
LBB-10	1161	1548	0.0305	0.0377
LBE-10	1253	1733	0.0093	0.0149
LBB/LBE-10	1261	1504	0.0180	0.0398
LBB/M-10	1008	1274	0.0266	0.034

Table 4.6: Values for the A constant and b exponent for the different sediment hydrate specimens.

Specimen	Surface area per m^3 of material (m^2)	Surface area of grains in specimen (m^2)
LBB-10	8 x10^3	2.75
LBE-10	112 x10^3	33.83
LBB/LBE-10	18 x10^3	6.85
LBB/M-10	124 x10^3	42.07

Table 4.7: Estimated surface areas for each specimen, calculated using the formulae by Thomsen (2004) for the surface area of scalene ellipsoids

with the results in Figure 4.27, it seems that the specimens with the smallest surface area, LBB-10 and LBB/LBE-10, correspond to the specimens that show the largest shear and longitudinal wave velocities when hydrate is formed.

Priest et al. (2005) showed that the seismic velocity for LBE sand, increased with increasing quantities of hydrate in the pore space, due to the increase in quantity of a bonding material at particle contacts. The change in grain surface area seen in the different sediment specimens from LBB-10 to LBB/M-10 means more water is required to cover the grain surfaces, and so less water will reside at grain contacts. Less water at grain contacts means less cement bonding the particles, and so a slower shear and longitudinal wave velocity.

This hypothesis can be investigated by considering the volume of water bound to grain surfaces. Olhoeft (1976) suggests that 7–8 monolayers of water, each 10^{-8}m thick, are bound to silica surfaces in partially saturated rocks. If this value is taken as an average for the grains in our specimens, the volume of water bound on grain surfaces can be calculated. Considering the initial volume of water added to each specimen, the percentage of that water bound to surfaces, for each specimen, is 0.9% for LBB-10; 2.6% for LBB/LBE-10; 10.3% for LBE-10; and 13.4% for LBB/M-10. These values show that the specimens with the smallest surface areas have more water available for bonding at particle contacts than the specimens with a high surface area.

The differences in seismic velocities for each specimen however, is not so great as would be suggested by the calculated differences in surface area. Longitudinal wave velocity from flexure results (Figure 4.27(b)) show specimen LBB/M-10 as having the slowest velocity, but the remaining specimens have longitudinal wave velocities at a similar value. The surface area hypothesis predicts a larger distinction between the results. Therefore, there must be another factor controlling how hydrate affects the sediment mixtures.

Sediment Grain and Hydrate Interaction

With material mixes such as those tested here, it is also necessary to consider the direct effect of

the range of grain sizes and shapes in each specimen. Research into mixes of granular and platy materials shows that the stiffness of a rotund sand changes with the inclusion of fines (Hight et al., 1999; Lee et al., 2007; Clayton et al., 2004; Georgiannou, 2006) as discussed previously in this section. The low shear and longitudinal wave velocities for specimen LBB/M-10 may be due to a combination of the interaction of the LBB and mica particles and the large surface area of grains inside the specimen. The inclusion of 10% by weight mica to an LBB sediment increases the void ratio of the main sand fraction, so that the load bearing frame of the sediment is in a loose state (see Table 3.8). The large surface area of the mica grains, and the spread of hydrate cement over each grain surface, means that the proportion of cement at the LBB contacts is reduced. Coupled with the initial loose state of the LBB load bearing frame, bonding is not as effective in specimen LBB/M-10 than in the other different sediment specimens, and results in specimen LBB/M-10 showing the lowest shear and longitudinal wave velocity results.

The addition of small diameter rotund particles to a clean sand of a larger grain size, has less effect on seismic velocity than the introduction of mica, but still alters bulk properties. Although the majority of the LBE grains may sit in the pore space and do not interact with the LBB grains (Georgiannou, 2006), the addition of LBE to LBB does appear to increase the void ratio of the main sand fraction, creating a medium–dense load bearing frame (Table 3.8). Figure 4.27 shows that the addition of gas hydrate to the LBB/LBE specimen, gives the same shear and longitudinal velocities as the hydrate bearing LBB specimen. As the baseline LBB/LBE specimen had a lower velocity than the LBB dry dense specimen, it appears to give the largest increase in seismic velocity of all the materials tested. This increased bonding affect may be due to the interaction of the hydrate cement with the LBE grains. Cement and concrete research shows that pore filling inclusions to cement mixes increases the cohesive characteristics of concrete (Murdock et al., 1991; Neville, 1995). This can be due to an increased number of nucleation and bonding points, or the inclusion of a solid material in the compliant hydrate cement.

4.3.3 The Effect of Different Sediment Type on Attenuation

Attenuation in the different sediment specimens was found through the free vibration decay method described in Section 3.2.1. Figures 4.28 gives the shear wave and longitudinal wave from flexure attenuation (Q_s^{-1} and Q_{lf}^{-1} respectively) found for all the different sediment tests against effective confining pressure. As in the excess water tests, the attenuation values decrease slightly with effective confining pressure, but overall the attenuation can be considered to be constant throughout the load cycle. Figure 4.29 plots the attenuation values for the dif-

ferent sediment tests in more detail, with reference to each sediment type. The plot shows that the inclusion of 10% hydrate in the sediment mixtures does not have a significant impact on the attenuation values from the control tests (dry dense specimens), which agrees with the attenuation results from Priest (2004) where the same formation technique was used. Priest obtained shear wave and longitudinal wave from flexure attenuation values of around 0.015 for LBE sand containing 10% hydrate content, a value which was also found for the LBE-10 specimen in this research. In all specimens, the attenuation increases from the dry dense state to the hydrate filled state, although to different degrees in each sediment type. No discernable pattern can be distinguished from this increase of attenuation when hydrate is included, however the low value, similar to that of Priest's (2004), agrees with the assumption that hydrate is bonding each different sediment specimen.

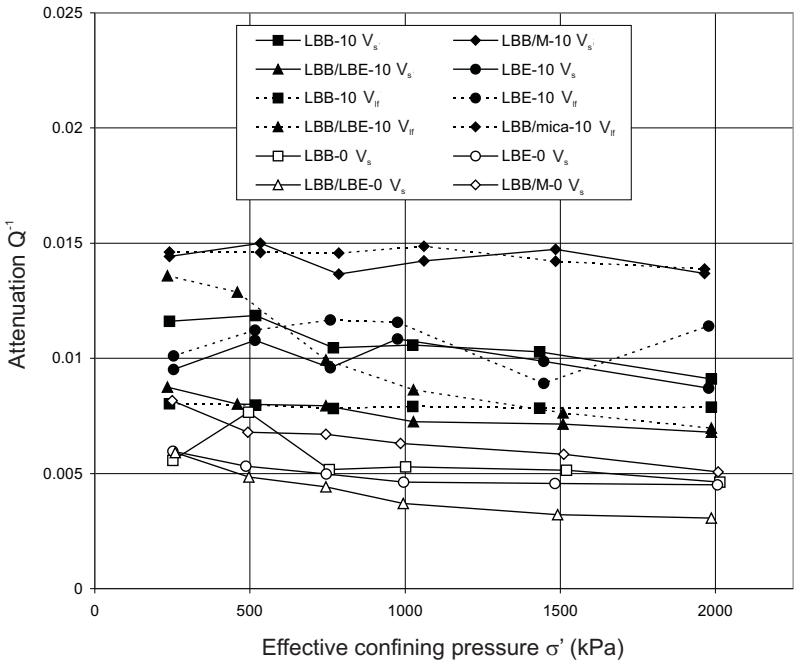

Figure 4.28: Shear and longitundinal wave attenuation Q^{-1} plotted against effective confining pressure σ' for all different sediment tests through the load cycle

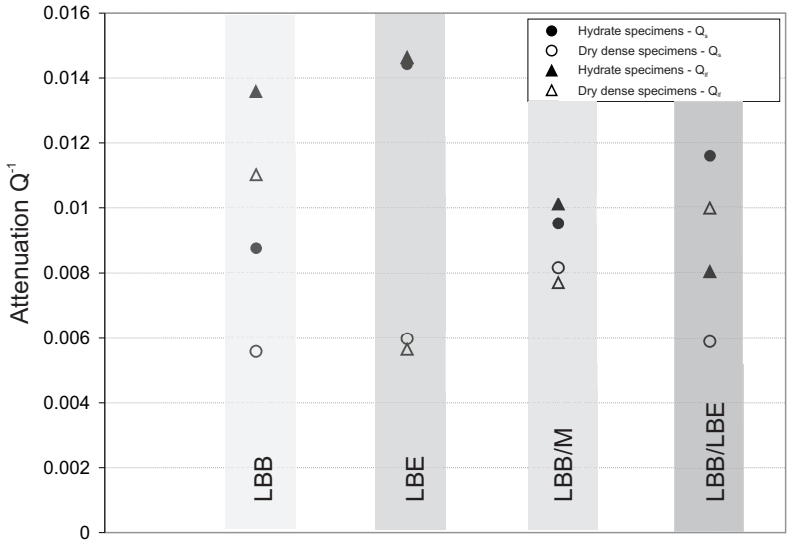

Figure 4.29: Shear and longitundinal wave attenuation Q^{-1} of all different sediment tests compared against dry dense specimens containing no hydrate.

Chapter 5

TESTS ON NATURAL HYDRATE SAMPLES

5.1 Introduction

Five core sections from the Indian National Gas Hydrate Program (NGHP) 01 expedition were supplied to the University of Southampton with the object of determining some dynamic geophysical properties of the hydrate bearing sediment. This chapter describes the processing of these cores through various stages of investigation into their properties, beginning with visual documentation of the morphology of the hydrate in the core sections, followed by attempts to test the samples in the GHRC, and finally the geotechnical analysis of the host sediment.

5.1.1 Sample Origin

The samples provided for testing were recovered from the Krishna–Godavari Basin, on the eastern margin of the Indian peninsula (Figure 5.1). The eastern margin of India is a passive continental margin, with a high rate of sediment deposition due to the Ganges–Brahmaputra river system draining into the Bay of Bengal and creating the Bengal Fan. This large sediment accumulation has a maximum thickness of 22km on the Bangladesh shelf, and is responsible for 8–10km of sediment located in the Krishna–Godavari basin. Modern deposits into the basin are dominated by input from the Godavari River, and so the sediments that were drilled in the basin during NGHP-1 were mainly clays with well defined sand horizons (Collett et al., 2008).

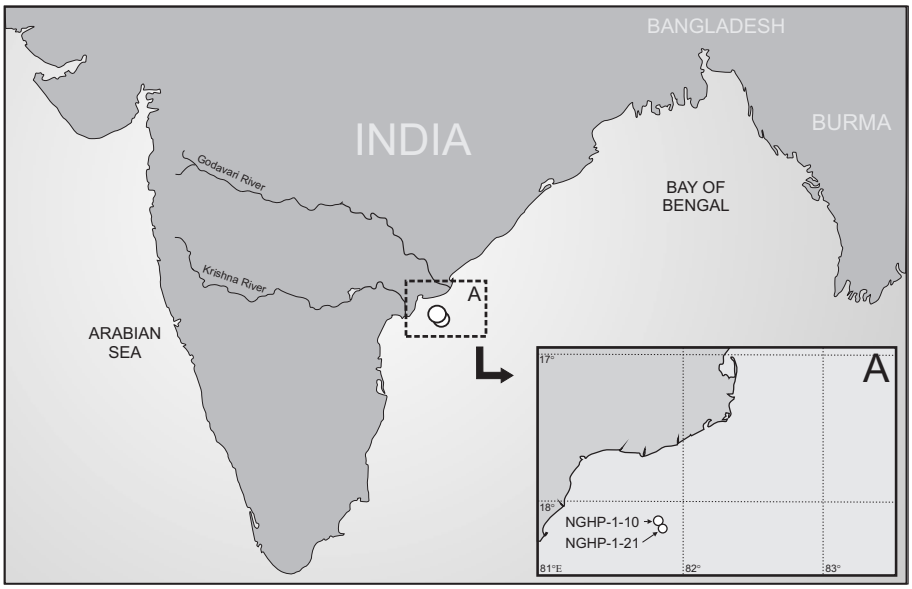

Figure 5.1: Location of the NGHP-1-10 and -21 drill sites (Collett et al., 2008).

Of the five core sections supplied to Southampton, four came from a single core drilled at site NGHP-1-10B, with a further section taken from a core drilled at site NGHP-1-21C. Both sites were in a water depth of 1049m with site NGHP-1-21C offset approximately 20m SE from hole NGHP-1-10B. The section cored from site NGHP-1-10B was taken using a Fugro pressure corer (FPC), which is capable of recovering a 1m core with a diameter of 57mm (Francis, 2001). Core NGHP-1-10B-08Y comprised of 86cm of sediment taken from 50.1m below sea floor (mbsf), which was sub–sectioned into 20cm lengths for testing. The section of core from site 21C was retrieved with a HYACINTH rotary corer (Francis, 2001), which can take a core of sediment approximately 1m in length and 51mm in diameter. Core NGHP-1-21C-02E consisted of 110cm of sediment from 56.5mbsf, of which the section from 23–46cm was taken for testing at Southampton. Both cores were taken from horizons identified as gas hydrate rich from LWD (logging whilst drilling) data. In the case of NGHP-1-10B, no BSR had been observed in the seismic data, however LWD showed extremely high electrical resistivities that were attributed to hydrate accumulation (Collett et al., 2008).

The sediments recovered at sites NGHP-1-10B and NGHP-1-21C show a similar lithology due to their close proximity. The sections supplied to Southampton were described as coming from sediments composed primarily of clays and silty clays with varying amounts of microscopic authigenic carbonate. Through analysis of the cyclicity of the stratigraphy, and the lack of certain nannoplankton species, the age of the sediment is considered Quaternary to recent (Collett et al., 2008).

5.1.2 Sample Management

Once cores NGHP-1-10B-08Y and NGHP-1-21C-02E had been recovered to the surface, each core was subjected to non–destructive analysis via the Multi Sensor Core Logger – Pressure (MSCL-P) (Schultheiss et al., 2008) prior to being sent to Southampton. Gamma density and P–wave velocity were obtained for each core, as well as some X–ray images. The cores were then transferred under pressure to Singapore, where further measurements in the MSCL-P were taken along with an X–ray computed tomography scan of each core length, conducted using a 16–slice Phillips Mx8000 (voxel resolution of approximately 0.5mm). Once scanned, the cores were rapidly depressurised and sectioned before being wrapped in aluminium foil, placed in a canvas bag and submerged into liquid nitrogen. The cores were exposed to atmospheric pressure for no longer than 90 seconds prior to being frozen (Collett et al., 2008).

5.1.3 Programme for Testing NGHP-1 Samples

Following the delivery of the core sections to Southampton, a programme was developed so as to optimize the collection of data from the natural hydrate samples. Seven stages were scheduled for the total investigation:

1. Visual observation of the geometry, persistance and orientation of the hydrate inside the samples, through X–ray computed tomography. Hydrate content and disturbance of the samples was assessed at this stage.
2. Documentation of the state of the frozen samples by standard photographic methods, following the removal of the plastic core liners.
3. Resonant column testing of the best preserved specimen in the GHRC following analysis of CT scans and photographic observations.
4. Selection of small sub–samples of frozen core (preferably containing no hydrate) for moisture content, organic content and salinity testing.
5. The unfreezing of the core sections and the collection of the subsequent gases.
6. Imaging of sub–samples via scanning electron microscopy.
7. Geotechnical analysis of the host sediment properties including particle size distribution, moisture content, plasticity and triaxial shear strength testing.

By comparison with the early data obtained from the cores whilst at *in–situ* pressures, it was hoped that this sequence of testing would provide valuable information on the effect of hydrate

on natural fine grained sediments. The CT scanning of the core sections before and after depressurisation and freezing also gave the opportunity to evaluate the methods of natural hydrate sample handling and storage.

5.2 X–Ray Computed Tomography Scans of Natural Hydrate Samples

X–ray computed tomography (CT) is a non–destructive radiographic method that allows for analysis of planar and volumetric structures in three dimensions (ASTM-E1441-00). The principle of the technique is to take a number of two dimensional X–ray images through an object at different rotation angles. CT software can then compile the 2D images to produce a 3D volume showing the internal structure of the object. The main advantage in CT scanning is the quantitative densitometric (density and geometry) measurements that can be obtained for slices of an object. In the case of gas hydrate bearing sediments, CT scanning allows internal hydrate morphology to be observed, and hydrate volume quantified, without destruction of the sample.

5.2.1 Methodology for X–ray and Photographic Imaging of Frozen Cores

The process of a CT scan requires the sample to be removed from liquid nitrogen and exposed to room temperatures for an extended time. To investigate the temperature increase experienced by a frozen sample when left at room temperature, a number of representative clay core specimens were manufactured. The first of these specimens was submerged in liquid nitrogen for 24 hours before being removed and placed on the worktop at a room temperature of $20°\mathrm{C}$ without any insulation. Temperature change on the outside edge of the specimen was then measured and showed an increase from $-145°\mathrm{C}$ to $-25°\mathrm{C}$ over a 50 minute period. A second frozen specimen was then removed from liquid nitrogen and placed in a cylindrical polystyrene container, measuring 250mm in height, with walls 30mm thick. The temperature was measured once again on the outside edge of the specimen. The recorded temperature change showed an increase from $-155°\mathrm{C}$ to $-107°\mathrm{C}$ in 50 minutes, with the temperature of the specimen reaching $-62°\mathrm{C}$ in 130 minutes. The degree of specimen warming inside the polystyrene container was considered low enough to limit gas hydrate dissociation over a period of 2 hours. The containers would therefore be used as a vessel to hold the NGHP core sections whilst CT scans were conducted, with the time for a full scan of the specimens limited to a time period of two hours (see below).

Apparatus

The X–ray CT equipment at the University of Southampton is an X–tek Benchtop CT 160Xi. It uses a 160kV, 60 Watt microfocus X–ray source and a CMOS flat panel detector (1248x1248 pixels) with a maximum scan area of 100mm by 100mm. The X–tek apparatus also has a movable stage that allows for different size objects to be scanned, with an ultimate resolution of 5μm for small objects of 5mm maximum width. Due to the width of the cores, resolution achieved for the NGHP-1 core sections gave a pixel size of 80μm. As the maximum height of the scannable area is 100mm, the NGHP-1 core sections required the top and bottom of samples to be scanned separately.

Resolution and scan quality in the X–tek equipment also depends on the imaging conditions. For one scan, the number of rotation steps must be set, with a maximum of 1800 steps in the full 360°C rotation giving the best resolution. For each rotation step, the exposure time for the X–ray shot (up to 2ms), as well as the number of shots taken at that step (up to 4 shots) will also increase the quality of the scan. If all settings were at a maximum, a single CT scan could therefore take up to four hours to complete.

In order to limit the scan time of each NGHP-1 sample but also maximise resolution and scan quality, the number of rotation steps was set to 901, and only one shot at each step (with an exposure time of 2ms) was taken. These settings reduced the scan time to approximately one hour, so that total time for the samples to be out of liquid nitrogen did not exceed two hours.

Post–Scan Photographic Documentation

Once each core section had been scanned in the X–Tek machine, the plastic core liners could be removed so as to photograph the cores in their frozen state. After scanning, the samples were once again immersed in liquid nitrogen for a minimum of 24hrs. They were then removed and the plastic liners were sliced down each side, using an electric disc cutter, taking care to avoid disturbing the core section inside. At this point, each sample was photographed at laboratory temperatures before being placed back into liquid nitrogen. The total time samples spent out of liquid nitrogen was kept under 5 minutes so as to minimise hydrate dissociation. From previous investigations, the sample temperature would not have risen to above -100°C in these 5 minutes.

5.2.2 Imaging Results

Each of the core sections were scanned in two sections, barring section NGHP-1-10B-08Y 26-66cm, where only 100mm of core had been retained in the plastic liner, and so did not necessitate two scans to image the entire length. Figure 5.2 gives a comparison of the X–rays taken during the NGHP-1 cruise and those taken in Southampton. An X–ray image shows density difference across an object, with areas of low density giving the least absorption and the lightest colour. The X–Tek scans show large regions of white in each core, which refer to large voided areas. The on board X–ray scans show none of these voided areas as they were taken on the cores whilst still at *in–situ* pressures.

Although X-ray images were obtained for all 9 core sub–sections, three dimensional reconstruction of the cores could not take place for the sections NGHP-1-10B-08Y 26-46cm and 66-86cm: top.

Reconstructed CT Scan Images

Figure 5.3 shows two images of the core NGHP-1-10B-08Y section 46–66cm, that were reconstructed from CT scans. Figure 5.3(a) gives an external view of the core, and does not highlight the hydrate and void features present in the section. Even without this emphasis however, the difference in density (grayscale value) of hydrate and sediment clearly shows the hydrate veins in this view, with a thick hydrate vein evident down the right–hand–side of the core section.

In order to better visualise hydrate distribution, and to allow for quantification of the volume of hydrate in the core sections, the hydrate was "segmented" out of the reconstruction. The process of segmentation allows the user to highlight a band of grayscale values that represent features in a reconstructed volume of a particular density. The higher the density, the lighter the grayscale values become. Although actual density values are unobtainable from these particular scans, hydrate shows up as darker features inside the lighter sediment due to it's lower density, and so can be segmented. Figure 5.3(b) shows an image of the same core shown in (a) (although at a slightly different orientation) with the voids removed, and the hydrate highlighted in white. The sediment has also been darkened to emphasise the hydrate.

During segmentation of the hydrate in the 3D reconstruction, it was found that a thin layer of several pixels thick was highlighted around the edges of the voids. There are two possibilities for these regions, which were observed in all core sections surrounding voids. Firstly, it may be evidence of post–depressurisation hydrate formation that occurred during specimen storage

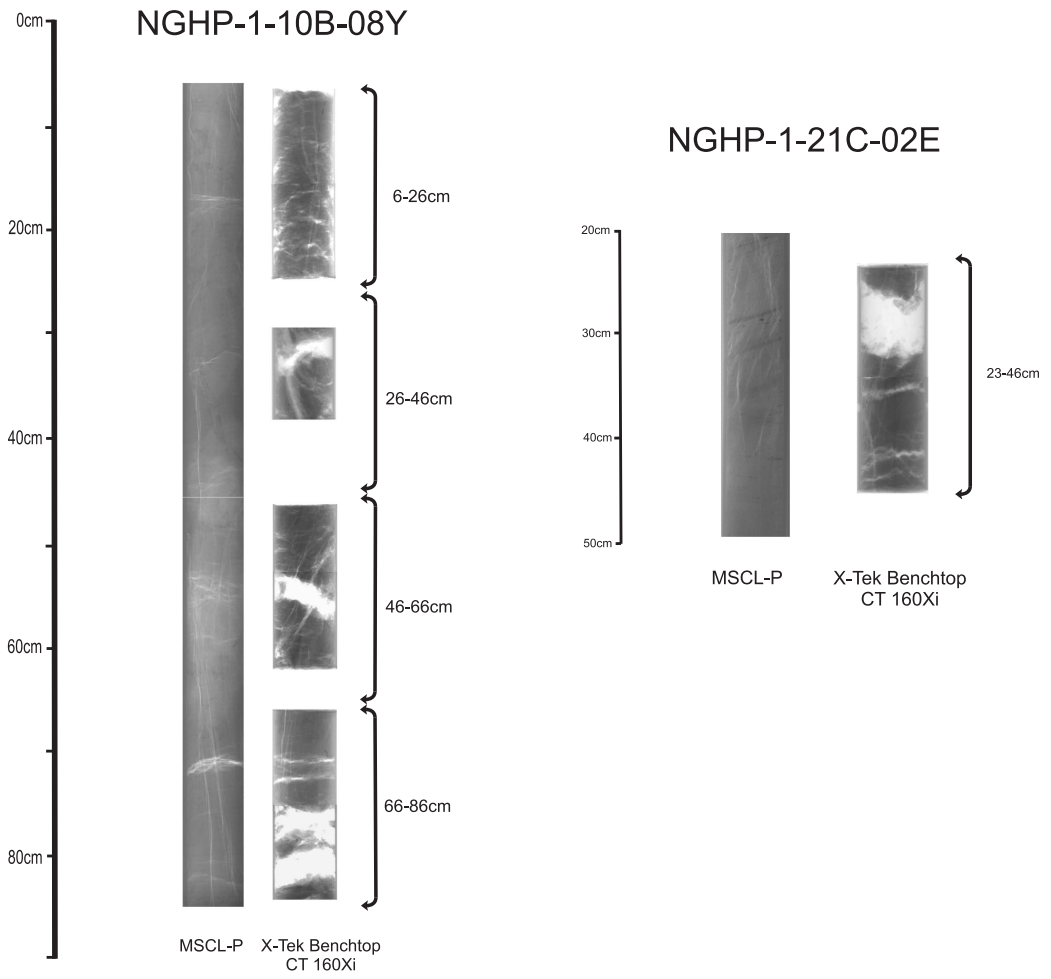

Figure 5.2: A comparison of single shot X-ray images of cores NGHP-1-10B-08Y and NGHP-1-21C-02E taken by the expedition scientific party inside a Geotek Multisensor Core Logger – Pressure (MSCL-P), and the author using a X-Tek Benchtop CT 160Xi scanner.

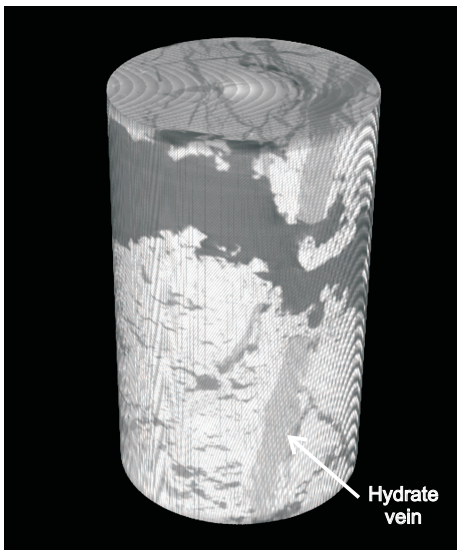

(a) Image of initial CT reconstruction, with no colouring to highlight internal features. Voids can be identified as the darkest regions, as they shown the lowest density, with the sediment the palest as it has the highest density. A vein of hydrate can be seen down the RHS of the section.

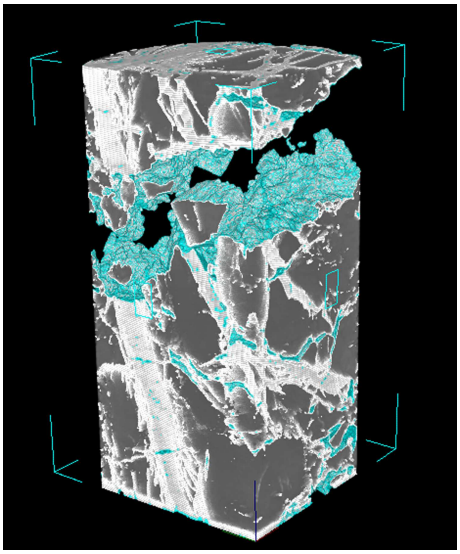

(b) Image of the core section with the hydrate highlighted in white. The blue colour depicts the areas bordering the voids, and may be ice rather than hydrate. The image has been cut away on two sides so that the hydrate structure can be observed clearly.

Figure 5.3: 3D CT images of core section NGHP-1-10B-08Y 46-66cm: bottom.

in liquid nitrogen. Rapid hydrate formation could have occurred on the wet surface of the sediment when methane was driven out of solution from the pressure drop. The second possibility is that the region represents the formation of frost onto the surface of the core during the CT scanning process. Ice and hydrate have a similar density such that segmentation of a certain band of grayscale values may highlight ice as well as hydrate. The formation of frost was observed on the core sections when they were digitally photographed after the CT scanning, and so it is assumed that this is the cause of the "halo" regions around the voids. It was also found that these regions could be distinguished from the rest of the hydrate by segmenting a darker grayscale value (shown in blue in Figure 5.3(b)).

Further 3D reconstructions of some of the cores sections can be found in Appendix B.

Images of Frozen Core Sections

Figure 5.4 shows one of the digital photographs that were taken of the frozen core sections after CT scanning. The particular core section shown in this figure is the portion from 66–86cm from the top of core NGHP-1-10B-08Y. The image shows that the section has been considerably disrupted. Voids varying in size from approximately 0.2cm to 2cm depth are

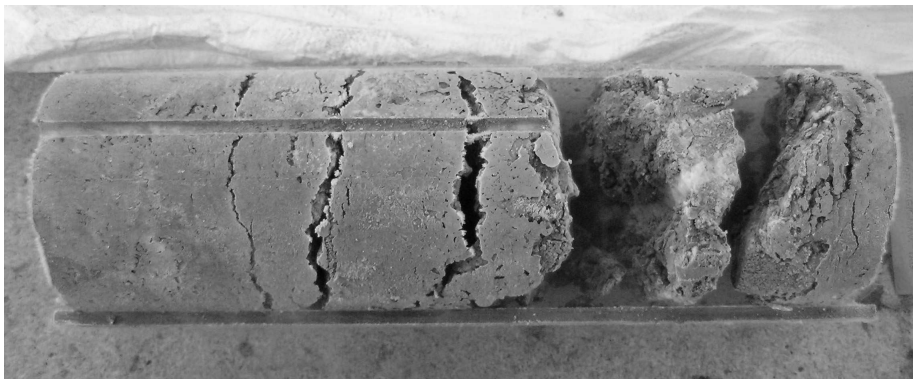

Figure 5.4: Photograph of core NGHP-1-10B-08Y, section 66-86cm after being removed from the core liner. The horizontal line running along the length of the core was made by the disc blade when cutting away the plastic liner.

evident throughout the section, with the two largest voids displacing the core so that it is no longer a complete section. In addition, each of the core sections show extensive voids over each of the section surfaces. Digital images of all the core sections can be found in Appendix B.

5.2.3 Observations From Digital and CT imaging

The preliminary X-ray scans and visual observations made on the boat immediately after pressurised core recovery during cruise NGHP-1 provided an insight into the morphology of the gas hydrate in the sediments of sites 10 and 21 even before analysis of detailed CT scans. The gas hydrate was identified in cores NGHP-1-10B-08Y and NGHP-1-21C-02E to be in the form of nodules, discrete horizontal veins, and thin, wispy subvertical to vertical hydrate structures (Collett et al., 2008; Holland et al., 2008). It was also described to be "grain displacing", a term used to define hydrate that does not form in the pore spaces of a sediment, but forces grains apart forming veins, layers and lenses of pure gas hydrate (Holland et al., 2008).

Initial study of the three dimensional CT reconstructions appears to confirm the statements made by the NGHP-1 scientific party. Each core shows hydrate in the form of discrete subvertical veins, varying in thickness between 7mm and less than 0.5mm. The high resolution of CT scanning obtained by the X-Tek equipment means that the geometry and volume of these hydrate veins can be analysed, and any potential preference in vein orientation detected.

The horizontal veins described by the NGHP-1 crew cannot be seen in the CT scanned samples, but may have been lost during the transfer of the samples to liquid nitrogen. The disturbance

seen in the core samples will be discussed at the end of this section.

Hydrate Geometry

The computed tomography data from each core section was manipulated using the Volume Graphics software VGStudio MAX. Orientation and dimensional data was collected on individual hydrate veins by analysing two dimensional slices of the 3D volume. Figure 5.5 shows the process by which orientation data was determined.

As the core sections were delivered from the NGHP-1 cruise without any reference to original orientation in the ground nor to how they relate to each other, dimensional analysis can only be made on each core section individually. Although this does not allow for conclusions to be drawn across the whole core, any patterns in vein orientation and dip may still be highlighted. Measurements on each core section were therefore taken with respect to *x,y,z* coordinates displayed by the Volume Graphics software, with the *y* axis direction indicating "North" (Figure 5.5(a)). Once a point of reference was established, slices through the core at 45° intervals were taken from 0° through to 360°. Axial slices at regular intervals were then taken throughout the section. At each axial slice, orientation of the major veins was recorded as a strike between 0 to 180°. To obtain the corresponding dip of the veins, the predominant strike direction at each axial slice was determined and the frontal slice that would give the best true dip was chosen (Figures 5.5(b) and 5.5(c)). These two sets of readings can then be displayed on a histogram to show the predominant dips and strikes of the veins.

NGHP-1-21C-02E 23-46cm This core section was scanned in two sections. After initial scanning it was found that the bottom section was 69% void space. Vein orientation measurements were therefore not conducted on this part of the section. All geometry information described here was therefore taken from the top portion. The veins observed in this core section had a thickness of 1.5mm or less. No thick veins were present, however, there was an abundance of the fine veins throughout the measured core section. Some of the detected veins had a thickness of less than 0.5mm. Visual observation of the 3D volume show a predominant orientation of the veins running in a N-S and NW-SE direction. Histogram data (Figure 5.6) confirms these observations, with the most abundant strike orientations between 0° and 20°. Histogram dip data shows that the majority of the veins in this section are at a dip between 65° and 90°.

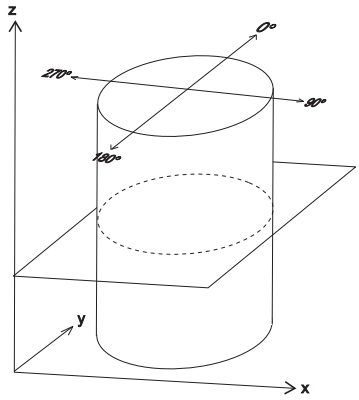

(a) Diagram illustrating the orientation of the core sections and the determination of dip and strike direction relative to each core.

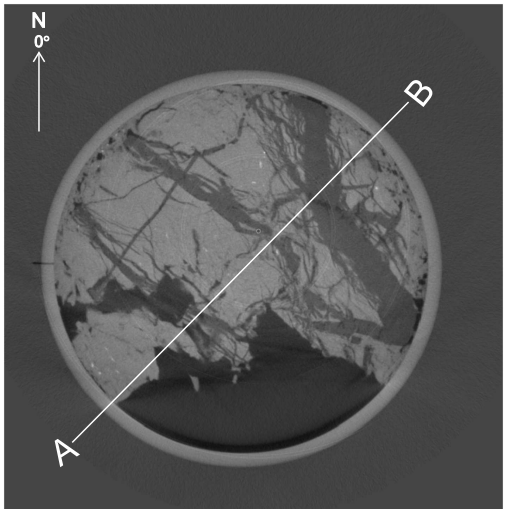

(b) An axial *x,y* slice (number 996) through core section NGHP-1-10B-08Y 46-66cm:top. The north arrow indicates 0° orientation.

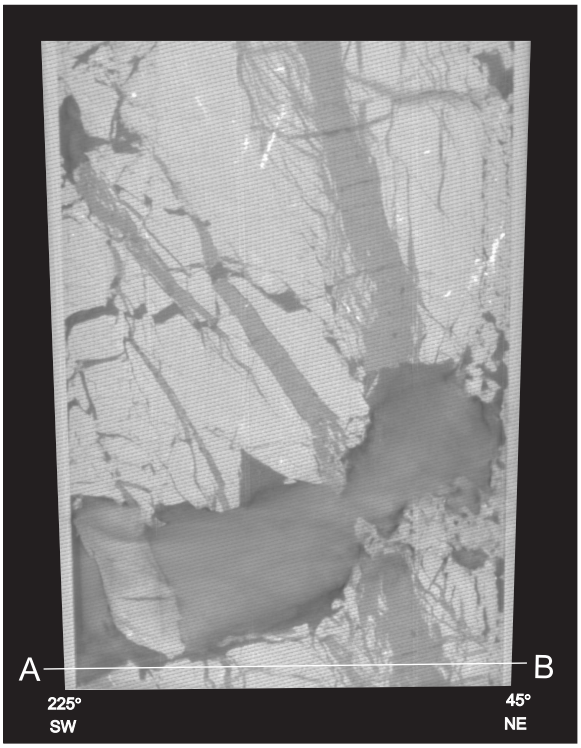

(c) A frontal *x,y,z* slice corresponding to the axial slice above, taken at line A-B.

Figure 5.5: Process of obtaining the hydrate vein orientation data.

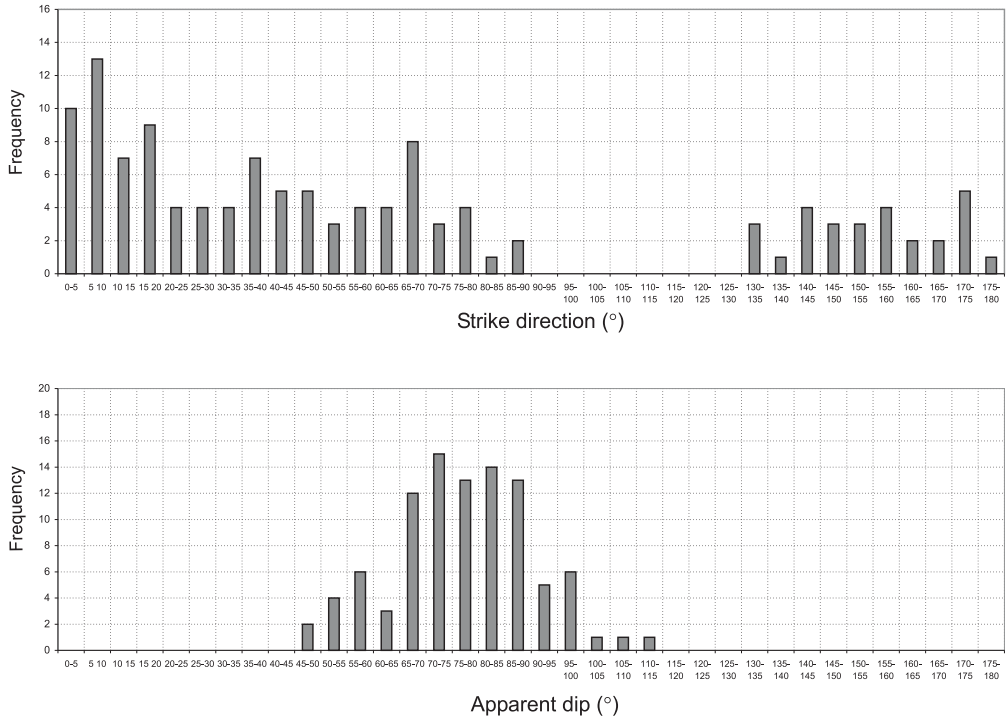

Figure 5.6: Accumulated data of strike direction and apparent dip for all slices of core section NGHP-1-21C-02E 23-46cm:top

NGHP-1-10B-08Y 6-26cm Both the top and bottom of this core section were scanned successfully and found to have few voided portions. Visual observation of the top of the section showed that there were very few veins running through the core, with only one large vein persistent along the length of the core. The dominant dip of this vein was found to be 80°, with an approximate dip direction of 135° and average thickness of 2.5mm. As no axial slices were recovered for this section, further orientation analysis was not possible. Subsequently, orientation data was taken mainly from the bottom portion of the core section. The bottom part also showed veins with a thickness of 2.5mm or more, with one particular vein fattening to a maximum of 4mm near the base of the section. These large veins showed a high dip, between 70 and 90°. In addition, a number of smaller fibrous veins branched off from the main veins in places. Figure 5.7 gives the orientation and apparent dip for all the veins in the bottom section of this core. Once again, the dips cluster between 55 and 90°, with the orientations showing a tendency toward 130 to 150° and 15 to 45°.

The small portion of core NGHP-1-10B-08Y 26-46cm that remained was successfully scanned, and although contained a voided portion, had still maintained enough hydrate volume for anal-

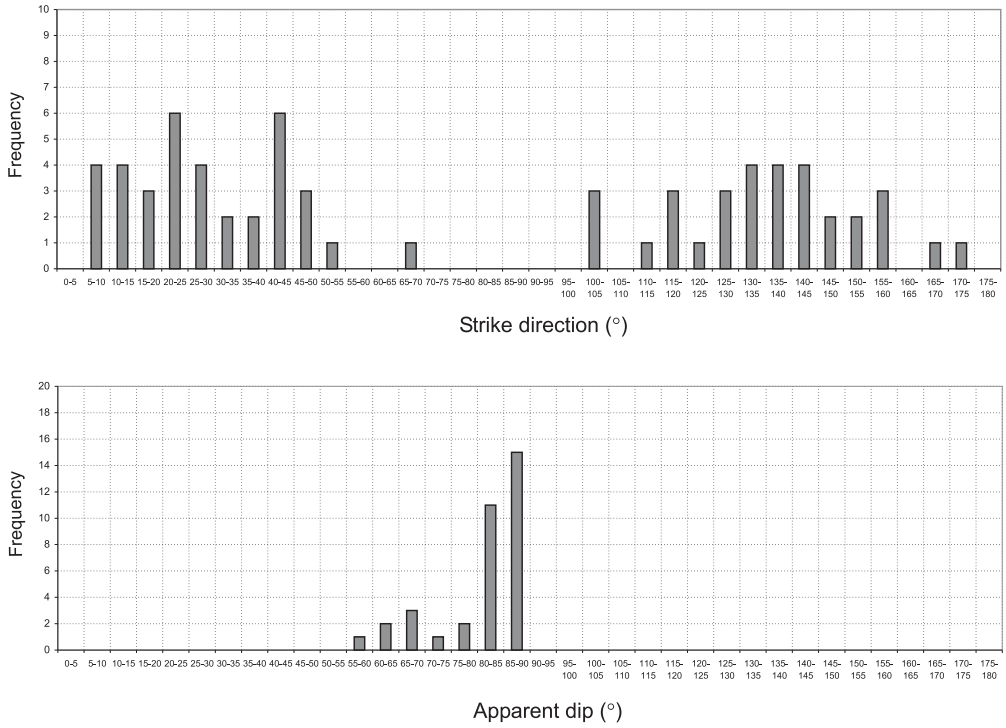

Figure 5.7: Accumulated data of strike direction and apparent dip for all slices of core section NGHP-1-10B-08Y 6-26cm:bottom

ysis. This dataset was lost however before any orientation information could be taken, and so is not included in this stage of analysis.

NGHP-1-10B-08Y 46-66cm This core section was successfully scanned and both top and bottom portions analysed. It was found that one major vein (between 4 and 6mm thickness) dominated the top core section and also appeared in the bottom part, passing through one corner before being cut off by the core liner. The vein did not have finite edges, but split into fibrous sub-millimetre veins that persisted for 10-20mm once broken away from the main vein structure. Some of these microveins also joined back onto the main vein. These fibrous microveins can be observed in both the axial and frontal slices. Additional to the major vein, another large vein (average 2.5mm thickness) could be seen in the centre of the section, but lensed towards the top of the core with a maximum length of 45mm. Apart from the two major vein structures described, there were few individual smaller veins present in the top portion of the section. Figure 5.8 shows the plot of the major vein apparent dip and strike orientation for the top portion of section 46-66cm. It appears that the majority of the dips recorded are a little

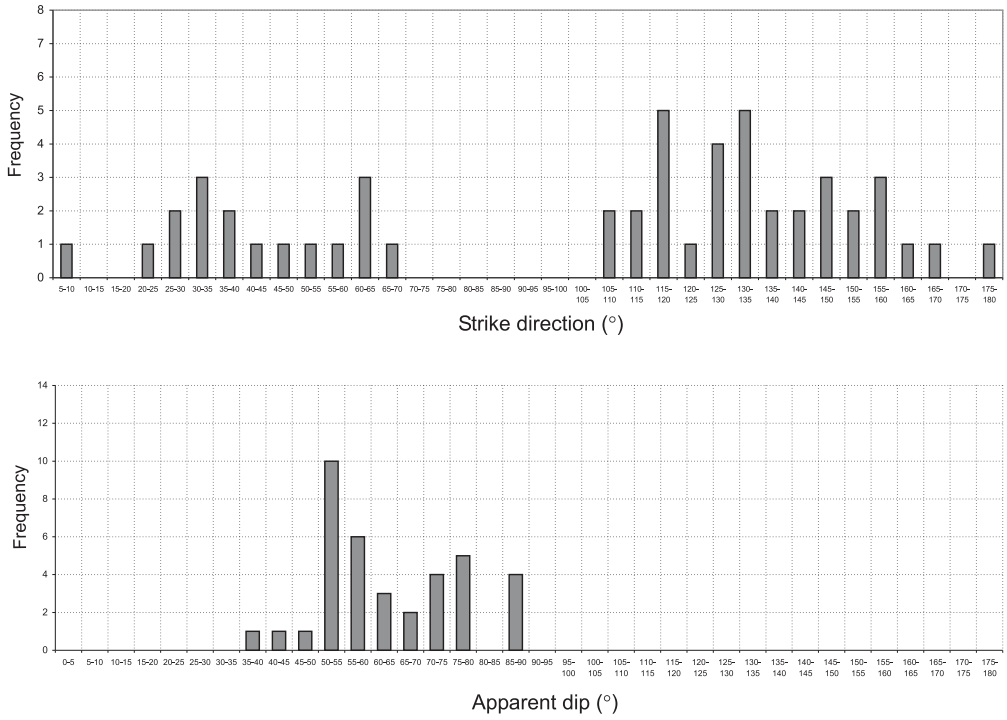

Figure 5.8: Accumulated data of strike direction and apparent dip for all slices of core section NGHP-1-10B-08Y 46-66cm:top

less than seen in the previous core sections, mostly tending between 50 and 80°. The largest of the veins had a strike orientation of 115 to 140°, with the majority of the other veins showing a similar trend.

The bottom portion of core section NGHP-1-10B-08Y 46-66cm overlapped the top portion where the major void running through this section could be seen. As mentioned above, the largest vein from the top portion was observed in the top corner, and showed the same orientation and dip as recorded for it above. There was also another large lenticular vein prominent in this portion, with a maximum thickness of 4.5mm near the base of the portion. As the vein lenses into the centre of the section, the end splits into thin fibrous veins approximately 1mm thick, that continue through the sediment until they are truncated by the major void. Again, aside from the two thick veins, smaller veins were prevalent in this part of the core. Histogram data in Figure 5.9 shows a similar dip pattern to the top portion, with dips clustering between 45 and 75°. Unfortunately, due to the different original orientation of the top and bottom sections when scanned, the two datasets cannot be directly combined, however, a dominant strike orientation of 10 to 50° can be identified for the bottom portion.

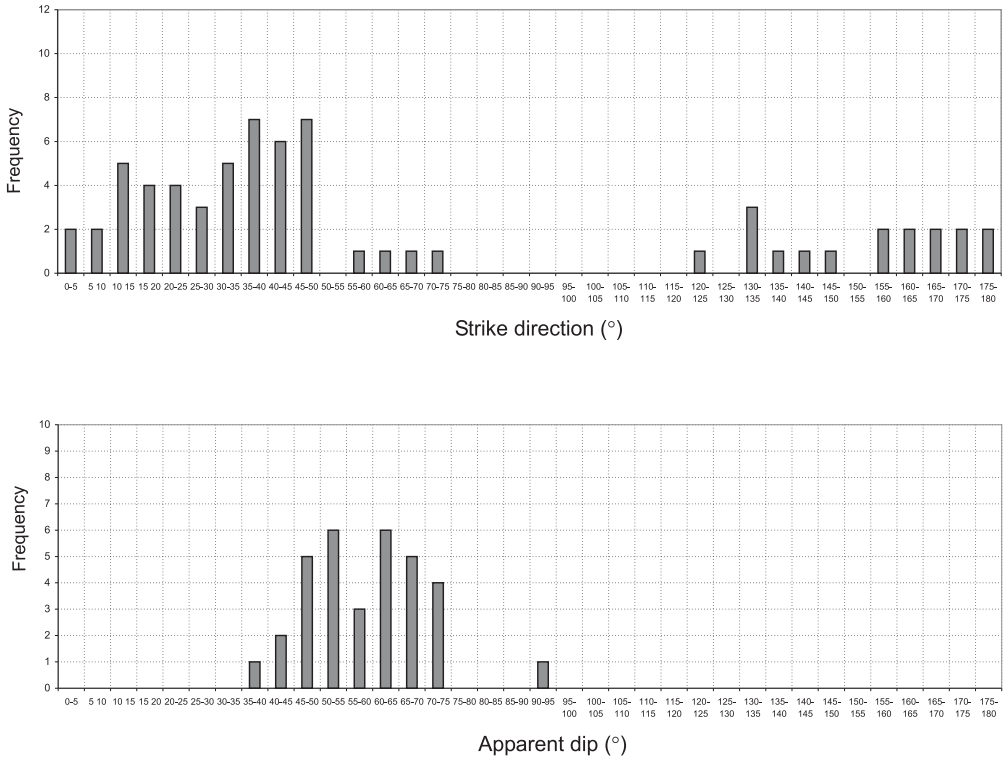

Figure 5.9: Accumulated data of strike direction and apparent dip for all slices of core section NGHP-1-10B-08Y 46-66cm:bottom

Stereonet Analysis

Once the general strike orientation and apparent dip had been recorded for each core section, it was found that a number of individual veins could be recognised in both frontal and axial slices for a few of the core sections. From these veins, true dip and strike information could be taken and the poles to these planes plotted on an equal–area lower–hemisphere projection to identify any potential patterns to the hydrate vein growth in the NGHP-1 core samples. A total of 4 readings could be taken from the 6-26cm section, which was not enough to be significant. However, 15, 16 and 33 dip and strike readings could be taken from sections NGHP-1-10B-08Y 46-66cm:bottom, NGHP-1-10B-08Y 46-66cm:top and NGHP-1-21C-02E 23-46cm respectively. Figure 5.10 shows the resultant contour plots, when the poles to the planes of each vein were plotted using an equal–area (Schmidt) net. As with the histogram data, the orientations in each equal–area projection are not comparable with each other.

Although the datasets are small, the readings taken from each core section show preferential hydrate vein orientation. In each of the plots in Figure 5.10 a concentration of points can be

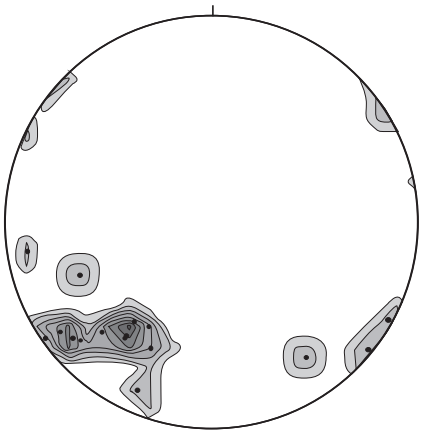

(a) NGHP-1-10B-08Y 46-66cm: top

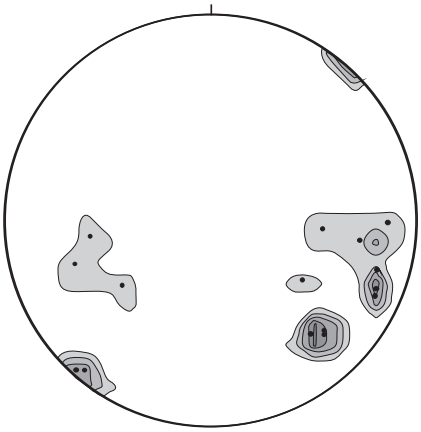

(b) NGHP-1-10B-08Y 46-66cm: bottom

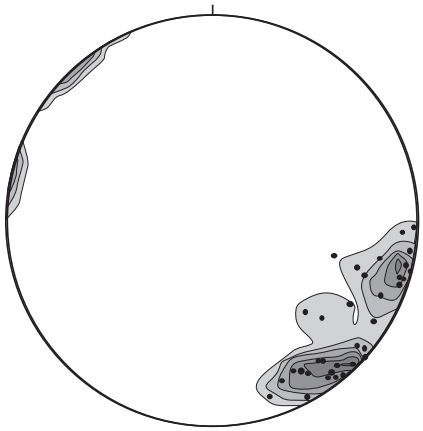

(c) NGHP-1-21C-02E 23-46cm

Figure 5.10: Equal–area lower–hemisphere projection contour plots generated from the poles to the planes of individual veins identified in axial and frontal slices from each core section. The datasets are small in each plot: 16 points in plot (a), 15 in plot (b) and 33 in plot (c). The actual data points are also plotted as black dots.

identified. In Figure 5.10(a) the mean vector of the plotted veins indicates a preferred dip and dip direction of 66°/040°, although a few points suggest another vein set with a dip of 85° and dip direction of 305°. Similarly, two vein orientations are suggested in Figure 5.10(b). The mean vector of the larger cluster of poles indicates a vein set with a dip of 62° with a dip direction of 294°, with another vein set dipping 63° with a dip direction of 054°. The vein data from Figure 5.10(c) suggests two vein sets close to one another, with the mean vectors of the two sets giving a dip and dip direction of 80°/321° for one set and 77°/287° for the other.

The preferential vein orientations seen in Figure 5.10 would suggest that there is some controlling influence on their formation in the sediment column. Systematic vein growth can form

in sediments due to sedimentary features or *in-situ* pressure regimes. Grain size or water content variation in a body of sediment can lead to preferential hydrate growth along particular horizons, and increased overburden or hydraulic pressure in a sedimentary sequence can cause deformation or fracturing along which hydrate can form.

In sediments where there are interbedded coarse and fine grained materials, hydrates are more likely to grow in the layers of higher permeability and pore size due to thermodynamic and kinetic effects (Handa & Stupin, 1992; Ginsburg & Soloviev, 1997; Clennell et al., 1999). As the lithostratigraphic analysis describes the sediment in both of the NGHP-1 cores as homogeneous (Collett et al. (2008) and data analysis in Section 5.3), it does not appear that sedimentary discontinuities control hydrate vein orientation here. Water content distribution in a sediment may also cause hydrate to form in distinct regions, as water availability has been shown to control hydrate morphology in the Okhotsk Sea and the Gulf of Mexico (Soloviev & Ginsburg, 1997). However, there is no evidence to suggest that water segregation is controlling the distribution of veins in the NGHP-1 cores.

The vein growth in the NGHP-1 cores is therefore more likely to have been controlled by the stress regime in the Krishna-Godavari basin. The location of sites NGHP-1-10 and NGHP-1-21 is significant in this respect, as they are situated at the top of a tightly folded ridge structure. Fractures in the strata underlying the gas hydrate stability zone provide conduits for gas and fluid migration, creating potentially elevated pressures beneath the gas hydrate bearing sediments. This type of site is classified as "focused, high–flux" (Trehu et al., 2006), and the hydrate morphology observed from the CT imaging can often be found where this flux regime exists (Holland et al., 2008; Trehu et al., 2006). A high pore pressure system could induce hydraulic fracturing in the clay into which hydrate would form. Further evidence for this fracturing mechanism is by the presence of "sets" of veins, which could indicate episodic fracturing events (Holland et al., 2008). Collett et al. (2008) commented on the presence of vein sets in some of the NGHP-1 sediments, but were unable to make conclusive remarks about the stress regime in conjunction with hydrate vein formation.

Hydrate Volume Analysis

The Volume Graphics software used to analyse the CT imagery of the NGHP-1 cores allowed the determination of hydrate volume by segmentation. As mentioned in Section 5.2.2, segmentation highlights areas of a particular grayscale (and therefore density) value, which can then be isolated from the total reconstructed volume. By segmenting out the void space and the hydrate veins, the volume of hydrate in each core could be quantified as a percentage of

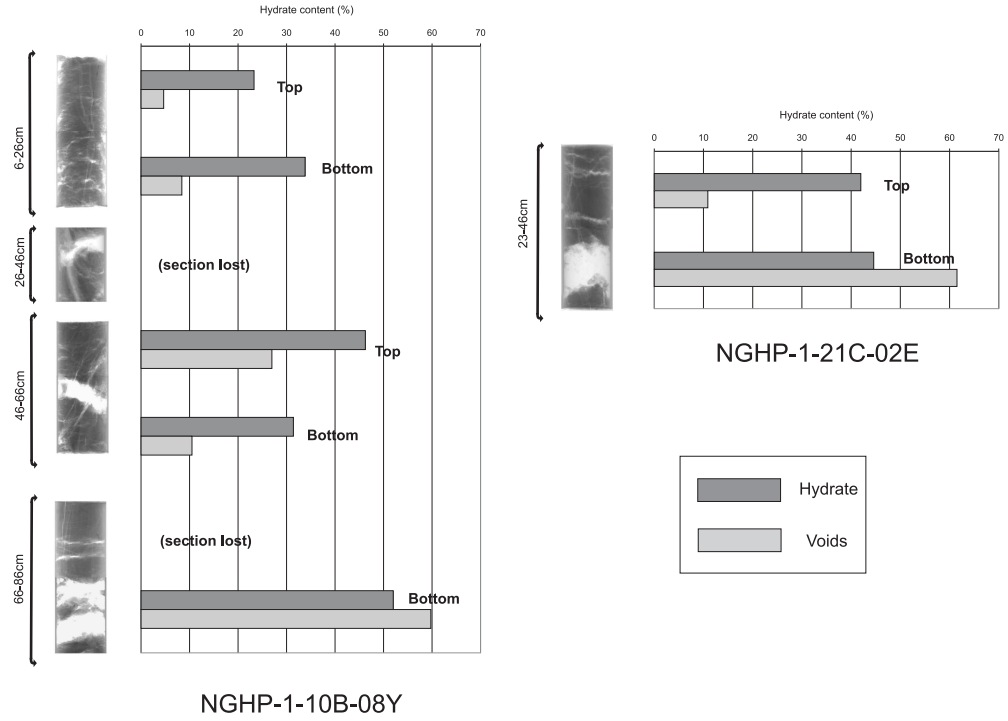

(a) Volume of hydrate and voids in all sections for both cores as a percentage of the total core volume.

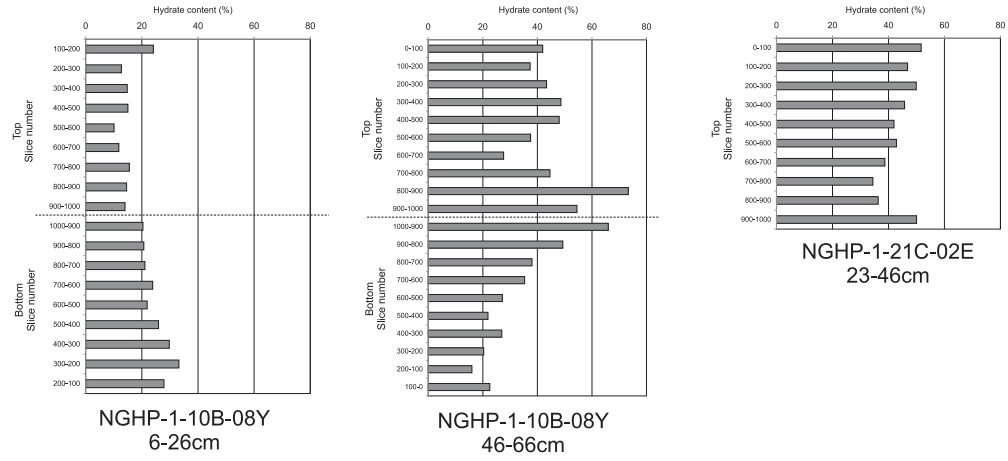

(b) Detailed volumes obtained from selected cores. Volume of hydrate represented as a percentage of the total frozen solids in each 100mm sliced section

Figure 5.11: Volume analysis for the NGHP-1 core sections.

the frozen sediment mass. From this, and by determination of the void ratio of the host sediment (Section 5.3), an estimate of hydrate content as a percentage of the pore space was found. Figure 5.11(a) shows the hydrate content from each core section, as well as the percentage of the core that was comprised of large voided space. In order to get a more detailed view of hydrate volume, certain cores were split into 100 slice portions (100 slices equates to approximately 10mm). Figure 5.11(b) shows the detailed volume analysis for core sections NGHP-1-10B-08Y 6-26cm, NGHP-1-10B-08Y 46-66cm, and NGHP-1-21C-02E 23-46cm: top. The slight disparity between the whole core volume values (Figure 5.11(a)) and the more detailed breakdown (Figure 5.11(b)), is due to the segmentation method used, which approximates the volumes according to individual core section analysis.

Section 6-26cm shows a variation from over 33% to 10% hydrate volume over the length of the section (approximately 200mm). Similarly, section 46-66cm has a large variation in volume through the core, with highs of almost 75% seen in the centre part of the section. It must be noted that this portion of the core section is dominated by void space, and the high volume of hydrate recorded may also include an element of ice, as discussed in Section 5.2.2. Section 23-46cm from core NGHP-1-21C-02E has a much more consistent hydrate volume distribution, with a variation of around 15% through the core.

The main observation from Figure 5.11 is that the volume of hydrate present in these cores is very high. The analysis suggests that in the sections with few voided areas (and so less opportunity for the inclusion of ice to the volume estimate), hydrate contents reach 50% of the pore space. These findings are slightly higher than those recorded during the NGHP-1 cruise (Collett et al., 2008). On board data shows gas hydrate contents to be between 17 and 25% of the pore space for samples taken at site 10. Gas concentrations recorded from a sample depressurised at site 21 also suggest a similar hydrate content, at around 30% of the pore volume (Collett et al., 2008). However, estimates of hydrate content from analysis of resistivity and sediment porosity show high hydrate contents in the region of 85% for the sediments between 27-90mbsf (Collett et al., 2008).

The results show that large volumes of hydrate can exist in this vein–filling, “grain displacing” (Riedel et al., 2006; Holland et al., 2008) morphology. The question that arises is whether these large accumulations can be detected and quantified accurately by current seismic surveying and remote geophysical techniques. Many of the current methods assume hydrate occupies the pore space of the sediment in a homogeneous distribution. Estimates from the 3D imaging state hydrate contents up to 73% of the pore space, but this hydrate does not occupy the pore space. Hydrate in the NGHP-1 cores comes as discrete pure veins, heterogeneously distributed

throughout the sediment. Although resistivity measurements can successfully detect hydrate accumulations of this nature, accurate quantification is not a guarantee (Riedel et al., 2006; Collett et al., 2008).

Sample Disturbance

As described previously, each of the core samples delivered to Southampton University showed sample disturbance in the form of large void spaces. As the on board X-rays of the cores show no sign of disturbance (Figure 5.12), it appears that the large voids developed during the transfer of the samples from the pressurised core barrel into liquid nitrogen. The issues arising from this are whether the disturbance was caused by dissociating hydrate during the depressurisation and rapid freezing procedure or some other effect.

It is clear from the images of the reconstructed CT volumes, that a significant volume of hydrate was present in the Southampton NGHP-1 cores suggesting that hydrate survived depressurisation and storage in liquid nitrogen. Detailed study of these images shows that not only were large hydrate veins still evident, but also that fibrous microveins also remained (Box A, Figure 5.12). The large remaining volume of hydrate seen in the cores does not suggest dissociation was prevalent as a disturbance mechanism. The void pattern also implies a process other than hydrate decomposition, with the majority of voids orientated perpendicular and cross cutting the predominant hydrate trend. If gas was evolving from hydrate dissociation, voids could be expected to develop along the vein orientation. As there are no observable gas expansion zones alongside hydrate veins, it is unlikely that much hydrate dissociation occurred in the samples during depressurisation and subsequent storage in liquid nitrogen.

The more likely cause of sample disturbance is therefore the expansion of methane gas coming out of solution in the pore water. The cores were recovered from a pressure of 110bar. The solubility of methane in sea water at this pressure and ocean bottom temperatures is approximately 68 times higher than at surface pressure and temperature (Handa, 1990). The pore water of the cored sediment would be expected to contain an amount of methane in solution, most of which would come out once the core was removed from the pressure vessel. The depressurisation process would also cause any compressed free gas in the sediment to expand rapidly to approximately 100 times its pressurised volume.

Analysis of the volume of voids with regard to the volume of hydrate seen in each core suggests hydrate volume dictates how much a sample will be disturbed after depressurisation. Figure 5.13 shows the volume of voids plotted against the volume of hydrate for each core section

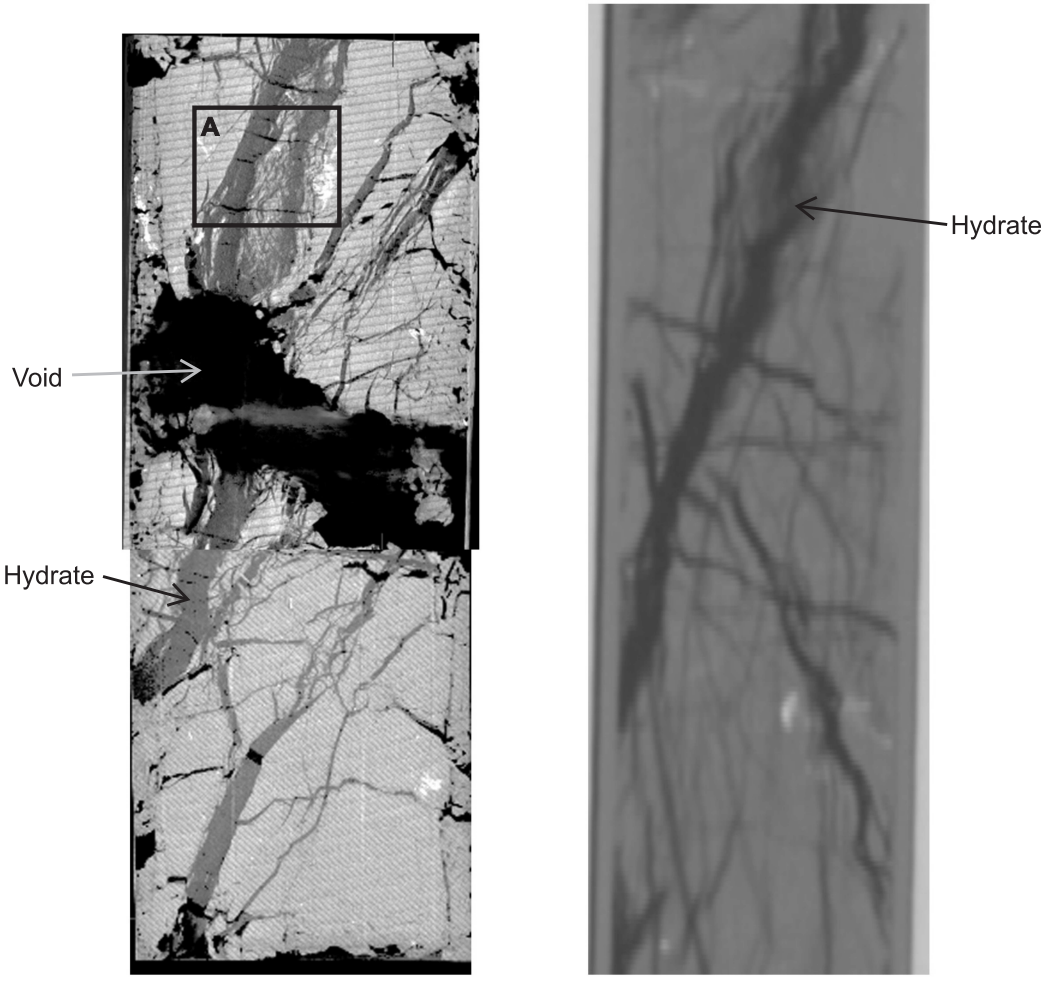

(a) Vertical slice through the centre of core volume, reconstructed from CT scanning using the X-Tek CT 160Xi. The top and bottom scans of the core have been stiched together.

(b) Vertical slice through the core taken before depressurisation using a Phillips Mx8000 CT scanner. Scan conducted by NGHP-1 Scientific party.

Figure 5.12: A comparison of CT images taken of core NGHP-1-10B-08Y section 46–66cm before and after depressurisation and storage in liquid nitrogen.

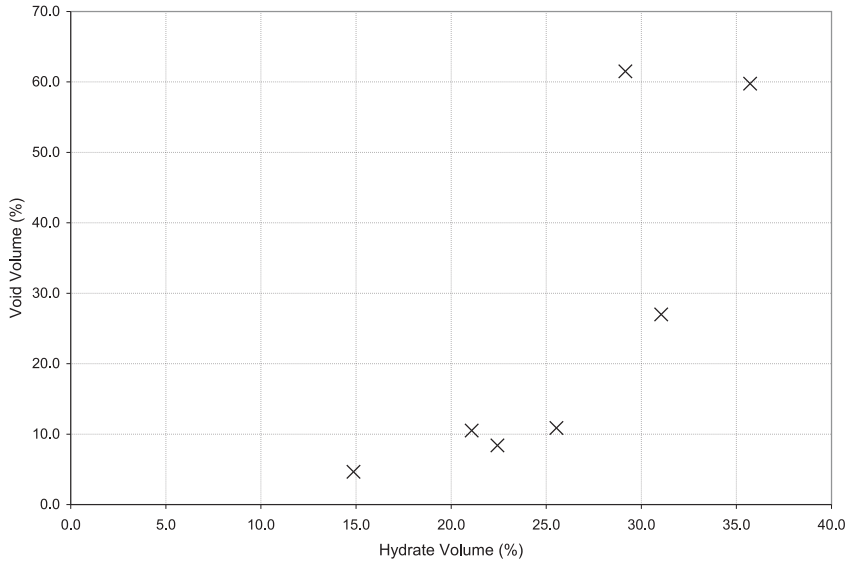

Figure 5.13: Volume of hydrate plotted against volume of voids for each measurable NGHP-1 core section

where volume data could be taken (Figure 5.11). The plot implies that the volume of voids in a core (magnitude of disturbance) increases with hydrate content.

The repercussions of extensive sample disturbance are considerable when attempting to mechanically test natural hydrate samples in the laboratory. The development of any voids prior to testing will result in sample collapse once inside an apparatus with total stress applied. In the case of the NGHP-1 samples, one of the programme aims (Section 5.1.3) was to conduct resonant column testing on the best preserved core sections. Section NGHP-1-10B-08Y 6-26cm was chosen to be tested. The trimmed sample was placed in the apparatus in a frozen state, at which point a confining pressure was applied by the use of nitrogen gas. The resonant column apparatus has a very low tolerance for sample settlement, due to the configuration the magnets on the drive plate and the surrounding coils (Section 3.2.3) Once isotropic stress had been applied to the core section, the voids collapsed reducing the height of the section by over 5mm. This made testing of this core section impossible. As the remaining core sections contained much larger voids than section 6-26cm, no further resonant column testing was attempted on the NGHP-1 samples.

If successful laboratory testing of natural hydrate samples is to be achieved, storage and transportation methods must be developed that will consider the depressurisation effects on sample

integrity. Alternatively, steps must be taken to reduce the expansion inside cores as they are depressurised and frozen in liquid nitrogen.

5.3 Host Sediment Properties

The dissociation of hydrates in a sediment can change vital mechanical properties. Not only will the loss of a stiff and potentially supportive material in the pore space have an effect on the strength of a material, but the changes in water content and salinity provided by dissociation will also have an impact. The understanding of the geotechnical properties of the host sediment is therefore of vital importance when gauging the effects of hydrate dissociation on the integrity of well bores drilled through hydrate bearing zones, as well as submarine slope stability. Although index and strength tests are routinely conducted on cored sediments at sea, little work has been done in the laboratory to evaluate hydrate host sediment properties.

This section describes the series of geotechnical tests carried out on the NGHP-1 core samples, and hypothesises on the effect of hydrate dissociation on the sediment. Initially, index tests were conducted on small sub–samples from the frozen cores. Of the initial sub–sample tests, organic content and water content analysis was undertaken by the author. Particle size distribution and salinity tests were conducted by research staff at the National Oceanography Centre, Southampton. After testing, the sub–samples were then combined with the rest of the core sediment after hydrate dissociation in order to provide a single sample for plasticity, specific gravity and strength testing. This index and strength testing was undertaken by SGC (Surrey Geotechnical Consultants, Limited).

5.3.1 Sub–sample Testing

Sub–samples of around 10-20g were taken from each frozen core. Care was taken to sample portions of the core that contained as little hydrate as possible, so that the *in–situ* properties of the host sediment could be ascertained without contamination from dissociating hydrate. It was assumed that water content and pore water salinity would be affected by hydrate dissociation if mixed samples were taken. This would be due to fresh water being added to the sediment as it was released during dissociation. Once brought to room temperature, basic tests were conducted on the subsamples, namely particle size distribution analysis, water content determination, pore water salinity and organic content. Table 5.1 gives the results from these tests, with reference to sub–samples taken from different parts of the core sections. The correspond-

ing core section parts can be seen in Appendix B.

Organic Content and Particle Size Distribution

Total organic carbon, as well as inorganic carbon were determined for 9 subsamples. The tests were carried out using a UIC Coulometrics Carbon Dioxide Coulometer, following the procedure set out in BS EN ISO-21068-2:2008. The results in Table 1.1 show that the total organic content in the sediment is low, less than 3%, which corresponds to the findings from the NGHP-1 scientific team (Collett et al., 2008).

Particle size distribution was determined for 34 different samples of the core using the laser diffraction technique (ISO 13320-1 1999). A Malvern Mastersizer was used to conduct the tests in conjunction with an autosampler to speed sample processing. Results from these tests (Figure 5.14) suggests that the sediment is uniform, with approximately 20% of the particles clay-sized, 75% silt-sized and the remainder sand-sized. There is little variation between the subsamples, or the sediment analysed from the two separate cores. This consistent particle size, combined with the low organic content means the sediment can be considered devoid of fabric (Rowe, 1972). Standard soil mechanics tests could therefore be carried out and analysed without the need to account for heterogenetity in the samples.

Water Content

The water content of the sub-samples was determined in accordance with BS1377: Part 2 1990. Each sub-sample was weighed before and after being oven dried, with water content then expressed as a percentage of the dry weight of the sediment (Table 5.1). The water contents obtained for the subsamples range between 64 and 82%, a range that corresponds to the water contents recorded during the NGHP-1 cruise (Collett et al., 2008). The overall arithmetic mean of the water contents from all the samples is 73.3%. The high values (+80%) recorded from section 66-86cm may be due to the inclusion of extra water freed by hydrate dissociation. Although care was taken to avoid hydrate accumulations when collecting the subsamples, some hydrate may have been included and thus influenced the measured water contents.

Salinity

The salinity of the pore water was found from the chloride ion concentration, using a Dionex ICS2500 ion chromatograph. Pore water was extracted from the samples by use of a centrifuge. Nine salinity values were then obtained that corresponded to the parts shown in Appendix B. The validity of the readings were ensured through calibration of the equipment with single anion and seawater standard solutions. The average salinity for all the samples was found to be 36.7g/l, a value slightly higher than that of seawater (34g/l). The chloride ion concentrations

Core	Section	Part	Water Content (%)	Total Organic carbon content (%)	Inorganic carbon content (%)	Salinity (g/litre)	Chloride (Mmol/kg)
NGHP-1-10B-08Y	6–26cm	Part A*	64	2.6	0.8	41	634
		Part B	72	2.5	0.7	35	550
	26–46cm	Part A(i)	68	2.7	0.9	44	689
		Part A(ii)	76				
		Part B	69	2.7	0.8	40	–
	46–66cm	Part A(i)	77	3.0	0.8	38	588
		Part A(ii)	75				
		Part B(i)	71	2.6	0.8	38	585
		Part B(ii)	77				
		Part C	72	–	–	–	–
	66–86cm	Part A(i)	78				
		Part A(ii)	82	2.8	0.7	27	419
		Part A(iii)	81				
		Part B	81	–	–	–	–
		Part C	69	–	–	–	–
NGHP-1-21C-02E	23–46cm	Part A*	56	2.1	0.5	31	488
		Part B	69	2.8	0.5	33	513

Table 5.1: Details of section sub–samples of the frozen cores delivered from NGHP-1. Core section parts are illustrated on the frozen core photographs in Appendix B. *Denotes sample reserved for resonant column testing.

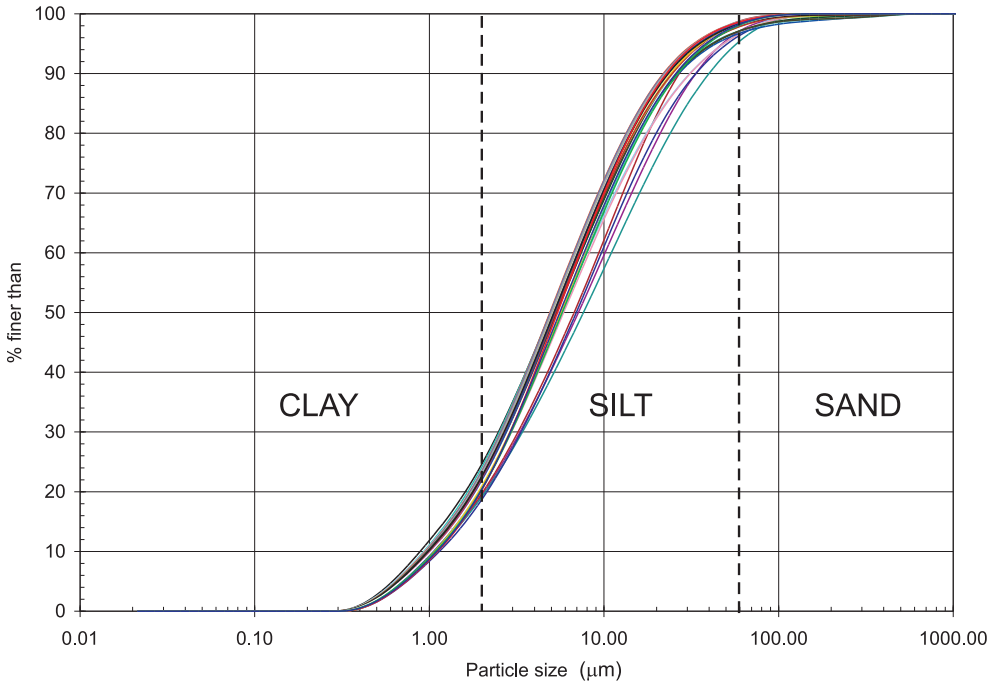

Figure 5.14: Particle size distribution for 34 sub–samples of the NGHP-1 sediment

of the cores measured during the NGHP-1 cruise give a slightly lower value than those measured here. A range of concentrations between 398 and 634mM/kg were recorded on the boat, whereas laboratory tests give a variety of values between 419 and 689mM/kg. It is possible that the formation of hydrate in a sediment drives up the pore water salinity as fresh water is incorporated into the hydrate structure. The high values of salinity found in the sub–samples could therefore represent the actual pore water salinity of the sediment when hydrate is present, whereas the pore water salinity observed by the NGHP-1 scientific crew may have been lower due to hydrate dissociation.

5.3.2 Index and Strength Testing

Once the core sections had been sub-sampled, the remaining material was unfrozen so that index and strength tests could be undertaken. Tests on the subsamples had shown that the sediment across the cores was uniform, so all the core sections were combined to give approximately 1.5kg of material for testing. Specific gravity, undrained shear strength, liquid and plastic limit tests were conducted on this combined material. As the sediment contained hydrate before being unfrozen, the combined material would contain additional water to its *in-situ* content due to hydrate dissociation.

Specific Gravity

The density of the sediment grains relative to water (specific gravity or grain density) is determined by using the density bottle method for fine grained sediments, as described in BS1377:2 (1990). The value for the combined NGHP-1 material was found to be 2.74 in laboratory tests, which fit withiin the range of values found during the cruise (found using the method given by ASTM-D5550-06). On board measurements recorded grain densities ranging between 2.44 to 2.86g/cm3, but with an average of 2.71.

Liquid and Plastic Limit

The plasticity of the combined NGHP-1 sediment was determined using the cone method for the liquid limit, and rolling method for the plastic limit (BS1377:2 (1990)). The initial water content of the combined material was found to be 75.5% and so lower water contents were acheived through air drying, whilst higher water contents were obtained by adding more water to the material. Water with a salinity of 35g/l was used to increase the material's water content, so as to match the high pore water salinity observed from the subsamples. Additionally, a further liquid limit test was conducted on the material after it had been air dried, ground down and washed with distilled water to remove it's salinity. The results of both tests are shown in

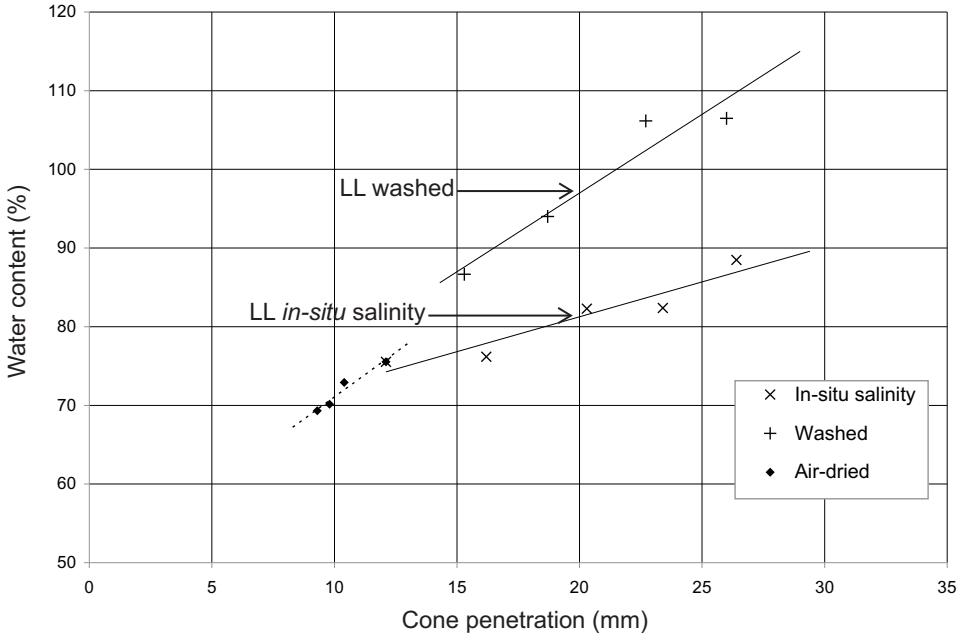

Figure 5.15: The liquid limit of the NGHP-1 combined material (BS1377:2, 1990) represented by cone penetration plotted against water content.

Figure 5.15, presented as cone penetration against water content.

The liquid limit is defined as the water content where penetration of a 80g, 60° cone is equal to 20mm. Figure 5.15 shows this to be at 81% for the material at *in-situ* salinty, but that this value increases once the material has been washed and wetted with distilled water to 96%. The plastic limit was found to be 33% for both the orignal and washed material. The liquid and plastic limits of a material can be considered as indicators of shear strength at two different water contents (Powrie, 1997). The liquid limit for the materials tested here represents a shear strength of 1.7kPa, whereas the plastic limit is approximately 100 times this value, at 170kPa. At a given water content, it is clear from Figure 5.15 that pore water salinity has an effect on the shear strength of a clay, with the liquid limit increasing by 15% as the pore water was freshened in the combined material.

One of the basic phenomena of clay colloid chemistry is the effect of salt on dispersed clay particles in water. A few tenths of a percent of salt is enough to cause dispersed clay particles to start sticking together. This occurrence, called “flocculation”, is due to the natural electrical charge on the surface of clay particles, and the interference of salt ions on the repulsive forces of this charge. In a fresh water solution, the negative charge on each clay particle causes them to attract oppositely charged water molecules that become bound to the surface of the particle

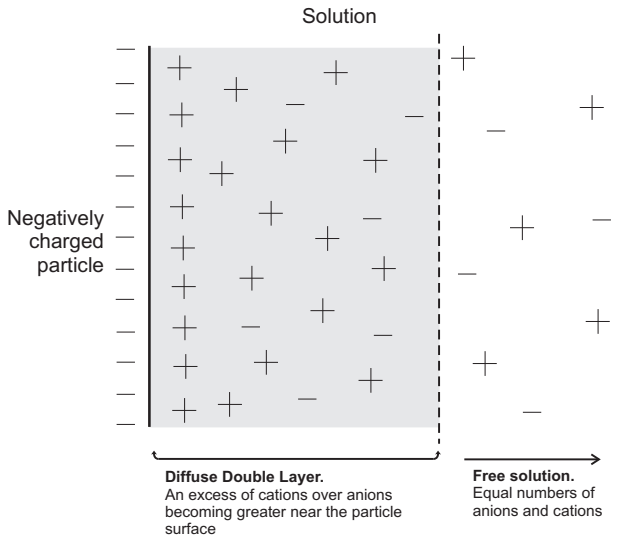

Figure 5.16: A schematic representation of the diffuse double layer as described by Van Olphen (1977)

in what is called the "diffuse double layer" or DDL (Figure 5.16). The thickness of the DDL in fresh water (less than 10^{-6}cm (Weaver, 1989)) means attractive Van der Waals forces are unable to overcome the natural repulsion of each clay particle with the other, and the material remains dispersed. The addition of salt brings ions into the solution that counteract the negative charge on the particle surfaces, and so the DDL is reduced in thickness. Once particle repulsion is reduced and the DDL is thinner, the Van der Waals forces in the atoms of every clay particle cause them to be attracted to one another and they flocculate (Van Olphen, 1977). Flocculation causes clay sediments to have a higher strength than sediments where the clay particles are dispersed (Van Olphen, 1977). It could be expected therefore, that by washing the NGHP-1 material, one would decrease the strength of the material as the clay would no longer be flocculated. The liquid limit results shown in Figure 5.15 suggest that this is not the case for the NGHP-1 material, so there must be a different interaction between clay particles and the DDL than that suggested above.

Van Olphen (1977) suggests that clay particles may have a variable charge across their shape, with the flat surfaces (faces) holding a different charge to the edges. This means that the clay particles have the potential to flocculate even when the DDL is thick (i.e. in fresh water). Van Olphen (1977) suggests there are three ways the particles can interact with each other: face-to-face (FF), edge-to-face (EF), and edge-to-edge (EE) (Figure 5.17). The EF and EE associations create flocs that have a voluminous "card house" structure, and can form due to the differing electrostatic charges on the edges and faces of the particles (Van Olphen, 1977). FF associations are generally caused by Van der Waals attractive forces and are referred to as

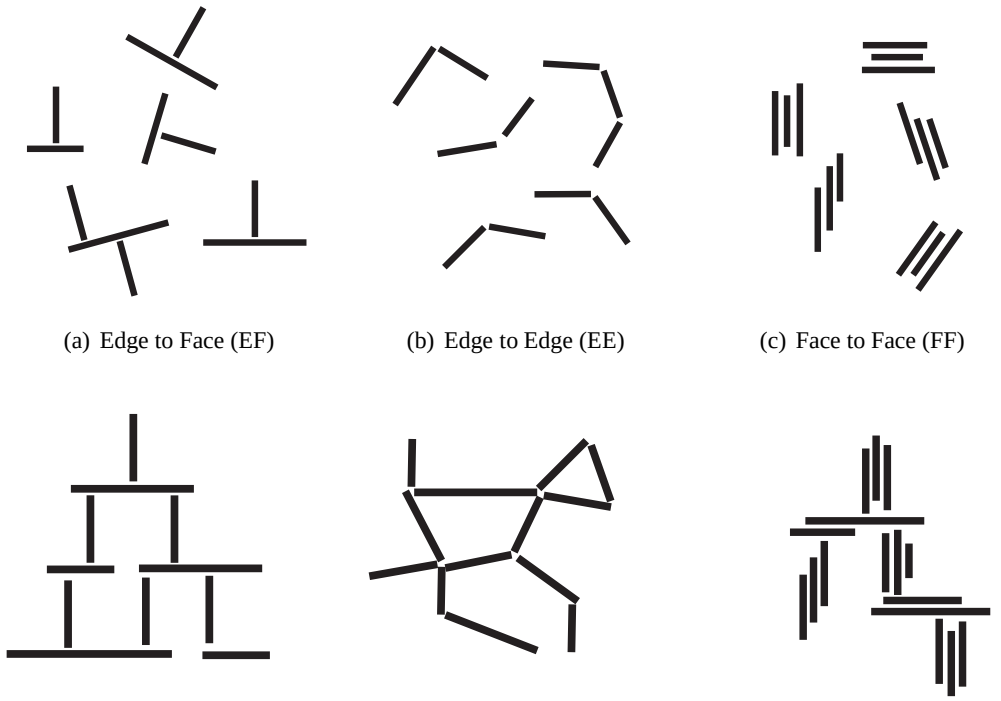

(a) Edge to Face (EF)

(b) Edge to Edge (EE)

(c) Face to Face (FF)

(d) Dispersed but flocculated (EF and EE associations only)

(e) Aggregated but flocculated (EF and FF associations)

Figure 5.17: Clay particle arrangements, from Van Olphen (1977)

aggregated rather than flocculated particles. In fresh water, FF associations do not happen, but dispersed flocculation can occur (Figure 5.17(d)). The sediment could show a high strength but still remain in a dispersed state. The addition of salt promotes FF associations and the flocculation of aggregated particles can occur (Figure 5.17(e)), which also increases the strength of the sediment.

Van Olphen (1977) states that the associations in Figure 5.17 can occur over a range of pore water salinity values, but that there will be a point where the combination of repulsive electrostatic and attractive Van der Waals forces will result in a minimum amount of flocculation (and therefore a minimum shear strength of the clay sediment). Through detailed studies, Van Olphen (1977) has shown that this point occurs at different salinity values, depending on the clay mineral. With regard to the NGHP-1 sediments, it appears that dispersed flocculation may occur when the sediment is mixed with fresh water, giving it a higher strength in comparison to the *in–situ* salinity conditions.

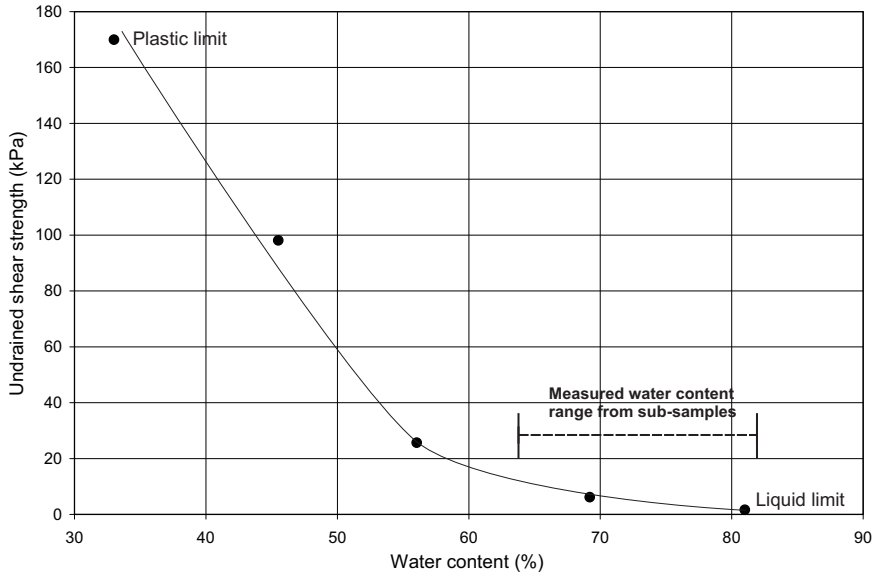

Figure 5.18: The undrained shear strength against water content for the NGHP-1 combined material

Strength Testing

Once the liquid and plastic limits had been determined for the NGHP-1 material, an undrained triaxial compression test was conducted to obtain a measure of strength under more controlled conditions. The test was carried out on a 38mm diameter and 76mm high specimen, formed from the combined NGHP-1 material. The specimen was tested according to BS1377:7 1990. Values for undrained shear strength were obtained for the original water content, as well as those achieved after consolidation at 100kPa and 200kPa. Combined with the results from the plasticity tests the change in undrained shear strength with water content could be plotted for the NGHP-1 sediment (Figure 5.18).

The triaxial test on the sediment at it's original water content (69.3% was recorded for the combined material) yielded an undrained shear strength of 6.2kPa. After the sediment had been consolidated to 100kPa and 200kPa, the undrained shear strength increased to 26kPa and 98kPa respectively. The other points on Figure 5.18 are the undrained shear strengths found from the liquid limit and plastic limit tests described previously.

Chandler (2000) has investigated the relationship between undrained shear strength and vertical effective stress for reconstituted natural clay samples at *in–situ* conditions. By using data from the literature, it was found that the undrained strength ratio varied very little at any given vertical effective stress, for a range of normally consolidated natural clays, regardless of plasticity

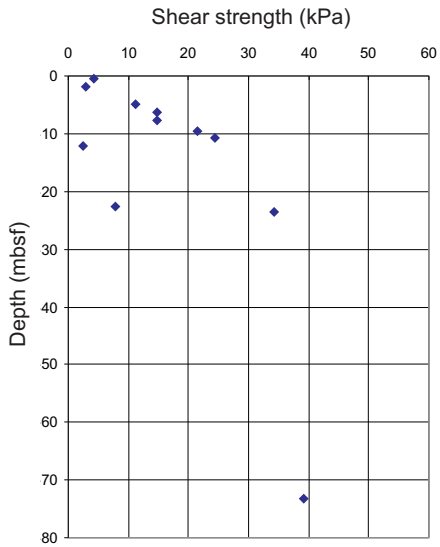

(a) Mini–vane strength measurements taken down hole NGHP-1-10B

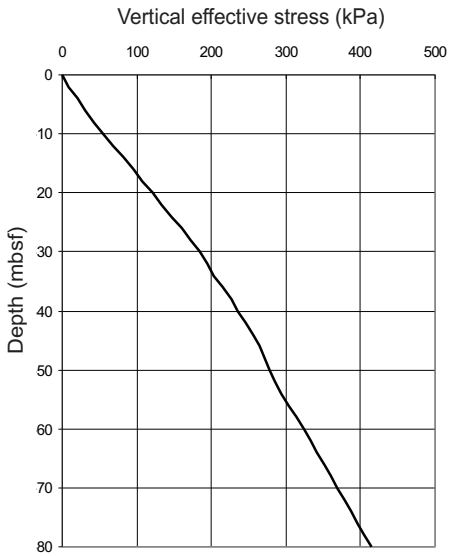

(b) *In–situ* vertical effective stress down hole NGHP-1-10B

Figure 5.19: Strength results and corresponding vertical effective stresses from down hole NGHP-1-10B. From Collett et al. (2008)

index. A mean value of 0.34 was obtained that describes the change in undrained shear strength of any reconstituted natural clay with the effective stress at *in–situ* conditions. If considering this relationship for the NGHP-1 sediment, the undrained shear strength of a reconstituted sample should have been in the region of 95kPa, if taking the vertical effective stress *in–situ* to be approximately 280kPa. By comparison, the values for shear strength recorded during the NGHP-1 cruise, suggested the shear strength for the undisturbed material at 50mbsf to be between 35–40kPa (Figure 5.19) (Collett et al., 2008).

It is possible that the low strength of the NGHP-1 core sediment is attributable to the high water contents retained in the material. The presence of high water contents, and the strength results given above suggest that the sediment was under–consolidated *in–situ*. The shear strength analysis conducted on the sediments from hole NGHP-1-10B (core disturbance did not allow strength tests to be conducted at hole NGHP-1-21C) by the NGHP-1 scientific crew (Collett et al., 2008), suggest that clays near the surface were normally consolidated, and had not been subjected to any geological processes that may have caused over–consolidation. However, further down the sediment column the measured strength of the sediment remained consistent (around 35-40kPa) to a depth of 80mbsf, reinforcing the hypothesis that the sediment was under–consolidated (Figure 5.19).

Under–consolidation can occur in deep sea sediments due to overpressure (Gibson, 1958; Dugan & Flemings, 2000; Dugan & Germaine, 2008). Overpressure is the condition in a sediment when the pore pressure is higher than hydrostatic pressure. It can occur in regions where there is rapid sedimentation, such as continental shelf environments with sediment influx from large river systems (Dugan & Flemings, 2000). The sedimentation rate on the Bengal Fan is estimated as 1.2mm/yr (Worm et al., 1998), a high value conducive to elevated pore pressure development. Additionally, Dugan & Flemings (2000) suggest that fluid influx can also cause overpressure in a formation. The site of holes NGHP-1-10B and -21C are situated on the crest of a tightly folded ridge structure, with many fractures providing conduits for gas and fluid flow. The sedimentation rate and underlying geological structures are appropriate for an area exhibiting overpressure, which in turn may have allowed for the under–compaction of the NGHP-1 sediments and the sediment to retain a high water content.

An alternative consideration is the influence of salinity in creating an under–consolidated material. As mentioned previously in the liquid and plastic limit section above, pore water salinity has an effect on the fabric of a clay sediment. The interaction of clay particles determines the internal arrangement of sediment grains, which in turn affects the ultimate void ratio of the clay sediment. Van Passen & Gareau (2004) observed similar strength results to those for the NGHP-1 samples in clays from the Caspian Sea. The geological conditions where the cores were taken was not conducive to under–consolidation processes, and so it was suggested that the under–compacted state of the clays was due to salinity variation. They found that the Caspian Sea clay had an edge–to–face particle interaction, which had created a flocculated fabric and high void ratio. The EF particle arrangement is a stable structure that resists the volume change caused by increasing overburden pressure (Van Passen & Gareau, 2004). Considering this, the high salinity of the pore water in the NGHP-1 samples may have given the clay a structure *in–situ* that was destroyed when the sediment was remoulded for triaxial testing.

There is also another component of the sediment that may have contributed to it's structure at depth. The sediments from the NGHP-1 cruise contained a large quantity of gas hydrate (Section 5.2.3) in the form of cross–cutting veins. If the hydrate formed in the sediment before significant overhead sedimentation and application of overburden pressure, the hydrate may have formed a framework that would support the sediment and allow it to maintain a high void ratio. It is therefore possible that the presence of hydrate in the NGHP-1 cores is responsible for the apparent under–consolidation of the sediment.

Core Section	Length	Part	Void Ratio	Hydrate Content (%)	Salinity (g/litre)	Drop in salinity (g/litre)	Original water content (%)	Increase in water content (%)
NGHP-1-10B-08Y	6–26cm	top	1.76	23.3	41	7.3	64.3	13.9
		bottom	1.97	33.8	35	9	71.9	24.7
	26–46cm	all	–	–	–	–	–	–
	46–66cm	top	2.04	46.3	38	13.1	74.5	39.4
		bottom	2.04	31.4	38	9.1	74.5	23.4
	66–86cm	top	–	–	–	–	–	–
		bottom	2.19	52.0	27	10.5	80.1	51.1
NGHP-1-21C-02E	23–46cm	top	1.55	42.0	31	9.5	56.7	25.2
		bottom	1.89	44.6	33	10.9	69.0	34.2

Table 5.2: Tabulated volume, salinity and water content measurements for NGHP-1 core sections. Includes estimated values for decrease in salinity and increase in water content due to hydrate dissociation

5.3.3 The Impact of Hydrate Dissociation on a Host Sediment

Having conducted a number of geotechnical tests on the material from the NGHP-1 core sections, the influence of gas hydrate dissociation on host sediment properties can be discussed. Index tests such as water content, porosity, bulk density, grain density and strength tests were conducted during the NGHP-1 cruise, however more complex testing on the hydrate bearing sediments was not possible due to poor sample recovery. The tests conducted at Southampton University are therefore the first of their kind to shed light on the effects of changing salinity, water content and structure of a sediment when hydrate dissociates in a specific natural sediment.

The Effect of Salinity

Hydrate dissociation in a sediment will reduce the salinity of the pore water by the release of fresh water. The degree of freshening depends on the initial salinity of the pore water, and the hydrate content of the pore space. By taking the measured salinities of the sub–samples in Table 5.1 as the *in–situ* values for pore water salinity in the presence of hydrate, the expected freshening from dissociation can be calculated in each core. The large volumes of hydrate, which are not pore filling, mean that large fresh water influx would occur during dissociation. Table 5.2 gives the reduction in salinity and the corresponding hydrate content for each core section. The data shows that hydrate dissociation would cause a drop in salinity ranging from 7.3g/l for section NGHP-1-1-B-08Y 6-26cm top, to 13.1g/l for section NGHP-1-10B-08Y 46.66cm top.

Previous experimental results on the strength of clay materials with regard to salinity, highlight the complexity of the subject. Skempton & Northey (1952) observed a reduction in the liquid limit of artificially sedimented clays when the salinity of the sediment was reduced from 35g/l to 5g/l. Converse to this, Van Passen & Gareau (2004) saw an exponential increase in

liquid limit as they decreased the salinity of remoulded clay samples towards zero. Bjerrum & Rosenqvist (1956) have shown a reduction in liquid limit as the salinity was reduced in artificially sedimented clays similar to Skempton & Northey (1952), but once the salinity was reduced to zero, recorded the highest strength of all sediments tested. The results from tests on the NGHP-1 sediment also showed an increase in liquid limit from the sediment with *in–situ* salinity compared with the value using fresh water. Van Olphen (1977) has shown that different clay particles actually have different initial double–layer structures, and so their reaction to electrolytes differ dramatically. As a result, Van Olphen states that it is difficult to predict the behaviour of any particular clay with changing salt content.

The Effect of Water Content

Table 5.2 gives the estimated increase in water content from hydrate dissociation, if the values given in Table 5.1 are taken as the true water content *in–situ* in the presence of hydrate. The water released from hydrate dissociation was simply added to the original value in order to determine the change in water content. The table shows that the high volume of hydrate in the cores would cause a significant increase in the water content of the host sediment. The smallest increase is seen in the NGHP-1-10B-08Y core section 6-26cm: top, at 13.9%, with the large hydrate contents recorded in section 66-86cm of the same core giving a 51.5% increase. The curve in Figure 5.18 shows that such changes in water content could cause significant decreases in strength of the host sediment.

The Effect of Hydrate Morphology

It is suggested that the main impact from hydrate dissociation in the NGHP-1 sediment would be the loss of a structural component that may be supporting much of the overburden pressure. Visual observation and CT imaging techniques have revealed significant crosscutting vein structures, which may have allowed the sediment to retain a high water content and low undrained shear strength. Hydrate dissociation would see the removal of this rigid supporting framework, meaning the application of the full overburden pressure on the remaining sediment. It is likely that this would cause significant instability in overlying strata as the previously hydrate bearing sediment undergoes significant settlement.

5.4 Summary of Natural Sediment Testing

Observations and measurements have been made on a number of core sections made available to Southampton University from the NGHP-1 cruise. Interpretation of 3D CT imaging revealed high volume, sub–vertical vein structures with preferential orientations. The nature of the veins

coupled with the tectonic history of the area, suggests that hydrate was formed from hydraulic fracturing by the influx of fluid and gas from below (Holland et al., 2008). The high volumes of hydrate observed in these veins challenges the ability of remote geophysical and seismic methods to quantify hydrate accumulations.

3D imaging and external visual observation of the cores also highlighted severe sample disturbance due to handling methods. Current methods of transporting and storing natural hydrate samples need to be improved if successful laboratory testing is to be undertaken in the future.

Investigation into the geotechnical properties of the host sediment revealed it to have a very low remoulded undrained shear strength, in conjunction with a high water content and high plasticity. The results indicate a sediment that is under–consolidated, however, the high salinity of the pore water may have induced a structure within the clay that was destroyed during remoulding, so giving an unexpected low undrained shear strength. It is also suggested that hydrate may have formed a framework that supported the overlying sediment, and allowed the host clay to retain a high water content.

The effects that the dissociation of a body of hydrate such as this could have on the mechanical properties of its host sediment appear to be significant. Dissociation would cause an increase in water content, decrease in salinity and also result in the removal of a potentially key structural component of the sediment. The complexity of clay colloid chemistry means definitive conclusions with regard to the effect of salinity on the NGHP-1 sediment are not possible, but it can be estimated that the reduction in salinity with hydrate dissociation may cause a large increase in sediment strength. However, the water content changes seen with dissociation may very well mask any salinity effects. The large volumes of hydrate in the NGHP-1 cores means the water content of the host sediment could increase by up to 50%. This would cause significant changes to the strength of the material, which would have a major impact on the stability of the sediments in the region. Finally, the supportive nature of vein–like gas hydrate can only be evaluated when reliable methods of testing natural hydrate samples at *in–situ* conditions can be developed.

Chapter 6

CONCLUSIONS AND SUGGESTIONS FOR FURTHER WORK

Accurate assessment of the value and distribution of global gas hydrate requires the understanding of how hydrate affects host sediment properties. From observations of natural hydrate deposits, it has been established that gas hydrate can take on a number of morphologies in sediments, which in turn will dictate the impact of hydrate on its host material. To determine which hydrate morphology will be found in each sedimentary environment, controlled laboratory experiments must be carried out that will generate data that is comparable with seismic surveying results. Alternatively, numerical modelling methods can be used to predict the impact of hydrate presence on sediment properties, but these methods require a full understanding of the interaction of hydrate with sediment particles.

This thesis presents a review of laboratory investigations into the gas hydrate phenomena, and identifies the points where information on the formation of methane hydrate in sediments is lacking (Chapter 2). In response to the gap in the knowledge highlighted in Chapter 2, a set of experiments were designed to form methane hydrate in sand, under water rich conditions (Chapter 3). Further investigations were made into hydrate formation by constructing four specimens of different sediment types and growing hydrate inside them (Chapter 3). The results from both sets of laboratory experiments were analysed with regard to the affect of hydrate on seismic velocity and attenuation (Chapter 4). Finally, a number of natural hydrate samples gave the opportunity to observe the morphology of hydrate in fine grained materials in detail, as well as undertake detailed geotechnical tests to investigate the affect of hydrate dissociation

on sediment properties (Chapter 5). This chapter summarises the conclusions that can be drawn from each set of investigations, before making some suggestions on how the GHRC can be used to continue with work on gas hydrates.

6.1 Conclusions

Firstly, a number of conclusions can be drawn from the literature review which highlight the deficiencies in gas hydrate knowledge to date. It is apparent that due to the range of seismic velocities gained during deep sea drilling and seismic surveying, researchers are still uncertain of the velocity profiles expected from gas hydrate bearing sediments. The laboratory testing of natural samples that could augment results from remote sensing techniques have been limited, as the methods to transfer intact hydrate samples into equipment for in–depth geotechnical testing do not currently exist. Laboratory testing of gas hydrates is therefore focused on synthetic hydrate bearing sediments. The challenges involved in artificially growing gas hydrate in the laboratory have caused some researchers to move away from using methane as the hydrate former. Additionally, hydrates are often formed in materials such as glass beads and silica gel instead of natural sediment types. Evidence from the literature suggests that the results from tests such as these may be distorted, and not applicable to natural hydrate deposits. By looking at published results from different hydrate tests, it appears that formation methodology for synthetic hydrates influences the morphology of hydrate in the pore space. To date, no work has been done where hydrate has been formed in comparable materials and under consistent conditions so that hydrate morphology can be analysed with regard to formation methodology. Additionally, little work had been conducted on forming hydrate in sediments other than homogeneous sands.

By considering the above conclusions from the literature, an experimental methodology was developed to form hydrate in fully water saturated sands out of the free gas phase, and a new technique for synthesising methane gas hydrate in the Gas Hydrate Resonant Column was established. This method allowed for the direct comparison of results with those from the work of Priest (2004), where hydrate was formed in partially saturated sands, and a number of conclusions about the morphology of hydrate in the pore space could be drawn from this comparison.

Primarily, it was found that hydrates formed in fully saturated or “excess water” conditions have no effect on host sediment shear and longitudinal wave velocities until 30% of the pore

space has been filled with hydrate. Further analysis of the effective stress dependency of sediments containing hydrates grown in excess water conditions showed that there was little change in dependency from 0% to 40% hydrate content. Hydrates grown in these conditions therefore, do not bond the host sediment at hydrate contents of 40% and below. This observation is in contrast to the results of Priest (2004) who showed hydrate acting as a bonding agent when formed in partially saturated or "excess gas" conditions. Comparison of results from this research and a number of numerical models suggests that formation conditions greatly influence the morphology of methane hydrate in the pore space. It can be concluded that a consideration of the conditions of hydrate formation must be made when attempting to interpret the seismic signatures of natural hydrate deposits.

Additional findings from the investigations into hydrate formation technique relate to the attenuation results from the set of excess water tests. It was found that sediments containing hydrates formed in excess water conditions show an almost linear relationship between hydrate content and attenuation increase. It is suggested that this increase was due to the increase in pore surface area that occurs due to hydrate presence, and the resultant increase in "squirt flow". It is also possible that the porous hydrate grains allow water movement through hydrate grains themselves, and thus also contribute to viscous fluid losses. It would appear therefore, that attenuation change is more sensitive than seismic velocity to hydrate content fluctuations in excess water environments. It is possible that measurements in attenuation could become a more useful tool in quantifying hydrate content in deep seas deposits in the future.

Along with successfully developing a method of forming homogeneous methane hydrate in sands in excess water conditions, the secondary aim of this research was to form methane hydrate in sediments with a variety of particle size and shape, but out of excess gas conditions. This was achieved by forming hydrate in sediments comprising of a mixture of different sand grades and 0.1mm mica particles. Initially, the results from these tests showed that the addition of 10% methane hydrate to specimens of a variety of sediment types caused bonding in each case, although the degree of bonding, and therefore increase in shear and longitudinal wave velocity in each specimen varied depending on sediment type. Analysis of the shear and longitudinal wave velocities from each specimen showed that the addition of 10% by weight fine grained LBE sand to coarse grained LBB sand increased the bonding affect of methane hydrate, when compared with bonding in a pure LBB sand specimen. The addition of 10% by weight 0.1mm Mica to an LBB specimen, decreased the bonding affect of hydrate. It could be concluded therefore, that the surface area of the grains influences the change in shear and longitudinal wave velocity seen in each specimen that is caused by hydrate inclusion, and that the largest surface areas of grains inside a specimen correlate to the lowest increase in seismic

velocity.

The final aim of this research was to observe and analyse the morphology of natural gas hydrate deposits. Five samples from the Indian National Gas Hydrate Program were made available to the University of Southampton, containing methane hydrate within frozen fine grained sediment. CT scanning and a series of geotechnical tests were conducted on the samples, from which a number of conclusions could be drawn. Firstly, the imaging of the samples revealed that there was significant disturbance in each sample due to the expansion of dissolved gas in the pore water as the sample was removed from the pressure corer and transferred to liquid nitrogen. Further high resolution three–dimensional imaging of hydrate samples revealed high volumes of gas hydrate formed in vein structures in a fine grained clay. Analysis of the geometry of the hydrate veins showed a preference for the veins to grow in two distinct orientations. Volume analysis revealed high hydrate contents in each sample measured (from 8% up to 60% in places). It was concluded from these observations that large volumes of hydrate could exist in veins in a fine grained host sediment.

Once the five core samples had been scanned and photographed, it became obvious that the degree of disturbance of the samples would make direct testing in the GHRC impossible. The methane hydrate was therefore dissociated and the host sediment analysed to discover the potential impact of large scale hydrate dissociation.

A number of geotechnical tests were conducted on the host material including water content, particle size distribution, organic content, salinity and index and strength tests. The sediment was comprised predominantly of silt–sized particles with a low organic content and so was presumed to exhibit no fabric (Rowe, 1972). The water content of the sediment cohabiting with the hydrate was found to be high, at 73%, with a high salinity measured at 36.7g/l. The sediment was found to have a high plasticity, with a liquid limit of 81% and plastic limit of 33% at *in–situ* salinity. Once the sediment had been washed to remove salinity, the liquid limit increased by 15%. This increase in strength was thought to be due to the flocculating nature of the particular clay particles in the NGHP-1 samples, although firm conclusions on this subject can not be made without further investigation into the clay mineralogy of the sediment.

When the host sediment was tested in a triaxial apparatus, it was revealed to have a very low remoulded undrained shear strength (about 6kPa), which led to the assumption that the sediment was under–consolidated *in–situ*. The geological location of the sediment was such that sedimentation rates and upward migrating pore fluids could have contributed to overpressure in the formation, and allowed the sediment to retain a high water content. It was concluded how-

ever, that a number of factors could have given the sediment a structure *in–situ* that may have caused this under–consolidation. Initially, the high salinity of the pore water may have caused flocculation of the clay particles that gave the sediment a structure that was destroyed during remoulding. Additionally, the presence of a "honeycomb" of hydrate veins may also have given the sediment support which allowed it to retain a high water content and low strength at almost 300kPa overburden pressure.

When considering the volumes of hydrate seen in the NGHP-1 samples, it was found that dissociation of such a hydrate presence could increase the water content of the sediment by up to 50%. This would cause significant changes in the strength of the material. The decrease in salinity caused by this hydrate dissociation may cause the sediment to increase in strength, however this affect may be masked by the impact of water content increase. It was concluded therefore, that hydrate dissociation would not only alter the strength of the host sediment by causing an influx of fresh water, but also result in the removal of a potentially important structural component of the sediment.

6.2 Recommendations for Further Work

Following on from the research presented in this thesis, there are a number of suggestions that can be made for future work involving the Gas Hydrate Resonant Column. Further investigations into synthetic, laboratory grown hydrates could take the following directions:

- It is clear that methane hydrate affects sediments differently depending on particle size and shape in "excess gas" conditions. The formation of hydrate in different sediment types, using "excess water" conditions would investigate if this were true for hydrates which do not cement the sediment, but form part of the load bearing frame. The sediment mixes utilised in the different sediment type tests described in Section 3.4 could be used, with the results directly comparable to the results given in this thesis.
- The concerns highlighted in the literature regarding the affect of hydrate former could be investigated in the GHRC by using an alternative gas to form hydrate. The substitution of carbon dioxide for methane gas could be made with identical tests carried out as those presented in this research, allowing for direct comparison of how methane and carbon dioxide hydrate affect sediment properties.
- Developments in methods of making hydrate from dissolved gas (Spangenberg & Ku-

lenkampff, 2005) could allow for methane or carbon dioxide hydrate to be made out of solution. Slight modifications to the GHRC may be necessary for this to be carried out. These tests would also give a direct comparison with the results in this thesis, which would increase information on the morphology of hydrate grown under different conditions.

With regard to apparatus development, it would be advantageous to be able to measure compressional wave velocity of saturated specimens directly, rather than the indirect method currently used from flexure. Conversion of the GHRC to take such measurements could be done via the addition of a Drnevich "Long–Tor" drive head.

The testing of natural methane hydrate samples in the GHRC has a long way to go before becoming a serious application of the apparatus. At present, there are not the facilities to transfer hydrate samples at *in–situ* conditions into the resonant column. If depressurisation of samples could be done without the degree of sample disturbance documented in Chapter 5, it may be possible to transfer them into the GHRC for resonant column testing. However, a better coarse of action may be to use the GHRC in conjunction with pressurised core loggers such as Geotek's multi–sensor core logger: pressure (Schultheiss et al., 2008).

The high resolution CT scanning equipment available at the University of Southampton could provide further insight into hydrate morphology, in natural and synthetic samples. Forming hydrate in a number of sediments in the GHRC and freezing before depressurisation would allow for the hydrate to be observed through CT scanning. If samples 10mm in size were scanned, features larger than 8μm could be distinguished by the scanner. With regard to imaging natural samples, any further observation at high resolution progresses the knowledge of hydrate morphology in the field, and so can surely be a worthwhile endeavour.

APPENDIX A

Cementing Models

The contact cement theory (CCT) predicts the effective bulk and shear modulus of a dry cemented sphere pack to be (Dvorkin et al., 2000):

$$K_{CCT} = \frac{n(1-\phi_c)}{6}(K_c + \frac{4}{3}G_c)S_n$$
$$G_{CCT} = \frac{3}{5}K_{CCT} + \frac{3n(1-\phi_c)}{20}G_c S_\tau$$

Where K_c and G_c are the bulk and shear moduli of the cement respectively; ϕ_c is the critical porosity of the uncemented grain pack; and n is the average number of contacts per grain. Parameters S_n and S_τ relate to the normal stiffness of a cemented two grain combination. It depends on the amount of contact cement and the properties of the grains and cement as defined by the following relationships (Mavko et al., 1998; Dvorkin et al., 2000):

$$S_n = A_n\alpha^2 + B_n\alpha + C_n$$
$$A_n = -0.024153\Lambda_n^{-1.3646}$$
$$B_n = 0.20405\Lambda_n^{-0.89008}$$
$$C_n = 0.00024649\Lambda_n^{-1.9864}$$
$$S_\tau = A_\tau(\Lambda_\tau,\nu)\alpha^2 + B_\tau(\Lambda_\tau,\nu)\alpha + C_\tau(\Lambda_\tau,\nu)$$
$$A_\tau(\Lambda_\tau,\nu) = -10^{-2}(2.26\nu^2 + 2.07\nu + 2.3)\Lambda_\tau^{0.079\nu^2+0.1754\nu-1.342}$$
$$B_\tau(\Lambda_\tau,\nu) = (0.0573\nu^2 + 0.0937\nu + 0.202)\Lambda_\tau^{0.0274\nu^2+0.0529\nu-0.8765}$$
$$C_\tau(\Lambda_\tau,\nu) = -10^{-4}(9.654\nu^2 + 4.945\nu + 3.1)\Lambda_\tau^{0.01867\nu^2+0.4011\nu-1.8186}$$
$$\Lambda_n = \frac{2G_c}{\pi G}\frac{(1-\nu)(1-\nu_c)}{1-2\nu_c}$$
$$\Lambda_\tau = \frac{G_c}{\pi G}$$

Where G and ν are the shear modulus and Poisson's ratio of the grain material respectively; and G_c and ν_c are the shear modulus and Poisson's ratio of the cement, respectively. The parameter

α defines the amount of contact cement, by relating the critical porosity ϕ_c and the reduced porosity of the grain pack with hydrate presence $\overline{\phi}$ to the number of grain contacts n (Dvorkin et al., 2000). The cement configurations depicted in figure 2.6 are accounted for by two forms of α:

$$\text{(a)} : \alpha = 2\left[\frac{\phi_c - \overline{\phi}}{3n(1-\phi_c)}\right]^{0.25}$$

$$\text{(b)} : \alpha = \left[\frac{2(\phi_c - \overline{\phi})}{3(1-\phi_c)}\right]^{0.5}$$

The above CCT theory is only valid for small concentrations of cement, namely those that give a residual porosity greater than approximately 25%. Dvorkin et al. (1999b), however, have extended CCT to higher cement concentrations by combining it with other effective medium modelling techniques.

Pore filling model

Gassmann (1951) found the bulk modulus of a saturated sediment by using the bulk moduli of the constituent parts:

$$K = K_d + \frac{(1 - \frac{K_d}{K_m})^2}{\frac{\phi}{K_f} + \frac{1-\phi}{K_m} - \frac{K_d}{K_m^2}}$$

Where K_f is the bulk modulus of the fluid; K_m is the average bulk modulus of the soil grains; K_d is the bulk modulus of the dry frame; and ϕ is the porosity of the rock.

The altered fluid bulk moduli can be found from the Reuss (1929) isostress average of the water and gas hydrate bulk moduli (K_f and K_h respectively):

$$K_{fh} = \left[\frac{S_h}{K_h} + \frac{1 - S_h}{K_f}\right]^{-1}$$

Where K_{fh} is the resultant bulk modulus for the hydrate/water mix and S_h is the volumetric concentration of hydrate in the pore space.

As G is not affected by water content, shear modulus is found for the dry sediment frame, via the Hertz–Mindlin contact theory, and modified Hashin–Shtrikman bounds (Dvorkin et al.,

2000).

The effective bulk K_{HM} and shear G_{HM} moduli of a dry sediment frame at critical porosity are:

$$K_{HM} = \left[\frac{n^2(1-\phi_c)^2 G^2}{18\pi^2(1-\nu)^2} P\right]^{\frac{1}{3}}$$
$$G_{HM} = \frac{5-4\nu}{5(2-\nu)} \left[\frac{3n^2(1-\phi_c)^2 G^2}{2\pi^2(1-\nu)^2} P\right]^{\frac{1}{3}}$$

Where G and ν are the shear modulus and Poisson's ratio of the solid phase respectively; P is the effective pressure; and n is the average number of contacts per grain.

For a sediment at less than critical porosity, a modified lower Hashin–Shtrikman bound is used (Dvorkin & Nur, 1996):

$$K_{dry} = \left[\frac{\phi/\phi_c}{K_{HM} + \frac{4}{3}G_{HM}} + \frac{1-\phi/\phi_c}{K + \frac{4}{3}G_{HM}}\right]^{-1} - \frac{4}{3}G_{HM}$$
$$G_{dry} = \left[\frac{\phi/\phi_c}{G_{HM} + Z} + \frac{1-\phi/\phi_c}{G + Z}\right]^{-1} - Z$$
$$Z = \frac{G_{HM}}{6}\left(\frac{9K_{HM} + 8G_{HM}}{K_{HM} + 2G_{HM}}\right)$$

Frame Building Model

To calculate the altered solid phase bulk modulus (K_{mh}) and shear modulus (G_{mh}), Hill's average formula can be used (Hill, 1952). :

$$K_{mh} = \frac{1}{2}\left[\sum_{i=1}^{N} \varphi_i K_i + \left(\sum_{i=1}^{N} \frac{\varphi_i}{K_i}\right)^{-1}\right]$$
$$G_{mh} = \frac{1}{2}\left[\sum_{i=1}^{N} \varphi_i G_i + \left(\sum_{i=1}^{N} \frac{\varphi_i}{G_i}\right)^{-1}\right]$$

Where φ_i is the volumetric fraction of the i-th constituent, K_i anf G_i are the bulk and shear moduli for each constituent respectively, and N is the number of mineral constituents.

APPENDIX B

3D CT images of NGHP-1 core sections

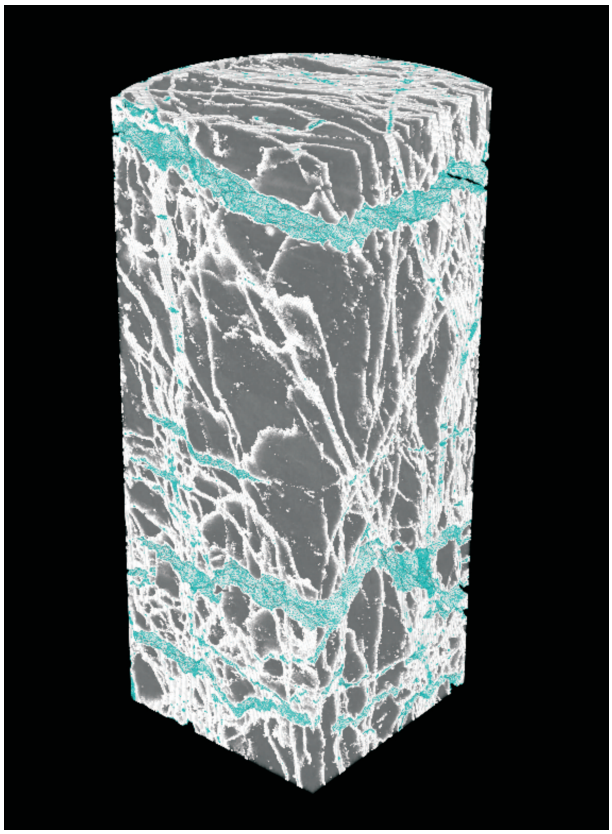

Figure B-1: Image of core section NGHP-1-21C-02E 23-46cm: top with the hydrate highlighted in white and the voids stripped away. The rims of the voids are highlighted in blue.

(a) Initial CT reconstruction of the top of the section

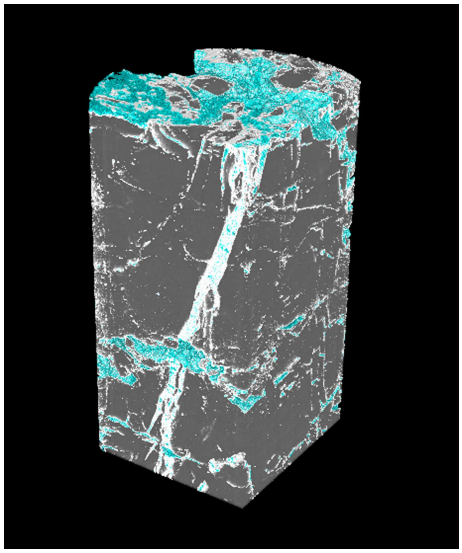

(b) Image of the core section with the hydrate highlighted in white and the voids stripped away. The rims of the voids are highlighted in blue.

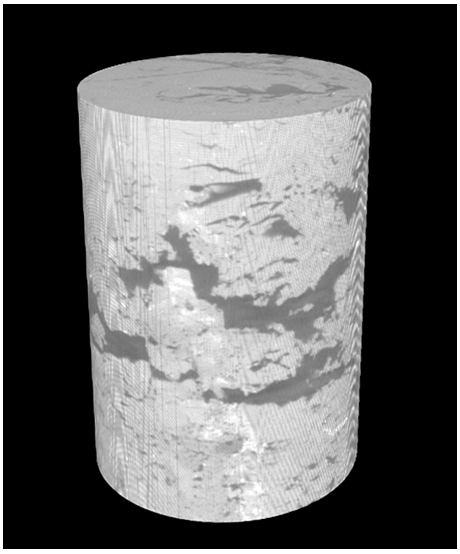

(c) Initial CT reconstruction of the bottom of the section

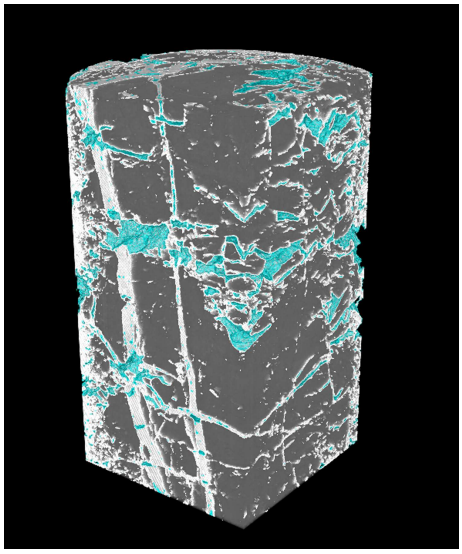

(d) Initial CT reconstruction of the bottom of the section

Figure B-2: 6-26 3D CT images

Images of frozen cores

(a) 6-26cm

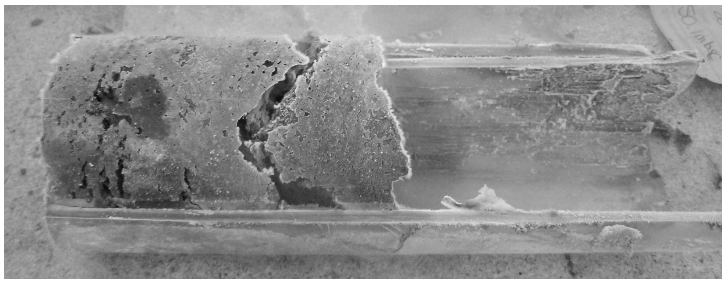

(b) 26-46cm

Figure B-3: Photographs of cores NGHP-1-10B-08Y, sections 6–26cm and 26–46cm in their frozen state

(a) 46-66cm

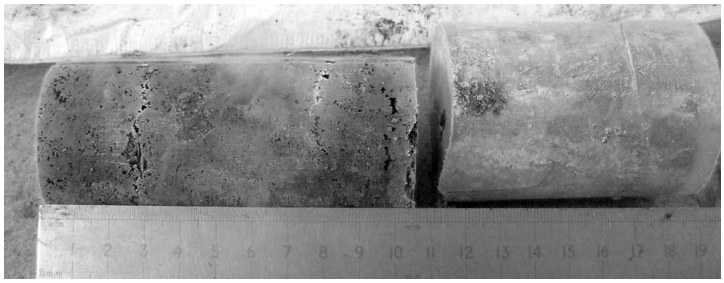

(b) NGHP-1-21C-02E core, section 23-46cm

Figure B-4: Photographs of cores NGHP-1-10B-08Y section 46–66cm and NGHP-1-21C-02E, section 23–46cm in their frozen state

(a) 6-26cm

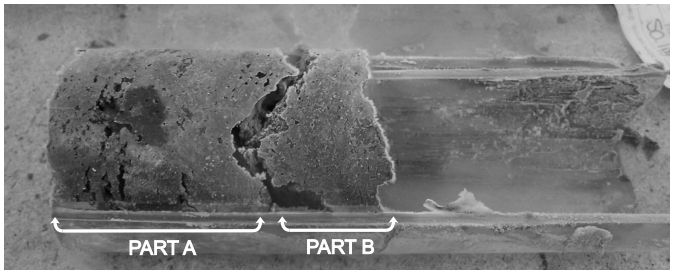

(b) 26-46cm

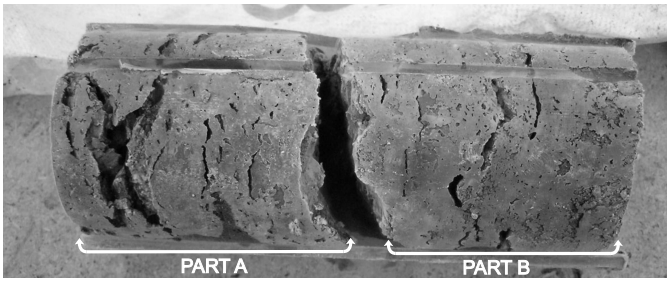

PART C = Leftover trimmings

(c) 46-66cm

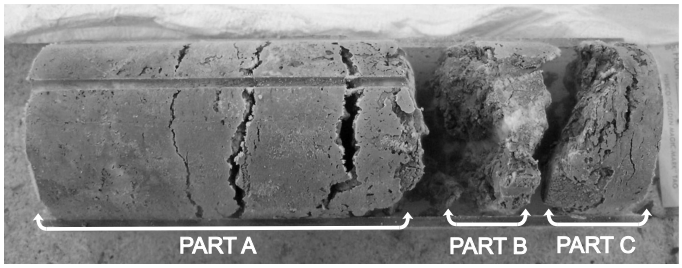

(d) 66-86cm

Figure B-5: Photographs of frozen core sections from core NGHP-1-10B-08Y with parts indicated.

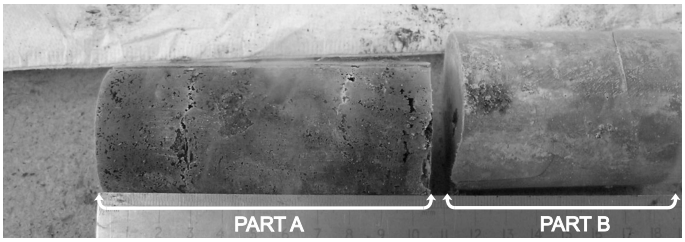

Figure B-6: Photograph of frozen core section NGHP-1-21C-02E 23-46cm with parts indicated.

References

Ashi, J. (1999). Large submarine landslides associated with decomposition of gas hydrates. *Landslide News*, 12, 17–19.

Ashi, J., Tokuyama, H., & Tiara, A. (2002). Distribution of methane hydrate bsrs and its implication for the prism growth in the nankai trough. *Marine Geology*, 187(1), 177–191.

ASTM-D5550-06 (1997). Standard test method for specific gravity of soil solids by gas pycnometer. *American Standard of Testing Methods*, ASTM International, West Conshohocken, PA.

ASTM-E1441-00 (2000). Standard guide for computed tomography (CT). *American Standard of Testing Methods*, ASTM International, West Conshohocken, PA.

Atkinson, J. H. (2000). Non–linear soil stiffness in routine design. *Géotechnique*, 50(5), 487–508.

Aubouin, J., von Huene, R., Azema, J., Coulbourn, W. T., Cowan, S. S., Curiale, J. A., Dengo, C. A., Faas, R. W., Harrison, W. E., Hesse, R., Ladd, J. W., Muzylov, N., Shiki, T., Thomson, P. R., Westberg, M., & Orlofsky, S. (1982). *Initial Reports of the Deep Sea Drilling Project covering Leg 67*, volume Initial Reports of the Deep Sea Drilling Project 67. College Station, TX.

Baker, P. E. (1974). Experiments on hydrocarbon gas hydrates in unconsolidated sand. In I. R. Kaplan (Ed.), *Natural Gases in Marine Sediments* (pp. 227–234). New York: Plenum Press.

Bathe, M., Vagle, S., Saunders, G. A., & Lambson, E. F. (1984). Ultrasonic wave velocities in the structure ii clathrate hydrate THF-17H2O. *Journal of Material Science Letters*, 3, 904–906.

Bennell, J. D. & Smith (1991). A review of laboratory shear wave techniques and attenuation measurement with particular reference to the resonant column. In J. Hovem, M. D. Richardson, & R. D. Stoll (Eds.), *Shear Waves in Marine Sediment*. Kluwer Academic Publishers.

Berge, L. I., Jacobsen, K. A., & Solstad, A. (1999). Measured acoustic wave velocities of R11 hydrate samples with and without sand as a function of hydrate concentration. *Journal of Geophysical Research*, 104(B7), 15415–15424.

Best, A. I., Huggett, Q. J., & Harris, A. J. K. (2001). Comparison of *in–situ* and laboratory acoustic measurements on Lough Hyne marine sediments. *Journal of the Acoustical Society of America*, 110(2), 695–709.

Bjerrum, L. & Rosenqvist, I. (1956). Some experiments with artificially sedimented clays. *Géotechnique*, 6(3), 124–136.

Boadu, F. K. (1997). Fractured rock mass characterization parameters and seismic properties: Analytical studies. *Journal of Applied Geophysics*, 36, 1–19.

Boadu, F. K. & Long, L. T. (1996). Effects of fractures on seismic–wave velocity and attenuation. *Geophysical Journal International*, 127, 86–110.

Bolton, M. D. (1986). The strength and dilatency of sands. *Géotechnique*, 36(1), 65–78.

Booth, J. S., Winters, W. J., & Dillon, W. P. (1994). Circumstantial evidence of gas hydrate and slope failure associations on the united states atlantic continental margin. In E. D. Sloan, J. Happel, & W. J. Hnatow (Eds.), *International Conference on Natural Gas hydrates*, number 715 in Annals of the New York Academy of Sciences (pp. 487–489).

Booth, J. S., Winters, W. J., Dillon, W. P., Clennell, M. B., & Rowe, M. M. (1998). Major occurrences and reservoir concepts of marine clathrate hydrates: implications of field evidence. In P. Henriet & J. Meinert (Eds.), *Gas Hydrates: relevance to world margin stability and climate change* (pp. 113–128). Geol. Soc. Spec. Publ.

Brewer, P. G., Orr, F. M., Friederich, G., Kvenvolden, K. A., Orange, D. L., McFarlane, J., & Kirkwood, W. (1997). Deep ocean field test of methane hydrate formation from a remotely operated vehicle. *Geology*, 25(5), 407–410.

Brooks, J. M., Kennicutt, M. C., Fay, R. R., Macdonald, T. J., & Sassen, R. (1984). Thermogenic gas hydrates in the Gulf of Mexico. *Science*, 225, 409–411.

BS-EN-ISO-21068-2 (2008). Chemical analysis of silicon-carbide containing raw materials and refractory products. Part 2: Determination of loss on ignition, total carbon, free carbon and silicon carbide, total and free silica and total and free silicon (ISO 21068-2:2008). *British Standards Methods of Test for Soils for Civil Engineering Purposes*, British Standards Institution, London.

BS1377:2 (1990). Classification tests. *British Standards Methods of Test for Soils for Civil Engineering Purposes*, British Standards Institution, London.

BS1377:7 (1990). Shear Strength Tests (total stress tests). *British Standards Methods of Test for Soils for Civil Engineering Purposes*, British Standards Institution, London.

Buckingham, M. (2005). Compressional and shear wave properties of marine sediments: Comparisons between theory and data. *The Journal of the Acoustical Society of America*, 17(1), 137–152.

Buffett, B. A. & Zatsepina, O. Y. (2000). Formation of gas hydrate from dissolved gas in natural porous media. *Marine Geology*, 164, 69–77.

Bui, M. T. (2009). *Influence of some particle characteristics on the small strain response of granular materials*. PhD thesis, University of Southampton.

Cabalar, A. F. (2007). *A study of some impacts of structure on the mechanical behaviour of geomaterials*. PhD thesis, University of Southampton.

Cameron, I., Handa, Y. P., & Baker, T. H. W. (1990). Compressive strength and creep behaviour of hydrate–consolidated sand. *Canadian Geotechnical Journal*, 27, 255–258.

Cascante, G. (1996). *Propagation of Mechanical Waves in Particulate Materials*. PhD thesis, University of Waterloo, Ontario.

Cascante, G., Santamarina, C., & Yassir, N. (1998). Flexural excitation in a standard torsional-resonant column device. *Canadian Geotechnical Journal*, 35, 478–490.

Chand, S. & Minshull, T. A. (2003). Seismic constraints on the effects of gas hydrate on sediment physical properties and fluid flow: a review. *Geofluids*, 3, 275–289.

Chand, S., Minshull, T. A., Gei, D., & Carcione, J. M. (2004). Elastic velocity models for gas–hydrate–bearing sediments—a comparison. *Geophysical Journal Institute*, 159, 573–590.

Chandler, R. J. (2000). Clay sediments in depositional basins: the geotechnical cycle. *Quarterly Journal of Engineering Geology and Hydrogeology*, 42(2), 7–39.

Chapoy, A., Mohammadi, A. H., Richon, D., & Tohidi, B. (2004). Gas solubility measurement and modeling for methane–water and methane–ethane–*n*–butane–water systems at low temperature conditions. *Fluid Phase Equilibria*, 220, 113–121.

Clayton, C. R. I., Abbireddy, C. O. R., & Schiebel, R. (2008a). A method of estimating the form of coarse particulates. *Géotechnique*, ahead of print, doi: 10.1680/geot.2007.00195.

Clayton, C. R. I., Priest, J. A., & Best, A. I. (2005). The effects of disseminated methane hydrate on the dynamic stiffness and damping of a sand. *Géotechnique*, 55(6), 423–434.

Clayton, C. R. I., Priest, J. A., Bui, M., Zervos, A., & Kim, S. G. (2008b). The Stokoe resonant column apparatus: effects of stiffness, mass and specimen fixity. *Géotechnique*, ahead of print, doi: 10.1680/geot.2007.00096.

Clayton, C. R. I., Theron, M., & Vermeulen, N. J. (2004). The effect of particle shape on the behaviour of gold tailings. *Advances in Geotechnical Engineering: The Skempton Conference*, 1, 393–404.

Clayton, C. R. I., Xu, M., & Bloodworth, A. G. (2006). A laboratory study of the development of earth pressure behind integral bridge abutments. *Géotechnique*, 56(8), 561–571.

Clennell, M. B., Hovland, M., Booth, J. S., Henry, P., & Winters, W. J. (1999). Formation of natural gas hydrates in marine sediments. 1. conceptual model of gas hydrate growth conditioned by host sediment properties. *Journal of Geophysical Research*, 104(B10), 22985–23003.

Collett, T., Riedel, M., Cochran, J., Boswell, R., Presley, R., Kumar, P., Sathe, A., Sethi, A., Lall, M., Sibal, V., & the NGHP Expedition 01 Scientists (2008). Indian national gas hydrate program expedition 01 initial reports. *Indian Directorate General of Hydrocarbons*.

Collett, T. S. (1993). Natural gas hydrates of the prudhoe bay and kuparuk river area, north slope, alaska. *A A P G Bulletin*, 77(5), 793–812.

Collett, T. S. (2004). Gas hydrates as a future energy resource. *Geotimes*.

Collett, T. S. & Dallimore, S. R. (2000). Permafrost-associated gas hydrate. In M. D. Max (Ed.), *Natural Gas Hydrate in Oceanic and Permafrost Environments* (pp. 9–16). The Netherlands: Kluwer Academic Publishers.

Collett, T. S. & Ginsburg, G. D. (1998). Gas hydrates in the messoyakha gas field of the west siberian basin – a re-examination of the geologic evidence. *International Journal of Offshore and Polar Engineering*, 8(1).

Comins, J. D. (2001). Surface brillouin scattering. In M. Levy, H. Bass, R. Stern, & V. Keppens (Eds.), *Handbook of Elastic Properties of Solids, Liquids, and Gases. Volume 1: Dynamic Methods for Measuring the Elastic Properties of Solids* (pp. 349–378). New York: New York, Academic Press.

Coop, M. R. & Atkinson, J. H. (1993). The mechanics of cemented carbonate sands. *Géotechnique*, 43(1), 53–67.

Davidson, D. W. (1983). Gas hydrates as clathrate ices. In J. Cox (Ed.), *Natural gas hydrates: Properties, Occurrence and Recovery* (pp. 1–15). Boston: Butterworth.

Davy, H. (1811). The bakerian lecture: on some of the combinations of oxymuriatic acid and oxygen, and on the chemical relations to these principles to inflammable bodies. *Philosophical Transactions of the Royal Society of London*, 101, 1.

Dawe, R. A. & Thomas, S. (2007). A large potential methane source – natural gas hydrates. *Energy sources: Part A*, 29, 217–229.

Dickens, G. R., O'Neil, J. R., Rea, D. K., & Owen, R. M. (1995). Dissociation of oceanic methane hydrate as a cause of the carbon isotope excursion at the end of the paleocene. *Paleoceanography*, 10(6), 965–971.

Dickens, G. R., Wallace, P. J., Paull, C. K., & Borowski, W. S. (2000). Detection of methane gas hydrate in the pressure core sampler (PCS): volume–pressure–time relations during controlled degassing experiments. In C. K. Paull, R. Matsumoto, P. J. Wallace, & W. P. Cillon (Eds.), *Proceedings of ODP Scientific Results, Volume 164* (pp. 113–126). College Station. TX: Ocean Drilling Program.

Dillon, W. P. & Max, M. D. (2000). Oceanic gas hydrate. In M. D. Max (Ed.), *Natural Gas Hydrate in Oceanic and Permafrost Environments* chapter 2, (pp. 9–16). The Netherlands: Kluwer Academic Publishers.

Dugan, B. & Flemings, P. A. (2000). Overpressure and fluid flow in the new jersey continental slope: Implications for slope failure and cold seeps. *Science*, 289, 288–291.

Dugan, B. & Germaine, J. T. (2008). Near-seafloor overpressure in the deepwater Mississippi Canyon, northern Gulf of Mexico. *Geophysical Research Letters*, doi:10.1029/2007GL032275.

Durham, W., Stern, L., Kirby, S., & Circone, S. (2005). Rheological comparisons and structural imaging of sI and sII end–member gas hydrates and hydrate/sediment aggregates. In *Proceedings of the 5th International Conference on Gas Hydrates*, volume 2 (pp. 607–614). Trondheim, Norway.

Durham, W. B., Kirby, S. H., Stern, L. A., & Zhang, W. (2003). The strength and rheology of methane clathrate hydrate. *Journal of Geophysical Research*, 108(B4), doi:10.1029/2002JB001872.

Dvorkin, J., Helgerud, M. B., Waite, W. F., Kirby, S. H., & Nur, A. (2000). Introduction to physical properties and elasticity models. In M. D. Max (Ed.), *Natural Gas Hydrate in*

Oceanic and Permafrost Environments chapter 20, (pp. 245–260). The Netherlands: Kluwer Academic Publishers.

Dvorkin, J. & Nur, A. (1993). Rock physics for characterisation of gas hydrates. *US Geologcial Survey Professional Paper*, 1570, 293–298.

Dvorkin, J. & Nur, A. (1996). Elasticity of high porosity sandstones: theory for two North Sea data sets. *Geophysics*, 61, 1363–1370.

Dvorkin, J., Prasad, M., Sakai, A., & Lavoie, D. (1999a). Elasticity of marine sediments: Rock physics modeling. *Geophysical Research Letters*, 26(12), 1781–1784.

Dvorkin, J. A., Berryman, J., & Nur, A. (1999b). Elastic moduli of cemented shear packs. *Mechanics of Materials*, 31, 461–469.

Dvorkin, J. A., Nur, A., & Yin, H. (1994). Effective properties of cemented granular materials. *Mechanics of Materials*, 18(4), 351–366.

Ecker, C., Dvorkin, J., & Nur, A. (1998). Sediments with gas hydrates: Internal structure from seismic avo. *Geophysics*, 63(5), 1659–1669.

Ecker, C., Dvorkin, J., & Nur, A. M. (2000). Estimating the amount of gas hydrate and free gas from marine seismic data. *Geophysics*, 65(2), 565–573.

Francis, T. J. G. (2001). The HYACINTH project and pressure coring in the ocean drilling program. http://www.geotek.co.uk/hyacinth/reports/HYACINTH-ODP.pdf.

Gassmann, F. (1951). Elasticity of porous media. *Vierteljahrsschrift der Naturforchenden Gesselschaft*, 96, 1–23.

Gei, D. & Carcione, J. M. (2003). Acoustic properties of sediments saturated with gas hydrate, free gas and water. *Geophysical prospecting*, 51, 141–157.

Genov, G., Kuhs, W. F., Staykove, D. K., Goreshnik, E., & Salamatin, A. N. (2004). Experimental studies on the formation of porous gas hydrates. *American Mineralogist*, 89, 1228–1239.

Georgiannou, V. N. (2006). The undrained response of sands with the additions of particles of various shapes and sizes. *Géotechnique*, 56(9), 639–649.

Gibson, R. E. (1958). The progress of consolidation in a clay layer increasing in thickness with time. *Géotechnique*, 8(1), 171–182.

Ginsburg, G. D. (1998). Gas hydrate accumulation in deep–water marine sediments. In P. Henriet & J. Meinert (Eds.), *Gas Hydrates: relevance to world margin stability and climate change* (pp. 51–62). Geol. Soc. Spec. Publ.

Ginsburg, G. D. & Soloviev, V. A. (1997). Methane migration within the submarine gas–hydrate stability zone under deep–water conditions. *Marine Geology*, 137, 49–57.

Goldberg, D. (1997). The role of downhole measurements in marine geology and geophysics. *Reviews of Geophysics*, 35(3), 315–342.

Goldberg, D., Moos, D., & Anderson, R. N. (1985). Attenuation changes due to diagenesis in marine sediments. *SPWLA twenty-sixth annual logging symposium*, 26.

Goldberg, D. S., Collett, T. S., & Hyndman, R. D. (2000). Ground truth: In–situ properties of hydrate. In M. D. Max (Ed.), *Natural Gas Hydrate in Oceanic and Permafrost Environments* chapter 2, (pp. 9–16). The Netherlands: Kluwer Academic Publishers.

Guerin, G. & Goldberg, D. (2002). Sonic waveform attenuation in gas hydrate–bearing sediments from the mallik 2l–38 research well, mackenzie delta, canada. *Journal of Geophysical Research*, 107(B5), 10.1029/2001JB000556.

Guerin, G., Goldberg, D., & Meltser, A. (1999). Characterization of in situ elastic properties of gas hydrate–bearing sediments on the blake ridge. *Journal of Geophysical Research*, 104(B8), 17781–17795.

Hamilton, E. L. (1972). Compressional-wave attenuation in marine sediments. *Geophysics*, 37, 620–646.

Handa, Y. P. (1990). Effect of hydrostatic pressure and salinity on the stability of gas hydrate. *Journal of Physical Chemistry*, 94, 2652–2657.

Handa, Y. P. & Stupin, D. (1992). Thermodynamic properties and dissociation characteristics of methane and propane hydrates in 70 å radius silica gel. *Journal of Physical Chemistry*, 96, 8599–8603.

Hardin, B. O. & Drnevich, V. P. (1972). Shear modulus and damping in soils: design equations and curves. *Journal of the Soil Mechanics and Foundations division ASCE*, 98(7), 667–691.

Hardin, B. O. & Richart, F. E. (1963). Elastic wave velocities n granular soils. *ASCE Journal of Soil Mechanics and Foundations Division*, 89(SM1), 33–65.

Hatcher, R. D. (1995). *Structural Geology. Principles, concepts and problems*. New Jersey: Prentice Hall, 2nd edition.

Helgerud, M. B. (2001). *Wave Speeds in Gas Hydrate and Sediments containing gas hydrates: A laboratory and modeling study*. PhD thesis, Stanford University.

Helgerud, M. B., Dvorkin, J., & Nur, A. (2000). Rock physics characterization for gas hydrate reservoirs. *Annals of the New York Academy of Sciences*, 912, 116–125.

Helgerud, M. B., Dvorkin, J., Nur, A., Sakai, A., & Collett, T. (1999). Elastic wave velocity in marine sediments with gas hydrates: Effective medium modeling. *Geophysical Research Letters*, 26(13), 2021–2024.

Hesselbo, S. P., Grocke, D. R., Jenkyns, H. C., Bjerrum, C. J., Farrimond, P., Morgans-Bell, H. S., & Green, O. R. (2000). Massive dissociation of gas hydrate during a jurassic oceanic anoxic event. *Nature*, 406, 392–395.

Hight, D. W., Georgiannou, V. N., Martin, P. L., & Mundegar, A. K. (1999). Flow slides in micaeous sands. *Problematic Soils*, 1, 945–958.

Hill, R. (1952). The elastic behaviour of a crystalline aggregate. *Proceedings of the Physical Society of London*, A65, 349–354.

Holbrook, W. S., Hoskins, H., Wood, W. Y., Stephen, R. A., & Lizarralde, D. (1996). Methane hydrate and free gas on the blake ridge from vertical seismic profiling. *Science*, 273, 1840–1843.

Holland, M., Schultheiss, P., Roberts, J., & Druce, M. (2008). Observed gas hydrate morphologies in marine sediments. In *Proceedings of the 6th International Conference on Gas Hydrates*, volume 1 Vancouver, Canada.

Hulse, R. & Cain, J. (2000). *Structural Mechanics*. Basingstoke, Hampshire: Palgrave, 2nd edition.

Hyndman, R. D. & Davis, E. E. (1992). A mechanism for the formation of methane hydrate and seafloor bottom–simulating reflectors by vertical fluid expulsion. *Journal of Geophysical Research*, 97(B5), 7025–7041.

Hyndman, R. D. & Spence, G. D. (1992). A seismic study of methane hydrate marine bottom simulating reflectors. *Journal of Geophysical Research*, 97, 6683–6698.

Ismail, M. A., Joer, H. A., Sim, W. H., & Randolph, M. F. (2002). Effect of cement type on shear behaviour of cemented calcareous soil. *Journal of Geotechnical and Geoenvironmental Engineering*, 128(6), 520–529.

ISO-13320-1 (1999). Particle size analysis - Laser diffraction methods - Part 1: General Principles. *International Standardisation Organisation*.

Iwasaki, T. & Tatsuoka, F. (1977). Effects of grain size and grading on dynamic shear moduli of sand. *Soils and Foundations*, 17(3), 19–35.

Jahren, A. H., Arens, N. C., Sarmiento, G., Guerrero, J., & Amundson, R. (2001). Terrestrial record of methane hydrate dissociation in the early cretaceous. *Geology*, 29(2), 159–162.

Jakobsen, M., Hudson, J. A., Minsull, T. A., & Singh, S. C. (2000). Elastic properties of hydrate-bearing sediments using effective medium theories. *Journal of Geophysical Research*, 105, 561577.

Johnston, D. H., Toksoz, M. N., & Timur, A. (1979). Attenuation of seismic waves in dry and saturated rocks: mechanisms. *Geophysics*, 44, 691–711.

Jones, T. D. (1986). Pore fluids and frequency dependent wave propagation in rocks. *Geophysics*, 51(10), 1939–1953.

Kaplan, I. R. (1974). *Natural Gases in Marine Sediments*. New York: Plenum Press, 1st edition.

Katz, D. L. & Lee, R. E. (1990). *Natural gas engineering*. New York: McGraw–Hill.

Kiefte, H., Clouter, M. J., & Gagnon, R. E. (1985). Determination of acoustic velocities of clathrate hydrates by brillouin spectroscopy. *Journal of Physical Chemistry*, 89, 3103–3108.

Kirchner, M. T., Boese, R., Billups, E., & Norman, L. R. (2004). Gas hydrate single–crystal structure analyses. *Journal of the American Chemical Society*, 126, 9407–9412.

Kneafsey, T. J., Tomisuta, L., Moridis, G. J., Seol, Y., Friefeld, B. M., Taylor, C. T., & Gupta, A. (2007). Methane hydrate formation and dissociation in a partially saturated core-scale sand sample. *Journal of Petroleum Science and Engineering*, 56(1-3), 108–126.

Koh, C. A. (2002). Towards a fundamental understanding of gas hydrates. *Chemical Society Review*, 31, 157–167.

Kuhs, W. F., Klapproth, A., Gotthardt, F., Techmer, K., & Heinrichs, T. (2000). The formation of meso– and macroporous gas hydrates. *Geophysical research letters*, 27(18), 2929–2932.

Kvenvolden, K. (1988). Methane hydrate a major reservoir of carbon in the shallow geosphere? *Chemical Geology*, 71(1), 41–51.

Kvenvolden, K. & McDonald, T. (1985). Gas hydrates of the middle america trench, deep sea drilling project leg 84. In R. Von-Huene & J. Aubouin (Eds.), *Initial Reports of the Deep Sea Drilling Project* (pp. 664–682). Washington D.C.: U.S. Government Printing Office.

Kvenvolden, K. A. (1995). A review of the geochemistry of methane in natural gas hydrate. *Organic Geochemistry*, 23(11–12), 997–1007.

Kvenvolden, K. A., Ginsburg, G. D., & Soloviev, V. A. (1993). Worldwide distribution of subaquatic gas hydrates. *Geo–Marine Letters*, 13, 32110.

Larsen, H. C., Duncan, R. A., Allan, J. F., & Brooks, K. (1999). *Southest Greenland margin*, volume Proceedings of the Ocean Drilling Program Scientific Results, Leg 163. College Station, TX: Ocean Drilling Program.

Lee, J. S., Guimaraes, M., & Santamarina, C. (2007). Micaeous sands: Microscale mechanisms and macroscale responses. *Journal of Geotechnical and Geoenvironmental Engineering*, 133(9), 1136–1143.

Lee, M., Watkins, J. S., Moore, C. J., Bachman, S. B., Beghtel, F., Butt, A., Didyk, B. M., Dmitriev, Y. I., Leggett, J. K., Lundberg, N. F., McMillen, K. J., Niitsuma, N., Rodriguez-Torres, R., Shephard, L. F., Shipley, T. H., Stephan, J.-F., & Stradner, H. (1982). *Leg 66 of the cruises of the drilling vessel Glomar Challenger; March to May, 1979*, volume Initial Reports of the Deep Sea Drilling Project 66. College Station, TX.

Lee, M. W. & Collett, T. S. (2001). Elastic properties of gas hydrate bearing sediments. *Geophysics*, 66, 763–771.

Lee, M. W. & Collett, T. S. (2008). Unique problems associated with seismic analysis of partially gas-saturated unconsolidated sediments. *Marine and Petroleum Geology*, in–press.

Lee, M. W., Hutchinson, D. R., Collett, T. S., & Dillon, W. P. (1996). Seismic velocities for hydrate–bearing sediments using weighted equation. *Journal of Geophysical Research*, 101(B9), 20347–20358.

Leucci, G. & Giorgi, L. D. (2006). Experimental studies on the effects of fracture on the P and S wave velocity propagation in sedimentary rock ("Calcarenite del Salento"). *Engineering Geology*, 84, 130–142.

Majarowicz, J. A. & Osadetz, K. G. (2001). Gas hydrate distribution and volume in canada. *AAPG Bulletin*, 85(7), 1211–1230.

Makogon, Y., Makogon, T., & Malyshev, A. (2008). Technical limits for development of natural gas hydrate deposits. In *Proceedings of the 6th International Conference on Gas Hydrates*, volume 1 Vancouver, Canada.

Makogon, Y. F., Holditch, S. A., & Makogon, T. Y. (2007). Natural gas-hydrates – a potential energy source for the 21st century. *Journal of Petroleum Science and Engineering*, 56(1–3), 14–31.

Malone, R. D. (1985). Gas hydrates. *Technical Report, U.S. Dep. of Energy, Washington, DC.*, DOE/METC/SP-218.

Matsushima, J. (2005). Attenuation measurements from sonic waveform logs in methane hydrate–bearing sediments at the nankai trough exploratory well of tokai, central japan. *Geophysical Research Letters*, 32(L03306).

Mavko, G., Mukerji, T., & Dvorkin, J. (1998). *Rock Physics Handbook. Tools for seismic analysis in porous media*, volume 1. Cambridge University Press.

Mavko, G. & Nur, A. (1979). Wave attenuation in partially saturated rocks. *Geophysics*, 44, 161–178.

Max, M. D. (2000). Hydrate resource, methane fuel and a gas-based economy? In M. D. Max (Ed.), *Natural Gas Hydrate in Oceanic and Permafrost Environments* chapter 2, (pp. 9–16). The Netherlands: Kluwer Academic Publishers.

Meirovitch, L. (2001). *Fundamentals of Vibrations*. New York: McGraw–Hill, international edition.

Mienert, J. & Buenz, S. (2001). Are storegga slide multi-phase events off the mid-norwegian margin triggered by gas hydrate destabilisations? *AGU Fall Meeting Abstracts*.

Mikami, J., Masuda, Y., Uchida, T., Satoh, T., & Takeda, H. (2000). Dissociation of natural gas hydrates observed by x-ray ct scanner. In G. D. Holder & P. R. Bishnoi (Eds.), *Gas hydrates: Challenges for the future* (pp. 1011–1020). New York: New York Academy of Sciences.

Milkov, A. V. (2004). Global estimates of hydrate–bound gas in marine sediments: How much is really out there? *Earth–science review*, 66, 183–197.

Miller, J. J., Lee, M. W., & von. Huene, R. (1991). A quantitative analysis of gas hydrate phase boundary reflection (bsr), offshore peru. *A A P G Bulletin*, 75, 910–924.

Minshull, T., Singh, S., & Westbrook, G. (1994). Seismic velocity structure of a gas hydrate reflector, offshore western columbia, from full waveform inversion. *Journal of Geophysical Research*, 99, 4715–4734.

Miranda, C. & Matsuoka, T. (2008). First-principles study on mechanical properties of ch_4 hydrate. In *Proceedings of the 6th International Conference on Gas Hydrates*, volume 1 Vancouver, Canada.

Mitchell, J. K. (1976). *Fundamentals of soils behaviour*. New York: Wiley.

Murdock, L. J., Brook, K. M., & Dewar, J. D. (1991). *Concrete: Materials and Practice*. Edward Arnold, 6 edition.

Murphy, W. F., Winkler, K. W., & Kleinberg, R. L. (1986). Acoustic relaxation in sedimentary rocks: Dependence on grain contacts and fluid saturation. *Geophysics*, 5, 757766.

Neville, A. M. (1995). *Properties of Concrete*. Longman group Ltd, 4 edition.

Novak, M. & Kim, T. C. (1981). Resonant column technique for the dynamic testing of cohesive soils. *Canadian Geotechnical Journal*, 18, 443–455.

Olhoeft, G. R. (1976). *Electrical properties of rocks*. Physics and Chemistry of Rocks and Minerals. Wiley.

Paull, C. K., III, W. U., & Dillon, W. P. (2000). Potential role of gas hydrate decomposition in generating submarine slope failures. In M. D. Max (Ed.), *Natural Gas Hydrate in Oceanic and Permafrost Environments* chapter 2, (pp. 9–16). The Netherlands: Kluwer Academic Publishers.

Paull, C. K., Matsumoto, R., Wallace, P., & Party, O. L. . S. (1996). Proceedings of the odp initial reports. *Ocean Drilling Program, College Station. TX*, 164.

Pearson, C., Murphy, J., & Hermes, R. (1986). Acoustic and resistivity measurements on rock samples containing tetrahydrofuran hydrates: laboratory analogues to natural gas hydrate deposits. *Journal Geophysical Research*, 91(B14), 14132–14138.

Pecher, I. A. & Holbrook, W. S. (2000). Seismic methods for marine methane hydrate/free gas reservoirs. In M. D. Max (Ed.), *Natural Gas Hydrate in Oceanic and Permafrost Environments* chapter 22, (pp. 275–294). The Netherlands: Kluwer Academic Publishers.

Pecher, I. A., Minshull, T. A., Singh, S. C., & von. Huene, R. (1996). Velocity structure of a bottom simulating reflector, offshore peru. results from waveform inversion. *Earth and Planetary Science Letters*, 139, 459–469.

Peng, D. Y. & Robinson, D. B. (1976). A new two–constant equation of state. *Industrial and Engineering Chemistry Fundamentals*, 15(1), 59–64.

Pettigrew, T. L. (1992). The design and operation of a wireline pressure core sampler (pcs). *ODP Technical note*, 17.

Pooladi-Darvish, M. (2004). Gas production from hydrate reservoirs and it's modelling. *Journal of Petroleum Technology*, 61, 65–71.

Powrie, W. (1997). *Soil mechanics: concepts and applications*. Abingdon: SPON Press, 2 edition.

Priest, J. A. (2004). *The Effects of Methane Gas Hydrate on the Dynamic Properties of a Sand*. PhD thesis, University of Southampton.

Priest, J. A., Best, A., & Clayton, C. R. I. (2005). A laboratory investigation into the seismic velocities of methane gas hydrate-bearing sand. *Journal of Geophysical Research*, 110, B04102.

Priest, J. A., Best, A., & Clayton, C. R. I. (2006). Attenuation of seismic waves in methane gas hydrate-bearing sand. *Geophysical Journal International*, 164, 149–159.

Reuss, A. (1929). Calculation of flow limits of mixed crystals on the basis of plasticity of single crystals. *Zeitschrift fur Angewandte Mathematic und Mechanik*, 9, 49–58.

Richart, F. E., Hall, J. R., & Woods, R. D. (1970). *Vibrations of soils and foundations*. New Jersey: Prentice Hall, 1 edition.

Riedel, M., Collett, T. S., Malone, M. J., & Expedition 311 Scientists (2006). Cascadia margin gas hydrates. *Proceedings of the IODP Expedition Reports*, 311.

Rowe, P. W. (1972). The relevance of soil fabric to site investigation practice. *Géotechnique*, 22(2), 195–300.

Sakai, A. (2000). Can we estimate the amount of gas hydrate by seismic methods? In G. D. Holder & P. R. Bishnoi (Eds.), *Gas hydrates: Challenges for the future*, number 912 (pp. 374391). New York: New York Academy of Sciences.

Saxena, S. K., Avramidis, A. S., & Reddy, K. R. (1988). Dynamic moduli and damping ratios for cemented sands at low strains. *Canadian Geotechnical Journal*, 25, 353–367.

Schultheiss, P., Holland, M., Roberts, J., & Humphrey, G. (2008). Pressure core analysis: the keystone of a gas hydrate investigation. In *Proceedings of the 6th International Conference on Gas Hydrates*, volume 1 Vancouver, Canada.

Shaw, G. (1986). Elastic properties and equation of state of high pressure ice. *Journal of Chemical Physics*, 84, 5862–5868.

Shibuya, S., Hwang, S. C., & Mitachi, T. (1997). Elastic shear modulus of soft clays from shear wave velocity measurement. *Géotechnique*, 47(3), 593–601.

Shipley, T. H., Houston, M. H., Buffler, R. T., Shaub, F. J., McMillen, K. J., Ladd, J. W., & Worzel, J. L. (1979). Seismic evidence for widespread possible gas hydrate horizons on continental slopes and rises. *A A P G Bulletin*, 63, 2204–2213.

Singh, S. C., Minshull, T. A., & Spence, G. D. (1993). Velocity structure of a gas hydrate reflector. *Science*, 260, 204–207.

Skempton, A. W. & Northey, R. D. (1952). The sensitivity of clays. *Géotechnique*, 3(1), 30–52.

Sloan, E. D. (1998). *Clathrate Hydrates of Natural Gases*. New York: Marcel Dekker Inc., 2 edition.

Soloviev, V. A. & Ginsburg, G. D. (1997). Water segregation in the course of gas hydrate formation and accumulation in submarine gas–seepage fields. *Marine Geology*, 137, 59–68.

Spangenberg, E. & Kulenkampff, J. (2005). Physical properties of gas hydrate bearing sediments. In *Proceedings of the 5th International Conference on Gas Hydrates*, volume 2 (pp. 587–595). Trondheim, Norway.

Stern, L. A., Kirby, S. H., Durham, W. B., Circone, S., & Waite, W. F. (2000). Laboratory synthesis of pure methane hydrate suitable for measurement of physical properties and decomposition behaviour. In M. D. Max (Ed.), *Natural Gas Hydrate in Oceanic and Permafrost Environments* (pp. 9–16). The Netherlands: Kluwer Academic Publishers.

Stoll, R. D. (1974). Effects of gas hydrates in sediments. In I. R. Kaplan (Ed.), *Natural Gases in Marine Sediments* (pp. 235–248). New York: Plenum Press.

Stoll, R. D. (2002). Velocity dispersion in water-saturated granular sediment. *Journal of the Acoustical Society of America*, 111(2), 785–793.

Stoll, R. D. & Bryan, G. M. (1979). Physical properties of sediments containing gas hydrate. *Journal of Geophysical Research*, 84(B4), 1629–1634.

Stoll, R. D., Ewing, J., & Bryan, G. M. (1971). Anomalous wave velocities in sediments containing gas hydrates. *journal of Geophysical Research*, 76(8), 2090–2094.

Suess, E., Torres, M. E., Bohrmann, G., Collier, R. W., Rickart, D., Goldfinger, C., Linke, P., Heuser, A., Sahling, H., Heeschen, K., Jung, C., Nakamura, K., Grienert, J., o Pfannkuche, Trehu, A., Klinkhammer, G., Whiticar, M. J., Eisenhauer, A., Teichert, B., & Elvert, M. (2001). Sea floor methane hydrates at hydrate ridge, cascadia margin. *Natural Gas Hydrates: Occurrence, Distribution and Detection*, Geophysical Monograph 124, 87–98.

Theron, M. (2004). *The influence of fine particles of the behaviour of a rotund sand*. PhD thesis, University of Southampton.

Thevanayagam, S. (1998). Effect of fines and confining stress on the un–drained shear strength of a silty sand. *Journal of Geotechnical and Geoenvironmental Engineering*, 124(6), 479–491.

Thomsen, K. (2004). Surface area of an ellipsoid. http://home.att.net/ numericana/answer/ellipsoid.htm. last accessed 15 January 2009.

Thomson, W. T. (1993). *Theory of vibration with applications*. Prentice Hall, 4 edition.

Tinivella, U. & Accaino, F. (2000). Compressional velocity structure and poissons ratio in marine sediments with gas hydrate and free gas by inversion of refracted seismic data (south shetland islands, antarctica). *Marine Geology*, 164, 13–27.

Tohidi, B., Anderson, R., Clennell, M. B., Burgass, R. W., & Biderkab, A. B. (2001). Visual observation of gas–hydrate formation and dissociation in synthetic porous media by means of glass micromodels. *Geology*, 29(9), 867–870.

Tréhu, A. M., Bohrmann, G., Torres, M. E., & Colwell, F. S. (2006). *Drilling Gas Hydrates on Hydrate Ridge, Cascadia Continental Margin*, volume Proceedings of the Ocean Drilling Program Scientific Results, Leg 204. College Station, TX: Ocean Drilling Program.

Trehu, A. M., Long, P. E., Torres, M. E., Bohrmann, G., Rack, F. R., Collett, T. S., Goldberg, D. S., Milkov, A. V., Reidel, M., Schultheiss, P., Bangs, N. L., Barr, S. R., Borowski, W. S., Claypool, G. E., Delwiche, M. E., Dickens, G. R., Gracia, E., Guerin, G., Holland, M., Johnson, J. E., Lee, Y.-L., Liu, C.-S., Su, X., Teichart, B., Tomaru, H., Vanneste, M., Watanabe, M., & Weinberger, J. L. (2004). Three–dimensional distribution of gas hydrate beneath southern hydrate ridge: constraints from ODP leg 204. *Earth and Planetary Science letters*, 222, 845–862.

Trehu, A. M., Ruppel, C., Holland, M., Dickens, G. R., Torres, M. E., Collett, T. S., Goldberg, D., Riedel, M., & Schultheiss, P. (2006). Gas hydrates in marine sediments: lessons from scientific ocean drilling. *Oceanography*, 19(4), 124–142.

Udachin, K. A. & Ripmeester, J. A. (1999). A complex clathrate hydrate structure showing bimodal guest hydration. *Nature*, 397, 420–423.

Van Olphen, H. (1977). *An introduction to clay colloid chemistry*. New York: John Wiley and Sons Inc.

Van Passen, L. A. & Gareau, L. F. (2004). Effect of pore fluid salinity on compressibility and shear strength development of clayey soils. In R. Hack, R. Azzam, & R. Charlier (Eds.), *Engineering Geology for Infrastructure Planning in Europe*, Lecture notes in Earth Sciences (pp. 327–340). Berlin: Springer.

Vucetic, M. & Dobry, R. (1991). Effect of soil plasticity on cyclic response. *Journal of Geotechnical Engineering*, 117(1), 89–107.

Waite, W. F., Helgerud, M. B., Nur, A., Pinkston, J. C., Stern, L. A., Kirby, S. H., & Durham, W. B. (2000). Laboratory measurements of compressional and shear wave speeds through methane hydrate. *Annals of the New York Academy of Sciences*, 912, 1003–1010.

Waite, W. F., Winters, W. J., & Mason, D. H. (2004). Methane hydrate formation in partially saturated ottawa sand. *American Mineralogist*, 89, 1221–1227.

Weaver, C. E. (1989). *Clays, muds and shales*, volume 44 of *Developments in Sedimentology*. Amsterdam: Elsevier.

Wellsbury, P. & Parkes, R. J. (2000). Deep biosphere: source of methane for oceanic hydrate. In M. D. Max (Ed.), *Natural Gas Hydrate in Oceanic and Permafrost Environments* chapter 2, (pp. 9–16). The Netherlands: Kluwer Academic Publishers.

Whiffen, B. L., Keifte, H., & Clouter, M. J. (1982). Determination of acoustic velocities in xenon and methane hydrates by brillouin spectroscopy. *Geophysical Research Letters*, 9, 645648.

Winkler, K., Nur, A., & Gladwin, M. (1979). Friction and seismic attenuation on rocks. *Nature*, 277, 528531.

Winters, W. J., Dallimore, S. R., Collett, T. S., Katsube, T. J., Jenner, K. A., Cranston, R. E., Wright, J. F., Nixon, F. M., & Uchida, T. (1999). Physical properites of sediments from the JAPEX/JNOC/GSC mallik 2L–38 gas hydrate research well. In S. Dallimore, T. Uchida, & T. S. Collett (Eds.), *Scientific results from JAPEX/JNOC/GSC Mallik 2L–38 gas hydrate research well, Mackenzie Delta, Northwest Territories, Canada*, number 544 (pp. 95–100). Canada: Geological Survey of Canada Bulletin.

Winters, W. J., Dillon, W. P., Pecher, I. A., & Mason, D. H. (2000). GHASTLI–determining physical properties of sediment containing natural and laboratory formed gas hydrate. In M. D. Max (Ed.), *Natural Gas Hydrate in Oceanic and Permafrost Environments* chapter 24, (pp. 311–322). The Netherlands: Kluwer Academic Publishers.

Winters, W. J., Pecher, I. A., F, W., & Mason, D. H. (2004). Physical properties and rock physics models of sediment containing natural and laboratory–formed methane gas hydrate. *American Mineralogist*, 89, 1221–1227.

Worm, H. U., Ahmed, A. M. M., Ahmed, N. U., Islam, H. O., Hug, M. M., Hambach, U., & Lietz, J. (1998). Large sedimentation rate in the bengal delta; magnetostratigraphic dating of cenozoic sediments from northeastern bangladesh. *Geology*, 26(6), 487–490.

Yuan, T., Spence, G. D., Hyndman, R. D., Minshull, T. A., & Singh, S. C. (1999). Seismic velocity studies of a gas hydrate bottom–simulating reflector on the northern cascadia continental margin; amplitude modelling and full waveform inversion. *Journal of Geophysical Research*, 104, 1179–1191.

Yun, T. S. (2005). *Mechanical and thermal study of hydrate bearing sediments*. PhD thesis, Georgia Institute of Technology.

Yun, T. S., Francisca, F. M., Santamarina, J. C., & Ruppel, C. (2005). Compressional and shear wave velocities in uncemented sediment containing gas hydrate. *Geophysical Research Letters*, 32(10), L10609.

Zimmerman, R. W. (1991). *Compressibility of Sandstones*. Elsevier, New York.